Modeling of diffraction effects for specimen echoes simulations in ultrasonic Non-Destructive Testing (NDT)

Audrey Kamta Djakou

École Doctorale SPIGA

Thèse

Présentée pour l'obtention du grade de DOCTEUR

DE L'UNIVERSITE DU MAINE

par

Audrey KAMTA DJAKOU

Modélisation des effets de diffraction pour le calcul des échos de géométrie en CND par ultrasons

---

Spécialité : Acoustique

Soutenance prévue le 26 septembre 2016 devant le jury composé de :

Rapporteur	**M. LEBEAU Gilles**	(Professeur, Université de Nice Sophia-Antipolis, Nice)
Rapporteur	**M. MOLINET Frédéric**	(Ancien directeur de MOTHESIM, Docteur d'Etat)
Examinateur	**M. TOURNAT Vincent**	(Directeur de recherche CNRS, LAUM, Le Mans)
Examinatrice	**Mme FRADKIN Larissa**	(Professeur émerite, Directrice de Sound Mathematics Ltd., UK)
Examinateur	**M. BOUCHE Daniel**	(Directeur de recherche CEA, HDR, CEA/DAM, Arpajon)
Examinateur	**M. CALMON Pierre**	(Directeur de recherche CEA, CEA LIST, Gif-sur-Yvette)
Directrice de thèse	**Mme POTEL Catherine**	(Professeur, Université du Maine, Le Mans)
Encadrant CEA	**M. DARMON Michel**	(Expert CEA, HDR, CEA LIST, Gif-sur-Yvette)

Thèse effectuée au sein du **CEA LIST**

dans le Laboratoire de Simulation et de Modélisation en Acoustique (LSMA)

CEA Saclay, DIGITEO LABs, bât 565

91191 Gif-sur-Yvette cedex

France

en collaboration avec le

Laboratoire d'Acoustique de l'Université du Maine - UMR CNRS 6613 (LAUM)

Avenue Olivier Messiaen

72085 Le Mans cedex 09

France

Résumé

Cette thèse s'inscrit dans le cadre du développement de modèles de Contrôle Non Destructif (CND) par ultrasons intégrés dans la plateforme logicielle CIVA d'expertise en CND. Ce logiciel est notamment doté d'un modèle issu de la théorie des rayons pour le calcul des échos générés par la géométrie (surfaces d'entrée, de fond, ...) ou les structures internes des pièces inspectées. Ce modèle "rayon", dénommé « modèle spéculaire », est fondé sur l'élastodynamique géométrique et ne prend donc en compte que les réflexions spéculaires sur les diffuseurs. L'objectif de cette thèse est d'étendre ce modèle pour intégrer la diffraction par les dièdres des structures de la géométrie. La Théorie Géométrique de la Diffraction (GTD), modèle rayon de diffraction, a été un point de départ pour réaliser cette extension, mais elle diverge aux directions d'observation proches des directions de transmission vers l'avant et de réflexion spéculaire.

Cette thèse propose donc, en élastodynamique, une théorie uniforme de la GTD, appelée Théorie Uniforme de la Diffraction (UTD), qui permet d'obtenir un champ total (champ géométrique et champ diffracté) uniforme, et qui s'avère simple à implémenter. Elle a été développée dans un premier temps pour le cas simple d'un demi-plan afin de démontrer sa faisabilité, puis pour le cas d'un dièdre à interface solide/vide par la suite. Les solutions UTD développées ont été validées numériquement et l'UTD pour le dièdre a été implémentée avec succès dans CIVA dans une configuration 2D (incidence et observation perpendiculaires à l'arête infinie du dièdre). Le modèle combiné « modèle spéculaire + UTD » a ensuite été comparé aux autres modèles de simulation d'échos de géométrie existant dans CIVA, et un bon accord est obtenu entre ces différents modèles, permettant ainsi de valider notre approche.

Outre la non-uniformité, une autre limitation de la GTD est qu'elle n'est définie que pour des géométries canoniques (demi-plan, dièdre,...) et ne modélise donc la diffraction que par des arêtes de longueur infinie. Pour prendre en considération la taille finie de l'arête, deux modèles « incrémentaux » 3D consistant à sommer des ondes sphériques émises par des points de discrétisation de l'arête ont été développés. Le premier modèle, appelé Incremental Theory of Diffraction (ITD), est inspiré de l'électromagnétisme et le second, appelé « modèle Huygens », repose sur le principe de Huygens. Ces modèles ont été couplés dans CIVA à la solution GTD du demi-plan pour fournir une modélisation 3D d'échos de diffraction de défauts et ont ensuite été validés avec succès par comparaison à des résultats expérimentaux dans des configurations CND 3D. Ces méthodes incrémentales ne sont pas appliquées au modèle UTD dièdre développé, ce dernier étant 2D (arête infinie et invariance du problème de diffraction le long de l'arête), mais seront utiles lorsqu'une solution GTD de diffraction par un dièdre inclus dans un solide isotrope sera mise au point en 3D.

La solution UTD pour le dièdre, développée au cours de cette thèse, a été élaborée en se servant d'une solution GTD limitée à des dièdres d'angle inférieur à $180°$ (méthode de la Transformée de Laplace). Elle ne permet donc pas de traiter toutes les configurations d'intérêt en CND par ultrasons. Une étude préliminaire a tout d'abord été réalisée pour un dièdre à interface liquide/vide afin de traiter la diffraction pour tout angle de dièdre. Celle-ci est modélisée en employant la méthode dite des "fonctions spectrales". Les résultats obtenus par cette méthode ont été comparés à ceux de la méthode de Sommerfeld pour ce problème de diffraction. Cette comparaison nous permet de connaitre la précision de calcul de la méthode des "fonctions spectrales" dont l'extension au cas élastodynamique pourra être envisagée afin de traiter la diffraction pour des dièdres d'angle quelconque et inclus dans un solide.

Mots-clé:

Elastodynamique, Diffraction, TGD, TUD, élastodynamique géométrique, Méthodes rayons, Simulation du CND, Ultrasons.

Modeling of diffraction effects for specimen echoes simulations in ultrasonic Non-Destructive Testing (NDT)

Abstract

This thesis is part of the development of models integrated in the Non-Destructive Testing (NDT) software platform CIVA. So far, the specimen echoes (entry or backwall surfaces, ...) or echoes produced by specimen interfaces have been modeled in CIVA using a "ray" model. This model, called "specular model", is based on geometrical elastodynamics and therefore is mainly concerned with specular reflections on scatterers. The aim of this thesis is to extend this ray model to account for specimen wedges diffraction. The Geometrical Theory of Diffraction (GTD), a diffraction ray model, was a starting point to do such an extension. However, GTD diverges at observation directions close to incident and reflected shadow boundaries.

In this thesis, we then formulate a GTD uniform theory within the context of elastodynamics, the Uniform Theory of Diffraction (UTD), which leads to a uniform total field (geometrical + diffracted fields) and is amenable to simple implementation. First, UTD was developed for a simple canonical geometry, a half-plane, to show its feasibility and then for a complex canonical geometry, a wedge whose faces are stress-free. The developed UTD solutions were validated numerically and UTD for a wedge was implemented in CIVA in a 2D configuration (incidence and observation directions are in the plane perpendicular to the wedge edge). The mixed model "specular model + UTD" was compared to other CIVA models for specimen echoes simulation and a good agreement was obtained between these models, then allowing us to validate our approach.

In addition to its non-uniformity, another drawback of the GTD methodology is its restricted application to canonical geometries (half-plane, wedge, ...) , as it mainly allows for the treatment of infinite edge diffraction. To overcome this limitation, two incremental methods involving a sum of spherical waves emitted by discretization points on the diffracting edge have been developed. The first model, called the Incremental Theory of Diffraction (ITD), is extended from electromagnetism, and the second, called "Huygens model", is based on the Huygens principle. These models have been applied to the GTD solution for a half-plane in CIVA to model 3D defects echoes diffraction and have then been successfully validated against experimental data in 3D NDT configurations. These incremental models are not applied to the developed UTD wedge, this last model being 2D (infinite wedge and the diffraction problem is invariant along the edge wedge), but they will be useful when a GTD solution for the diffraction by a solid wedge will be developed in 3D configurations.

The UTD solution for a wedge developed during this thesis has been established using a GTD solution limited to wedge angles less than $180°$ (Laplace transform method). Therefore, this UTD approach does not cover all ultrasonic NDT configurations. A preliminary study has then been

carried out for a wedge at interfaces fluid/void in order to extend the results to a wider range of wedge angles. In this study, diffraction is modeled using to the so-called “spectral functions method”. Results obtained with this method are compared with those of the Sommerfeld method for this diffraction problem. This comparison allows us to assess the accuracy of the “spectral functions method”, which could also be used in elastodynamics to treat diffraction problems with all wedge angles.

Keywords:

Elastodynamics, Diffraction, GTD, UTD, Geometrical Elastodynamics, Rays methods, NDT simulation, Ultrasounds.

Contents

List of Figures

Introduction

Inspection of industrial products from fabrication to daily usage is crucial to ensure their integrity and reliability. It is clear that failure to properly quantify and identify defaults in these materials could result into undesired events for end users, especially in areas such as aeronautics, civil engineering, nuclear energy and automotive industry. The Non Destructive testing, also known as NDT, is an efficient technique for material inspection which preserves the overall structure of the material and limits its alteration.

A wide range of NDT techniques are available in the literature. In this work, we particularly emphasize on Ultrasonic Testing. In this approach, ultrasonic waves are emitted to a specimen and scattered waves are analysed to detect defaults in the specimen. Ultrasonic waves are vibrations of frequencies above 20 kHz, which is approximately the upper limit of the audible range for humans. These waves then get scattered by the specimen boundaries or other inhomogeneities. Typically, such waves would propagate through the specimen without causing any structural change. These are therefore elastic waves since the material regains its initial form after the wave passage. The signal, i.e. scattered wave, received by the receiver transducer contains relevant information about the component and therefore has to be analysed.

Modelling appears to be an efficient technique to predict the feasibility of ultrasonic inspections of industrial components and to improve data analysis of the received signals. Given the important role of the numerical simulation for ultrasonic NDT, CEA-LIST (Commissariat à l'Énergie Atomique et aux Énergies nouvelles - Laboratoire d'Intégration des Systèmes et Technologies) proposes NDT simulation tools via the software platform CIVA. This software uses principally semi-analytic models to achieve lower computation time, albeit at the expense of offering limited range of validity. These models have very often limits of validity. CIVA is thus in continual improvement in order to extend its validity domain.

The aim of this thesis is to extend the validity domain of a model used in CIVA to simulate the specimen echoes which are echoes produced by entry or backwall surfaces and by the specimen interfaces (see Fig. 1). The model to extend is the CIVA "ray" model called "specular model" since it is based on the geometrical elastodynamics. This model respects the Snell-Descartes law of reflection and refraction at interfaces. Indeed, it models the propagation of the waves in the specimen and also the reflection and refraction of the waves at interfaces. The "specular model"

does not take into account the diffraction by the specimen irregularities such as the wedge edges in the specimen (see Fig. 1).

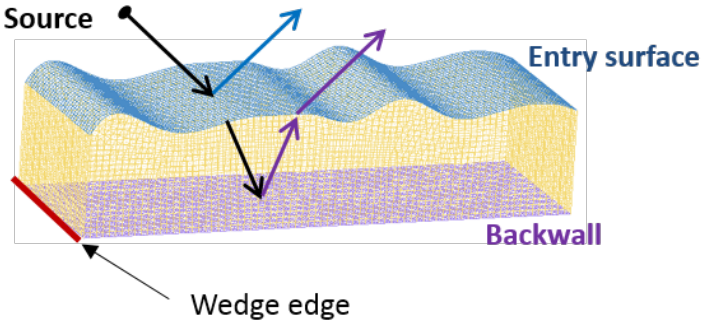

Figure 1: Echoes from the entry surface (blue arrow) and from the backwall (purple arrow).

Besides the "specular model" for the specimen echoes simulation, CIVA proposes two other models which take into account reflection and refraction at interfaces as well as diffraction by the specimen irregularities. These two models are given hereafter.

- CIVA-Athena 2D model only for 2D configurations (the configuration is invariant along the direction perpendicular to the plane of inspection). It is a hybrid method. The waves emitted by the (emitter) transducer are propagated to the boundaries of a box using the CIVA "ray" model. This box embraces the specimen irregularities, and propagation and scattering of the wave are calculated using Finite Elements Method (FEM). FEM models all the scattering phenomena such as diffraction by irregularities as well as reflection and refraction. The scattered waves in this FEM box are propagated from the box boundaries to the receiver transducer, still using the CIVA "ray" model. This method is time consuming since the mesh size must be less than a fraction of the emitted wavelength (in the range of a few millimetres) in order to achieve reasonable accuracy.
- Kirchhoff model for 2D and 3D configurations. This method requires an integration over the scatterer surface and also uses the geometrico-elastodynamic approximation at each element on the scatterer surface. It models reflection, refraction and diffraction by edges. According to validations for half-cracks especially for transversal waves (see Fig. 1.7 in chapter 1), the Kirchhoff model is considered to be less accurate in modelling edge diffraction compared to a ray method for diffraction, the Geometrical Theory of Diffraction (GTD). This can be explained by the fact that the Kirchhoff model is based on the geometrico-elastodynamic approximation and is therefore more suitable to model reflection than diffraction. Being an integral method, it can be time consuming for large scatterers.

GTD is a ray model already implemented in CIVA for calculating the echoes diffracted by the

edges of embedded planar cracks. This ray method for diffraction could also been used for calculating specimen echoes. However, this method has an important drawback: it diverges at observation directions close to incident and specular directions. To overcome this GTD drawback, there exists a GTD uniform correction, the Uniform Theory of Diffraction (UTD), developed initially in electromagnetism which removes the divergence of GTD and models a spatially continuous total field when it is combined with Geometrical Optics. This uniform correction, UTD, can therefore be used in CIVA and combined with the CIVA specular model (based on the Geometrical-Elastodynamics) which already models reflection and refraction in order to simulate in addition diffraction effects as done by CIVA-Athena and Kirchhoff models. Sor far, UTD has never been developed in elastodynamics.

The aim of this thesis is then to develop UTD within the context of elastodynamics with the final view of extending the validity domain of the CIVA specular model. During this thesis, a model for specimen echoes simulation based on UTD has been created. Throughout this work, this model is called "specular + UTD" model, as the specular model for the simulation of reflected echoes has been combined to the UTD model for the simulation of diffracted echoes. With the mixed "specular + UTD" model, reflection and refraction as well as diffraction by the specimen irregularities are taken into account.

This thesis is divided into 5 chapters.

In Chapter 1, a short review of high frequency scattering models in elastodynamics is proposed for a better understanding of the methods employed throughout this thesis. This chapter describes the Geometrical-Elastoynamics (GE), the Kirchhoff Approximation (KA) and the Geometrical Theory of Diffraction (GTD) and its existing uniform corrections in elastodynamics, the Physical Theory of Diffraction (PTD) and the Uniform Asymptotic Theory of Diffraction (UAT).

In chapter 2, the Uniform Theory of Diffraction (UTD) is developed for a simple canonical geometry, a half-plane, to show its feasibility in elastodynamics. UTD is obtained by applying the Pauli-Clemmow approximation (detailed in appendix A) to the exact solution of the scattering of a plane wave from a half-plane which is expressed in terms of an integral over a complex path. This chapter also proposes the UTD formulation for other kinds of illumination (incident cylindrical or spherical wave).

In addition to its non-uniformity, another drawback of the GTD methoology is its restricted application to canonical geometries (half-plane, wedge, ...). GTD thus models diffraction by an infinite edge. The finite length of the edge is not considered with GTD. That is therefore problematic for NDT applications where defects or specimen irregularities have a finite extension. To overcome this limitation, two incremental methods are developed in Chapter 3: they model the diffraction from a finite edge by considering a sum of spherical waves emitted by discretization points on the diffracting edge. The first model, called the Incremental Theory of Diffraction (ITD), is extended from electromagnetism, and the second, called “Huygens model”, is based on the Huygens principle. With these models, the contribution of the edge extremities is taken into

account. These models are useful for 3D configurations for which the final extent of the diffracting edge is influent. These models are therefore applied to the GTD solution for a half-plane in CIVA to model 3D echoes diffraction from embedded planar defects, and are then validated against experimental data in 3D NDT configurations. For the two left chapters, the study is done in a 2D configuration and therefore incremental models are useless since the extension is infinite in the perpendicular direction to the plane of inspection.

The chapter 4 of this thesis deals with the diffraction of an elastic plane wave by a wedge in 2D configuration because wedges are encountered geometries in inspected specimens. A review of two existing GTD solutions for this problem both limited to wedge angles less than π - the Sommerfeld integral (SI) and the Laplace transform (LT) - is first done. Then, UTD solution for this problem is developed. This UTD solution is applied to the LT GTD solution and compared to the existing UAT solution. It is then implemented in the software platform CIVA and is coupled to the specular model in order to design a generic model of specimen echoes accounting for both reflection and diffraction. For its validation, this mixed model is compared to the other models for specimen echoes simulation in CIVA.

The UTD solution for a wedge developed in chapter 4 has been established using a GTD solution limited to wedge angles less than π (LT method). Therefore, this UTD approach does not cover all ultrasonic NDT configurations. In chapter 5, a preliminary study has then been carried out for a wedge at fluid/void interfaces in order to model diffraction for a wider range of wedge angles. In this study, diffraction is modelled using the so-called "spectral functions method". Results obtained with this method are compared with those of the well-known GTD analytic solution for this diffraction problem. This comparison allows us to assess the accuracy of the "spectral functions method", which could also be used in elastodynamics to treat diffraction problems with all wedge angles.

Chapter 1

Review of high frequency scattering models in elastodynamics

Le Contrôle Non Destructif (CND) par ultrasons permet de contrôler les pièces industrielles sans les altérer afin de détecter d'éventuels défauts. La simulation du CND apparaît être une solution efficace pour qualifier les méthodes d'inspection ultrasonores employées et analyser les résultats. Les défauts recherchés dans les pièces inspectées sont généralement de l'ordre de quelques centimètres. Pour pouvoir détecter de tels défauts, des ultrasons haute fréquence sont émis. En effet, aux fréquences ultrasonores de l'ordre du MHz, ces ondes ont une longueur d'onde de l'ordre du millimètre et des défauts de cette taille ou plus grands sont généralement détectés. Il est donc impératif de savoir modéliser l'interaction des ultrasons haute fréquence avec des structures.

Ce chapitre fait un état de l'art des différents modèles semi-analytiques de diffusion des ondes élastiques par des obstacles en hautes fréquences. Certains de ces modèles sont implémentés dans la plateforme logicielle de CND CIVA développé par le Commissariat à l'Énergie Atomique et aux Énergies Alternatives (CEA LIST). Ce chapitre énonce les avantages et inconvénients de chaque modèle de simulation. Il décrit aussi brièvement les principales étapes de l'implémentation de ces modèles dans CIVA.

1.1 Introduction

Ultrasonic testing is a popular Non Destructive Testing (NDT) technique used since 1930. Modelling appears to be an efficient technique to predict the feasibility of ultrasonic inspections of industrial components and structures and to improve data analysis of the received signals. In ultrasonic NDT, ultrasonic transducers often radiates high frequency waves ($f_c = 1 - 10$ MHz, f_c being the central frequency of the emitted signal) in order to detect flaws of few centimetres long. These waves interact with flaws and boundaries of the inspected components. Simulation must then be in high frequency regime for NDT applications. Among the existing simulation methods, numerical methods such as Finite Elements Method (FEM) are time consuming since the mesh size must be less than the emitted wavelength ($\sim$ few millimetres) to have an accurate result. Indeed, there is a relationship between the wavelength and the maximum size mesh with FEM [1]. Some developments as the Partition of Unity Finite Element Method (PUFEM) have enabled finite element methods to be applied to high frequency scattering problems [2]. This last method does not constraint the size mesh as the classical finite elements does. However, PUFEM requires to compute high oscillatory integrals for the matrix elements which lead to computational costs.

There also exist asymptotic high frequency methods which give an approximated solution to the elastodynamic scattering problem. As they generally provide fast results, they are then still usually preferred to numerical methods for NDT applications [3]. They are commonly obtained by evaluating integrals representing an exact solution of a scattering problem with methods such as the steepest descent method (also called saddle point method) or the stationary phase method. High frequency approximations respect the Sommerfeld radiation condition which stipulates that the energy radiate from the sources is scattered to infinity; outgoing energy cannot be radiated from infinity into the source [4, 5]. Asymptotic high frequency methods also satisfy the Meixner conditions which ensure the boundedness of the wave-field energy near diffracting edges. They give accurate results as some parameters approach a limiting value: particularly the far-field parameter ks must be bigger than 1 ($ks \gg 1$, with k being the wavenumber of the scattered wave and s the distance from the observation point to the diffraction point). Consequently, these methods have a domain of validity and are generally obtained for canonical structures such as half-plane, sphere, cylinder, cone and wedge. Furthermore, these methods can be used for complex geometries due to their local nature [6]. Significant amount of researchers worked on these asymptotic high frequency methods in all physical fields (optics [7, 8], acoustics [9–11], seismology [9], electromagnetism [9, 12–20] and elastodynamics [21–25]).

There exist many asymptotic high frequency scattering models in elastodynamics. Many of them are implemented in the NDT software platform CIVA developed by CEA LIST and its partner. This software platform allows to simulate a complete ultrasonic inspection [26], from the transducer radiation (beam propagation [27]) to its interaction with flaws [3, 28] and specimen boundaries. In this chapter, the most important asymptotic high frequency scattering models in elastodynamics are presented and for the ones implemented in CIVA, the main implementation steps

are briefly described.

1.2 Geometrical Elastodynamics (GE)

In all the thesis, the symbols α and β are used to denote the wave type, i.e. $\alpha, \beta = L, TV$ or TH (Longitudinal, Transverse Vertical or Transverse Horizontal, respectively). In general, α is used for the incident wave and β for reflected and diffracted waves. Scalar quantities are generally labelled by taking α and β as subscripts, while α is used as superscripts for vectors related to the incident wave and β as subscripts for vectors related to scattered waves. For scalar quantities which link incident and scattered waves, α is used as superscript and β as subscript.

Geometrical Elastodynamics (GE) is the simplest way to model propagation and scattering of elastic waves. It is a ray method which just considers incident rays, refracted and reflected rays by interfaces scatterers. Along a ray, the characteristics of the GE field (amplitude, phase, propagation and polarisation directions) are determined using Snell-Descartes law of reflection and the energy conservation.

In the CIVA platform software, the computation of the field radiated by a transducer is based on GE and more precisely the pencil method [27]. A pencil is a tube of rays which emanate from a source point (see Fig. 1.1). The axial ray of this tube respects Snell-Descartes law at interfaces. The pencil is then parametrized by this axial ray and by the cone aperture angle which is the solid angle covered by the pencil at the point source. The pencil then respects refraction and reflection at interfaces and is characterised by its time of flight, its amplitude, its mean polarisation and the wave vector directions [29]. When the pencil propagates, the energy through its cross section remains constant. Therefore, the divergence factor of the pencil corresponds to the one of a spherical wave emitted by a point source.

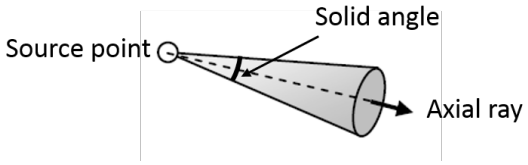

Figure 1.1: Pencil for a point source.

The pencil method for field computation is used for calculating the specimen echoes in CIVA. The corresponding model of specimen echoes calculation is called "specular model" since it models only the specular reflection on the specimen boundaries. Each elementary point source on the radiating transducer crystal generates pencils which propagate through the specimen to observation points located on the receiver transducer crystal (in Fig. 1.2, such a pencil is reflected twice by the backwall).

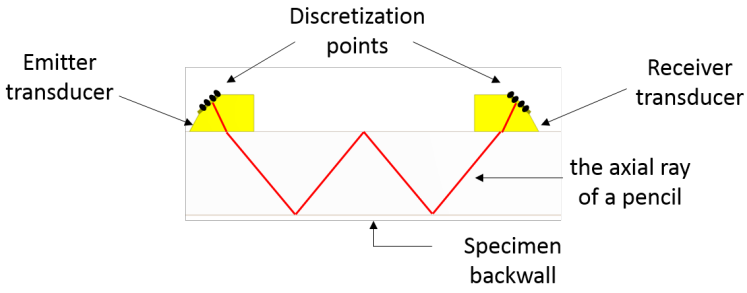

Figure 1.2: Principle of the specular model integrated in the CIVA software platform

When an incident wave impacts a scatterer, the GE total field is constituted of regions separated by Shadow Boundaries (SB) of either the incident or the reflected waves depending on the scatterer geometry. For example, when an acoustic plane wave impinges a crack half-plane, GE divides the space in three regions (see Fig. 1.3): the region illuminated by both incident and reflected waves (zone I+R), the region only insonified by the incident waves (zone I) and the shadow region where no wave propagate. In this case, these regions are separated by respectively the reflected and incident shadow boundaries.

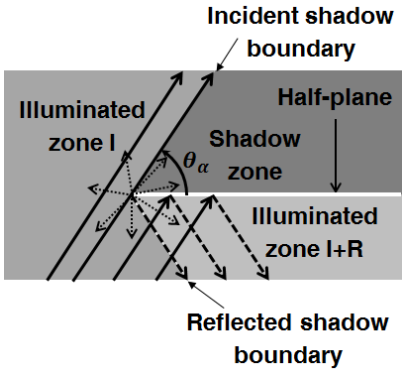

Figure 1.3: Scattering of an acoustic plane wave by a semi-infinite crack. Thick arrows - incident waves, dash arrows - reflected waves, dotted arrows - diffracted waves.

The scattering of a plane wave by a semi-infinite crack embedded in an elastic homogeneous solid is illustrated in Fig. 1.4. When an incident wave of wave vector $\mathbf{k}^\alpha$ impacts a semi-infinite crack, it gives rise to reflected waves (r) of wave vectors $\mathbf{k}^{rL}$ and $\mathbf{k}^{rTV}$ due to mode conversion. GE then divides the space into a maximum of four regions separated by shadow boundaries of incident and reflected waves. If the incident wave is a longitudinal wave ($\alpha = L$) of incidence angle θ_L with the half-plane (see Fig. 1.4a), the four regions are: the region where no wave propagates (zone I), the region only illuminated by the incident waves (zone II), the region insonified by both longitudinal incident and transversal reflected waves (zone III) and the region insonified by longitudinal incident and longitudinal and transversal reflected waves (zone IV).

For a transversal incident wave, $\alpha = TV$ of incidence angle θ_{TV} with respect to the half-plane (see Fig. 1.4b), the four regions are: the region where no wave propagates (zone I), the region only illuminated by the incident waves (zone II), the region insonified by both transversal incident and transversal reflected waves (zone III) and the region insonified by transversal incident and transversal and longitudinal reflected waves (zone IV). If the incidence angle is less than the longitudinal critical angle defined in Eq. (2.33) in chapter 2 ($\theta_{TV} < \theta_c$), there is no longitudinal reflected waves. Therefore, in this case, the zone IV does not exist.

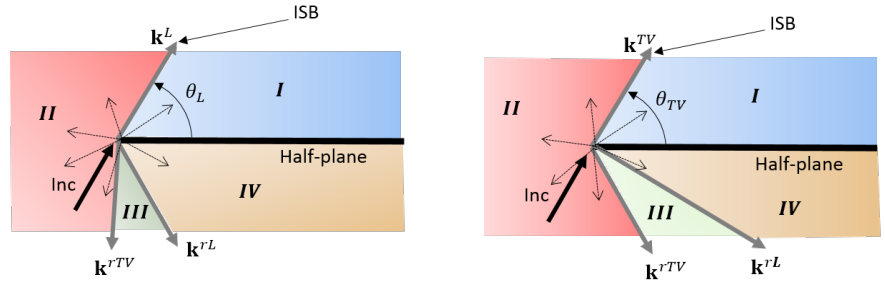

(a) Scattering of a longitudinal plane wave by a semi-infinite crack

(b) Scattering of a transversal plane wave by a semi-infinite crack

Figure 1.4: Scattering of an elastic plane wave by a semi-infinite crack.

Consequently, GE predicts a discontinuity of the elastodynamic total field when crossing these shadow boundaries. By example, on Fig. 1.4, in zone II, the total field is constituted of the incident field and in zone I, there is no more incident waves. The incident field is then discontinuous at the incident shadow boundary (ISB). The same applies for the reflected field. It also presents a discontinuity at the reflected shadow boundaries. These discontinuities of the elastodynamic total field are represented mathematically by a Heaviside step function $H(.)$. In addition to its discontinuity when crossing a SB, GE is also invalid at caustics for which GE predicts an infinite amplitude since the curvature radius of wavefronts is null. Caustics are areas of overload wave amplitude due to a local focus of reflected or refracted rays at these areas. A caustic thus represents an envelop of rays. Simple examples of caustics due to reflection on a concave surface are shown in Fig. 1.5. Caustics can be easily observed in the everyday life with light waves (see Fig. 1.5b which reproduces the phenomenon depicted on the ray tracing of Fig. 1.5a).

The "Specular model" in CIVA for the specimen echoes simulation is thus suitable to model specular reflection on the specimen boundaries but it presents discontinuities at the incident and reflected shadow boundaries and is not valid at caustics. These limits of the Geometrical Elastodynamics are overcome by the Kirchhoff Approximation.

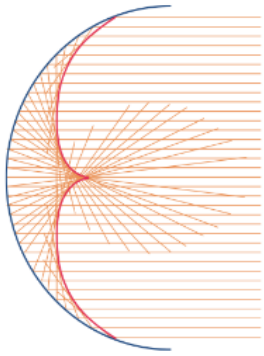

(a) (Taken from [30]) Caustic (represent in red) on a concave surface

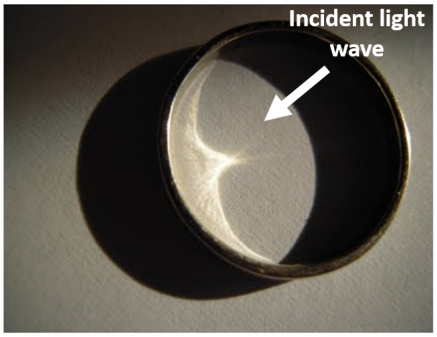

(b) Caustic caused by reflection of light waves on the ring concave surface. It corresponds to the bright region

Figure 1.5: Caustic on a concave surface.

1.3 Kirchhoff Approximation (KA)

The Kirchhoff Approximation (KA) also called Physical Optics (PO) has been first developed in optics to compute the diffraction of a plane wave propagating through an aperture [31] in 1950. It has been extended to electromagnetism [32, 33] and to acoustics [32] in 1969 and finally to elastodynamics [21] in 1982. In elastodynamics, KA is commonly used for NDT applications [34, 35].

KA is a high frequency approximation as the Geometrical Elastodynamics. Using the local nature of high frequency methods, it assumes that the scattering surface behaves locally, at each point, as an infinite plane. This tangent infinite plane at any diffraction point on the scattering surface is divided into a lit side and a shadowed side (see Fig. 1.6). On the shadowed side, the total displacement field is assumed to vanish and on the lit side, the total displacement is calculated using the Geometrico-Elastodynamics (GE). Subsequently, this approximation is used to calculate the unknown Crack Opening Displacement (COD), i.e. the jump in the total field displacement across the crack: the COD is a factor which is contained in the integrand of the exact integral representation of the scattered field at an observation point [see Eq. (1.1)] [21]. For a stress-free crack, in elastodynamics, this exact integral representation of the scattered field also called the Rayleigh-Sommerfeld integral is expressed as

$$u_p(\mathbf{x}) = \int_{S^+} [u_i(\mathbf{x}')] \Sigma_{ij}^{(p)}(\mathbf{x}, \mathbf{x}')\, n_j(\mathbf{x}')\, \mathrm{d}^2\mathbf{x}' \tag{1.1}$$

where $u_p(\mathbf{x})$ is the p-th coordinate of the displacement scattered field at the observation vector $\mathbf{x}$, S^+ the lit surface (see Fig. 1.6), $\Sigma_{ij}^{(p)}(\mathbf{x}, \mathbf{x}')$ the (ij) component of the Green's stress tensor $\boldsymbol{\Sigma}^{(p)}(\mathbf{x}, \mathbf{x}')$ - the stress produced at $\mathbf{x}$ by a unit traction acting along the $p-$axis at a point $\mathbf{x}'$ on the lit surface S^+, n is the outward normal to S^+ and $[u(\mathbf{x}')]$ is the COD. The expression of the

Green's tress tensor $\Sigma^{(p)}(\mathbf{x},\mathbf{x}')$ given in [21] is

$$4\pi\Sigma_{ij}^{(p)}(\mathbf{x},\mathbf{x}') = -\frac{2}{\kappa^2}\frac{\partial^3}{\partial x_i\,\partial x_j\,\partial x_p}(U_L^{3D}-U_T^{3D}) + \left(1-\frac{2}{\kappa^2}\right)\delta_{ij}\frac{\partial}{\partial x_p}U_L^{3D} + \left[\delta_{ip}\frac{\partial}{\partial x_j}+\delta_{jp}\frac{\partial}{\partial x_i}\right]U_L^{3D}, \tag{1.2}$$

where

$$U_L^{3D} = \frac{e^{ik_L s}}{s}, \quad U_T^{3D} = \frac{e^{ik_T s}}{s}, \quad s = |\mathbf{x}-\mathbf{x}'|. \tag{1.3}$$

U_L^{3D} and U_T^{3D} have respectively the divergence of a longitudinal and of a transversal spherical wave emitted from the source point $\mathbf{x}'$ on the scatterer surface towards observation point $\mathbf{x}$. k_L and k_T are respectively the longitudinal and transverse wavenumbers of the diffracted waves and $\kappa = k_T/k_L$. In far field, the integral (1.1) is reduced to

$$u_p(\mathbf{x}) = \int_{S^+} u_\alpha(\mathbf{x}')\, D_\beta^\alpha(\mathbf{k}^\alpha, \mathbf{k}_\beta(M))\, \frac{e^{ik_\beta S_\beta}}{S_\beta}\, \mathrm{d}^2\mathbf{x}' \tag{1.4}$$

where $\alpha = L, TV$ or TH is the incident type wave vector and where $\beta = L, TV$ or TH the scattered type vector. $u_\alpha(\mathbf{x}')$ is therefore the incident field amplitude at a point on the lit scatterer surface, D_β^α is the Kirchhoff diffraction coefficient with depends on the incidence propagation vector $\mathbf{k}^\alpha$ and on the observation propagation vector $\mathbf{k}_\beta(M)$. In (1.4), S_β is the distance from the integration point on the scatterer surface to the observation point.

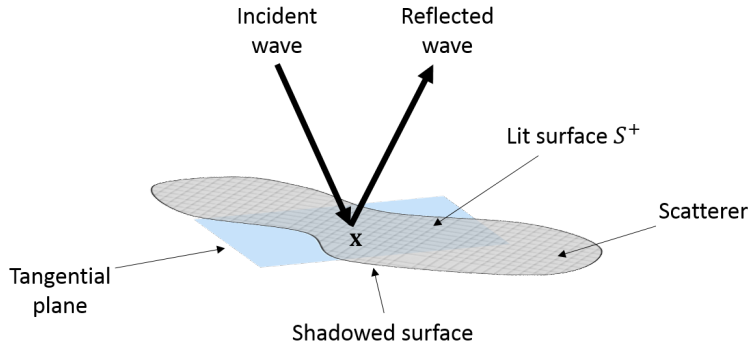

Figure 1.6: Local application of the Kirchhoff Approximation (KA) showing the mesh of the lit surface and an arbitrary point $\mathbf{x}$ on a scatterer illuminated by an incident wave and the plane tangent to the obstacle at this point.

The KA integral (1.1) then consists in propagating an approximated near-field solution (geometrical field on the obstacle) in the whole space using a Green function as propagator. It can be used in the near and far fields and its expression (1.4) is only used in far-field. KA describes

particularly well specular reflection since it is based on GE. It also models edge diffracted wave contrary to GE, and hence gives rise to a continuous field in the whole space, even at caustics. However, the amplitude of the diffracted waves produced by KA is not accurate, more specifically for transversal waves. Comparisons between KA, GTD (presented in section 1.4) and exact solution for a strip-like crack impinged by an elastic transversal incident wave have been done in [21, 36]. Results of [21] are reproduced here in Fig. 1.7. As expected, far away from the specular reflection, KA is less accurate than GTD which fits well the exact solution in that case. That is because GTD (see section 1.4) best describes the edge diffraction phenomena.

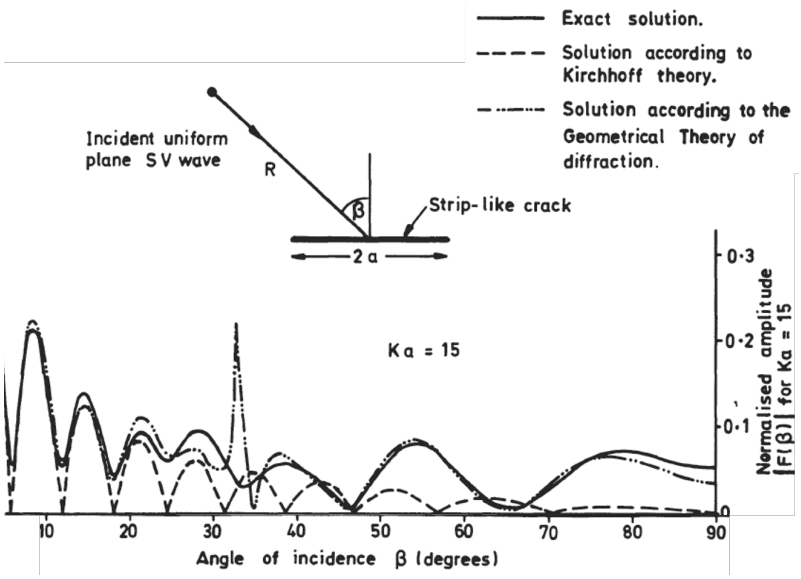

Figure 1.7: [taken from [21] (Fig. 1)] Scattering of a transversal (also called shear) plane wave in steel by a smooth strip-like crack of width $2a$. The far-field of the backscattered TV (noted SV here) waves according to Kirchhoff theory and GTD, compared with the exact solution, for $Ka = 15$ ($K = k_T$ = transverse wavenumber).

An ultrasonic NDT system model based on KA is also integrated in CIVA platform software to compute specimen and flaws echoes. It used the formulation (1.4) of KA in far-field. For NDT applications, observation points are points on the receiver transducer crystal. The displacement field p-th coordinate of the receiver transducer crystal is then the sum of the displacement field (1.4) over its surface. KA implementation in CIVA is thus based on the plane wave approximation for the incident field and on the field reciprocity principle described in [26] for calculating the echo generated by the scatterer surface to the receiver transducer. Indeed, the field radiated by the emitter transducer at a point on the scatterer surface $u^{\alpha}(\mathbf{x}')$ is calculated using the pencil method (introduced in the previous section). In far-field, this field can be approximated at each point on the scatterer surface by a local plane wave by extracting information from the field computation as its amplitude, its time of flight, its mean polarization and the wave vector directions at a given observation point. The echo generated by an elementary meshed surface on the scat-

terer is computed using the field reciprocity principle [26] which stipulates that the sensitivity of the receiver transducer to a spherical wave scattered from a point in the inspected specimen is proportional to the field radiated by the receiver towards this point. KA model thus requires the meshing of the scatterer surface and for each point on the scatterer surface, the fields emitted by both the emitter and the receiver acting as an emitter towards this point being calculated using the CIVA pencil method. The principle of the KA CIVA model is illustrated on Fig. 1.8.

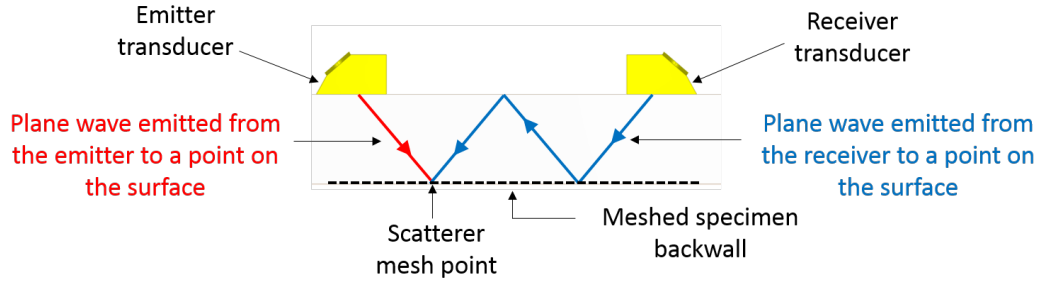

Figure 1.8: Kirchoff Approximation (KA) model principle in the CIVA platform software.

1.4 Geometrical Theory of Diffraction (GTD)

The Geometrical Theory of Diffraction (GTD) [22, 23, 37, 38] extends the Geometrical Elastodynamics (GE) [see section 1.2] by adding to it diffraction phenomena. It postulates the existence of rays diffracted from the structure irregularities such as edges or tips, in addition to the incident and reflected rays of GE. It also gives a recipe for calculating the amplitudes carried by these diffracted rays. These rays can propagate in unlit regions of GE (defined in Figs. 1.3 and 1.4 for the half-plane case). The existence of these rays is due to the generalized Fermat's principle [8]. For a given incident ray from an edge, this principle leads to a cone of diffracted rays from an edge, the Keller's cone. The axis of this cone is the diffracting edge (see Fig. 1.9). In 2007, Rahmat-Samii [39] made an observation of the Keller's cone existence in an hotel room with light waves (see Fig. 1.10). On this figure, a light beam impacts the edge of the table and is thus diffracted. The intersection of the diffracted waves with the front door forms a circle which is the cross-section of the Keller's cone of diffraction.

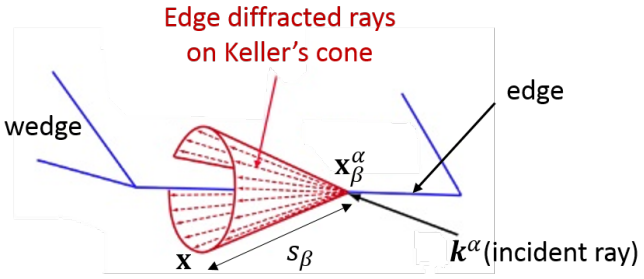

Figure 1.9: Keller's cone of diffraction.

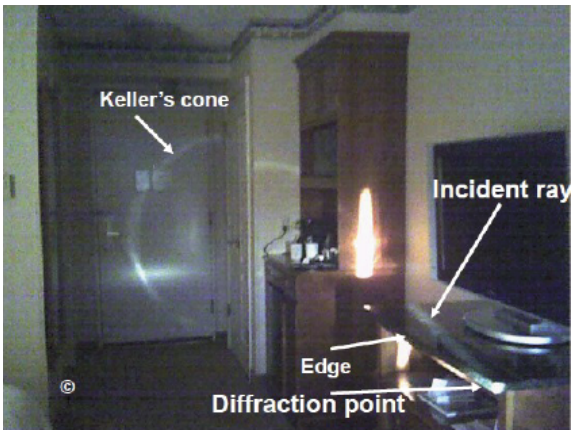

Figure 1.10: [taken from [39] (Fig. 4)] Observation made by Rahmat-Samii in a hotel room in Florida showing the intersection of the Keller's cone with the front door.

GTD is also a high frequency approximation method and therefore it stipulates that diffraction is a local phenomenon as reflection. Taking advantage of this locality principle, at each flash point on the diffracting edge, the obstacle can be replaced by a canonical geometry such as a half-plane or a wedge for which the GTD solution is known.

For an elastic incident plane wave of type $\alpha = L, TV$ or TH, on a half-plane or wedge, the total displacement field is expressed as

$$\mathbf{u}^{\mathrm{tot}}(\mathbf{x}) = \mathbf{u}^{\mathrm{GE}}(\mathbf{x}) + \sum_{\beta} \mathbf{u}_\beta^{\mathrm{diff}}(\mathbf{x}), \tag{1.5}$$

with $\mathbf{u}^{\mathrm{GE}}$ being the Geometrico-Elastodynamic displacement field and $\mathbf{u}_\beta^{\mathrm{diff}}$ being the diffracted displacement field of the scattered wave of type β. The GTD permits to approximate the diffracted

displacement field $\mathbf{u}_\beta^{\text{diff}}$ by

$$\mathbf{u}_\beta^{\text{diff(GTD)}}(\mathbf{x}) = \sum_\beta u_\alpha(\mathbf{x}_\beta^\alpha) D_\beta^{\alpha(\text{GTD})} \frac{e^{ik_\beta S_\beta}}{\sqrt{k_\beta L_\beta}} \mathbf{e}_\beta(\mathbf{x}) \tag{1.6}$$

where

$$u_\alpha(\mathbf{x}_\beta^\alpha) = \mathbf{u}^\alpha(\mathbf{x}_\beta^\alpha) \cdot \mathbf{d}^\alpha, \tag{1.7}$$

with $\mathbf{u}^\alpha(\mathbf{x}_\beta^\alpha)$ being the incident field at the diffraction point $\mathbf{x}_\beta^\alpha$ (see Fig. 1.9) and $\mathbf{d}^\alpha$ its polarisation vector. $\beta = L, TV$ or TH is the scattered wave mode, k_β its wave number and $\mathbf{e}_\beta$ its polarisation. S_β is the distance between the diffraction point $\mathbf{x}_\beta^\alpha$ and the observation point $\mathbf{x}$ and L_β is a parameter distance defined later in Eq. (2.7).

GTD is also implemented in the CIVA platform software using an incremental model defined in section 3 to compute the flaw response. Its implementation is also based on the plane wave approximation and on the field reciprocity principle as the one of the Kirchhoff Approximation method. Based on an incremental method [40], GTD implementation in CIVA requires the meshing of the diffracting edge (see Fig. 1.11). These points on the diffracting edge are sources of spherical waves. As for the implementation of KA model, The incident wave at a point on the diffracting edge $u_\alpha(\mathbf{x}_\beta^\alpha)$ is calculated using the CIVA pencil method and the echo generated by a point on the diffracting edge is calculated using the field reciprocity principle. For each discretization point of the diffracting edge, the fields emitted by both the emitter and the receiver acting as an emitter towards this point are calculated using the CIVA pencil method. This principle is illustrated on Fig. 1.11.

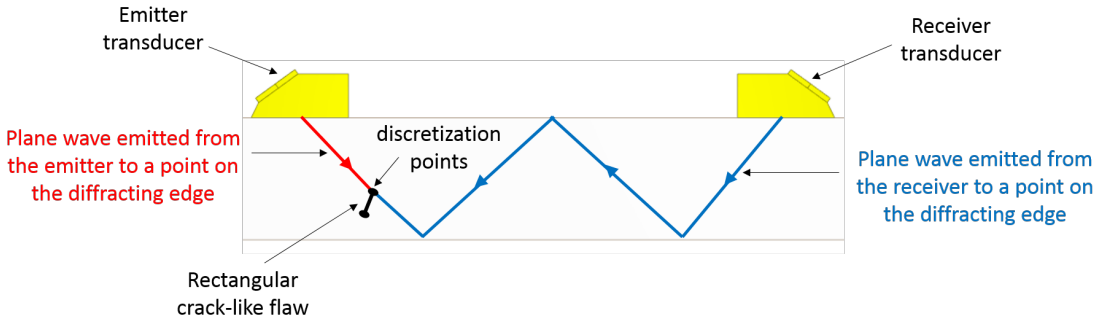

Figure 1.11: GTD model principle in the CIVA platform software

GTD gives a good analytical description of diffracted waves as shown in [21] (see Fig. 1.7). However, as GE, it fails at caustic regions and also in the transition zones (also called penumbrae) surrounding shadow boundaries (defined in Figs. 1.3 and 1.4), where edge diffracted waves interfere with incident or reflected waves. Indeed the GTD solution is infinite at such boundaries. For this last reason, GTD is said to be non-uniform. To overcome this shortcoming of GTD, sev-

eral uniform extensions of GTD have been developed in electromagnetism, such as the Uniform Asymptotic Theory of diffraction (UAT) [15, 16, 41–43], the Uniform Theory of Diffraction (UTD) [12, 14–16] and the Physical Theory of Diffraction (PTD) [19, 44]. Two of these uniform extensions of GTD have been developed recently in elastodynamics: the Physical Theory of Diffraction (PTD) [45] and the Uniform Asymptotic Theory (UAT) [22]. These theories in elastodynamics are presented hereafter in sections 1.4.1 and 1.4.2.

1.4.1 Physical Theory of Diffraction (PTD)

The Physical Theory of Diffraction (PTD) [45] combines GTD and KA to overcome the limitations of both models. The PTD consists in correcting the KA contribution for edge diffracted waves thanks to the GTD. This correction is done by adding to the KA field a corrective term which is the difference between the wave amplitudes diffracted by the edge given by GTD and KA. For an incident plane wave of type $\alpha = L, TV$ or TH, on an obstacle, the total PTD displacement field is expressed as

$$\mathbf{u}^{\mathrm{tot(PTD)}}(\mathbf{x}) = \mathbf{u}^{\alpha}(\mathbf{x}) + \mathbf{u}^{\mathrm{diff(PTD)}}(\mathbf{x}) \tag{1.8}$$

where

$$\mathbf{u}^{\mathrm{diff(PTD)}}(\mathbf{x}) = \sum_{\beta} \left[\mathbf{u}_{\beta}^{\alpha(\mathrm{KA})}(\mathbf{x}) + u_{\alpha}(\mathbf{x}_{\beta}^{\alpha}) \left(D_{\beta}^{\alpha(\mathrm{GTD})}(\mathbf{x}) - D_{\beta}^{\alpha(\mathrm{KA})}(\mathbf{x}) \right) \frac{e^{ik_{\beta}S_{\beta}}}{\sqrt{k_{\beta}L_{\beta}}} \mathbf{e}_{\beta}(\mathbf{x}) \right]. \tag{1.9}$$

In (1.9), β is the type of the scattered wave and the scattered field $\mathbf{u}_{\beta}^{\alpha(\mathrm{KA})}$ is obtained by (1.1) with the COD being calculated with GE. $D_{\beta}^{\alpha(\mathrm{GTD})}$ is the GTD diffraction coefficient and $D_{\beta}^{\alpha(\mathrm{KA})}$ is the Kirchhoff edge diffraction coefficient and is obtained by an asymptotic evaluation (for $k_{\beta}S_{\beta} \gg 1$) of the Kirchhoff integral. It corresponds to the contribution of the scatterer edges to the Kirchhoff integral. Near incident and specular directions, the GTD diffraction coefficient $D_{\beta}^{\alpha(\mathrm{GTD})}$ diverges in the same manner as the KA diffraction coefficient $D_{\beta}^{\alpha(\mathrm{KA})}$ leading to a cancellation of the diffracted field. The remaining term is the Kirchhoff integral

$$\mathbf{u}_{\beta}^{\alpha(\mathrm{PTD})}(\mathbf{x}) \approx \mathbf{u}_{\beta}^{\alpha(\mathrm{KA})} \tag{1.10}$$

which provides a good result near specular directions. PTD is therefore spatially uniform at shadow boundaries contrary to GTD and has a good description of the interference between reflected and diffracted waves.

Away from incident and specular directions, the Kirchhoff integral $\mathbf{u}_{\beta}^{\alpha(\mathrm{KA})}$ contribution to the

diffracted field can be approximated by the KA edge diffracted field

$$\mathbf{u}^{\mathrm{diff(KA)}}(\mathbf{x}) \approx \sum_{\beta} u_{\alpha}(\mathbf{x}_{\beta}^{\alpha}) D_{\beta}^{\alpha(\mathrm{KA})}(\mathbf{x}) \frac{e^{ik_{\beta}r}}{\sqrt{k_{\beta}s_{\beta}}} \mathbf{e}_{\beta}(\mathbf{x}). \tag{1.11}$$

Hence, the remaining term in the PTD diffracted field expressed as

$$\mathbf{u}^{\mathrm{diff(PTD)}}(\mathbf{x}) \approx \mathbf{u}^{\mathrm{diff(KA)}}(\mathbf{x}) + \sum_{\beta} u_{\alpha}(\mathbf{x}_{\beta}^{\alpha}) \left(D_{\beta}^{\alpha(\mathrm{GTD})}(\mathbf{x}) - D_{\beta}^{\alpha(\mathrm{KA})}(\mathbf{x}) \right) \frac{e^{ik_{\beta}S_{\beta}}}{\sqrt{k_{\beta}L_{\beta}}} \mathbf{e}_{\beta}(\mathbf{x}) \tag{1.12}$$

corresponds to the GTD diffracted field using Eq. (1.9)

$$\mathbf{u}^{\mathrm{diff(PTD)}}(\mathbf{x}) \approx \sum_{\beta} u_{\alpha}(\mathbf{x}_{\beta}^{\alpha}) D_{\beta}^{\alpha(\mathrm{GTD})}(\mathbf{x}) \frac{e^{ik_{\beta}r}}{\sqrt{k_{\beta}L_{\beta}}} \mathbf{e}_{\beta}(\mathbf{x}) \tag{1.13}$$

which gives a good description of the edge diffracted field away from shadow boundaries.

PTD is also a high frequency asymptotic method recently developed in the CIVA software platform [36] to compute only the flaw response as GTD. Combining the Kirchhoff Approximation and GTD, PTD implementation requires to mesh the flaw surface for the Kirchhoff model and also the flaw contour for GTD. Note that a comparison of NDT system models based on the Physical Theory of diffraction, the Geometrical Theory of Diffraction and on the Kichhoff Approximation is done in [36]. By system model, we mean a complete simulation tool for computing echoes from crack-like flaws.

There is another GTD uniform correction developed in elastodynamics, the Uniform Asymptotic Theory of diffraction (UAT), described in section 1.4.2.

1.4.2 Uniform Asymptotic Theory (UAT)

The Uniform Asymptotic Theory (UAT) is a GTD uniform correction extended from electromagnetism to elastodynamics [22]. UAT consists in modifying the GE field in order to remove the singularity appearing in the GTD diffracted field near incident and specular directions (see section A.3.1 in appendix A.4). For the scattering of an elastic plane wave by a half-plane, the total field (1.5) is modified as

$$\mathbf{u}^{\mathrm{tot(UAT)}}(\mathbf{x}) = \left[\overline{F}(\xi_{\alpha}) - \widehat{\overline{F}}(\xi_{\alpha}) \right] \mathbf{u}^{\mathrm{inc}} + \sum_{\beta} \left[\overline{F}(\xi_{\beta}) - \widehat{\overline{F}}(\xi_{\beta}) \right] \mathbf{u}^{\mathrm{ref}} + \mathbf{u}^{\mathrm{diff(GTD)}}(\mathbf{x}), \tag{1.14}$$

with $\overline{F}$ – the Fresnel function

$$\overline{F}(X) = \frac{1}{\sqrt{i\pi}} \int_{X}^{+\infty} e^{it^2} \mathrm{d}t \tag{1.15}$$

and

$$\widehat{\overline{F}}(X) = e^{i\frac{\pi}{4}} \frac{e^{iX^2}}{2X\sqrt{\pi}}. \tag{1.16}$$

$\mathbf{u}^{\text{inc}}$ is the incident field, $\mathbf{u}^{\text{ref}}$ the reflected field and $\mathbf{u}^{\text{diff(GTD)}}$ the GTD diffracted field. The parameters ξ_α and ξ_β are the detour parameters [42]. They allow to determine the proximity of an observation point to a shadow boundary. ξ_α is linked to the shadow boundary of the incident wave and ξ_β to the one of the reflected wave of type β. In UAT (1.14), the GTD diffracted field is kept untouched as in the GTD total field (1.5) whereas the Geometrico-Elastodynamic field is modified. For small detour parameter, meaning that the observation point is close to a shadow boundary, the function $\widehat{\overline{F}}$ introduces a singularity at shadow boundaries which compensates the one of the GTD diffraction coefficient. Moreover, the Fresnel function $\overline{F}$ smooths the discontinuities of the GE field when crossing a shadow boundary. Finally, the total UAT field is spatially uniform since it does not diverge as the GTD total field and it does not have any discontinuity as the GE field.

The smooth part of geometrical field obtained using only Fresnel functions extracted from (1.14) is expressed as

$$\mathbf{u}^{\text{smooth(GE)}}(\mathbf{x}) = \overline{F}(\xi_\alpha)\, \mathbf{u}^{\text{inc}} + \sum_\beta \overline{F}(\xi_\beta)\, \mathbf{u}^{\text{ref}}. \tag{1.17}$$

An example of a smooth geometrical field is shown in Fig. 1.12. In this figure, a longitudinal plane wave impacts a half-plane with an incidence angle of $60°$ to the half-plane. In GE, the space is then divided into 4 regions as specified in Fig. 1.4: the shadow zone where there is no geometrical incident or reflected waves ($\theta < 60°$) noted I, the zone where there are only incident longitudinal plane waves ($60° < \theta < 286°$) noted II, the zone where there are incident and reflected transversal plane waves ($286° < \theta < 300°$) noted III and the last zone where there are reflected transversal plane waves, incident and reflected longitudinal waves ($300° < \theta < 360°$) noted IV (see Fig. 1.4b). The GE field represented in red is discontinuous at shadow boundaries of these different regions ($60°, 286°$ and $300°$) as explained in section 1.2 whereas the smooth geometrical field (1.17) in blue is continuous at these shadow boundaries.

Since in (1.14) the incident and reflected fields are defined on the whole space, both incident and reflected fields have to be extended to their corresponding shadow region. This can be achieved by extending the illuminating face beyond the crack edge and tracing the resulting fictitious reflected rays (see dashed rays on Fig. 1.13) [15, 16]. UAT is therefore complicated to implement for complex geometries. There exist another GTD uniform correction, the Uniform Theory of Diffraction (UTD) which is simple to implement contrary to UAT. It has been derived in electromagnetism and in acoustic. As far as we are aware, UTD has never been extended to elastodynamics, and its extension has been done in this thesis (in chapter 2 for the half-plane and 4 for

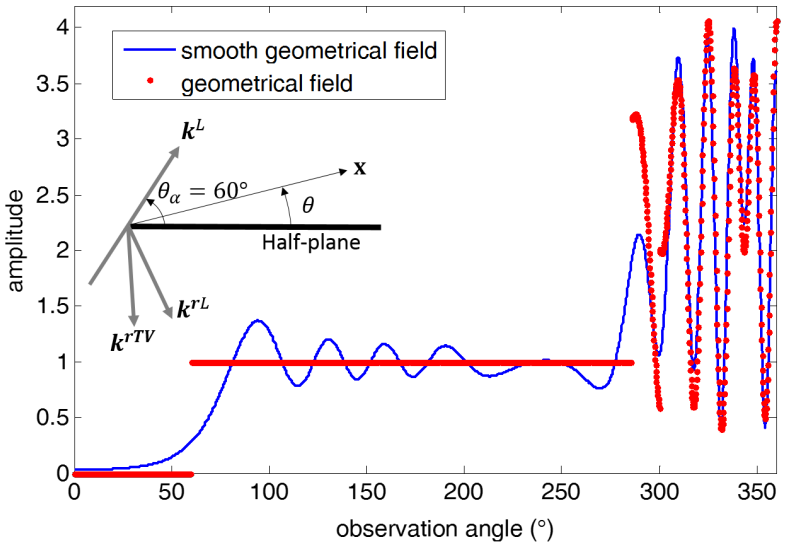

Figure 1.12: Scattering of a longitudinal plane wave from a half-plane contained in a ferritic steel component: amplitude of the geometrical field in red and of the smooth geometrical field in blue normalized by the incident amplitude. Observations points M spatially defined in terms of the angle θ and located at $2\lambda_L$ of the diffracting edge (λ_L being the longitudinal wavelength).

the 2D wedge).

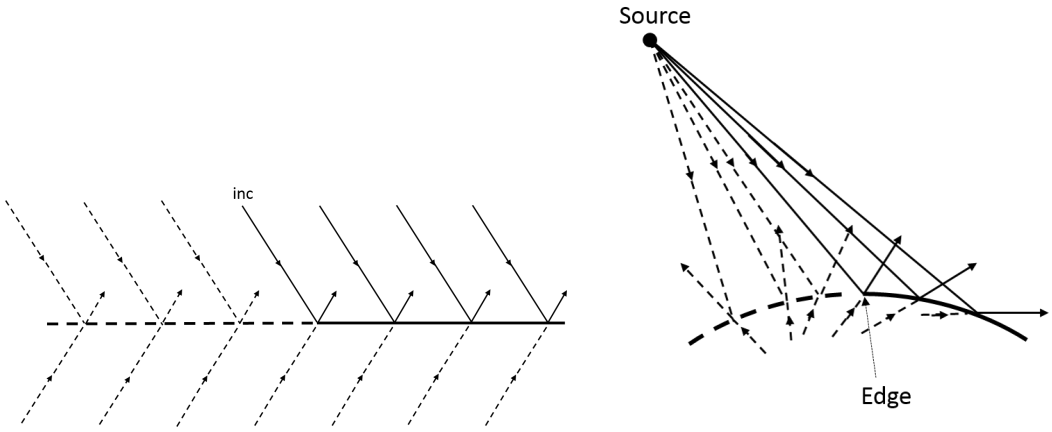

(a) (Reproduced from [15, 16]) half-plane (thick line) illuminated by a plane wave

(b) curved face (thick line) illuminated by a spherical wave

Figure 1.13: Extension of the reflected field to its shadow zone using fictitious rays. Dashed thick lines are the extensions of the scatterers beyond the crack edge and dashed thin lines are incident and fictitious reflected rays on these extensions.

1.5 Conclusion

There exists in the literature several high frequency scattering models in elastodynamics. Each of them has limits of validity. So far, in the software platform CIVA, the specimen echoes have been calculated either with the CIVA pencil method (GE, specular model) or with the Kirchhoff Approximation (KA). The Geometrical Elastocynamics (GE) and consequently the specular model does not take into account diffraction phenomena, contrary to the Kirchhoff Approximation (KA). Furthermore, the amplitude of diffracted waves, notably for transversal waves, are erroneously predicted by KA. On the other hand, GTD is an asymptotic model which has a realistic and a quantitative description of diffracted waves [21, 36]. It considers that such waves are generated along a cone of diffracted rays, the Keller's cone. Being a ray method as the specular model of CIVA, GTD could be used in CIVA to extend the actual specular model in order to propose a fast and accurate modelling both in specular and diffracted directions. However, GTD diverges near specular and incident directions. In fact, it does not model the interference of incident/reflected waves with diffracted waves. PTD and UAT, two existing uniform corrections of GTD can be used to overcome this problem. Nevertheless, PTD being an integral method on the scatterer surface can be time consuming for large scatterers and UAT is a non trivial method since it requires computing fictitious rays in order to remove the GTD divergence. There exists another GTD uniform correction, the Uniform Theory of Diffraction (UTD) which has already been developed in electromagnetism and acoustics but not in elastodynamics. It is simple to implement, contrary to UAT, and is a ray theory, contrary to PTD. That's why UTD represents an interesting solution to extend the ray method of the CIVA specular model.

GTD and consequently UTD being high frequency models, depend only on the local properties of the wave to flaw interaction. GTD and consequently its uniform corrections are then determined for simple scattering problems having these local properties called canonical problems.

The main objective of this thesis is to develop UTD in elastodynamics for diffraction by solid wedges. UTD for wedges will then permit to model diffraction and reflection by surface irregularities of a specimen. Scattering from wedges being a complex problem to deal with, we first began our study by the diffraction by a half-plane which is a wedge of 360° and for which an analytical solution of GTD exists.

Chapter 2

The Uniform geometrical Theory of Diffraction (UTD) for elastodynamics: Plane wave scattering from a half-plane

Le Contrôle Non Destructif (CND) par ultrasons est fondé sur la diffusion des ondes élastiques par des obstacles. Il existe deux principaux phénomènes de diffusion : la réflexion spéculaire et la diffraction. La Théorie Géométrique de la Diffraction (abrégée par GTD en anglais) est une méthode couramment utilisée pour modéliser la diffraction par des diffuseurs de géométrie canonique. Elle est obtenue par approximation asymptotique de la solution exacte du problème de diffusion d'une onde élastique par un objet de forme canonique. Cette approximation asymptotique possède des limites de validité. En effet, elle cesse d'être valide pour des directions d'observation proches de la direction de transmission vers l'avant et des directions de réflexion spéculaire.

Dans ce chapitre, l'UTD initialement développée en électromagnétisme a été établi en élastodynamique pour la diffusion d'une onde plane par un demi-plan contenu dans un solide élastique isotrope. Elle a ensuite été comparée à une autre correction uniforme de la GTD, l'UAT (la Théorie Uniforme Asymptotique de la diffraction). En champ lointain, un bon accord est obtenu entre ces deux théories uniformes.

2.1 Introduction

In this chapter, the underlying canonical problem is the scattering of a plane wave by a stress-free half-plane. Its exact solution is represented in the form of the Sommerfeld integral [22, 23] and the classical GTD solution is obtained using the steepest descent method. In GTD, the contribution of the stationary phase points represents the diffracted waves in far field using the so-called diffraction coefficients.

Since the method of steepest descent is inapplicable when the stationary phase point of the integrand coalesces with its pole, the classical GTD fails in the zones (penumbrae) surrounding shadow boundaries (explained in section 1.2) where edge diffracted waves interfere with incident or reflected waves. For this reason GTD is said to be non-uniform. Several uniform extensions of GTD (see chapter 1) have been developed in electromagnetism [15, 16], such as the Uniform Asymptotic Theory (UAT) [41, 43] based on the Van Der Waerden method [46], the Uniform Theory of Diffraction (UTD) [12, 14] based on the Pauli-Clemmow method [47] and the Physical Theory of Diffraction (PTD) [10, 19, 44], which combines GTD and Kirchhoff Approximation (KA).

The elastodynamic versions of UAT and PTD have been reported before in [38] and [45] respectively; at the leading order, when the scatterer is a half-plane, PTD is identical to UAT [45]. Due to the integral nature of the method, PTD appears to be computationally expensive, especially when the scatterers are large compared to the wavelength. In the literature, a procedure similar to PTD has been confusingly called by its author the Uniform Theory of Diffraction [48]. It relies on the Rayleigh Sommerfeld integral [see Eq. (1.1) in Chapter 1] where the crack-opening displacement is very difficult to compute since it is calculated without any approximation, contrary to the Kirchhoff approximation. Whenever applicable, ray methods are often preferred to integral methods, since highly optimized and therefore extremely fast ray tracing algorithms have become available. Both UAT and UTD are ray methods, producing continuous approximations to total fields. However, UAT involves artificial extension of the scattering surface and fictitious reflected rays (see Fig. 1.13 and Section 1.4.2), while UTD does not. For this reason, UTD is more used than UAT in acoustics [49] and electromagnetism [50].

This chapter is structured as follows: in Section 2.2, the exact solution of the canonical problem of a plane wave scattering from a stress-free half-plane is presented in the form of the Sommerfeld integral, and its non-uniform asymptotic approximation are given in a form convenient for use in the UTD recipe. In Section 2.3, uniform asymptotic approximation of the integral are derived using the Pauli-Clemmow procedure. As a result, the elastodynamic UTD is obtained, with the total field involving no fictitious rays and with diffraction coefficients, which are a simple modification of the GTD diffraction coefficients. Comparison of UTD and UAT is carried out in Section 2.4.

2.2 Scattering of a plane elastic wave by a half-plane crack : non uniform asymptotics

In this section, the non uniform asymptotic approximations of the canonical problem of a plane wave scattering from a stress-free half-plane are recalled [22, 24]. These non uniform asymptotic approximations consist in the sum of the Geometrico-Elastodynamics (GE, see section 1.2) and the GTD diffracted (see section 1.4) fields. There are called non uniform asymptotics because there are high frequency methods which give rise to a non-uniform total wave field. Indeed, at shadow boundaries, GE leads to a discontinuity, whereas GTD leads to a divergence. Links between these non-uniformities of GE and GTD are underlined in this section. This preliminary work is useful for a better understanding of the developed UTD recipe.

In the following, as said at the begining of chapter 1, the symbols α and β are used to denote the wave type, i.e. $\alpha, \beta = L, TV$ or TH (Longitudinal, Transversal Vertical or Transversal Horizontal, respectively). In general, α is used for the incident wave and β for reflected and diffracted waves. Scalar quantities are generally labelled by taking α and β as subscripts, while α is used as superscripts for vectors related to the incident wave and β as subscripts for vectors related to scattered waves. For scalar quantities which link incident and scattered waves, α is used as superscript and β as subscript.

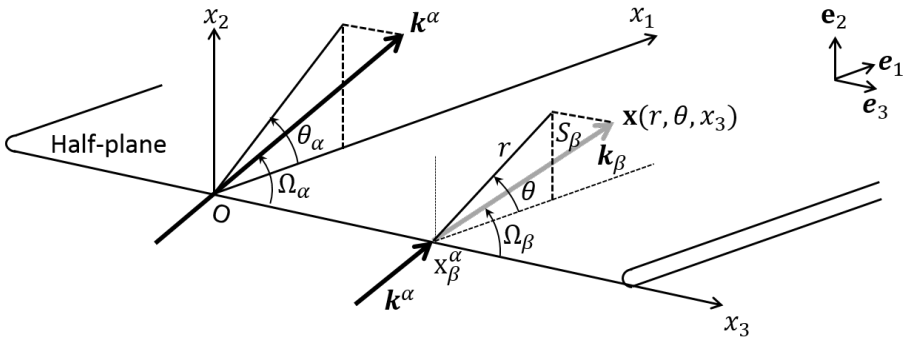

Figure 2.1: A plane wave of propagation vector $\boldsymbol{k}^\alpha$ incident on a semi-infinite stress free crack. Thick arrow - direction of the incident wave; thick gray arrow - direction of the diffracted wave $\boldsymbol{k}_\beta$.

The geometry of the problem is presented in Fig. 2.1, using the Cartesian system based on an orthonormal basis $\{\mathbf{e_1}, \mathbf{e_2}, \mathbf{e_3}\}$ and an origin O located on the crack edge. The crack is embedded in an elastic isotropic homogeneous space and its face lies in the half-plane $\{x_2 = 0, x_1 \geq 0\}$. The edge coincides with the x_3 axis and is irradiated by a plane wave, its particle displacement being written as

$$\mathbf{u}^\alpha(\mathbf{x}) = A_\alpha \, \mathbf{d}^\alpha e^{i(-\omega t + \mathbf{k}^\alpha \cdot \mathbf{x})}, \tag{2.1}$$

where A_α is the wave displacement amplitude, $\mathbf{d}^\alpha$ is its polarization, $\mathbf{k}^\alpha$ is its wave vector defined through the angles Ω_α and θ_α (described in Fig. 2.1), whose magnitude $k_\alpha = \omega/c_\alpha$, with c_α the speed of the corresponding mode and ω the circular frequency; t is time; and $\mathbf{x}$ is the position vector, which is expressed in the Cartesian coordinates as (x_1, x_2, x_3) and in the cylindrical coordinates as $(r, 0, x_3)$. The time convention $\exp(-i\omega t)$ is implied but omitted everywhere.

The resulting total displacement field of the scattering of a plane elastic wave by a half-plane is

$$\mathbf{u}^{\mathrm{tot}}(\mathbf{x}) = \mathbf{u}^\alpha(\mathbf{x}) + \sum_\beta \mathbf{u}^\alpha_\beta(\mathbf{x}), \tag{2.2}$$

where $\mathbf{u}^\alpha_\beta$ is the exact scattered field, expressed by Achenbach [22] as an angular spectral decomposition. It can be rewritten as the Sommerfeld integral

$$\mathbf{u}^\alpha_\beta(\mathbf{x}) = e^{ik_\alpha \cos\Omega_\alpha x_3} \int_\Gamma f_\beta(-q_\beta \cos\lambda, \mathrm{sgn}(\sin\theta))\, e^{i\zeta\cos(\lambda-\overline{\theta})}\, \mathbf{t}_\beta(-q_\beta\cos\lambda, \mathrm{sgn}(\sin\theta))\, \mathrm{d}\lambda. \tag{2.3}$$

Let us detail the different quantities involved in (2.3).

- The integrand amplitude $f_\beta(-q_\beta\cos\lambda, \mathrm{sgn}(\sin\theta))$ is defined as

$$f_\beta(-q_\beta\cos\lambda, \mathrm{sgn}(\sin\theta)) = i\,\frac{q_\beta\kappa_\beta}{2\pi}\sin\lambda\,\frac{g_\beta(-q_\beta\cos\lambda, \mathrm{sgn}(\sin\theta))}{q_\alpha\cos\theta_\alpha - q_\beta\cos\lambda}, \tag{2.4}$$

  with the subscript β denoting the scattered wave mode, $q_\beta = \kappa_\beta \sin\Omega_\beta$, $\kappa_\beta = c_L/c_\beta$ - the dimensionless slowness of the scattered wave, and $g_\beta(-q_\beta\cos\lambda, \mathrm{sgn}(\sin\theta))$, the numerator of the scattered wave potential being an analytical function defined in Ref. [22] (see sections 5.1 to 5.4 for the definition of all the involved terms). Expressions of g_β function for $\beta = L, TV$ or TH are recalled in appendix B. The integrand amplitude $f_\beta(-q_\beta\cos\lambda, \mathrm{sgn}(\sin\theta))$ has thus two poles $\lambda = \theta_\beta$ and $\lambda = 2\pi - \theta_\beta$, where $\theta_\beta \in [0, \pi]$ is defined as

$$q_\beta\cos\theta_\beta = q_\alpha\cos\theta_\alpha. \tag{2.5}$$

  This relation (2.5) between the poles is the Snell–Descartes law of reflection.

- ζ is the far-field parameter

$$\zeta = k_\beta L_\beta, \tag{2.6}$$

  where L_β, the distance parameter, can be written as

$$L_\beta = r\,\sin\Omega_\beta, \tag{2.7}$$

  with Ω_β being the angle of the diffraction cone (see Fig. 2.1) linked to the incidence angle Ω_α by the Snell-Descartes law of diffraction $k_\beta\cos\Omega_\beta = k_\alpha\cos\Omega_\alpha$.

- $\overline{\theta}$ is related to the position vector $\mathbf{x}$ (see Fig. 2.1) by

$$\begin{cases} \overline{\theta} = \theta & \text{if } 0 \leq \theta \leq \pi \\ \overline{\theta} = 2\pi - \theta & \text{if } \pi < \theta \leq 2\pi \end{cases} . \tag{2.8}$$

- Γ is the integration contour in the complex λ-plane determined in [22] and depicted in Fig. 2.2.

- $\mathbf{t}_\beta$ is the polarization vector of the scattered wave defined in the Cartesian basis $\{\mathbf{e_1}, \mathbf{e_2}, \mathbf{e_3}\}$ as [38]

$$\mathbf{t}_L(a,b) = \left(-a, b\,\left(q_L^2 - a^2\right)^{\frac{1}{2}}, \cos\Omega_L\right), \tag{2.9a}$$

$$\mathbf{t}_{TV}(a,b) = \frac{\sqrt{q_T^2 - a^2}}{\kappa\sqrt{a^2 + \cos^2\Omega_L}}\left(ab,\ \left(a^2 + \cos^2\Omega_L\right)\left(q_T^2 - a^2\right)^{-\frac{1}{2}},\ -b\cos\Omega_L\right), \tag{2.9b}$$

$$\mathbf{t}_{TH}(a,b) = -\frac{1}{\sqrt{a^2 + \cos^2\Omega_L}}\left(\cos\Omega_L, 0, a\right) \tag{2.9c}$$

where the positive square root $z^{1/2}$ is used for $\arg z \in]-\pi, \pi]$.

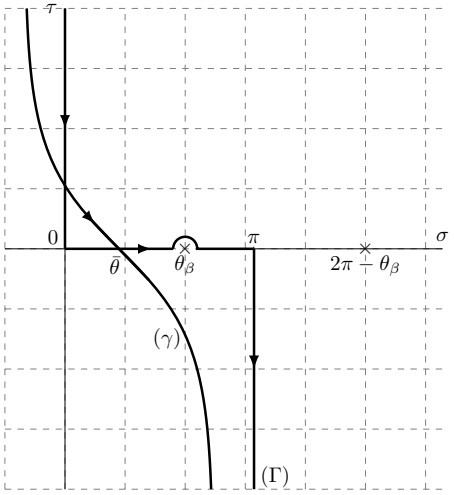

Figure 2.2: Integration path Γ and the steepest descent path γ in the complex plane $\lambda = \sigma + i\tau$. θ_β and $2\pi - \theta_\beta$ are the real poles of the integral (2.3) and $\bar{\theta}$ is its phase stationary point.

In the high frequency approximation, $\zeta \gg 1$, the integral (2.3) can be evaluated asymptotically. The main contributions are due to the integral critical points such as singularities of the integrand amplitude f_β (poles or branch points) or as the stationary points of the phase function. Each mathematical object is related to a physical one: the integrand poles permit to describe the

incident waves and the waves reflected by the half-plane as well as the surface waves (Rayleigh waves); the stationary points are related to the waves diffracted by the half-plane edge, and the branch points permit to describe the head waves (a detailed description of these waves are given in section 2.4). When these mathematical objects are far apart from each other, their contribution can be easily calculated. In this thesis, we are mainly interested in incident, reflected and diffracted waves. That's why the only integrand singularities considered below are the poles $\lambda = \theta_\beta$ and $\lambda = 2\pi - \theta_\beta$.

2.2.1 Contributions of isolated poles: Geometrico-Elastodynamic field (GE)

To evaluate the integral (2.3) asymptotically, the integration contour (Γ) is deformed to the steepest descent contour (γ) which passes through the phase stationary point $\bar{\theta} \in [0, \pi]$. This contour (γ) corresponds to points in the $\lambda = \sigma + i\tau$ plane satisfying:

$$\mathrm{Re}\left[\cos(\lambda - \bar{\theta})\right] = 1 \quad \text{[see Eq. (A.24) in Appendix A.2]}. \tag{2.10}$$

Using the complex definition of the cosinus function

$$\cos x = \frac{e^{ix} + e^{-ix}}{2}, \tag{2.11}$$

it can be shown that

$$\mathrm{Re}\left[\cos(\lambda - \bar{\theta})\right] = \cos(\sigma - \bar{\theta}) \cosh \tau. \tag{2.12}$$

The steepest descent path (γ) is then parametrized by the Gudermannian function gd

$$\sigma = \bar{\theta} - \mathrm{gd}(\tau) = \bar{\theta} - \mathrm{sgn}(\tau) \arccos\left(\frac{1}{\cosh \tau}\right), \tag{2.13}$$

where $\arccos$ is a multi-evaluated function. Its sign is chosen so that the angle between the steepest descent direction near the stationary phase point and the positive real axis is $\arg(\lambda - \bar{\theta}) = -\pi/4$ as a specification of the steepest descent contour (A.14). Among the two poles $\lambda = \theta_\beta$ and $\lambda = 2\pi - \theta_\beta$, only the isolated pole $\lambda = \theta_\beta$ (with $0 \leqslant \theta_\beta \leqslant \pi$) can lead to a non-zero contribution to the integral (2.3), since it might be crossed when deforming the contour. It is only crossed when

$$0 \leq \overline{\theta} \leq \theta_\beta \quad \text{(see Fig. 2.2)}. \tag{2.14}$$

Therefore, its contribution must be taken into account for the asymptotic evaluation of the integral (2.3). The GE field is the sum of this pole contribution and of the incident field. Combining (2.8) and (2.14), this pole $\lambda = \theta_\beta$ gives rise to two different physical contributions depending on the observation angle θ. When $\bar{\theta} = 2\pi - \theta$ [i.e. when $\pi \leqslant \theta \leqslant 2\pi$ according to (2.8)], the pole $\lambda = \theta_\beta$ is only crossed when $2\pi - \theta_\beta \leqslant \theta \leqslant 2\pi$ and its contribution then leads to the reflected

field. For $\bar{\theta} = \theta$, the pole θ_β is crossed when $0 \leqslant \theta \leqslant \theta_\beta$. It gives rise to the so-called compensating field which cancels the incident field when $\beta = \alpha$ and is zero otherwise. As a conclusion, the condition (2.14) ensuring non-zero pole contribution is checked when the observation point lies in irradiated areas of the GE field (see Fig. 1.4): the pole contribution is not null in the insonified zone of the reflected field ($2\pi - \theta_\beta \leqslant \theta \leqslant 2\pi$ and $\bar{\theta} = 2\pi - \theta$) and in that of the compensating field ($0 \leqslant \theta \leqslant \theta_\beta$, $\beta = \alpha$ and $\bar{\theta} = \theta$) [22]. Then, applying the residue theorem to integral (2.3) and using the clockwise contour around the pole (see Fig. 2.2) give the amplitudes of the reflected and compensating fields,

$$\lim_{\substack{\lambda \to \theta_\beta \\ \theta \in [2\pi - \theta_\beta, 2\pi]}} -2\pi i \, f(-q_\beta \cos\lambda, \operatorname{sgn}(\sin\theta)) \, (\lambda - \theta_\beta) = \kappa_\beta \, g_\beta \, (-q_\beta \cos\theta_\beta, -1)$$

$$= R_\beta^\alpha(\theta_\alpha^{'}), \tag{2.15a}$$

$$\lim_{\substack{\lambda \to \theta_\beta \\ \theta \in [0, \theta_\beta]}} -2\pi i \, f(-q_\beta \cos\lambda, \operatorname{sgn}(\sin\theta)) \, (\lambda - \theta_\beta) = \kappa_\beta \, g_\beta \, (-q_\beta \cos\theta_\beta, 1)$$

$$= -1, \quad \alpha = \beta, \tag{2.15b}$$

$$\lim_{\substack{\lambda \to \theta_\beta \\ \theta \in [0, \theta_\beta]}} -2\pi i \, f(-q_\beta \cos\lambda, \operatorname{sgn}(\sin\theta)) = \kappa_\beta \, g_\beta \, (-q_\beta \cos\theta_\beta, 1)$$

$$= 0, \quad \alpha \neq \beta, \tag{2.15c}$$

where R_β^α is the reflection coefficient in terms of displacement and $\theta_\alpha^{'}$ is the angle between the incident wave vector $\mathbf{k}^\alpha$ and $\mathbf{e}_1$. This angle is expressed as

$$\sin\theta_\alpha^{'} = \sin\Omega_\alpha \sin\theta_\alpha. \tag{2.16}$$

Reflection coefficients R_β^α in (2.15a) are given in [22] and are reproduced hereafter :

- For $\alpha = TH$,

$$R_L^{TH} = R_{TV}^{TH} = 0, \tag{2.17a}$$

$$R_{TH}^{TH} = 1. \tag{2.17b}$$

- for $\alpha = L$ with Snell–Descartes law of reflection $\cos\theta_L^{'} = \kappa \cos\theta_{rT}^{'}$,

$$R_L^L\left(\theta_L^{'}\right) = \frac{\sin\left(2\theta_L^{'}\right)\sin\left(2\theta_{rT}^{'}\right) - \kappa^2\cos^2\left(2\theta_{rT}^{'}\right)}{\mathcal{R}\left(\theta_L^{'}, \theta_{rT}^{'}\right)}, \tag{2.18a}$$

$$R_{TV}^L\left(\theta_L^{'}\right) = -\frac{2\kappa\sin\left(2\theta_L^{'}\right)\cos\left(2\theta_{rT}^{'}\right)}{\mathcal{R}\left(\theta_L^{'}, \theta_{rT}^{'}\right)}, \tag{2.18b}$$

$$R_{TH}^L\left(\theta_L^{'}\right) = 0. \tag{2.18c}$$

- for $\alpha = TV$ with $\cos\theta_{rL}^{'} = \kappa \cos\theta_T^{'}$,

$$R_L^{TV}\left(\theta_T^{'}\right) = \frac{\kappa\sin\left(4\theta_T^{'}\right)}{\mathcal{R}\left(\theta_{rL}^{'}, \theta_T^{'}\right)}, \tag{2.19a}$$

$$R_{TV}^{TV}\left(\theta_T^{'}\right) = \frac{\sin\left(2\theta_{rL}^{'}\right)\sin\left(2\theta_T^{'}\right) - \kappa^2\cos^2\left(2\theta_T^{'}\right)}{\mathcal{R}\left(\theta_{rL}^{'}, \theta_T^{'}\right)}, \tag{2.19b}$$

$$R_{TH}^{TV}\left(\theta_L^{'}\right) = 0. \tag{2.19c}$$

In these reflection coefficients,

$$\mathcal{R}(x, y) = \sin 2x\ \sin 2y + \kappa^2\cos^2 2y \tag{2.20}$$

is the Rayleigh function. In the following, for simplicity, $R_\beta^\alpha(\theta_\alpha^{'})$ will be denoted R_β^α. Equations (2.15a), (2.15b) and (2.15c) were not checked using a symbolic mathematics computation (as Mathematica) due to the complex expressions of functions g_β recalled in Appendix B. It has only been checked numerically with success by plotting the variation of $\kappa_\beta\, g_\beta$ for different observation points.

Adding the incident field to the poles contribution results in the Geometrico-Elastodynamic field

$$\mathbf{u}^{(\mathrm{GE})}(\mathbf{x}) = H\left(\eta_\alpha\right)\mathbf{u}^\alpha(\mathbf{x}) + \sum_\beta H\left(\eta_\beta\right)\mathbf{u}_\beta^{\alpha(\mathrm{ref})}(\mathbf{x}), \tag{2.21}$$

where $H(.)$ is the Heaviside function, and where

$$\mathbf{u}_{\beta}^{\alpha(\mathrm{ref})}(\mathbf{x}) = AR_{\beta}^{\alpha}\, e^{i\,k_{\beta}\,\mathbf{p}_{\beta}\cdot\mathbf{x}}\,\mathbf{d}_{\beta} \tag{2.22}$$

is the reflected field; the compensating field has been combined with the incident field to produce the first term of (2.21). In equation (2.22), $\mathbf{p}_{\beta} = (\sin\Omega_{\beta}\cos\theta_{\beta}, -\sin\Omega_{\beta}\sin\theta_{\beta}, \cos\Omega_{\beta})$ is the unit reflected wave vector and $\mathbf{d}_{\beta} = \mathbf{t}_{\beta}\,(-q_{\beta}\cos\theta_{\beta}, -1)$, $\mathbf{t}_{\beta}$ being defined in (2.9), is its polarisation vector defined as

$$\mathbf{d}_{L} = \mathbf{p}_{L} \tag{2.23a}$$

$$\mathbf{d}_{TV} = \frac{\mathbf{e}_2 - (\mathbf{e}_2\cdot\mathbf{p}_{TV})\mathbf{p}_{TV}}{\sqrt{1-(\mathbf{e}_2\cdot\mathbf{p}_{TV})^2}} \tag{2.23b}$$

$$\mathbf{d}_{TH} = -\frac{\cos\Omega_{TH}\,\mathbf{e}_1 - \sin\Omega_{TH}\cos\theta_{TH}\,\mathbf{e}_3}{\sqrt{1-(\mathbf{e}_2\cdot\mathbf{p}_{TH})^2}}. \tag{2.23c}$$

The arguments $\eta_{\alpha} = \mathrm{sgn}\,(\theta-\theta_{\alpha})$ and $\eta_{\beta} = \mathrm{sgn}(\theta - 2\pi + \theta_{\beta})$ of the respective Heaviside functions, also called wave indicators [22], determine whether the observation point is in the illuminated region or shadow of incident and reflected waves (see Fig. 1.4).

It should be noted that this expression of the geometrico-elastodynamics field is established for an incident plane wave. Kouyoumjian and Pathak [12] have shown that only the divergence factor of the reflected field is modified depending on the type of illumination (plane wave, cylindrical wave or spherical wave) using the ray theory. We can therefore define the Geometrico-Elastodynamics field for other types of illumination by:

$$\mathbf{u}^{(\mathrm{GE})}(\mathbf{x}) = H\,(\eta_{\alpha})\,\frac{\mathbf{u}^{\alpha}(\mathbf{x})}{\rho_{\alpha}^{(\mathrm{GE})}} + \sum_{\beta} H\,(\eta_{\beta})\,\frac{\mathbf{u}_{\beta}^{\alpha(\mathrm{ref})}(\mathbf{x})}{\rho_{\beta}^{(\mathrm{GE})}} \tag{2.24}$$

with $\rho_{\alpha}^{(\mathrm{GE})}$ being the divergence factor of the incident waves and $\rho_{\beta}^{(\mathrm{GE})}$ the divergence factor of the reflected waves. These divergence factors are given in [12] for scalar waves. Divergence factors in case of mode conversion at interfaces are given in [27]. The divergence factor of incident waves are then

$$\rho_{\alpha}^{(\mathrm{GE})} = \begin{cases} 1, & \text{for a plane wave incidence} \\ \sqrt{r_0(\mathbf{x})}, & \text{for a cylindrical wave incidence} \\ S_{\alpha}^{0}(\mathbf{x}) & \text{for a spherical wave incidence} \end{cases}. \tag{2.25}$$

with $r_0(\mathbf{x})$ being the distance from the source line to the observation point $\mathbf{x}$ and $S_{\alpha}^{0}(\mathbf{x})$ the distance from the source point to the observation point $\mathbf{x}$ (see Fig. 2.3). The divergence factor of the reflected wave are given subsequently.

- For an incident plane wave,

$$\rho_\beta^{\mathrm{pw(GE)}} = 1. \tag{2.26}$$

- For a spherical incident wave, the divergence factor of the reflected field is

$$\rho_\beta^{\mathrm{sph(GE)}} = \sqrt{\left(S_\alpha^0(\mathbf{x}_\beta^\alpha) + S_\beta \frac{\kappa_\alpha}{\kappa_\beta}\right)\left(S_\alpha^0(\mathbf{x}_\beta^\alpha) + S_\beta \frac{\sin^2\theta'_\alpha(\mathbf{x}_\beta^\alpha)}{\sin^2\theta'_\beta(\mathbf{x}_\beta^\alpha)}\frac{\kappa_\alpha}{\kappa_\beta}\right)} \tag{2.27}$$

where $S_\alpha^0(\mathbf{x})$ is the distance from the source point to the observation point $\mathbf{x}$, $\mathbf{x}_\beta^\alpha$ is the incidence point on the half-plane and S_β is the distance from this incidence point to the observation point (see Fig. 2.3 and 2.5). $\theta'_\alpha(\mathbf{x}_\beta^\alpha)$ is the angle between the incident wave vector at the incidence point on the half-plane $\mathbf{x}_\beta^\alpha$ and the x_1-axis. Its expression is given in Eq. (2.16). The angle $\theta'_\beta(\mathbf{x}_\beta^\alpha)$ is the reflection angle calculated thanks to Snell–Descartes law of reflection.

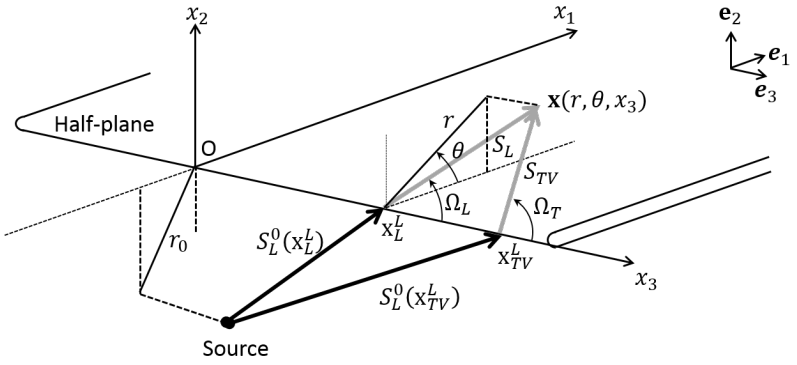

Figure 2.3: A semi-infinite stress free crack illuminated by a longitudinal spherical wave.

- For a cylindrical incidence, the divergence factor of the reflected wave is

$$\rho_\beta^{\mathrm{cyl(GE)}} = \sqrt{r_0(\mathbf{x}_\beta^\alpha) + r\frac{\sin^2\theta_\alpha(\mathbf{x}_\beta^\alpha)}{\sin^2\theta_\beta(\mathbf{x}_\beta^\alpha)}\frac{\kappa_\alpha}{\kappa_\beta}}, \tag{2.28}$$

where $\mathbf{x}_\beta^\alpha$ is the incidence point on the half-plane and $r_0(\mathbf{x}_\beta^\alpha)$ is the distance from this point to the source line (see Fig. 2.4). r is the distance from the source line to the observation point $\mathbf{x}$. $\theta_\alpha(\mathbf{x}_\beta^\alpha)$ is the angle between the x_1-axis and the incident wave vector at the edge point $\mathbf{x}_\beta^\alpha$ and $\theta_\beta(\mathbf{x}_\beta^\alpha)$ is the reflection angle calculated thanks to Snell–Descartes law of reflection (2.5). The considered cylindrical wave here is a line source of spherical waves along the x_3-axis. That's why the figure 2.4 is represented in the plane $(\mathbf{e}_1, \mathbf{e}_2)$.

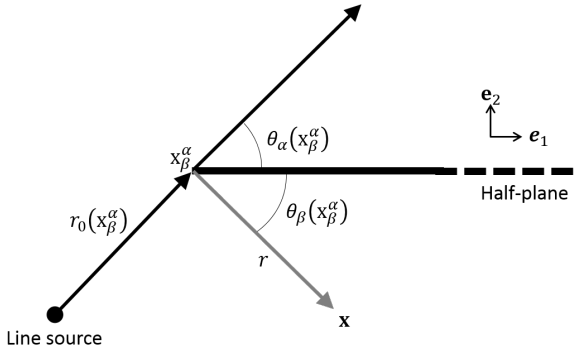

Figure 2.4: A semi-infinite stress free crack illuminated by a cylindrical incident wave.

The divergence factor of the spherical and cylindrical reflected waves can be explained by the fact that the reflected field can be seen to be generated by an image point (see Fig. 2.5 for the case without mode conversion $\beta = \alpha$). The distance of propagation of this emitted wave from the image source to the observation point is therefore $S_\alpha^0(\mathbf{x}_\beta^\alpha) + S_\beta$ for a spherical wave and $r_0(\mathbf{x}_\beta^\alpha) + r$ for a cylindrical wave, $\beta = \alpha$.

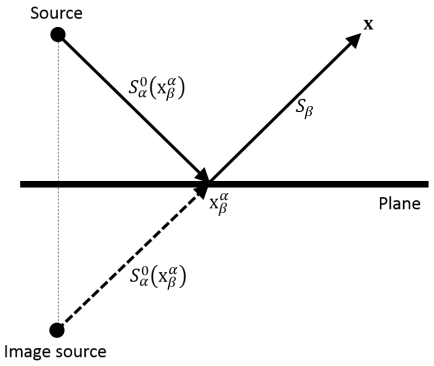

Figure 2.5: Principle of the image source for $\beta = \alpha$.

Having determined the contribution of the integrand poles being crossed during the deformation contour (Γ) to the steepest descent contour (γ), the contribution of the stationary phase point can now be calculated. On the steepest descent contour, the integrand falls off rapidly except in the neighbourhood of the saddle point $\lambda = \bar{\theta}$ (see appendix A.2). The remaining contribution to integral (2.3) is therefore the stationary phase point contribution.

2.2.2 Contributions of isolated stationary points: GTD

The contribution of each isolated stationary point $\lambda_s = \overline{\theta}$ can be found by applying the steepest descent method (see appendix A.2) to (2.3), producing the classical GTD recipe

$$\mathbf{u}_\beta^{\alpha(\mathrm{GTD})}(\mathbf{x}) = u_\alpha(\mathbf{x}_\beta^\alpha) D_\beta^{\alpha(\mathrm{GTD})}(\Omega_\alpha, \theta_\alpha, \theta) \frac{\mathrm{e}^{ik_\beta S_\beta}}{(k_\beta L_\beta)^{1/2}} \mathbf{e}_\beta(\Omega_\beta), \tag{2.29}$$

where the different parameters involved in (2.29) are:

- $\mathbf{x}_\beta^\alpha = (0, 0, x_3 - S_\beta \cos\Omega_\beta)$ is the diffraction point on the scattering edge (see Fig. 2.1);
- $u_\alpha(\mathbf{x}_\beta^\alpha) = \mathbf{u}^\alpha(\mathbf{x}_\beta^\alpha) \cdot \mathbf{d}^\alpha$ is the incident displacement field at the diffraction point $\mathbf{x}_\beta^\alpha$;
- S_β is the distance between the diffraction point $\mathbf{x}_\beta^\alpha$ and the observation point $\mathbf{x}$;
- $\mathbf{e}_\beta$ is the polarisation vector of the diffracted wave defined as

$$\mathbf{e}_\beta(\Omega_\beta) = \mathbf{t}_\beta\left(-q_\beta \cos\theta, \mathrm{sgn}(\sin\theta)\right); \tag{2.30}$$

- $D_\beta^{\alpha(\mathrm{GTD})}$ are GTD diffraction coefficients defined as

$$D_\beta^{\alpha(\mathrm{GTD})}(\Omega_\alpha, \theta_\alpha, \theta) = \frac{q_\beta \kappa_\beta}{\sqrt{2\pi}} \frac{g_\beta(-q_\beta \cos\theta, \mathrm{sgn}(\sin\theta))}{q_\alpha \cos\theta_\alpha - q_\beta \cos\theta} |\sin\theta| \, e^{\frac{i\pi}{4}}. \tag{2.31}$$

They contain poles at $\theta = \theta_\beta$ and $\theta = 2\pi - \theta_\beta$, which describe the shadow boundaries of incident and reflected rays respectively (see Fig. 1.4). Using residues (2.15a) - (2.15c), and defining near shadow boundaries, $\bar{\theta} = \theta_\beta + \epsilon$ (with $|\epsilon| \ll 1$), the limits of diffraction coefficients are

$$D_\beta^{\alpha(GTD)} \sim \frac{e^{i\frac{\pi}{4}}}{\sqrt{2\pi}} \begin{cases} L \in \mathbb{R} & \text{if } \theta \leq \pi \quad \text{and } \beta \neq \alpha \quad \text{(finite limit)} \\ -\dfrac{1}{\epsilon}, & \text{if } \theta \leq \pi \quad \text{and } \beta = \alpha \\ \dfrac{R_\beta^\alpha}{\epsilon}, & \text{if } \theta > \pi \end{cases}. \tag{2.32}$$

Note that at the incident and reflected shadow boundaries the total GE field (2.21) is finite but discontinuous due to the Heaviside function while the GTD diffracted field is infinite (see Figs. 2.6a, 2.7b, 2.7c and 2.7d) and its phase has a discontinuity of π at physical shadow boundaries (see Fig. 2.6b). Physical shadow boundaries refer to pole having non-zero residue and thus to waves which have a physical meaning. The discontinuity in the GTD coefficient phase on Fig. 2.6b when crossing a shadow boundary can be explained by Eq. (2.32) where ϵ changes of sign when the observation point crosses a shadow boundary.

At the non-physical incident shadow boundary $\theta = \theta_{\beta(\beta\neq\alpha)}$, GTD diffraction coefficient has a finite limit (see by example Fig. 2.7c at $\theta = \theta_L = 24°$). $\theta = \theta_{\beta\neq\alpha}$ is a non-physical incident shadow boundary because there is no wave conversion in transmission, only in reflection in this case, since the half-plane is a totally reflective surface. Transversal diffraction coefficients (as D_{TV}^{L} on Fig. 2.6c and as D_{TV}^{TV} on Figs. 2.7b and 2.7d) own additional discontinuities at $\theta = 56.8°$ and at $\theta = 303.2°$. These discontinuities are due to the longitudinal critical angle

$$\theta_c = \arccos\left(\kappa^{-1}\frac{\sin\Omega_L}{\sin\Omega_T}\right), \tag{2.33}$$

which corresponds to a branch point of the square root $(-q_\beta\cos\lambda + q_L)^{1/2}$ contained in the term (B.2a) of the transversal diffraction coefficient. Discussion about this critical angle is done in section 2.4. Note that UTD diffraction coefficients presented on Figs. 2.6 and 2.7 are commented in section 2.3.1. Due to the divergence of GTD diffraction coefficients and to discontinuities of GE field at shadow boundaries, the approximate GTD-based total displacement field

$$\mathbf{u}^{\mathrm{tot(GTD)}}(\mathbf{x}) = \mathbf{u}^{\mathrm{(GE)}}(\mathbf{x}) + \sum_{\beta}\mathbf{u}_{\beta}^{\alpha\mathrm{(GTD)}}(\mathbf{x}), \tag{2.34}$$

is therefore not spatially uniform particularly near shadow boundaries.

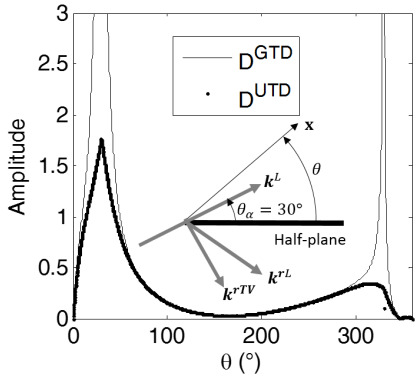

(a) Amplitude of the diffraction coefficient D_L^L

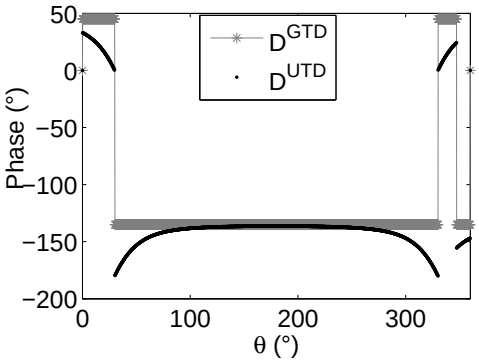

(b) Phase of the diffraction coefficient D_L^L

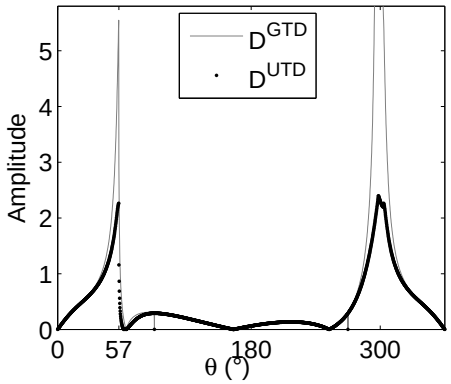

(c) Amplitude of the diffraction coefficient D_{TV}^L

Figure 2.6: Diffraction coefficient D_L^L for incident and diffracted longitudinal waves. $\Omega_L = 90°$ and $\theta_L = 30°$. The crack is embedded in a ferritic steel specimen.

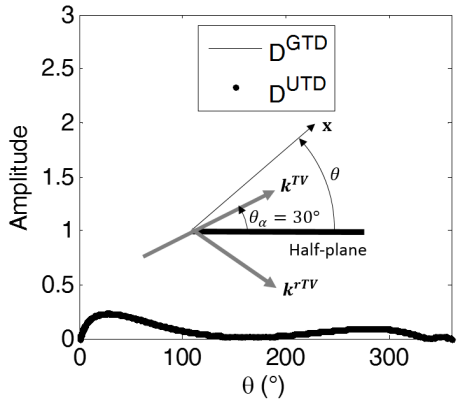

(a) Amplitude of the diffraction coefficient D_L^{TV}, $\theta_{TV} = 30°$

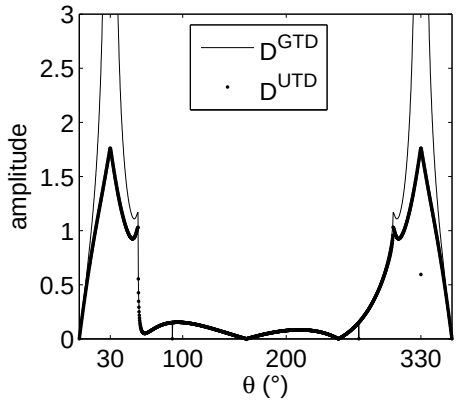

(b) Amplitude of the diffraction coefficient D_{TV}^{TV}, $\theta_{TV} = 30°$

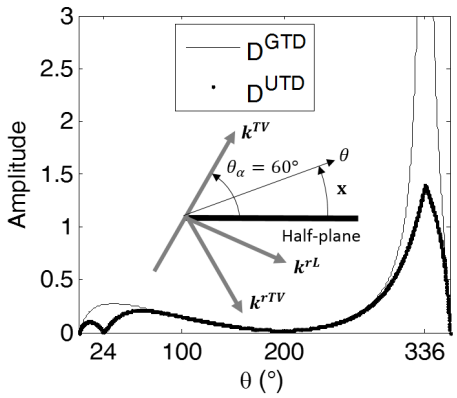

(c) Amplitude of the diffraction coefficient D_L^{TV}, $\theta_{TV} = 60°$

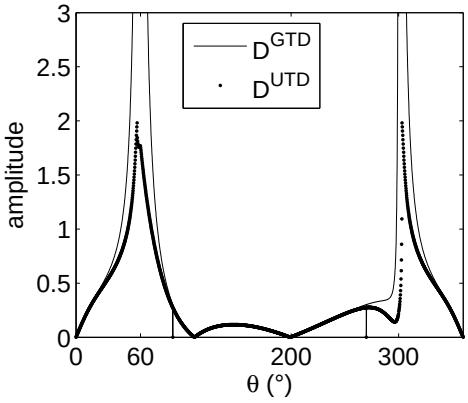

(d) Amplitude of the diffraction coefficient D_{TV}^{TV}, $\theta_{TV} = 60°$

Figure 2.7: Diffraction coefficient D_β^{TV}, $\beta = L, TV$, for transversal incident waves and diffracted waves of type β. $\Omega_{TV} = 90°$. The crack is embedded in a ferritic steel specimen.

As for reflection, only the divergence factor of the diffracted field is modified depending on the kind of illumination [8, 12, 23]. The GTD difracted field for other kinds of illumination are:

- for a cylindrical incident wave perpendicular to the edge according to [12],

$$\mathbf{u}_\beta^{\alpha(\mathrm{GTD})}(\mathbf{x}) = \frac{u^\alpha(\mathbf{x}_\beta^\alpha)}{\sqrt{r_0(\mathbf{x}_\beta^\alpha)}} D_\beta^{\alpha(\mathrm{GTD})}(\Omega_\alpha, \theta_\alpha, \theta)\, \frac{\mathrm{e}^{ik_\beta S_\beta}}{(k_\beta\, r)^{1/2}}\, \mathbf{e}_\beta(\Omega_\beta), \tag{2.35}$$

- for a spherical incident wave according to [23],

$$\mathbf{u}_{\beta}^{\alpha(\mathrm{GTD})}(\mathbf{x}) = \frac{u^{\alpha}(\mathbf{x}_{\beta}^{\alpha})}{S_{\alpha}^{0}(\mathbf{x}_{\beta}^{\alpha})} D_{\beta}^{\alpha(\mathrm{GTD})}(\Omega_{\alpha}, \theta_{\alpha}, \theta) \frac{\mathrm{e}^{ik_{\beta}S_{\beta}}}{\left(k_{\beta}\,\dfrac{S_{\beta}}{S_{\alpha}^{0}(\mathbf{x}_{\beta}^{\alpha})}\sin^{2}\Omega_{\beta}\right)^{1/2}\rho_{\beta}^{\mathrm{diff}}}\,\mathbf{e}_{\beta}(\Omega_{\beta}) \tag{2.36}$$

with

$$\rho_{\beta}^{\mathrm{diff}} = \sqrt{S_{\alpha}^{0}(\mathbf{x}_{\beta}^{\alpha}) + S_{\beta}\,\frac{\sin\Omega_{\alpha}\tan\Omega_{\alpha}}{\sin\Omega_{\beta}\tan\Omega_{\beta}}}. \tag{2.37}$$

In this diffracted field, the incidence point $\mathbf{x}_{\beta}^{\alpha}$ on the half-plane corresponds to the diffraction point on the edge. Using Snell-Descartes law of diffraction

$$\kappa_{\alpha}\cos\Omega_{\alpha} = \kappa_{\beta}\cos\Omega_{\beta}, \tag{2.38}$$

Eq. (2.37) could be reduced to

$$\rho_{\beta}^{\mathrm{diff}} = \sqrt{S_{\alpha}^{0}(\mathbf{x}_{\beta}^{\alpha}) + S_{\beta}\,\frac{\sin^{2}\Omega_{\alpha}}{\sin^{2}\Omega_{\beta}}\,\frac{\kappa_{\alpha}}{\kappa_{\beta}}}. \tag{2.39}$$

Using (2.16), (2.40) could one more time be reduced to

$$\rho_{\beta}^{\mathrm{diff}} = \sqrt{S_{\alpha}^{0}(\mathbf{x}_{\beta}^{\alpha}) + S_{\beta}\,\frac{\sin^{2}\theta'_{\alpha}}{\sin^{2}\theta'_{\beta}}\,\frac{\sin^{2}\theta_{\beta}}{\sin^{2}\theta_{\alpha}}\,\frac{\kappa_{\alpha}}{\kappa_{\beta}}}. \tag{2.40}$$

As previously said, the approximate GTD-based total field (2.34) is also not spatially uniform particularly near shadow boundaries for a cylindrical and a spherical incident waves.

Near shadow boundaries, the edge diffracted field interfers with the GE field (incident or reflected waves) meaning that the stationary phase point $\lambda = \bar{\theta}$ is close to the pole $\lambda = \theta_{\beta}$. In this case, the steepest descent method is not appropriated to find the contribution of two coalescing critical points to the exact integral solution, a pole and a stationary phase point. Other methods of approximation such as the Pauli-Clemmow method can be used to produce a uniform asymptotic solution near shadow boundaries.

2.3 Scattering of a plane elastic wave by a half-plane crack: uniform asymptotics

2.3.1 Uniform Theory of Diffraction (UTD)

In this section UTD is derived in elastodynamics, to overcome the non-uniformity of the approximate total displacement field (2.34). UTD has been first developed in electromagnetism in the early 1960s by Kouyoumjian and Pathak [12, 14] and is mainly used for antenna propagation [51, 52]. They used a modified Pauli-Clemmow method (see appendix A.3) to obtain an accurate asymptotic solution for the total field near shadow boundaries. This procedure introduces some correction factors referred as transition functions in the GTD diffraction coefficient. UTD then permits to easily calculate the total field in penumbrae.

Hence, the Pauli-Clemmow procedure [6, 15] (explained in appendix A.3) is used here in elastodynamics to approximate the Sommerfeld integral (2.3) when the phase stationary point $\lambda_s = \overline{\theta}$ in (2.3) coalesces with the simple pole $\lambda = \theta_\beta$ with $\theta_\beta \leqslant \pi$. This procedure leads to the Uniform Theory of Diffraction (UTD). Note that the integral (2.3) has the same form as Eq. (A.23):

$$I(\zeta) = \int_\gamma h(\lambda)\, e^{\zeta\, q(\lambda)} \mathrm{d}\lambda \tag{2.41}$$

where $\zeta \gg 1$ is the far-field parameter defined in (2.6), $h(\lambda)$ is the integrand function of (2.3) and $q(\lambda) = i\cos\left(\lambda - \overline{\theta}\right)$ are λ holomorphic functions, and γ is the steepest descent path defined in (2.13). Note also that $\overline{\theta}$ cannot coalesce with the simple pole $\lambda = 2\pi - \theta_\beta$, because $\overline{\theta}$ is always smaller than π, while $2\pi - \theta_\beta$ is always larger than π (see Fig. 2.2). Therefore the Pauli-Clemmow approximation to the scattered field is

$$\mathbf{u}_\beta^{\alpha(\mathrm{UTD})} = F(k_\beta L_\beta\, a)\mathbf{u}_\beta^{\alpha(\mathrm{GTD})}, \tag{2.42}$$

where a is the phase difference between the rays propagating in direction $\lambda = \overline{\theta}$ (edge diffracted ray) and $\lambda = \theta_\beta$ (incident or reflected ray because $\lambda = \bar{\theta}$ permits to treat observation points above and below the edge half-plane [see Eq. (2.8)])

$$a = 2\sin^2\left(\frac{\theta_\beta - \overline{\theta}}{2}\right), \tag{2.43}$$

and F is a transition function

$$F(X) = -2i\sqrt{X}\sqrt{i\pi}e^{-iX}\overline{F}\left(\sqrt{X}\right), \qquad -\frac{\pi}{2} < \arg X < \frac{3\pi}{2}, \tag{2.44}$$

with $\overline{F}$ – the Fresnel function (1.15). The transition function is the complex conjugate of the

Kouyoumjian function [12]. Due to the presence of $\sqrt{X}$, $F(X)$ is multivalued and is rendered single-valued in a standard manner, using the branch cut along the negative imaginary axis $\{\mathrm{Im}\, X < 0, \mathrm{Re}\, X = 0\}$. This branch cut then allows to work with $\arg X \in]-\pi/2, 3\pi/2[$ as it is specified in (2.44).

For other kind of incident waves (cylindrical and spherical), Kouyoumjian and Pathak [12] showed that depending of the incidence wave kind, the distance parameter L_β which is involved in the UTD diffraction coefficient (2.42) is expressed as:

$$L_\beta = \begin{cases} S_\beta \, \sin^2 \Omega_\beta, & \text{for a plane wave incidence} \\ \dfrac{r \, r_0(\mathbf{x}_\beta^\alpha)}{\left(\rho_\beta^{\mathrm{cyl(GE)}}\right)^2}, & \text{for a cylindrical wave incidence} \\ S_\beta S_\alpha^0(\mathbf{x}_\beta^\alpha) \left(\dfrac{\rho_\beta^{\mathrm{diff}}}{\rho_\beta^{\mathrm{sph(GE)}}} \right)^2 \sin^2 \Omega_\beta & \text{for a spherical wave incidence} \end{cases}, \tag{2.45}$$

where $\rho_\beta^{\mathrm{cyl(GE)}}$ is the divergence factor of the reflected wave for a cylindrical incident wave whose expression is given in (2.28). Parameters S_β, S_α^0 and $\mathbf{x}_\beta^\alpha$ for the spherical incident wave are indicated on Fig. 2.3. Here, the incidence point $\mathbf{x}_\beta^\alpha$ on the half-plane corresponds to the diffraction point on the edge. For an incident spherical wave, $\rho_\beta^{\mathrm{sph(GE)}}$ is the divergence factor of the reflected waves given in (2.27) and $\rho_\beta^{\mathrm{diff}}$ is the part of the divergence factor (2.40) of the diffracted wave (2.36). When there is no wave conversion, $\beta = \alpha$, $\rho_\beta^{\mathrm{diff}}$ is proportional to $\rho_\beta^{\mathrm{sph(GE)}}$. We expected to also have this proportionality in case of wave conversion, but it is not the case. Divergence factor $\rho_\beta^{\mathrm{sph(GE)}}$ has been found using two different methods in [27] and $\rho_\beta^{\mathrm{diff}}$ is given in [38] without demonstration for the case of mode conversion. Supplementary works must be done to check the validity of the factor $\rho_\beta^{\mathrm{diff}}$.

Using equation (2.42), a UTD diffraction coefficient can be defined as

$$D_\beta^{\alpha(\mathrm{UTD})} = F(k_\beta L_\beta \, a) \, D_\beta^{\alpha(\mathrm{GTD})}. \tag{2.46}$$

Parameters $(\Omega_\alpha, \theta_\alpha, \theta)$ of the diffraction coefficients are omitted but implied. Substituting (2.29), (2.35), (2.36) and (2.46) in (2.42), the UTD diffracted field for different kinds of incident wave can be expressed as:

- for an incident plane wave

$$\mathbf{u}_\beta^{\alpha(\mathrm{UTD})} = u^\alpha(\mathbf{x}_\beta^\alpha) D_\beta^{\alpha(\mathrm{UTD})} \frac{e^{ik_\beta S_\beta}}{\left(k_\beta \, S_\beta \sin^2 \Omega_\beta\right)^{1/2}} \mathbf{e}_\beta, \tag{2.47}$$

- for an incident cylindrical wave

$$\mathbf{u}_\beta^{\alpha(\mathrm{UTD})} = \frac{u^\alpha(\mathbf{x}_\beta^\alpha)}{\sqrt{r_0(\mathbf{x}_\beta^\alpha)}} D_\beta^{\alpha(\mathrm{UTD})} \frac{\mathrm{e}^{ik_\beta S_\beta}}{(k_\beta\, r)^{1/2}}\, \mathbf{e}_\beta, \tag{2.48}$$

- for an incident spherical wave

$$\mathbf{u}_\beta^{\alpha(\mathrm{UTD})} = \frac{u^\alpha(\mathbf{x}_\beta^\alpha)}{S_\alpha^0(\mathbf{x}_\beta^\alpha)} D_\beta^{\alpha(\mathrm{UTD})} \frac{\mathrm{e}^{ik_\beta S_\beta}}{\left(k_\beta \dfrac{S_\beta}{S_\alpha^0(\mathbf{x}_\beta^\alpha)} \sin^2\Omega_\beta\right)^{1/2} \rho_\beta^{\mathrm{diff}}}\, \mathbf{e}_\beta. \tag{2.49}$$

UTD diffraction coefficient differs from the GTD one by the transition function. When the observation point is far from the shadow boundaries, the UTD approximations (2.47), (2.48) and (2.49) are equivalent to GTD solutions. Indeed, the asymptotic value of the Fresnel function in the illuminated region given by Borovikov[53] permits to find that when $\bar{\theta}$ is far from the pole θ_β,

$$F(\zeta\, a) \underset{a\gg 1}{\longrightarrow} 1. \tag{2.50}$$

Since $\overline{F}(0) = 1/2$ near the shadow boundaries,

$$a \sim \frac{\epsilon^2}{2} \quad \text{and} \quad F(\zeta\, a) \sim e^{-i\frac{\pi}{4}}\, (\mathrm{sgn}\epsilon)\, \epsilon \sqrt{\frac{\pi}{2}} \sqrt{\zeta}, \tag{2.51}$$

where $\epsilon = \overline{\theta} - \theta_\beta$ is a small number ($|\epsilon| \ll 1$). One can multiply (2.51) and (2.32) to determine the asymptotic approximation of (2.46):

$$D_\beta^{\alpha(UTD)} \sim \begin{cases} 0 & \text{if } \theta \le \pi \quad \text{and } \beta \neq \alpha \\ -\dfrac{\mathrm{sgn}\,\epsilon}{2}\sqrt{k_\beta L_\beta}, & \text{if } \theta \le \pi \quad \text{and } \beta = \alpha \\ \dfrac{R_\beta^\alpha}{2}(\mathrm{sgn}\,\epsilon)\sqrt{k_\beta L_\beta}, & \text{if } \theta > \pi \end{cases}. \tag{2.52}$$

The UTD diffraction coefficients do not diverge at shadow boundaries as the GTD coefficients do due to the absence of $1/\epsilon$ in (2.52); however the sign function makes them discontinuous (see Figs. 2.7b, 2.7c, 2.7d and 2.6). It follows that near shadow boundaries, the leading-order

asymptotic approximations of the diffracted displacement fields (2.47), (2.48) and (2.49) are

$$\mathbf{u}_{\beta}^{\alpha(\mathrm{UTD})}(\mathbf{x}) \sim \mathbf{0}, \text{ if } \theta \leq \pi \text{ and } \beta \neq \alpha, \tag{2.53a}$$

$$\mathbf{u}_{\beta}^{\alpha(\mathrm{UTD})}(\mathbf{x}) \sim -A\,\frac{\operatorname{sgn}\epsilon}{2}\,\frac{1}{\rho_{\alpha}^{(\mathrm{GE})}}\,e^{ik_{\alpha}\cos\Omega_{\alpha}(x_3-S_{\alpha}\cos\Omega_{\alpha})}\,e^{ik_{\alpha}S_{\alpha}}\,\mathbf{d}^{\alpha}, \text{ if } \theta \leq \pi \text{ and } \beta = \alpha, \tag{2.53b}$$

$$\mathbf{u}_{\beta}^{\alpha(\mathrm{UTD})}(\mathbf{x}) \sim A\,\frac{R_{\beta}^{\alpha}}{2}(\operatorname{sgn}\epsilon)\,\frac{1}{\rho_{\beta}^{(\mathrm{GE})}}\,e^{ik_{\alpha}\cos\Omega_{\alpha}\left(x_3-S_{\beta}\cos\Omega_{\beta}\right)}\,e^{ik_{\beta}S_{\beta}}\,\mathbf{d}_{\beta}, \text{ if } \theta > \pi, \tag{2.53c}$$

where the exponential term $\exp\left[ik_{\alpha}\cos\Omega_{\alpha}\left(x_3 - S_{\beta}\cos\Omega_{\beta}\right)\right]$ is the phase of the incident wave (2.1) at the diffraction point $\mathbf{x}_{\beta}^{\alpha}$. A is the displacement wave amplitude of the incident wave and $1/\rho_{\alpha,\beta}$ are the divergence factors of the incident [see Eq. (2.25) for its expression] and reflected waves [see its expression in (2.26) for an incident plane wave, (2.28) for an incident cylindrical wave and (2.27) for an incident spherical wave] respectively near incident and reflected shadow boundaries.

At the incident shadow boundary:

- when $\beta \neq \alpha$ (the scattered wave mode is different from the incident wave one), $\theta = \theta_{\beta}$ is a non physical pole because there is no wave conversion in transmission, near this non physical shadow boundary, the UTD diffracted field vanishes [see Eq. (2.53a)],

- when $\beta = \alpha$ (no mode conversion), $\theta = \theta_{\alpha}$ is the real incident shadow boundary. Due to the presence of the sign function in (2.53b), it follows that the UTD diffracted field is discontinuous at the incident shadow boundary; the UTD diffracted field is discontinuous at reflected shadow boundaries too [see Eq. (2.53c)]. As a conclusion, we observe a discontinuity of the UTD diffracted field at all physical shadow boundaries.

The UTD total displacement field expressed as the sum of the elasto-geometrico field and UTD diffracted fields is continuous:

$$\mathbf{u}^{\mathrm{tot(UTD)}}(\mathbf{x}) = \mathbf{u}_{\beta}^{\alpha(\mathrm{GE})}(\mathbf{x}) + \sum_{\beta}\mathbf{u}_{\beta}^{\alpha(\mathrm{UTD})}(\mathbf{x}). \tag{2.54}$$

Indeed, substituting the perpendicular distance from the observation point to the edge

$r = S_{\alpha,\beta}\sin\Omega_{\alpha,\beta}$

[see Fig. 2.3] in (2.1) and (2.22), Eqs. (2.21) and (2.24) can be rewritten as

$$\mathbf{u}^{(\mathrm{GE})}(\mathbf{x}) = A\left(H(\eta_\alpha)\frac{1}{\rho_\alpha^{(\mathrm{GE})}} e^{ik_\alpha[S_\alpha+\cos\Omega_\alpha(x_3-S_\alpha\cos\Omega_\alpha)]\cos(\theta-\theta_\alpha)} e^{ik_\alpha\cos\Omega_\alpha x_3(1-\cos(\theta-\theta_\alpha))}\,\mathbf{d}^\alpha \right. \tag{2.55}$$

$$\left. + H(\eta_\beta)\frac{R_\beta^\alpha}{\rho_\beta^{(\mathrm{GE})}} e^{ik_\beta\left[S_\beta+\cos\Omega_\beta\left(x_3-S_\beta\cos\Omega_\beta\right)\right]\cos(\theta+\theta_\beta)} e^{ik_\alpha\cos\Omega_\beta x_3(1-\cos(\theta+\theta_\beta))}\,\mathbf{d}_\beta \right)$$

with $1/\rho_{\alpha,\beta}^{(\mathrm{GE})}$ being the divergence factor of the incident and reflected waves defined in (2.25) and (2.26)-(2.28) respectively. The arguments of the Heaviside functions are respectively,

$$\eta_\alpha = \mathrm{sgn}(\theta-\theta_\alpha) \tag{2.56a}$$

$$\eta_\beta = \mathrm{sgn}(\theta-2\pi+\theta_\beta). \tag{2.56b}$$

Therefore near the shadow boundaries, $\bar{\theta}=\theta_\beta+\epsilon$, the GE field can be approximated as

$$\mathbf{u}^{(\mathrm{GE})}(\mathbf{x}) \approx \begin{cases} A\dfrac{1}{\rho_\alpha^{(\mathrm{GE})}} e^{ik_\alpha[S_\alpha+\cos\Omega_\alpha(x_3-S_\alpha\cos\Omega_\alpha)]} H(\epsilon)\mathbf{d}^\alpha & \text{if } \theta\le\pi \\ AR_\beta^\alpha\dfrac{1}{\rho_\beta^{(\mathrm{GE})}} e^{ik_\beta\left[S_\beta+\cos\Omega_\beta\left(x_3-S_\beta\cos\Omega_\beta\right)\right]} H(-\epsilon)\,\mathbf{d}_\beta + \dfrac{1}{\rho_\alpha^{(\mathrm{GE})}}\mathbf{u}^\alpha(-\theta_\alpha) & \text{if } \theta>\pi. \end{cases} \tag{2.57}$$

Finally, expressing the Heaviside function as

$$H(\epsilon) = \frac{1}{2}(1+\mathrm{sgn}\,\epsilon), \tag{2.58}$$

$$\mathbf{u}^{(\mathrm{GE})}(\mathbf{x}) \approx \begin{cases} \dfrac{A}{2\rho_\alpha^{(\mathrm{GE})}} e^{ik_\alpha[S_\alpha+\cos\Omega_\alpha(x_3-S_\alpha\cos\Omega_\alpha)]}(1+\mathrm{sgn}\,\epsilon)\,\mathbf{d}^\alpha & \text{if } \theta\le\pi \\ \dfrac{AR_\beta^\alpha}{2\rho_\beta^{(\mathrm{GE})}} e^{ik_\beta\left[S_\beta+\cos\Omega_\beta\left(x_3-S_\beta\cos\Omega_\beta\right)\right]}(1-\mathrm{sgn}\,\epsilon)\,\mathbf{d}_\beta + \dfrac{1}{\rho_\alpha^{(\mathrm{GE})}}\mathbf{u}^\alpha(-\theta_\alpha) & \text{if } \theta>\pi. \end{cases} \tag{2.59}$$

It can be seen that near the incident and reflected shadow boundaries, the GE field (2.57) is discontinuous and its discontinuities cancel those of the UTD diffracted field (2.53), leading to a continuous UTD total field (2.54). The expression of the total field (2.54) at the physical incident shadow bounday is

$$\mathbf{u}^{\mathrm{tot(UTD)}}(\mathbf{x}) \approx \frac{A}{2\rho_\alpha^{(\mathrm{GE})}} e^{ik_\alpha[S_\alpha+\cos\Omega_\alpha(x_3-S_\alpha\cos\Omega_\alpha)]}\,\mathbf{d}^\alpha, \tag{2.60}$$

and at the reflected shadow boundaries, it is

$$\mathbf{u}^{\mathrm{tot(UTD)}}(\mathbf{x}) \approx \frac{AR_\beta^\alpha}{2\rho_\beta^{(\mathrm{GE})}} e^{ik_\beta\left[S_\beta+\cos\Omega_\beta\left(x_3-S_\beta\cos\Omega_\beta\right)\right]}\,\mathbf{d}_\beta + \frac{1}{\rho_\alpha^{(\mathrm{GE})}}\mathbf{u}^\alpha(-\theta_\alpha). \tag{2.61}$$

To sum up, UTD consists in adding diffracted rays by edges (half plane edge in the case detailed here) to incident and reflected rays of the Geometrico-Elastodynamic field. Amplitude of the UTD diffracted rays is that of a conical/cylindrical wave weighted by a GTD diffraction coefficient and by a transition function [see Eqs. (2.47) for an incident plane wave, (2.48) for an incident cylindrical wave and (2.49) for an incident spherical wave]. This transition function leads to a discontinuity of the UTD diffracted field near shadow boundaries which compensates the one of the GE field. UTD just then changes the amplitude of the GTD diffracted rays and is therefore simple to implement using ray tracing contrary to UAT, another GTD uniform correction, which requires fictitious rays (see section 1.4.2). The UAT solution for the half-plane scattering problem in elastodynamics already exists in literature and is recalled hereafter in section 2.3.2.

2.3.2 Uniform Asymptotic Theory of Diffraction (UAT)

The contribution of coalescing stationary phase point and pole can also be calculated by UAT [38] by using the Van Der Waerden approximation (see appendix A.4). The UAT approximation of the total field for a plane wave scattering by a half-plane is reproduced here

$$\begin{aligned}\mathbf{u}^{\mathrm{tot(UAT)}}(\mathbf{x}) = A\left[\overline{F}(\xi_\alpha)-\widehat{\overline{F}}(\xi_\alpha)\right]e^{i\mathbf{k}^\alpha\cdot\mathbf{x}}\,\mathbf{d}^\alpha + \sum_\beta AR_\beta^\alpha\left[\overline{F}(\xi_\beta)-\widehat{\overline{F}}(\xi_\beta)\right]\,e^{ik_\beta\,\mathbf{p}_\beta\cdot\mathbf{x}}\,\mathbf{d}_\beta \\ + \sum_\beta u^\alpha(\mathbf{x}_\beta^\alpha)D_\beta^{\alpha(GTD)}\frac{e^{ik_\beta S_\beta}}{\sqrt{k_\beta L_\beta}}\,\mathbf{e}_\beta\left(\Omega_\beta\right),\end{aligned} \tag{2.62}$$

where

$$\xi_\alpha = -\mathrm{sgn}\left(\theta-\theta_\alpha\right)\sqrt{2k_\alpha L_\alpha\sin^2\left(\frac{\theta_\alpha-\theta}{2}\right)} \quad \text{and} \tag{2.63}$$

$$\xi_\beta = -\mathrm{sgn}\left(\theta+\theta_\beta-2\pi\right)\sqrt{2k_\beta L_\beta\sin^2\left(\frac{\theta_\beta+\theta}{2}\right)} \tag{2.64}$$

are the detour parameters [42]. The Fresnel function $\overline{F}$ and the $\widehat{\overline{F}}$ function are defined in Eqs. (1.15) and (1.16) of chapter 1 and Rojas [54] has shown that the uniform asymptotic expansions for large far-field parameter using the Van-der-Waerden and the Pauli-Clemmow are exactly the same when all terms of order $(k_\beta L_\beta)^{-\frac{1}{2}}$ are considered in the Pauli-Clemmow approximation. To obtain the classical version of UTD, developed in elastodynamics during this thesis, only one term of order $(k_\beta L_\beta)^{-\frac{1}{2}}$ is considered, contrary to UAT which includes all terms of this order. In electromagnetism, Molinet [16] showed that the neglected terms in UTD do not

have an important contribution in far-field. A numerical comparison is done between UAT and UTD in elastodynamics to see if the same assumption can be done in elastodynamics.

2.4 Comparison of UTD and UAT - discussion

Let us first discuss the difference in the analytical properties of UTD and UAT fields. When comparing the UTD total displacement field (2.54) to the GTD-based non-uniform approximation (2.34), the GE field is unchanged while the diffraction coefficient is multiplied by the transition function (2.44). The argument $k_\beta L_\beta\, a$ of the transition function describes the proximity of the observation point to a shadow boundary. When the observation point moves away from such boundary $k_\beta L_\beta\, a$ increases, the transition function approaches 1 [see Eq. (2.50) and Fig. 2.8] and UTD diffraction coefficient approaches the GTD diffraction coefficient. When the observation point moves towards such boundary, $k_\beta L_\beta\, a$ and the transition function both vanish but as shown in section 2.3 the UTD diffracted field is discontinuous [see Eq. (2.53)]; its discontinuities are cancelled by those of the GE field [see Eq. (2.57) leading to a continuous UTD total field].

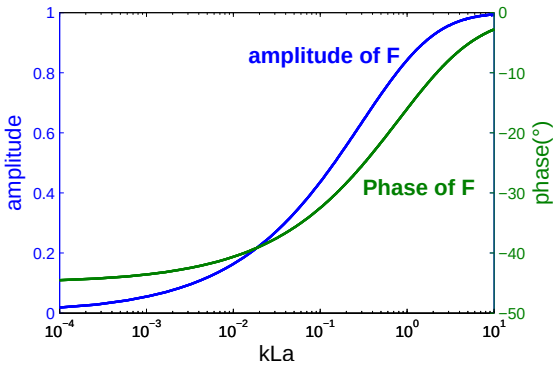

Figure 2.8: Transition function.

By contrast, when UAT is presented in the form (2.62), it is the diffracted field that remains the same as in the GTD-based non uniform approximation (2.34), while the GE field is modified. In this modified GE field [see Eq. (2.62)], the Fresnel function smooths the GE field discontinuity (see Fig. 1.12) and the second function $\widehat{\widehat{F}}(.)$ diverges at shadow boundaries as the GTD diffracted field, but the corresponding singularities cancel each other, leading to a continuous total UAT field. Since in (2.62) the incident and reflected fields are defined on the whole space, both incident and reflected fields have to be extended to their corresponding shadow region. As said in section 1.4.2, this can be achieved for the incident field by tracing the incident rays through the obstacle as if it was absent. Moreover, the reflected field has also to be extended to the shadow region of the reflected field. This can be achieved by extending the illuminated face beyond the crack edge and tracing the resulting fictitious reflected rays (see Figs. 1.13).

While reliance on fictitious rays is a definite disadvantage, it has been mentioned above that, unlike UTD, UAT is more consistent in that it contains all terms of order $(k_\beta L_\beta)^{-\frac{1}{2}}$. In electromagnetism, the terms missing in UTD are small. Therefore we move on to a numerical comparison of UTD and UAT to establish whether the same is true in elastodynamics. Note that the elastodynamic UAT has been tested previously, using the finite difference numerical method (see section 2.3.1 in Ref.[24]).

To compare UAT and UTD, both two-dimensional (2D) [$\Omega_\alpha = \pi/2$] and three-dimensional (3D) [$\Omega_\alpha \neq \pi/2$] configurations are considered below. In a 2D configuration, the incident wave is normal to the edge crack and thus the diffracted waves have cylindrical fronts, while in a 3D configuration the incidence is oblique and the diffracted waves have conical fronts. The total displacement field amplitude using GTD [see Eq. (2.34)], UTD [see Eq. (2.54)], UAT [see Eq. (2.62)] and a Modified UTD (MUTD) described later in this section are presented in the $(\mathbf{e}_1, \mathbf{e}_2)$ plane, which is perpendicular to the edge crack, since the problem is invariant in the x_3 direction (see Fig. 2.1). The observation point is specified using the cylindrical coordinates (r, θ) associated to the $(\mathbf{e}_1, \mathbf{e}_2)$ plane. In all simulations, the solid material is ferritic steel with Poisson's ratio $\nu = 0.29$, longitudinal velocity $c_L = 5900$ m s^{-1} and transversal velocity $c_T = 3230$ ms^{-1}.

In the far field from the flaw, the directivity patterns of the total displacement field amplitude exhibits many oscillation lobes. We present first results for$r = 2\lambda_\alpha$ (Fig. 2.9) and $r = 3\lambda_\alpha$ (Fig. 2.11) and then for $r = 8\lambda_\alpha$ (Fig. 2.13) [λ_α being the wavelength of the incident wave] so that the patterns have less lobes and lend themselves to a clear interpretation. In Figs. 2.9 and 2.11 all approximate total fields are calculated using all scattered modes, with the GTD-based non uniform asymptotic approximation given by (2.34), UAT - by (2.62), and UTD - by (2.54). In Figs. 2.9 and 2.11a, the configurations are 2D and in Fig. 2.11b, the configuration is 3D. As expected, both UTD and UAT are continuous at shadow boundaries and practically coincide far away from the shadow boundaries. Near the shadow boundaries they differ, but not by much. There are three shadow boundaries in Fig. 2.9 for an incident longitudinal plane wave, the incident L shadow boundary $\theta = 30°$, reflected SV shadow boundary $\theta \approx 300°$ and reflected L shadow boundary $\theta = 330°$. The peaks near critical angles $\theta_c \approx 56.8°$ and $2\pi - \theta_c \approx 303, 2°$ (less visible spike) are due to interferences of the diffracted T wave with the corresponding head waves generated by diffraction at the edge (see Fig. 2.10). The head waves are contributions of the integrand's branch points to the exact solution (2.3) [55]. The coalescence between the stationary phase points and branch points and poles in certain cases lies outside the scope of this chapter. However, it has been shown in [56] that while GTD and its uniform corrections are not valid near the critical angle, in far-field the spikes observed in the diffraction coefficient D^{α}_{TV} at the critical angles are physical in nature, since the head wave attenuates with the distance. The exact integral solution (2.3) is evaluated numerically in [56] when three critical points (stationary phase point, pole and branch point) are coalescing. An integration of this work has been done in CIVA during my thesis with the help of an intern, Yu-Lin Huang, supervised by Michel DARMON and I. Results are presented in [36].

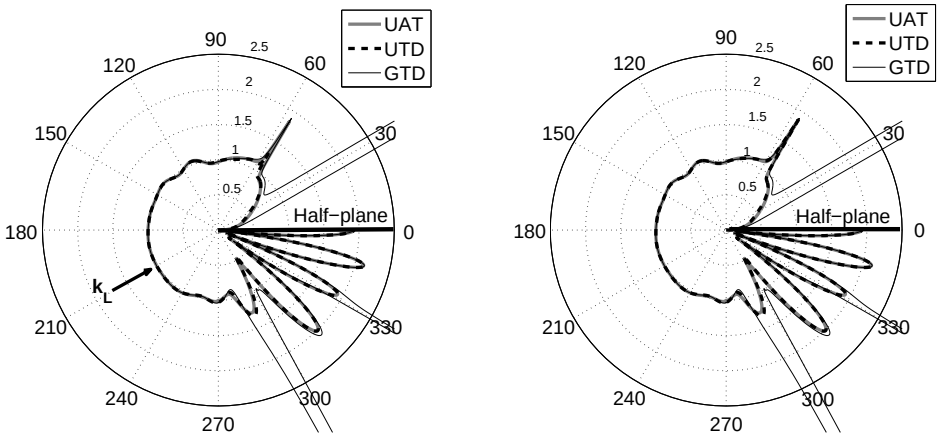

(a) UTD model is the one found using Pauli-Clemmow method (Eq. (2.54))

(b) Modified UTD model (Eqs. (2.65) and (2.68))

Figure 2.9: Directivity pattern of the total displacement field predicted by different models (GTD, UAT and UTD) for a longitudinal incident plane wave at $r = 2\lambda_L$; $\Omega_L = 90°$, $\theta_L = 30°$. Each circle represents amplitude of the total field normalized by the incident amplitude.

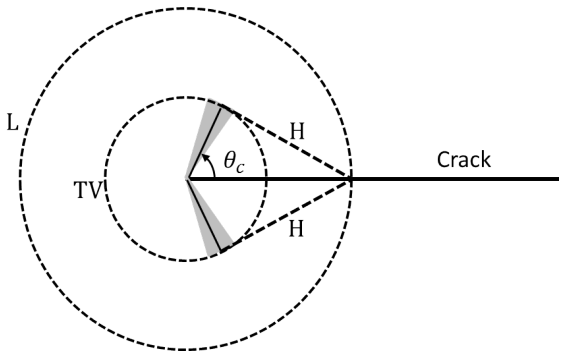

Figure 2.10: Wavefronts diffracted from a crack edge: L stands for longitudinal wave, TV for transversal and H for head wave; θ_c is the longitudinal critical angle.

In Fig. 2.9a, UAT reproduces the critical GTD peak exactly, while UTD has a smaller amplitude. The discrepancy can be explained by noting that each UTD diffraction coefficient has four poles, one at the incident angle θ_α, one at the reflection angle $2\pi-\theta_\alpha$, one at the reflection angle $2\pi-\theta_\beta$, and one at the angle θ_β. When $\beta \neq \alpha$, $2\pi - \theta_\beta$ is the propagation angle of a mode-converted reflected wave and θ_β is an angle associated with a non-physical mode-converted transmitted wave. It is non-physical, because there is no mode conversion in transmission. That's why its residue is zero [see Eq. (2.15c)] which means that such a non-physical geometrical wave has

zero amplitude and the diffraction coefficient D_β^α, $\beta \neq \alpha$ does not diverge (see Figs. 2.7a and 2.7c) at this mode-converted transmitted direction. In the vicinity of this pole, the transition function tends to 0 [see Eq. (2.51)] and if the GTD diffraction coefficient has another singular behaviour (for instance due to a critical angle) near this non-physical pole, the amplitude of the GTD coefficient near this critical angle is then reduced in the UTD coefficient. In Fig. 2.9a, the critical angle $\theta_c \approx 56.8°$ is close to the pole $\theta_{TV} \approx 61.7°$ (see Fig. 2.6c) and therefore near this critical angle the peak amplitude is reduced. Since the residue of the pole $\theta_{\beta,\beta\neq\alpha}$ is zero, there is no need to consider its coalescence with the stationary phase point. UTD performance can therefore be improved by introducing the following Modified UTD (MUTD) which removes the transition function in UTD when $\beta \neq \alpha$ at the vicinity of the non-physical pole.

- For $\beta \neq \alpha$,

$$\text{if } \theta_\alpha \leq \pi, \begin{cases} D_\beta^{\alpha(MUTD)} = D_\beta^{\alpha(GTD)} & \text{if } 0 \leq \theta \leq \pi \\ D_\beta^{\alpha(MUTD)} = F\left(k_\beta L_\beta \sin^2\left(\dfrac{\theta+\theta_\beta}{2}\right)\right) D_\beta^{\alpha(GTD)} & \text{if } \pi < \theta \leq 2\pi \end{cases} \tag{2.65}$$

and

$$\text{if } \theta_\alpha > \pi, \begin{cases} D_\beta^{\alpha(\mathrm{MUTD})} = F\left(k_\beta L_\beta \sin^2\left(\dfrac{\theta-\theta_\beta}{2}\right)\right) D_\beta^{\alpha(\mathrm{GTD})} & \text{if } 0 \leq \theta \leq \pi \\ D_\beta^{\alpha(\mathrm{MUTD})} = D_\beta^{\alpha(\mathrm{GTD})} & \text{if } \pi < \theta \leq 2\pi \end{cases} \tag{2.66}$$

except when both $\alpha = TV$ and $\theta_\alpha < \theta_c$: indeed, when the conditions $\alpha = TV$ and $\theta_\alpha < \theta_c$ are fulfilled, there is no reflected longitudinal waves as explained in the paragraph after Fig. 2.11. The longitudinal diffraction coefficient is therefore not modified by a transition function since it does not have any poles (see the GTD diffraction coefficient $D_{\beta=L}^{\alpha=TV}$ plotted in Fig. 2.7a):

$$D_\beta^{\alpha(\mathrm{MUTD})} = D_\beta^{\alpha(\mathrm{GTD})} \quad \text{for every observation point when } \alpha = TV \text{ and } \theta_\alpha < \theta_c. \tag{2.67}$$

- For $\beta = \alpha$,

$$D_\beta^{\alpha(MUTD)} = D_\beta^{\alpha(UTD)}. \tag{2.68}$$

With this Modified UTD, for the mode conversion, $\beta \neq \alpha$, the MUTD diffraction coefficient $D_\beta^{\alpha(\mathrm{MUTD})}$ is equal to the GTD one in a large neighbourhood of the mode-converted transmission direction (the non-physical pole) for which $D_\beta^{\alpha(\mathrm{GTD})}$ is finite. The UTD curve in Fig. 2.9b confirms that the Modified UTD reproduces the GTD critical peaks which are physical in far-field according to [56].

In Figs. 2.11a and 2.11b, there is a good agreement between UTD and UAT results. In these figures,

there are only two shadow boundaries, the incident SV shadow boundary $\theta = 30°$ and reflected SV shadow boundary $\theta = 330°$. Since the incidence angle θ_{TV} is subcritical ($\theta_{TV} < \theta_c$) there are no reflected longitudinal waves. In the configuration used in Fig. 2.12 the incident angle θ_{TV} is supercritical. An incident transversal wave gives rise to a reflected transversal and longitudinal waves in accordance with Snell-Descartes law ($\theta_L < \theta_{TV}$).

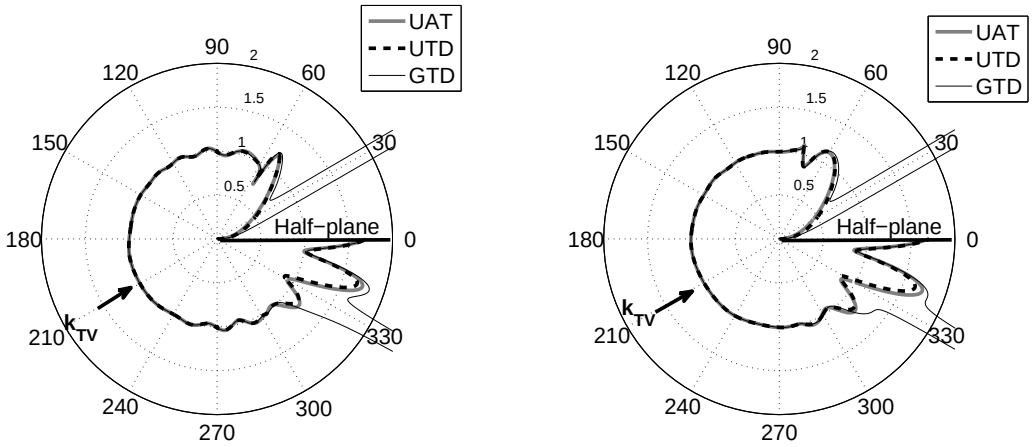

(a) UTD model is the one found using Pauli-Clemmow method (Eq. (2.54))

(b) Modified UTD model (Eqs. (2.65) and (2.68))

Figure 2.11: Directivity pattern of the total displacement field predicted by different models (GTD, UAT and UTD) for a transversal incident plane wave at $r = 3\lambda_T$; $\Omega_T = 90°$, $\theta_{TV} = 30°$. Each circle represents amplitude of the total field normalized by the incident amplitude.

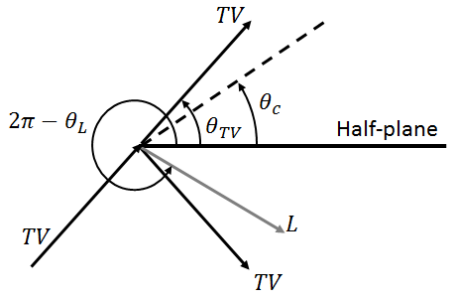

Figure 2.12: Reflection of a transversal wave by a half-plane crack.

The simulations reported in Fig. 2.13 have been performed using parameters similar to Fig. 2.9b but for a larger far-field parameter $\zeta = 16\pi \sin \Omega_\beta$ (so that $r = 8\lambda_L$). The resulting UAT and UTD fields are much closer than in Fig. 2.9b. As the observation point moves away from the crack (increase in distance r), near the shadow boundaries, the absolute error between UTD and

UAT approximations decreases from a maximum error of 50% at $r = 2\lambda_L$ to 5% at $r = 8\lambda_L$ (see Fig. 2.14). The Modified UTD produces a much smaller error near the critical angle $\theta_c \approx 56.8^\circ$ than UTD.

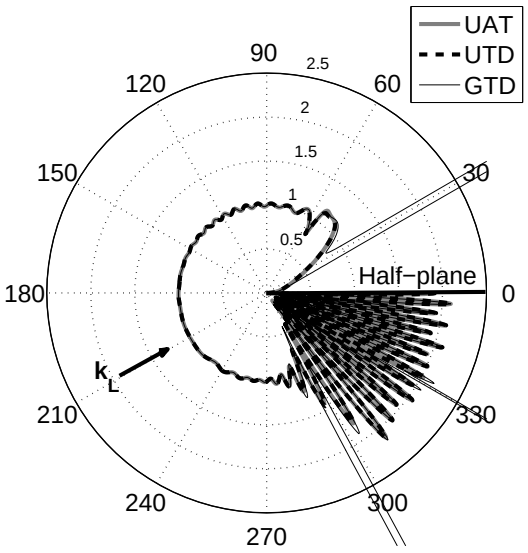

Figure 2.13: Directivity pattern of the total field predicted by different models (GTD, UAT and UTD) at $r = 8\lambda_L$; $\Omega_L = 90^\circ$, $\theta_L = 30^\circ$. Each circle represents amplitude of the total field normalized by the incident amplitude.

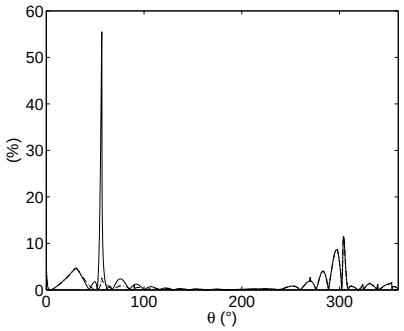

(a) $r = 2\lambda$. UAT, UTD and MUTD used here correspond to the ones presented on Fig. 2.9

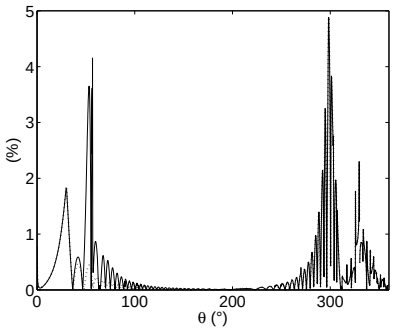

(b) $r = 8\lambda$. UAT, UTD and MUTD used here correspond to the ones presented on Fig. 2.13

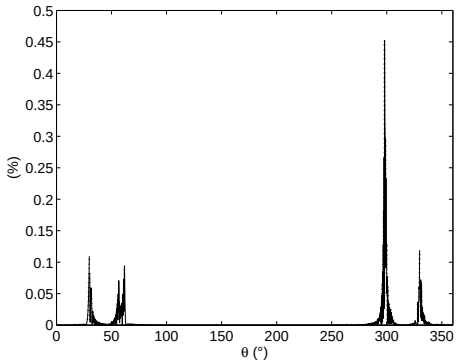

(c) $r = 500\lambda$, only MUTD is considered in this case

Figure 2.14: Absolute error between UAT and UTD total displacement fields [noted A in Eq. 2.1] versus the observation angle in percent of the incident amplitude at $\Omega_L = 90°$, $\theta_L = 30°$. Solid line represents the absolute error between initial UTD and UAT and dashed line represents absolute error between MUTD and UAT.

The above results are envisaged as particularly useful in Non-Destructive Testing (NDT) of cracks in materials. Let us discuss the validity of a UTD flaw measurement model to be developed for NDT applications. In NDT, the flaws are usually inspected in the far field of the used probes or else in their focal areas if they are focused. Consequently, often, at each point of the meshed flaw the incident wave-fields can be approximated by a wave that is locally plane [26, 34] and GE ray methods and GTD-based models can be easily applied in the probes far field [35]. Since the proposed UTD model relies on the same high-frequency assumptions as GTD, it should proved to be efficient in far field from the flaw since GTD is an efficient model for simulating the scattering of an elastic plane wave by a half-plane in far-field. The limits of validity of a GTD-based NDT system model are described in Ref.[36] for a rectangular flaw. It has been shown that PTD (explained in section 1.4.1) predictions are valid for flaw heights of more than one wavelength for longitudinal waves and more than two wavelengths for shear waves (whether incident and

diffracted). PTD consists in correcting the edge diffracted field obtained with the Kirchhoff approximation using the GTD edge diffracted field. At the leading order $(k_\beta L_\beta)^{-\frac{1}{2}}$, PTD is identical to UAT for a half-plane scatterer [45]. UTD is expected to give results similar to PTD ones and convenient for NDT applications. A UTD NDT system model is proposed in chapter 4.

2.5 Conclusion

The elastodynamic Uniform Theory of Diffraction (UTD) has been derived to describe the scattering of a plane wave from a stress-free half-plane. Unlike GTD, at the shadow boundaries, the UTD diffracted fields contain no singularities, only discontinuities, and such discontinuities cancel the discontinuities in the corresponding Geometrico-Elastodynamics (GE) field. Just like the total UAT field, the total UTD field is continuous. In the far field UTD practically coincides with UAT and the Modified version of UTD, MUTD, proposed in this chapter, improves UTD generally at the vicinity of a non-physical pole.

In ray tracing implementations, UTD is more convenient than UAT, because unlike UAT, it does not rely on fictitious rays. It is well understood that, unlike UAT, UTD misses some terms of the order $(k_\beta \zeta_\beta)^{-1/2}$, however the numerical comparisons carried out in this chapter confirm that near shadow boundaries, where the missing terms play a part, the resulting differences do not appear to be significant for practical applications (see for example Ref.[36]). The development of UTD in elastodynamics proposed here has been published recently [57].

A UTD NDT system model is proposed in chapter 4. However, GTD solution being known only for canonical geometries such as half-plane and wedge, GTD and consequently UTD do not take into account the finite extent of the scatterer diffracting edge. This finite length of the diffracting obstacle can be accounted for by using incremental models which are described in chapter 3.

Chapter 3

Two elastodynamic incremental models: a Huygens method and the Incremental Theory of Diffraction (ITD)

L'application de la Théorie Géométrique de la Diffraction (GTD) nécessite de déterminer le point de diffraction sur l'arête qui génère le cône de rayons diffractés passant par un point d'observation donné. A ce point de diffraction, la géométrie est remplacée par une structure canonique pour laquelle la solution GTD est connue. La GTD prédit alors une zone d'ombre des rayons diffractés pour une arête de taille finie. De plus, la GTD étant une méthode rayon, elle est aussi non valide aux caustiques comme l'élastodynamique géométrique (voir section 1.2).

Pour remédier à ces inconvénients de la GTD et notamment simuler la réponse ultrasonore d'une arête finie insonifiée par une onde élastique pour des applications au Contrôle Non Destructif (CND), deux méthodes incrémentales ont été développées. L'une est inspirée de travaux réalisés en électromagnétisme et l'autre est fondée sur le principe de Huygens: toutes les deux considèrent que les points de l'arête diffractante sont des sources d'onde sphérique. Elles sont donc des méthodes "intégrales le long de l'arête diffractante" et permettent ainsi d'avoir un champ diffracté d'arête continu et uniforme en tout point de l'espace. Elles ont été validées numériquement et expérimentalement de façon concluante.

3.1 Introduction

The Geometrical Theory of Diffraction (GTD) relies on the locality principle of high frequency phenomena, which stipulates that if the vicinity of each diffraction point along the obstacle contour can be described, even approximately, by an infinite tangent half-plane or else by an infinite planar wedge, then the diffracted field radiated by this point can be described using the corresponding GTD diffraction coefficients. In ultrasonic NDT it is not uncommon to encounter a flaw diffracting edge that cannot be approximated, even locally, by a straight line or a planar wedge. However, GTD has additional shortcomings to its non uniformity near and at shadow boundaries of the incident and of the reflected waves. Indeed, since the GTD field is null out of the diffraction cone, it produces a discontinuity at shadow boundaries emanating from the edge endpoints (for instance a corner of a rectangular defect) as shown in next Figs. 3.5a and 3.6a. Moreover, GTD has other drawbacks of ray tracing: searching for the diffraction point for each observation point is not so straightforward in complex 3D configurations, and the non validity of GTD at caustics requires a uniform correction using special functions [24].

Incremental methods have been developed, originally in electromagnetism, to overcome these GTD limitations: Incremental Theory of Diffraction (ITD) [58–60], Incremental Length Diffraction Coefficient (ILDC) [61] and Equivalent Edge Currents (EEC) [62]. They also have been extended to acoustics [63–65]. Unlike GTD, incremental methods do not require ray tracing. They treat points of the diffracting edge as fictitious sources of a field called incremental field, and the scattered field at an observation point is calculated as the sum of these incremental contributions. Incremental models provide an extension for observation angles out of the diffraction cone, and a natural uniform representation of the scattered field at caustics [58] or at the shadow boundaries emanating from edge endpoints. The incremental methods are then particularly useful to better take into account the finite length and shape of a defect contour. To model diffraction from an edge of finite size, ITD can be based on GTD or UTD [Uniform Theory of Diffraction (see chapter 2)] [58], UTD being a uniform correction of GTD, which is valid inside penumbras of incident or reflected rays as well as outside [12]. However, in ultrasonic NDT, cracks are usually no more than a few centimeters long [66, 67]. Thus, to be able to detect such cracks, inspections are carried out at high frequency (1 – 10 MHz), for which GTD can be employed, because cracks are usually large compared to the corresponding wavelengths. But theorically, GTD is only valid for an infinite edge, and modelling has to take into account the crack's finite extent.

This chapter aims at developing elastodynamic versions of incremental models, with applications to ultrasonic NDT. An elastodynamic incremental model has been developed before for an elliptical crack [24]. It is based on a Kirchhoff integral on a line and has consequently the inconvenients of the Kirchhoff approximation. Notably this existing method will necessarily predict erroneous amplitudes of edge diffracted fields; it is the reason why the elastodynamic Kirchhoff prediction has been improved using the Physical Theory of Diffraction (PTD) [45] especially for shear waves [36]. Methods proposed in this chapter are more effective than this Kirchhoff-based

method [24] since they rely on GTD or PTD which is a much better recipe than Kirchhoff for modelling edge diffraction. In section 3.2, an elastodynamic ITD is developed using the standard approach previously developed in electromagnetism [58]. A new elastodynamic incremental model based on the Huygens principle is also proposed. Section 3.3 describes experimental and numerical validation of both models. Section 3.4 offers conclusions to this chapter.

3.2 Incremental models

In this section, two incremental models are developed in the context of elastodynamics: the Incremental Theory of Diffraction and the Huygens model. The developed models in this section rely on GTD, but they could also rely on GTD uniform corrections such as UTD, UAT and PTD. Before describing these incremental models, let us begin by the statement of the problem: a curved stress-free crack of contour $\mathcal{L}$ embedded in an elastic homogeneous and isotropic space (see Fig. 3.1) is insonified by a plane wave, which displacement vector is given by

$$\mathbf{u}^{\alpha}(\mathbf{x}) = A\,\mathbf{d}^{\alpha} e^{i(-\omega t + \mathbf{k}^{\alpha}\cdot\mathbf{x})}, \tag{3.1}$$

where, as in the Chapter 2, the superscript $\alpha = L, TV$ or TH (Longitudinal, Transverse Vertical or Transverse Horizontal) is used to denote the incident wave mode, A is the wave displacement amplitude, $\mathbf{d}^{\alpha}$- its polarization vector, $\mathbf{k}^{\alpha}$- its wave vector whose magnitude $k_{\alpha} = \omega/c_{\alpha}$, with ω – the circular frequency and c_{α} – the speed of the corresponding mode, i – the imaginary unity, t is time and $\mathbf{x}$ is the position vector. Subsequently, the exponential factor $\exp(-i\omega t)$ is implied but omitted everywhere.

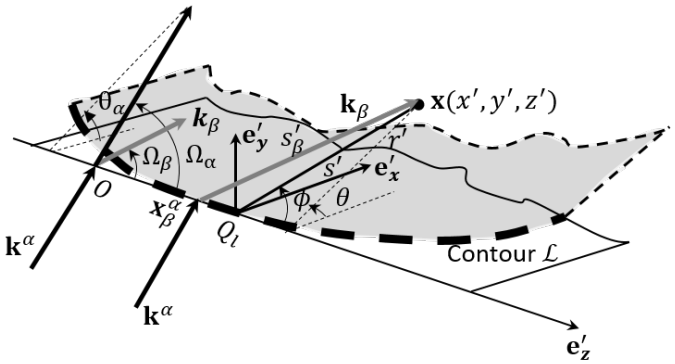

Figure 3.1: A plane wave with the propagation vector $\mathbf{k}^{\alpha}$ incident on a stress-free crack (in gray) of contour $\mathcal{L}$ - dashed black line. Thick black arrow – direction of the incident wave; thick gray arrow - direction of the wave scattered by the half-plane tangent to the crack at the flash point Q_l.

Incremental methods assume that flash points Q_l of the diffracting edge (see Fig. 3.1) are all ficti-

tious Huygens sources of a field defined as the incremental displacement field $\mathbf{F}_\beta(Q_l, \mathbf{x})$. Then, at an observation point $\mathbf{x}$ (see Fig. 3.1), the displacement field $\mathbf{v}_\beta^\alpha$ diffracted by the contour $\mathcal{L}$ is the integral over the contour $\mathcal{L}$ of an incremental field weighted by the incident wave amplitude at each flash point:

$$\mathbf{v}_\beta^\alpha(\mathbf{x}) = \int_{\mathcal{L}} u^\alpha(Q_l)\ \mathbf{F}_\beta(Q_l, \mathbf{x}) \mathrm{d}l, \tag{3.2}$$

with $\mathrm{d}l$ being the edge increment.

During this thesis, two new different methods have been developed to determine this incremental field in he context of elastodynamics: one based on the GTD locality principle (ITD) and one based on the Huygens principle.

3.2.1 The elastodynamic Incremental Theory of Diffraction (ITD)

At the flash point Q_l, let the crack edge be approximated by a half-plane tangent to the edge at this flash point (see Fig. 3.1). Let Q_l be the origin of the local Cartesian coordinate system $(Q_l; \mathbf{e}'_x, \mathbf{e}'_y, \mathbf{e}'_z)$ associated to this half-plane. It is convenient to express the incident wave vector $\mathbf{k}^\alpha$ as $k_\alpha(\sin\Omega_\alpha \cos\theta_\alpha, \sin\Omega_\alpha \sin\theta_\alpha, \cos\Omega_\alpha)$ in this Cartesian coordinate system and the observation point, using either the local Cartesian coordinates (x', y', z') or another set of associated local spherical coordinates (s', ϕ, θ) (see Fig. 3.1).

Following the procedure described in [58], the incremental field $\mathbf{F}_\beta(Q_l, \mathbf{x})$ radiated by the flash point Q_l is the field radiated by this same point Q_l treated as lying on the edge of the tangential half-plane to the contour $\mathcal{L}$. The incremental field $\mathbf{F}_\beta(Q_l, \mathbf{x})$ then corresponds to the incremental field radiated by the flash point Q_l on the half-plane edge. The scattered field $\mathbf{u}_\beta^\alpha(\Omega_\alpha, \mathbf{x})$ by a half-plane can be considered to be a superposition of incremental field contributions $\mathbf{F}_\beta(x'_3, \mathbf{x})$ excited with an incident plane wave of phase $k_\alpha x'_3 \cos\Omega_\alpha$ [59], i.e.,

$$\mathbf{u}_\beta^\alpha(\Omega_\alpha, \mathbf{x}) = \int_{-\infty}^{+\infty} \mathbf{F}_\beta(x'_3, \mathbf{x})\, e^{ik_\alpha x'_3 \cos\Omega_\alpha} \mathrm{d}x'_3 \tag{3.3}$$

where $\mathrm{d}x'_3$ is the edge increment of the tangential half-plane. This expression establishes a Fourier Transform pair relationship between the incremental contribution $\mathbf{F}_\beta(x'_3, \mathbf{x})$ and the solution $\mathbf{u}_\beta^\alpha(\Omega_\alpha, \mathbf{x})$ of the canonical problem. The related Fourier parameters are x'_3 and $k_\alpha \cos\Omega_\alpha$. Introducing the notation $\varsigma = \Omega_\alpha$, the incremental contribution is extracted from (3.3) by an inverse Fourier transform as

$$\mathbf{F}_\beta(x'_3, \mathbf{x}) = \frac{k_\alpha}{2\pi} \int_{\mathcal{C}_\varsigma} \mathbf{u}_\beta^\alpha(\varsigma, \mathbf{x})\ \sin\varsigma\ e^{-ik_\alpha x'_3 \cos\varsigma} \mathrm{d}\varsigma. \tag{3.4}$$

The contour $(\mathcal{C}_\varsigma)$ in Eq. (3.4) depicted on Fig. 3.2 in the complex plane $\varsigma = \sigma + i\tau$ is going from

$i\infty$ to $\pi - i\infty$. Thus, at any arbitrary observation point, using Snell-Descartes law of diffraction

$$k_\alpha \cos\varsigma = k_\beta \cos\Omega_\beta(\varsigma) \tag{3.5}$$

and substituting the exact scattered field $\mathbf{u}_\beta^\alpha(\varsigma, \mathbf{x})$ generated by a plane elastic wave irradiating a half-plane in (3.4) by its expression (2.3), the incremental contribution from the flash point $Q_l(x_3' = 0)$ to the diffracted field is

$$\mathbf{F}_\beta(Q_l, \mathbf{x}) = \frac{k_\alpha}{2\pi} \int_{\mathcal{C}_\varsigma} \int_\gamma f_\beta(-q_\beta \cos\lambda, \mathrm{sgn}(\sin\theta))\ \sin\varsigma\ e^{ig(\lambda,\varsigma)}\ \mathbf{t}_\beta(-q_\beta\cos\lambda, \mathrm{sgn}(\sin\theta))\, d\lambda\, d\varsigma. \tag{3.6}$$

Expression of the integrand function f_β is given in (2.4) and the polarisation vectors $\mathbf{t}_\beta$ are defined in (2.9). The phase function in (3.6) is

$$g(\lambda, \varsigma) = k_\beta \left[r' \sin\Omega_\beta(\varsigma) \cos\left(\lambda - \overline{\theta}\right) + z' \cos\Omega_\beta(\varsigma) \right]. \tag{3.7}$$

Using the coordinates relationship, i.e.

$$r' = s' \sin\phi \tag{3.8a}$$

$$z' = s' \cos\phi \tag{3.8b}$$

the phase function can be rewritten as

$$g(\lambda, \varsigma) = s' \left[\sin\phi\, \cos\left(\lambda - \overline{\theta}\right)\, \sqrt{k_\beta^2 - k_\alpha^2 \cos^2\varsigma} + k_\alpha \cos\phi \cos\varsigma \right], \tag{3.9}$$

with s' being the distance between the observation point and the flash point Q_l (see Fig. 3.1). The integral (3.6) has thus two stationary phase points:

$$(\lambda_s, \varsigma_s) = \left(\bar{\theta}, \arccos\left(\frac{k_\beta}{k_\alpha} \cos\phi \right) \right) \quad \text{and} \quad (\bar{\theta}, 0), \tag{3.10}$$

the second phase stationary point corresponding to grazing incidence. Diffraction coefficients generally do not deal with grazing incidence, that's why only the first stationary point is studied in this chapter. The obtained results are therefore non valid for any grazing incidence. Applying the steepest descent method (see appendix A.2) to the double integral (3.6) leads to the following high frequency approximation of the incremental field[1] (see calculation details in appendix C):

$$\mathbf{F}_\beta(Q_l, \mathbf{x}) = \frac{1}{\sqrt{2\pi i}}\, D_\beta^{\alpha(\mathrm{GTD})}(\Omega_\alpha(\phi), \theta_\alpha, \theta)\, \frac{e^{ik_\beta s'}}{s'}\, \mathbf{e}_\beta(\phi) \tag{3.11}$$

[1]Note that Eq. (3.11) is the same than the ITD incremental field [Eq. (4)] in [40] which presents a term $1/\sin\phi$. Here, in the thesis, this term is included in the GTD diffraction coefficient (2.31).

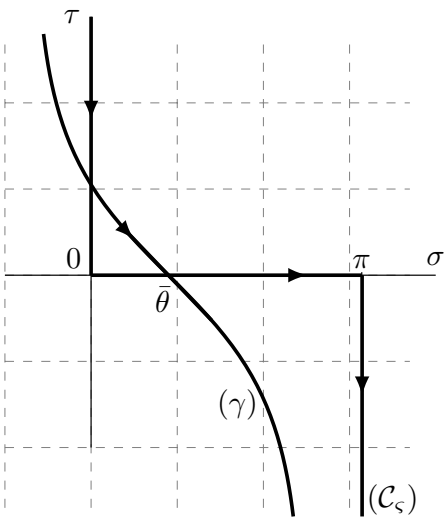

Figure 3.2: Integration path $\mathcal{C}_\varsigma$ and the steepest descent path γ in the complex plane $\lambda = \sigma + i\tau$.

where $D_\beta^{\alpha(\mathrm{GTD})}$ is the GTD diffraction coefficient defined in Eq. (2.31) and

$$\Omega_\alpha(\phi) = \arccos\left(\frac{k_\beta}{k_\alpha}\cos\phi\right). \tag{3.12}$$

Note that if the contour $\mathcal{L}$ is a straight line (the crack is a half-plane as the one presented on Fig. 2.1), then substituting (3.11) into (3.2) leads to the following diffracted field

$$\mathbf{v}_\beta^\alpha(\mathbf{x}') = \frac{1}{\sqrt{2\pi i}}\int_{-\infty}^{\infty} u^\alpha(Q_l)\, D_\beta^{\alpha(\mathrm{GTD})}(\Omega_\alpha(\phi(l)), \theta_\alpha, \theta)\ \mathbf{e}_\beta(\phi)\ \frac{e^{ik_\beta s'}}{s'}\mathrm{d}l. \tag{3.13}$$

Introducing a global Cartesian coordinate system $(O;\mathbf{e}_x,\mathbf{e}_y,\mathbf{e}_z)$ so that $Q_l(0,0,l)_{(O;\mathbf{e}_x,\mathbf{e}_y,\mathbf{e}_z)}$ is the flash point on this straight line $\mathcal{L}$. In this new Cartesian coordinate system, an arbitrary observation point is located by $\mathbf{x}(x,y,z)_{(O;\mathbf{e}_x,\mathbf{e}_y,\mathbf{e}_z)} = (x',y',z'+l)_{(O;\mathbf{e}_x,\mathbf{e}_y,\mathbf{e}_z)}$. The corresponding phase stationary point $l_s = z - r'/\tan\Omega_\beta$ of (3.13) is the z-coordinate of the diffraction point $\mathbf{x}_\beta^\alpha$ on the straight contour $\mathcal{L}$. At this stationary point, $\phi(l_s) = \Omega_\beta$, $s'(l_s) = S_\beta$ and the phase stationary point contribution to (3.13) is

$$\mathbf{v}_\beta^\alpha(\mathbf{x}) = A\, e^{ik_\alpha l_s\cos\Omega_\alpha}\, D_\beta^{\alpha(\mathrm{GTD})}(\Omega_\alpha,\theta_\alpha,\theta)\ \frac{e^{ik_\beta S_\beta}}{\sqrt{k_\beta S_\beta \sin^2\Omega_\beta}}\ \mathbf{e}_\beta(\Omega_\beta). \tag{3.14}$$

Consequently, when the crack edge is a straight line, ITD gives the same solution as GTD for a half-plane [see Eq. (2.29)].

The incremental field (3.11) which is valid in the far field zone $k_\beta s' \gg 1$ is a spherical wave weighted by a scattering coefficient. Thus, each point on the defect contour acts as a fictitious

source of spherical wave. Another method which has as starting point the Huygens principle has been derived in elastodynamics.

3.2.2 The Huygens method

Let us now utilize the Huygens principle, namely let us assume that points on the diffracting edge are fictitious sources of spherical waves which interfere with each other and give rise to the displacement field at any observation point. An ansatz is proposed in which each spherical wave is weighted by a coefficient proportional to the GTD diffraction coefficient $D_\beta^{\alpha(\mathrm{GTD})}$. Note that the UTD diffraction coefficient could be used rather than the GTD diffraction coefficient. The diffracted field at an observation point is then postulated as

$$\mathbf{v}_\beta^\alpha(\mathbf{x}) = \int_{\mathcal{L}} C\, u^\alpha(Q_l)\, D_\beta^{\alpha(\mathrm{GTD})}(\Omega_\alpha(l), \theta_\alpha(l), \theta)\ \mathbf{e}_\beta(\Omega_\beta, \theta)\ \frac{e^{ik_\beta s'}}{s'} \mathrm{d}l, \tag{3.15}$$

where $\mathcal{L}$ is the crack contour; C is an unknown parameter to be determined and dl is the length of an elementary arc along the contour $\mathcal{L}$. If the contour $\mathcal{L}$ is a straight segment with the ends a and b, the angles of incidence $\Omega_\alpha(l)$ and $\theta_\alpha(l)$ are the same at any discretization points on the diffracting edge. In the global frame $(O; \mathbf{e}_x, \mathbf{e}_y, \mathbf{e}_z)$ introduced in the previous section, the distance between an observation point of coordinates $(x, y, z)_{(O;\mathbf{e}_x,\mathbf{e}_y,\mathbf{e}_z)} = (x', y', z'+l)_{(O;\mathbf{e}_x,\mathbf{e}_y,\mathbf{e}_z)}$ and a flash point $Q_l(0, 0, l)_{(O;\mathbf{e}_x,\mathbf{e}_y,\mathbf{e}_z)}$ is

$$s' = \sqrt{(z-l)^2 + r'^2}, \tag{3.16}$$

where $r' = (x'^2 + y'^2)^{1/2}$. Using Snell-Descartes law of diffraction (3.5), the phase function of the diffracted field (3.15) can be written as

$$q(l) = \sqrt{(z-l)^2 + r'^2} + l\cos\Omega_\beta. \tag{3.17}$$

The stationary phase point is the edge diffraction point $(0, 0, l_s)_{(O;\mathbf{e}_x,\mathbf{e}_y,\mathbf{e}_z)}$ with

$$l_s = z - \frac{r'}{\tan\Omega_\beta}. \tag{3.18}$$

Therefore in the far-field ($k_\beta r' \gg 1$), the diffracted field (3.15) can be approximated by the phase stationary method, and the contribution of the diffraction point is

$$\mathbf{v}_\beta^\alpha(\mathbf{x}') = A\, C\, H(l_s - a)\, H(b - l_s)\, e^{ik_\alpha l_s \cos\Omega_\alpha}\, D_\beta^\alpha(\Omega_\alpha, \theta_\alpha, \theta)\sqrt{2i\pi}\, \frac{e^{ik_\beta S_\beta}}{\sqrt{k_\beta S_\beta \sin^2\Omega_\beta}}\, \mathbf{e}_\beta(\Omega_\beta) \tag{3.19}$$

when the phase stationary point is far apart from the edge extremities points a and b. $H()$ is the Heaviside step function. The coefficient C can be chosen to be

$$C = \frac{1}{\sqrt{2i\pi}} \tag{3.20}$$

so that for a straight line, the stationary phase point contribution leads to the GTD edge diffracted field (2.29).

The formulation of Huygens method (3.15) has similitudes with Eq. (45) of the paper [24]. But this cited equation was simply a step of calculation in [24] and led to no modelling application. Moreover this equation has been established only for an elliptical crack and for compressional waves. By contrast, the Huygens method proposed here can be applied for any crack shape and for shear waves also.

Finally, incremental fields in the ITD and Huygens models can be represented respectively by

$$\mathbf{F}_\beta(Q_l,\mathbf{x})\big|_{\text{Huygens}} = \frac{1}{\sqrt{2i\pi}}\, D^\alpha_\beta(\Omega_\alpha,\theta_\alpha,\theta)\,\frac{e^{ik_\beta s'}}{s'}\,\mathbf{e}_\beta(\Omega_\beta) \tag{3.21a}$$

and

$$\mathbf{F}_\beta(Q_l,\mathbf{x})\big|_{\text{ITD}} = \frac{1}{\sqrt{2i\pi}}\, D^\alpha_\beta(\Omega_\alpha(\phi),\theta_\alpha,\theta)\,\frac{e^{ik_\beta s'}}{s'}\,\mathbf{e}_\beta(\phi). \tag{3.21b}$$

It is clear that the Huygens based formula (3.21a) differs from the ITD based formula (3.21b) by the incidence angle Ω_α in the diffraction coefficient. Huygens method is parametrized by the incidence angle Ω_α at the flash point Q_l whereas ITD is parametrized by the observation angle ϕ which characterizes the ray issuing from the flash point Q_l to the observation point $\mathbf{x}$. Both methods add endpoints contribution to the classical edge contribution. Even if these endpoints contribution does not model really the corner diffraction, ITD and Huygens models lead to a more physical description than GTD's one [see Figs. 3.5a and 3.6a in next section]. Whatever the incremental scattering model, a complete flaw ultrasonic measurement model [26] based on the field reciprocity briefly explained in section 1.3 can be deployed to simulate echoes from the flaw (see section 1.4).

These two incremental methods have been validated against experiments and numerical results in the section (3.3).

3.3 Results

3.3.1 Experimental validation

The echoes diffracted by the top tip of a 40 mm long and 10 mm high planar notch breaking the backwall of an isotropic ferritic steel component have been simulated with the help of the two incremental methods described above and compared to experimental results. The objective

of this experimental validation is to evaluate the ability of the developed incremental models to simulate the echo amplitude of an edge of finite extent. The diffraction echoes have been measured in the TOFD (Time Of Flight Detection) configuration (see Fig. 3.3) using two 6.35 mm diameter mono-elements probes emitting $L45^\circ$ waves at 2.25 MHz with a 60 mm PCS (Probe Centre Spacing). The associated global Cartesian coordinates (X,Y,Z) are shown in Fig. 3.3. First, the defect is perpendicular to the X-axis, that is, a 2D configuration has been investigated. Then, the skew angle (the angle between the top edge of the notch and Y-axis, see Fig. 3.3) has been varied from 0° to 70° by rotating the specimen around the Z-axis. A side-drilled hole of 2 mm diameter and 40 mm length (see Fig. 3.3) has been used for calibration.

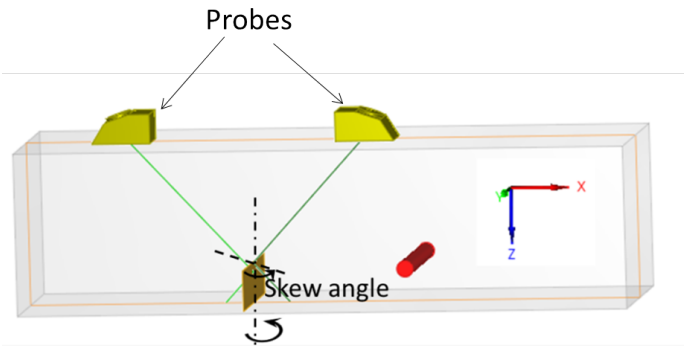

Figure 3.3: TOFD configuration.

The experimental data and simulated results are presented on Fig. 3.4. The Huygens/GTD is the Huygens method based on the GTD diffraction coefficients. Results of the Huygens/2.5D GTD is added to these results. Huygens/2.5D GTD is the Huygens method based on the 2.5D GTD diffraction coefficients, the latter related to the projections of the incoming and scattered wave vectors on the plane normal to the crack edge. In that 2.5D configuration, $\Omega_\beta = 90^\circ$ as in a 2D configuration. Fig. 3.4 shows that the Huygens/GTD and ITD simulations give results which are similar and close to experimental results, even when the skew angle is important. The Huygens/2.5D GTD model breaks down for skew angles greater than 30°. The maximum difference between the simulated results (whether obtained with the ITD or Huygens method) and experimental results is 2dB, which is of order of the measurement error in NDT [68]. Therefore the experimental validation of both ITD and Huygens methods in a 3D configuration and a finite size flaw has been successful.

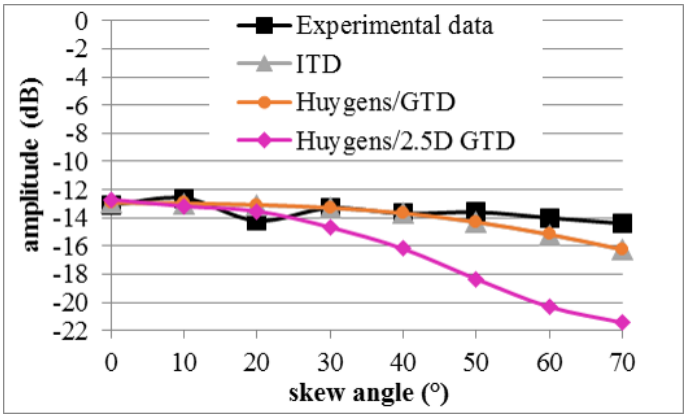

Figure 3.4: Echo amplitude diffracted by the top tip.

After experimental validation, Huygens model was compared to GTD for the diffraction of a longitudinal plane wave by half-plane edges of various lengths.

3.3.2 Numerical tests

In the previous section, it has been shown that ITD and the Huygens method give similar results for a straight diffracting edge. Thus, only the Huygens model has been subject to a numerical test, which involved comparison with GTD. The incident wave vector $\mathbf{k}^L$ has been chosen to be normal to the crack plane $(\mathbf{e}'_y, \mathbf{e}'_z)$ (see Fig. 3.1), making $\theta_\alpha = 90°$ or $\theta_\alpha = 270°$. The numerical tests involved longitudinal incident and diffracted waves. The longitudinal speed of the incident wave used for simulations is $c_L = 5900$ m/s. The frequency of the incident wave is $f = 1$ MHz. The results for a normal incidence ($\Omega_L = 90°$) and oblique incidence ($\Omega_L = 60°$) are presented in Figs. 3.5 and 3.6 respectively. Observation points are chosen to lie in the plane normal to the crack plane and containing the crack edge, so that they are described by the same value of the diffraction coefficient D_L^L. It follows that the diffracted field in this plane is proportional to the diffraction coefficient value in both GTD and the Huygens model.

GTD is a ray method. Given an observation point, the diffraction point on the edge can be found, which gives rise to a diffracted ray satisfying Snell-Descartes law of diffraction, which reaches this observation point. The amplitude of the diffracted field at the observation point is then evaluated using the GTD formula given in Eq. (2.29). The classical GTD diffracted field produces a discontinuity at shadow boundaries emanating from the edge endpoints (see Figs. 3.5a and 3.6a).

Unlike GTD, the Huygens model involves summing up the wavelets generated by the fictitious sources on the edge. Therefore, in this model (and also in ITD) the edge endpoints contribute to the diffracted field, making it continuous (see Figs. 3.5b and 3.6b).

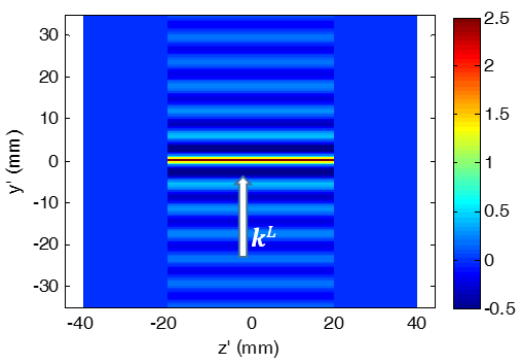

(a) Real part of GTD solution

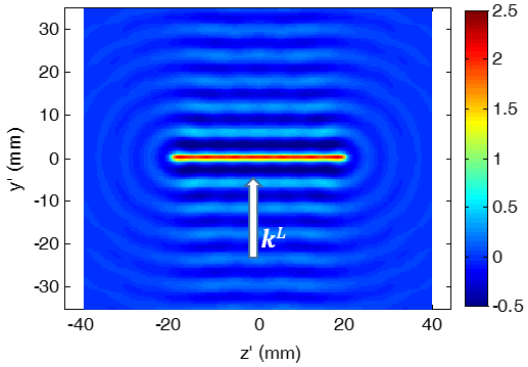

(b) Real part of Huygens solution

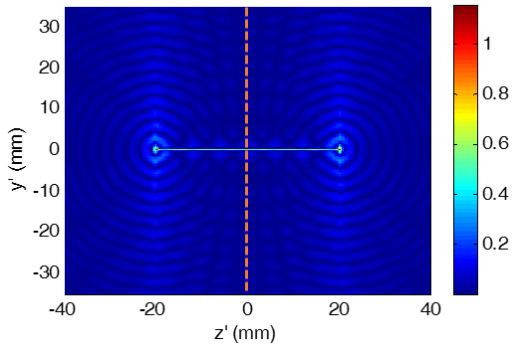

(c) Absolute difference between the real parts of Huygens and GTD solutions

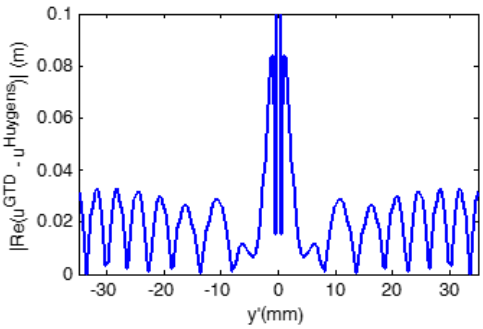

(d) Absolute difference between the real parts of Huygens and GTD displacement fields (normalized by the incident amplitude) obtained along the orange line in Fig. (c)

Figure 3.5: Diffraction of a normal incident wave ($\Omega_\alpha = 90°$) by a planar 40 mm long crack, observed in the plane normal to the crack and containing the crack edge. Huygens and GTD results in Figs. (a) - (c) are normalized by the incident amplitude.

Since GTD is discontinuous at the shadow boundary of the edge endpoints and Huygens continuous, the difference between GTD Huygens and Huygens GTD solutions is discontinuous and behaves as a sign function. The appearance of the sign function can be mathematically shown by calculating as in [53] the asymptotic uniform contribution of coalescing extremity points and stationary phase points in the Huygens integral. Extremities points then correspond to the waves diffracted by the edge endpoints and stationary phase points to waves diffracted from the edge itself. Consequently, due to the sign function, the absolute difference between the real parts of GTD and Huygens solutions - which has been plotted along the line $z' \simeq 0$ mm in Fig. 3.5d and along the line $z' \simeq -10$ mm in Fig. 3.6d – is continuous at shadow boundaries. Besides, this difference highlights the Huygens spherical waves emitted by the endpoints which interfere with each other [see Figs. 3.5c and 3.6c] and render the Huygens field continuous at endpoints shadow

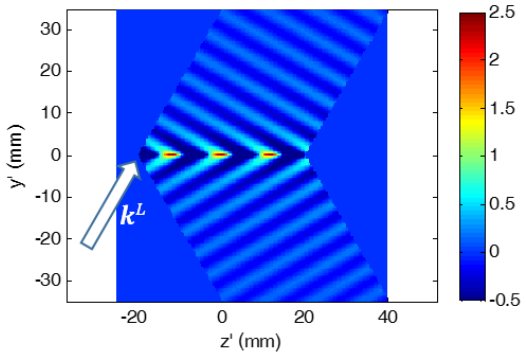

(a) Real part of GTD solution

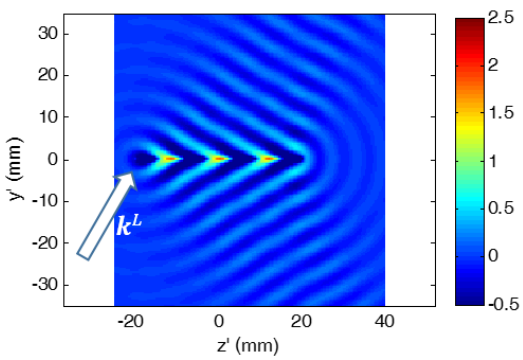

(b) Real part of Huygens solution

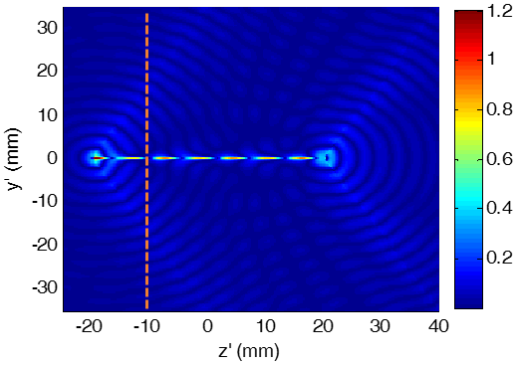

(c) Absolute difference between the real parts of Huygens and GTD solutions

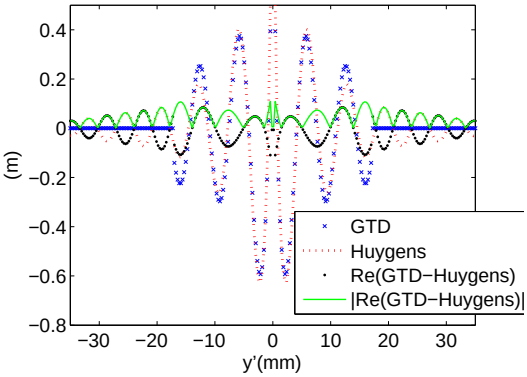

(d) Absolute difference between the real parts of Huygens and GTD displacement fields (normalized by the incident amplitude) obtained along the orange line in Fig. (c)

Figure 3.6: Diffraction of an oblique incident wave ($\Omega_\alpha = 60°$) by a planar 40 mm long crack, observed in the plane normal to the crack and containing the crack edge. Huygens and GTD results in Figs. (a) - (c) are normalized by the incident amplitude.

boundaries contrary to GTD. On these figures, the GTD/Huygens difference increases near the edge, $y' \simeq 0$ mm. That does not matter because near the edge, neither GTD nor Huygens provide a valid result since they are far field approximations.

Echoes from the endpoints contributions obtained with ITD and Huygens models are not exact since they still rely on canonical GTD solutions (infinite half-plane or wedge). Nevertheless these incremental methods produce a spatially continuous field and consequently a more physical representation than the GTD one's.

In Fig. 3.7, the diffracted fields simulated with the Huygens model for the cracks of different length L are compared to the diffracted field simulated using the canonical GTD solution for the half plane (a crack of infinite length) [see Eq. (2.3)]. The choice of the incident wave vectors is

the same as in Fig. 3.5, normal incidence, and observation points are along the orange line $z' \simeq 0$ mm (see Fig. 3.5). As the edge length increases, the Huygens model converges to GTD.

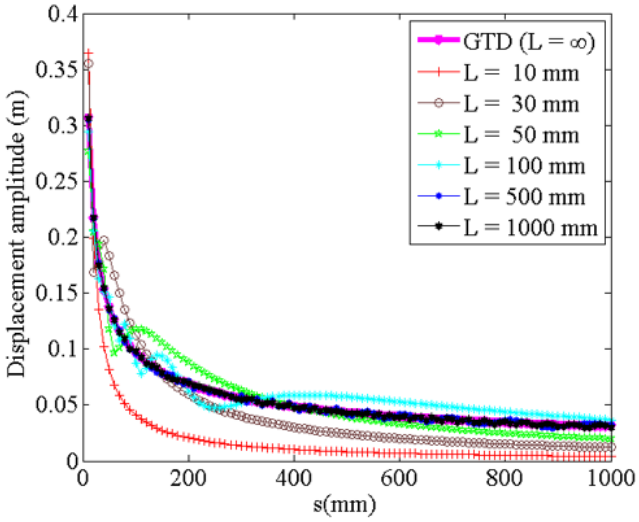

Figure 3.7: Displacement amplitude versus the observation distance using the Huygens model for cracks of finite length L and GTD for an infinite crack.

3.4 Conclusion

Two incremental methods have been proposed in elastodynamics to predict diffraction from edges of a finite length, the elastodynamic incremental theory of diffraction and the Huygens model. Both methods are based on the edge integral approach: points on the diffracting edge are fictitious sources of spherical wave. For a plane wave incident on a half-plane, both methods reproduce the canonical GTD solution, but, unlike the latter, they lead to a field, which is spatially continuous notably at the shadow boundaries due to edge endpoints. The methods have been tested numerically and validated against experiments for a backwall planar crack. In conclusion of these validations:

- experimental tests showed that the Huygens model gives similar results as the ITD model in one 3D realistic NDT configuration,

- numerical comparisons between the Huygens model and the GTD for defects of various lengths highlighted the benefits of incremental models compared to GTD. Indeed, they have a more physical description of the scattered field by the defect extremities which gives rise to a uniform edge diffracted field contrary to the GTD model. Furthermore, for an infinite edge, incremental models are equal to GTD.

The versions of the incremental methods presented here are based on the classical GTD but it is also possible to utilize the recently developed elastodynamic GTD corrections, which are valid in the vicinity of shadow boundaries, the Physical Theory of Diffraction (PTD) [see section 1.4.1] and the Uniform Theory of Diffraction (UTD) introduced in chapter 2 for the case of a half-plane.

To be able to simulate diffraction by the specimen irregularities, a Uniform Theory of Diffraction for the wedge (geometry usually encountered in the inspected specimen) scattering problem in a 2D configuration[2] is proposed in chapter 4. This UTD wedge model being 2D, incremental models are not applied to it, but they will be useful when a GTD solution for the diffraction by a solid wedge will be developed in 3D configurations.

The works realized in this chapter are submitted in a peer reviewed journal [69].

[2]The wedge edge is infinite and the diffraction problem is invariant along the edge wedge

Chapter 4

The Uniform geometrical Theory of Diffraction (UTD) for elastodynamics: plane wave scattering by a two-dimensional traction-free elastic wedge and application to NDT

Au chapitre 1 de cette thèse, la Théorie géométrique Uniforme de la Diffraction (UTD) a été développée en élastodynamique pour modéliser l'interférence des ondes réfléchies par la surface d'un demi-plan et celles diffractées par son arête. Le cas du demi-plan a ainsi permis d'avoir une meilleure compréhension du fonctionnement de l'UTD et la solution UTD pour le cas du dièdre a donc ensuite pu être abordée plus aisément.

La solution UTD permettant de modéliser par une méthode rayon l'interférence des ondes réfléchies par les surfaces du dièdre et des ondes diffractées par son arête est développée dans ce chapitre à l'aide de la formulation du problème de diffraction d'arête sous forme d'intégrale de Sommerfeld. En fonction de l'angle du dièdre et de l'angle d'incidence sur les faces du dièdre, des réflexions multiples peuvent avoir lieu au sein du dièdre, générant ainsi plusieurs frontières d'ombre en réflexion. La détermination de ces frontières d'ombre est faite en utilisant l'algorithme de propagation des pôles de la solution Sommerfeld. L'UTD ainsi développée, a été comparée à l'UAT pour une onde plane incidente. Un modèle UTD de calcul d'échos de géométrie est mis au point dans CIVA et comparé aux modèles existants d'échographie de CIVA tels que le modèle spéculaire et l'approximation de Kirchhoff (tous les deux introduis au chapitre 1), ainsi qu'au modèle aux éléments finis CIVA/Athena dans certains cas concrets d'inspections ultrasonores. Ces comparaisons donnent lieu à des résultats convaincants quant à l'utilité du modèle UTD développé.

4.1 Introduction

The Uniform geometrical Theory of Diffraction (UTD) is a powerful engineering tool. It is the reason why it is widely used in electromagnetism softwares as FEKO [70], XGTD [71] and PROMAN [72] to simulate electromagnetic waves propagation at high frequencies. In these softwares, the obtacles are represented by simple geometrical objects for which UTD solution is known. To design such a propagation and scattering code in elastodynamics, it is important to derive UTD solution for a plane wave scattering by a wedge to deal with surface irregularities. To develop UTD for the wedge, one first needs the GTD solution to model diffraction from wedge tip. This GTD solution requires to express the edge diffracted field as a cylindrical/conical wave weighted by a directivity coefficient, the so-called diffraction coefficient.

Diffraction by an elastic wedge is a challenging mathematical problem. It has been treated by many authors in the past thirty years: Rayleigh wave scattering by a solid wedge [25, 73–78], acoustic wave scattering by a solid wedge [11] and elastic wedge scattering [37, 38]. Nonetheless, in all the proposed resolutions in elastodynamics, there is not a pure analytical solution as in electromagnetism or in acoustics in non viscous fluids where there is only one type of scalar wave which propagates through the medium. In elastodynamics, there exist different types of waves with different velocities, which interact with each other. These waves cannot be mathematically separated in the boundary conditions and that brings difficulties for elastodynamics problems. Katmoski and Lebeau [79] have shown the existence and the uniqueness of the solution for this complex problem.

There exist two main approaches for the diffraction of a plane wave by a traction-free elastic wedge, one based on the Sommerfeld integral (SI) [37] and another based on the Laplace transform (LT) [38]. These two methods are limited to wedge angles less than π. They lead to a GTD solution which diverges at shadow boundaries of the Geometrico-Elastodynamic field as expected. CEA LIST retains the Laplace Transform code developed in collaboration with Sound Mathematics Ltd. - company led by Larissa Fradkin and specialized notably in mathematical modelling of ultrasonic Non Destructive Testing (NDT).

In this section, a UTD solution for the wedge still based on the Pauli-Clemmow approximation as in the case of the half-plane (see chapter 1) is proposed in order to provide a GTD correction uniform in the whole space. To apply the Pauli-Clemmow approximation, all the reflected poles which give rise to reflected waves, have to be known. For the reflected poles determination, the algorithm proposed by the Sommerfeld integral method is used. In section 4.2, a review of the two main GTD solutions is done with a particular emphasis on the pole propagation algorithm proposed by the Sommerfeld integral. An existing UAT solution for the wedge is recalled in section 4.3 and the UTD solution for the wedge is developed in this same section. Section 4.4 describes numerical validation of the developed UTD model: comparison with UAT solution and comparison with other CIVA models for the specimen echoes in section 4.4.1. Conclusions of this chapter are provided in section 4.4.2.

4.2 Review of Scattering models for the diffraction of a plane wave by an elastic wedge: non uniform asymptotics

The geometry of the two dimensional problem is presented in Fig. 4.1, using the Cartesian system based on an orthonormal basis $(\mathbf{e}_{x_1}, \mathbf{e}_{y_1}, \mathbf{e}_z)$ and the origin O at the tip wedge. The edge of the wedge coincides with the z-axis. The wedge of angle 2φ is constituted of an isotropic solid and is irradiated by a plane wave which propagates along the direction

$$\mathbf{p}_{\text{inc}} = -(\cos\theta_{\text{inc}}, \sin\theta_{\text{inc}})_{(\mathbf{e}_{x_1}, \mathbf{e}_{y_1})}, \tag{4.1}$$

where θ_{inc} is the angle between the incident propagation vector and the x_1-axis (see Fig. 4.1). The problem is therefore invariant along the z direction. The components of any position vector $\mathbf{x}$ in the Cartesian coordinates system are $(x_1, y_1)_{(\mathbf{e}_{x_1}, \mathbf{e}_{y_1})}$ and they are $(r, 0)_{(\mathbf{e}_r, \mathbf{e}_\theta)}$ in the associated polar coordinates system.

In this chapter, the time convention $\exp(-i\omega t)$, ω being the circular frequency and t being the time, is implied but omitted everywhere.

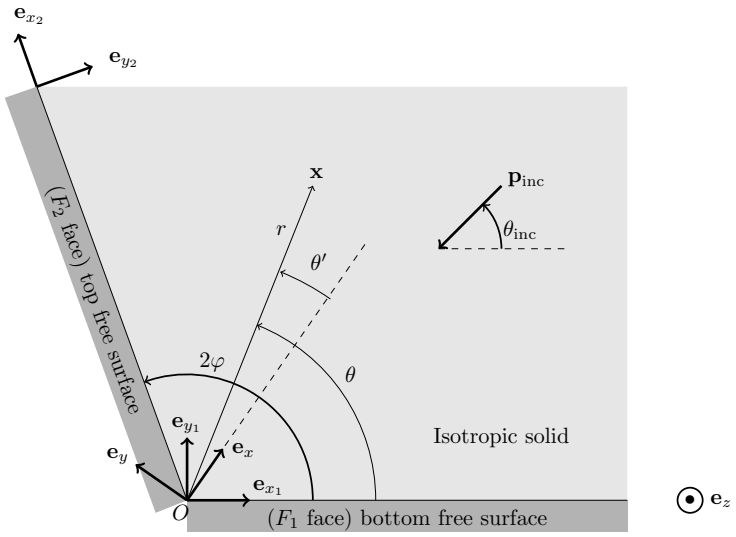

Figure 4.1: The wedge of angle 2φ whose faces are stress-free is illuminated by a plane wave of propagation vector $\mathbf{p}_{\text{inc}}$.

Due to the symmetry of the wedge with respect to its bisector, the problem can be split into one symmetric and one antisymmetric problems. Let us introduce the new Cartesian system based on the orthonormal frame $(O; \mathbf{e}_x, \mathbf{e}_y)$ where $\mathbf{e}_x$ is along the wedge bisector (see Fig. 4.1). Any observation point is expressed in this new Cartesian coordinates as (x, y) and in the associated

polar coordinates as (r, θ') where

$$\theta' = \theta - \varphi. \tag{4.2}$$

The basis $(\mathbf{e}_{x_1}, \mathbf{e}_{y_1})$ and $(\mathbf{e}_x, \mathbf{e}_y)$ are linked by the relations

$$\mathbf{e}_x = \cos\varphi\, \mathbf{e}_{x_1} + \sin\varphi\, \mathbf{e}_{y_1}, \tag{4.3a}$$

$$\mathbf{e}_y = -\sin\varphi\, \mathbf{e}_{x_1} + \cos\varphi\, \mathbf{e}_{y_1}. \tag{4.3b}$$

The incidence angle with respect to the bisector in this new Cartesian coordinates in then $\theta'_{\text{inc}} = \theta_{\text{inc}} - \varphi$. Let us introduce the symmetric to the incident plane wave with respect to the wedge bisector (see Fig. 4.2a). It corresponds to a plane wave of incidence angle $-\theta'_{\text{inc}} = \varphi - \theta_{\text{inc}}$ in the orthonormal frame $(O; \mathbf{e}_x, \mathbf{e}_y)$. This symmetric wave propagates along the direction

$$\mathbf{p}_{\text{sym}} = (-\cos\theta'_{\text{inc}}, \sin\theta'_{\text{inc}})_{(\mathbf{e}_x, \mathbf{e}_y)}. \tag{4.4}$$

The problem is therefore the sum of two problems, one which is symmetric and another which is antisymmetric with respect to the wedge bisector regarding the polarization vectors. Figure 4.2 shows these two problems. For an incident longitudinal plane wave, the polarization vector $\mathbf{d}^L$ is the same than the propagation vector $\mathbf{p}^L$ ($\mathbf{d}^L = \mathbf{p}^L$). Thus, the figure 4.2a corresponds to a symmetric problem and the figure 4.2b to an antisymmetric problem for an incident longitudinal plane wave. In contrast, the figure 4.2a corresponds to an antisymmetric problem and the figure 4.2b to a symmetric problem for an incident transversal plane wave. That is because the polarization vector of an incident transversal plane wave $\mathbf{d}^T$ is perpendicular to its propagation vector $\mathbf{p}^T$ ($\mathbf{d}^T \perp \mathbf{p}^T$). In Fig. 4.2a, the respective propagation and polarization vectors of incident and symmetric transversal waves are the following ones:

$$\mathbf{p}^T_{\text{inc}} = (-\cos\theta'_{\text{inc}}, -\sin\theta'_{\text{inc}})_{(\mathbf{e}_x, \mathbf{e}_y)} \quad \text{and} \quad \mathbf{d}^T_{\text{inc}} = (-\sin\theta'_{\text{inc}}, \cos\theta'_{\text{inc}})_{(\mathbf{e}_x, \mathbf{e}_y)}, \tag{4.5a}$$

$$\mathbf{p}^T_{\text{sym}} = (-\cos\theta'_{\text{inc}}, \sin\theta'_{\text{inc}})_{(\mathbf{e}_x, \mathbf{e}_y)} \quad \text{and} \quad \mathbf{d}^T_{\text{sym}} = (\sin\theta'_{\text{inc}}, \cos\theta'_{\text{inc}})_{(\mathbf{e}_x, \mathbf{e}_y)}. \tag{4.5b}$$

$\mathbf{d}^T_{\text{sym}}$ (the opposite to $-\mathbf{d}^T_{\text{sym}}$ on Fig. 4.2b) is thus the antisymmetric of $\mathbf{d}^T_{\text{inc}}$ (represented on Fig. 4.2b) with respect to the wedge bisector in this case. It then confirms that Fig. 4.2a illustrates the antisymmetric problem for incident transversal waves. In Fig. 4.2b for which the opposite polarization of the symmetric wave $-\mathbf{d}^T_{\text{sym}}$ is considered, $-\mathbf{d}^T_{\text{sym}}$ is the symmetric of $\mathbf{d}^T_{\text{inc}}$. Note that the considered transversal wave (T wave) in this chapter corresponds to the vertical transverse wave whose polarization is contained in the plane $(\mathbf{e}_{x_1}, \mathbf{e}_{y_1})$ perpendicular to the edge like the one of the longitudinal wave.

This diffraction problem can always be split into symmetric and antisymmetric problems for any wave in the wedge, as seen in the case of an incident plane wave. Thus, the symmetric to this wave with respect to the wedge bisector is introduced in order to split the problem.

Both of the two resolution approaches of a plane wave diffraction by a wedge tip existing in elastodynamics, the Sommerfeld integral method [37] and the Laplace transform method [38], treat separately the symmetric and antisymmetric problems.

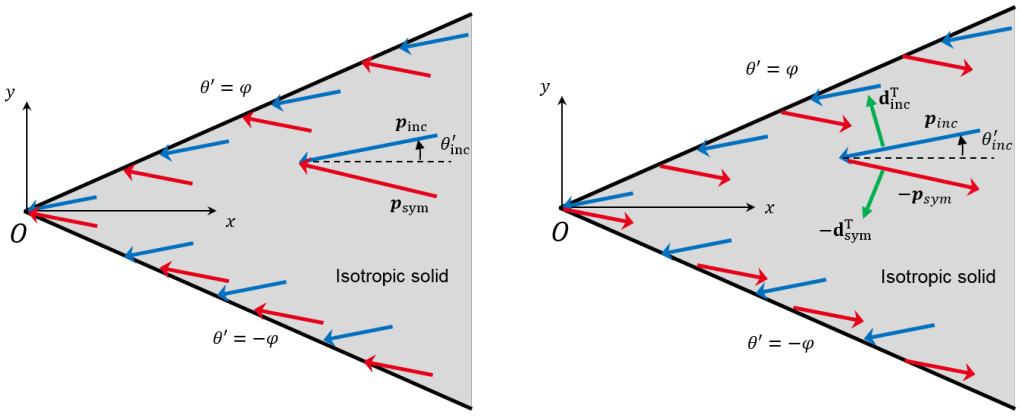

(a) Symmetric problem for an incident longitudinal plane wave and antisymmetric problem for an incident transversal plane wave

(b) Antisymmetric problem for an incident longitudinal plane wave and symmetric problem for an incident transversal plane wave

Figure 4.2: Symmetric and antisymmetric problems. Blue and red vectors are the propagation vectors. Green vectors are the polarization vectors of the incident and symmetric transversal waves.

4.2.1 Sommerfeld integral (SI)

In this approach, the considered orthonormal frame is $\{O, \mathbf{e}_x, \mathbf{e}_y\}$. This resolution method of the problem of plane wave diffraction by a 2D (two-dimensionnal) traction-free isotropic elastic wedge is based on the Sommerfeld integral. The Sommerfeld integral is a solution of the Helmholtz equation which satisfies the radiation conditions at infinity [17] and the Meixner conditions under certain conditions. In this approach, the scalar and the vector elastodynamic displacement potentials, ψ_L and $\psi_T \mathbf{e}_z$ respectively, satisfying the Helmholtz equations in the elastic angular domain

$$\triangle \psi_L + k_L^2 \psi_L = 0, \quad \triangle \psi_T + k_T^2 \psi_T = 0, \quad |\theta| < \varphi, \tag{4.6}$$

$\triangle = \partial_r^2 + \partial_r / r + \partial_{\theta'}^2 / r^2$ being the Laplace operator, and the Neumann condition for the stresses $\sigma_{r\theta'}$ and $\sigma_{\theta'\theta'}$ on the wedge faces

$$\sigma_{r\theta'} = 0, \quad \sigma_{\theta'\theta'} = 0, \quad |\theta'| = \varphi, \tag{4.7}$$

are represented in the form of Sommerfeld integrals so that the scattered waves by a wedge are modelled as a superposition of plane waves propagating in all directions including complex ones:

$$\psi_\beta(k_\beta r, \theta') = \int_{\gamma_+} e^{-ik_\beta r \cos\lambda} [\Psi_\beta(\theta' + \lambda) - \Psi_\beta(\theta' - \lambda)]\, d\lambda, \tag{4.8}$$

with $\beta = L$ or T. λ in integral (4.8) is a polar complex angle in the orthonormal frame $(O; \mathbf{e}_x, \mathbf{e}_y)$ and the plane waves in (4.8) propagates in the direction of decreasing distance r. In these equations, Ψ_β are the unknown scalar Sommerfeld amplitudes and γ_+ is the Π-shaped Sommerfeld contour represented in Fig. 4.3. By introducing γ_- the symmetric to the contour γ_+ with respect to the origin of the complex plane λ (see Fig. 4.3), potentials ψ_β can be rewritten as

$$\psi_\beta(k_\beta r, \theta') = \int_{\gamma_+ + \gamma_-} e^{-ik_\beta r \cos\lambda}\, \Psi_\beta(\theta' + \lambda)\, d\lambda. \tag{4.9}$$

The construction of the Sommerfeld contours γ_+ and γ_- is explained in Babich et al. [17].

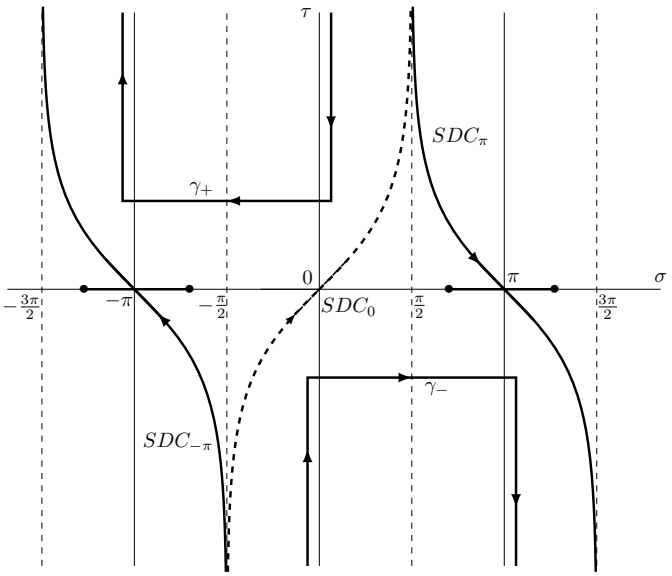

Figure 4.3: Sommerfeld contours of integration γ_+ and γ_- in the complex plane $\lambda = \sigma + i\tau$; steepest descent contours $\mathrm{SDC}_{-\pi}$, SDC_π and SDC_0 in thick dashed lines. The thick segments are the branch cuts of the g function in (4.12).

The problem is divided into symmetric and antisymmetric problems as specified at the beginning of this section. Let us denote the symmetric longitudinal (respectively transversal) potential by Ψ_L^+ (respectively Ψ_T^+) and the antisymmetric longitudinal (respectively transversal) potential by Ψ_L^- (respectively Ψ_T^-). The superscript " $+$ " then refers to the symmetric problem and the superscript " $-$ " to the antisymmetric problem. The problem being split, the Sommerfeld amplitudes

can therefore be written as

$$\Psi_\beta(\lambda) = \Psi_\beta^+(\lambda) + \Psi_\beta^-(\lambda) \quad \text{with} \quad \begin{cases} \Psi_L^\pm(\lambda) & = \frac{1}{2}[\Psi_L(\lambda) \pm \Psi_L(-\lambda)] \\ \Psi_T^\pm(\lambda) & = \frac{1}{2}[\Psi_T(\lambda) \mp \Psi_T(-\lambda)] \end{cases}. \tag{4.10}$$

The term $\Psi_\beta(-\lambda)$ thus introduces the symmetric wave of the plane wave of angle λ in the wedge with respect to the wedge bisector. Its coefficient " $-$ " means that it is the opposite polarization of this symmetric wave which is considered contrary to " $+$ " coefficient which means that the polarization of this symmetric wave is conserved. Symmetric and antisymmetric potentials of (4.10) thus respect what has been explained before this section in the case of an incident plane wave. For a longitudinal plane wave in the wedge, in the symmetric problem, the polarization of the symmetric wave is considered and in the antisymmetric problem, its opposite polarization is considered (see Fig. 4.2). For a transversal plane wave, it is the contrary. That explains the difference of sign between L and T potentials in (4.10).

These two problems, symmetric and antisymmetric, must also satisfy the boundary conditions given in (4.7). Expressions of $\psi_\beta^\pm$ in terms of Sommerfeld integrals [Eq. (4.9)] are then substituted in (4.7). Kamotski et al. [37] have shown that this procedure leads to the following systems of functional equations

$$\begin{aligned} \begin{pmatrix} \Psi_L^\pm(g(\lambda)+\varphi) \\ \Psi_T^\pm(\lambda+\varphi) \end{pmatrix} = \pm \begin{pmatrix} r_L^L(\lambda) & r_L^T(\lambda) \\ r_T^L(\lambda) & r_T^T(\lambda) \end{pmatrix} \begin{pmatrix} \Psi_L^\pm(g(\lambda)-\varphi) \\ \Psi_T^\pm(\lambda-\varphi) \end{pmatrix} \\ + \kappa^2 c_1^\pm \frac{\sqrt{\kappa^{-2}-\cos^2\lambda}}{\Delta(\lambda)} \begin{pmatrix} \cos 2\lambda - \tan\varphi \, \sin 2\lambda \\ \sin 2\lambda + \tan\varphi \dfrac{\sin\lambda \, \cos 2\lambda}{\sqrt{\kappa^{-2}-\cos^2\lambda}} \end{pmatrix}. \end{aligned} \tag{4.11}$$

Let us detail the involved terms in these systems of equations.

- The function

$$g(\lambda) = \arccos\left(\kappa \cos\lambda\right), \tag{4.12}$$

with

$$\kappa = k_T/k_L, \tag{4.13}$$

links the transversal incidence angle θ'_{T} to the longitudinal reflection angle θ'_{rL}:

$$\theta'_{\mathrm{rL}} = g(\theta'_{\mathrm{T}}). \tag{4.14}$$

It is a multivalued function. Its branch point is the longitudinal critical angle $\theta'_c = \arccos\, \kappa^{-1}$. The chosen branch cuts are the segments $[-\theta'_c + \pi m, \theta'_c + \pi m]$, $m \in \mathbb{N}$ (see Fig. 4.3).

- The reflection coefficients in terms of potential on a stress-free half-plane are

$$r_L^L(\lambda) = \frac{2\sin 2\lambda\,\cos\lambda\sqrt{\kappa^{-2}-\cos^2\lambda}-\cos^2 2\lambda}{\Delta(\lambda)} = R_L^L(g(\lambda)), \tag{4.15a}$$

$$r_T^T(\lambda) = -r_L^L(\lambda) = R_{TV}^{TV}(\lambda), \tag{4.15b}$$

$$r_L^T(\lambda) = -\frac{4\cos 2\lambda\,\cos\lambda\sqrt{\kappa^{-2}-\cos^2\lambda}}{\Delta(\lambda)} = \frac{1}{\kappa}R_{TV}^{L}(g(\lambda)), \tag{4.15c}$$

$$r_T^L(\lambda) = -\frac{2\sin 2\lambda\,\cos 2\lambda}{\Delta(\lambda)} = -\kappa R_L^{TV}(\lambda) \tag{4.15d}$$

  with R_L^L, R_{TV}^{TV}, R_{TV}^L and R_L^{TV} being the reflection coefficients in terms of displacement presented in Eq. (2.18) and (2.19).

- $c_1^{\pm}$ are unknown constants.

- $\Delta(\lambda)$ function defined as

$$\Delta(\lambda) = \cos^2 2\lambda + 2\sin 2\lambda\,\cos\lambda\sqrt{\kappa^{-2}-\cos^2\lambda} = \kappa^{-2}\,\mathcal{R}(g(\lambda),\lambda), \tag{4.16}$$

  is proportional to the Rayleigh function $\mathcal{R}$ defined in (2.20).

These systems of functional equations could be used to find all the reflected waves in the wedge knowing the incident plane wave on each face of the wedge. The Geometrico-Elastodynamic (GE) field can therefore be determined using (4.11). The procedure leading to the knowledge of the incident wave and of all the reflected waves on the wedge faces using these systems of functional equations is explained in section 4.2.1.1.

4.2.1.1 Sommerfeld integral poles propagation

The Sommerfeld integral defined here in (4.8) or (4.9) represents the total solution (incident and scattered waves) contrary to the one of a plane wave scattering by a half-plane (see chapter 2) for which the involved Sommerfeld integral represents only the scattered waves. It is well known that the poles of the Sommerfeld amplitudes Ψ_β describe the geometrical field which is constituted of incident waves and those reflected from the wedge faces as well as surfaces waves like Rayleigh waves. To determine the GE field, we then need to find all the poles of the Sommerfeld amplitudes Ψ_β. Let us begin by determining the initial poles of Ψ_β, $\beta = \alpha$ being the type of the incident wave, in order to find the incident potential.

4.2.1.1.a Initial poles

Let the incident potential displacement field of type α at an observation point $\mathbf{x}$ be expressed as

$$\psi_\alpha^{\text{inc}}(k_\alpha r, \theta') = \frac{1}{ik_\alpha} e^{-ik_\alpha r\cos(\theta'-\theta'_{\text{inc}})}. \tag{4.17}$$

Below, the displacement decomposition

$$\mathbf{u} = \mathbf{u}^L + \mathbf{u}^T \tag{4.18}$$

is used. The longitudinal wave displacement $\mathbf{u}^L$ is related to the scalar displacement potential ϕ_L as

$$\mathbf{u}^L = \nabla\psi_L, \tag{4.19}$$

$\nabla = (\partial_x, \partial_y)_{(\mathbf{e}_x,\mathbf{e}_y)}$ being the gradient operator, and the transversal wave displacement $\mathbf{u}^T$ is related to the vector displacement potential $\phi_T\,\mathbf{e}_z$ as

$$\mathbf{u}^T = \nabla\times(\psi_T\,\mathbf{e}_z), \tag{4.20}$$

$\nabla\times$ being the curl operator. Eqs. (4.17), (4.19) and (4.20) then lead to a unit displacement vector

$$\mathbf{u}^{L(\text{inc})} = \nabla\psi_L = -e^{-ik_L r\cos(\theta'-\theta'_{\text{inc}})}(\cos\theta'_{\text{inc}}, \sin\theta'_{\text{inc}})_{(\mathbf{e}_x,\mathbf{e}_y)} \tag{4.21}$$

for incident longitudinal wave or

$$\mathbf{u}^{T(\text{inc})} = \nabla\times(\psi_T\,\mathbf{e}_z) = e^{-ik_T r\cos(\theta'-\theta'_{\text{inc}})}(-\sin\theta'_{\text{inc}}, \cos\theta'_{\text{inc}})_{(\mathbf{e}_x,\mathbf{e}_y)} \tag{4.22}$$

for incident transversal wave. The factor $1/(ik_\alpha)$ in the incident potential (4.17) is implied but omitted everywhere.

In the following, the notation $\alpha\to\beta$ means that an incident plane wave of type α gives rise to a scattered wave of type β. Note that in term of displacement, applying formula (4.20), the factor $1/(ik_\alpha)$ induces a proportional factor κ [defined in Eq. (4.13)] with the incident displacement amplitude for conversion of longitudinal waves to transversal waves. In terms of equations, it corresponds to

$$|\mathbf{u}^{L\to T}| = \kappa\,|k_L\,\psi_{L\to T}|. \tag{4.23}$$

The term $|k_L\,\psi_{L\to T}|$ is the displacement amplitude of the incident longitudinal wave. With the formula (4.19), the factor $1/(ik_\alpha)$ induces a proportional factor $1/\kappa$ with the incident displacement amplitude for conversion of transversal waves to longitudinal waves

$$|\mathbf{u}^{T\to L}| = \frac{1}{\kappa}\,|k_T\,\psi_{T\to L}|. \tag{4.24}$$

As in the previous case, the term $|k_T\,\psi_{T\to L}|$ is the displacement amplitude of the incident transversal wave.

In order to obtain the incident potential field (4.17) using the residue theorem to calculate integral (4.9), the Sommerfeld amplitude $\Psi_{\beta=\alpha}(\lambda)$ can be expressed as

$$\Psi_\alpha^{\text{inc}}(\lambda) = \frac{1}{4\pi i}\cot\left(\frac{\lambda-\theta'_{\text{inc}}}{2}\right) \tag{4.25}$$

which has a pole at $\lambda=\theta'_{\text{inc}}$. Indeed, substituting Ψ_β in (4.9) for $\beta=\alpha$ by (4.25), the pole of the integrand function $\Psi_\beta(\lambda+\theta')$ is thus $\lambda=\theta'_{\text{inc}}-\theta'$. knowing that

$$\cot(x)\sim\frac{1}{x}\quad\text{when}\quad x\to 0, \tag{4.26}$$

the residue of this pole $\lambda=\theta'_{\text{inc}}-\theta'$ in integral (4.9) given by the residue theorem is

$$\lim_{\lambda\to\theta'_{\text{inc}}-\theta'} 2\pi i\,(\lambda+\theta'-\theta'_{\text{inc}})\,\Psi_\alpha^{\text{inc}}(\lambda+\theta')e^{-ik_\alpha r\cos\lambda} = e^{-ik_\alpha r\cos(\theta'-\theta'_{\text{inc}})}. \tag{4.27}$$

Thus, for a longitudinal incident plane wave, Eq. (4.25) can be split into symmetric and antisymmetric parts using (4.10):

$$\Psi_L^{\text{inc}(+)}(\lambda) = \frac{1}{8\pi i}\left[\cot\left(\frac{\lambda-\theta'_{\text{inc}}}{2}\right)+\cot\left(\frac{\lambda+\theta'_{\text{inc}}}{2}\right)\right], \tag{4.28}$$

$$\Psi_L^{\text{inc}(-)}(\lambda) = \frac{1}{8\pi i}\left[\cot\left(\frac{\lambda-\theta'_{\text{inc}}}{2}\right)-\cot\left(\frac{\lambda+\theta'_{\text{inc}}}{2}\right)\right]. \tag{4.29}$$

The same thing can be done with a transversal incident plane wave. The symmetric and antisymmetric parts are:

$$\Psi_T^{\text{inc}(+)}(\lambda) = \frac{1}{8\pi i}\left[\cot\left(\frac{\lambda-\theta'_{\text{inc}}}{2}\right)-\cot\left(\frac{\lambda+\theta'_{\text{inc}}}{2}\right)\right], \tag{4.30}$$

$$\Psi_T^{\text{inc}(-)}(\lambda) = \frac{1}{8\pi i}\left[\cot\left(\frac{\lambda-\theta'_{\text{inc}}}{2}\right)+\cot\left(\frac{\lambda+\theta'_{\text{inc}}}{2}\right)\right]. \tag{4.31}$$

Those incident potential give us information about initial poles for symmetric and antisymmetric problems with their corresponding residue. The initial pole $\lambda=\theta'_{\text{inc}}$ corresponds to the incident wave on the wedge faces and the initial pole $\lambda=-\theta'_{\text{inc}}$ corresponds to the symmetric wave of the incident plane wave with respect to the wedge bisector (see Fig. 4.1). Knowing them, the system of functional equations (4.11) can be used to find all the poles of the Sommerfeld amplitudes with their corresponding residues which give rise to reflected waves on the wedge faces. It gives an iterative scheme to propagate the initial poles.

Let us suppose that functions $\Psi_\beta^{\pm}(\lambda)$ have simple poles at $\lambda=\lambda_\beta$ with their corresponding

residue $\mathrm{res}_\beta^\pm$. They can therefore be written as

$$\Psi_\beta^\pm(\lambda) = \frac{\mathrm{res}_\beta^\pm}{\lambda - \lambda_\beta}. \tag{4.32}$$

The generation of longitudinal and transversal reflected poles using an iterative scheme is explained hereafter.

4.2.1.1.b Generation of longitudinal reflected waves

Longitudinal reflected waves are generated by the reflection of an incident longitudinal or transversal wave with a mode conversion on the wedge faces. The first line of system (4.11) allows to find these longitudinal reflected waves with the relations

$$\Psi_L^\pm(g(\lambda)+\varphi) = \pm\left[r_L^L(\lambda)\,\Psi_L^\pm(g(\lambda)-\varphi) + r_L^T(\lambda)\,\Psi_T^\pm(\lambda-\varphi)\right]. \tag{4.33}$$

Let introduce the angle $\eta_L = g(\lambda)+\varphi$, thus, $\lambda = g^{-1}(\eta_L-\varphi)$ and (4.33) becomes

$$\Psi_L^\pm(\eta_L) = \pm\left[r_L^L(g^{-1}(\eta_L-\varphi))\,\Psi_L^\pm(\eta_L-2\varphi) + r_L^T(g^{-1}(\eta_L-\varphi))\,\Psi_T^\pm(g^{-1}(\eta_L-\varphi)-\varphi)\right]. \tag{4.34}$$

Substituting (4.32) in (4.34), we got

$$\Psi_L^\pm(\eta_L) = \pm\left[r_L^L(g^{-1}(\eta_L-\varphi))\,\frac{\mathrm{res}_L^\pm}{\eta_L-(2\varphi+\lambda_L)} + r_L^T(g^{-1}(\eta_L-\varphi))\,\frac{\mathrm{res}_T^\pm}{g^{-1}(\eta_L-\varphi)-(\varphi+\lambda_T)}\right]. \tag{4.35}$$

The generated longitudinal poles of (4.45) are obtained for:

$$\eta_L-(2\varphi+\lambda_L)=0 \iff \eta_L=\lambda_{LL}=2\varphi+\lambda_L, \tag{4.36a}$$

$$g^{-1}(\eta_L-\varphi)-(\varphi+\lambda_T)=0 \iff \eta_L=\lambda_{TL}=g(\varphi+\lambda_T)+\varphi \tag{4.36b}$$

with their respective residues

$$\begin{aligned}\mathrm{res}_{LL}^\pm &= \lim_{\eta_L\to\lambda_{LL}}(\eta_L-\lambda_{LL})\,\Psi_L^\pm(\eta_L)\\ &= \mathrm{res}_L^\pm\, r_L^L(g^{-1}(\lambda_{LL}-\varphi))\\ &= \pm\,\mathrm{res}_L^\pm\, r_L^L(g^{-1}(\varphi+\lambda_L))\\ &= \pm\,\mathrm{res}_L^\pm\, R_L^L(\varphi+\lambda_L), \qquad \text{using (4.15a)}\end{aligned} \tag{4.37}$$

and

$$\begin{aligned}
\mathrm{res}_{TL}^{\pm} &= \lim_{\eta_L \to \lambda_{TL}} (\eta_L - \lambda_{LT})\, \Psi_L^{\pm}(\eta_L) \\
&= \mathrm{res}_T^{\pm}\, r_L^T(g^{-1}(\lambda_{TL} - \varphi)) \lim_{\eta_L \to \lambda_{TL}} \frac{\eta_L - \lambda_{LT}}{g^{-1}(\eta_L - \varphi) - (\varphi + \lambda_T)} \\
&= \mathrm{res}_T^{\pm}\, r_L^T(g^{-1}(\lambda_{TL} - \varphi)) \lim_{\eta_L \to \lambda_{TL}} \frac{(\eta_L - \varphi) - (\lambda_{LT} - \varphi)}{g^{-1}(\eta_L - \varphi) - (\varphi + \lambda_T)} \\
&= \mathrm{res}_T^{\pm}\, r_L^T(g^{-1}(\lambda_{TL} - \varphi)) \lim_{\eta_L \to \lambda_{TL}} \frac{g\left[g^{-1}(\eta_L - \varphi)\right] - g(\varphi + \lambda_T)}{g^{-1}(\eta_L - \varphi) - (\varphi + \lambda_T)} \\
&= \pm\, \mathrm{res}_T^{\pm}\, r_L^T(\varphi + \lambda_T)\, g'(\varphi + \lambda_T).
\end{aligned} \tag{4.38}$$

Expression (4.38) can be simplified using

$$g'(\lambda) = \frac{\kappa \sin \lambda}{\sqrt{1 - \kappa^2 \cos^2 \lambda}} \tag{4.39}$$

since

$$r_T^L(\lambda) = r_L^T(\lambda)\, g'(\lambda), \tag{4.40}$$

r_T^L and r_L^T being defined respectively at (4.15d) and (4.15c). Using (4.40) and (4.15d), (4.38) then reduces to

$$\mathrm{res}_{TL}^{\pm} = \pm\, \mathrm{res}_T^{\pm}\, r_T^L(\varphi + \lambda_T) = \mp\, \kappa\, \mathrm{res}_T^{\pm}\, R_L^{TV}(\varphi + \lambda_T). \tag{4.41}$$

Having a longitudinal or transversal wave of incidence angle $\lambda_{L,T}$ on the bottom face of the wedge (face 1) with a given residue, this incident wave is reflected by the wedge faces and gives rise to longitudinal reflected waves of angle λ_{LL} [see Eq. (4.36a)] and λ_{TL} [see Eq. (4.36b)] with the bottom face of the wedge respectively. The residue of these reflected waves are respectively found using Eqs. (4.37) and (4.41). These generated longitudinal poles can also be propagated. They are then considered as initial longitudinal poles in the form of (4.32) for the pole propagation algorithm. Thus, for the propagation of these generated poles $\lambda_{L\beta}$, initial poles on the form (4.32) are:

$$\lambda_\beta = \lambda_{\beta L} \quad \text{and} \quad \mathrm{res}_\beta^{\pm} = \mathrm{res}_{\beta L}^{\pm}. \tag{4.42}$$

It is then an iterative scheme. On a later step, these poles will be used to determine the GE field in section 4.2.1.1.e and also the UTD diffracted field in section 4.3.2.

The generated transversal poles are found similarly.

4.2.1.1.c Propagation of transversal reflected waves

Transversal reflected waves are obtained by the reflection of an incident transversal or longitudinal wave with a mode conversion on the wedge faces. The second line of system (4.11) allows

to find these transversal reflected waves with the relations

$$\Psi_T^{\pm}(\lambda+\varphi) = \pm\left[r_T^L(\lambda)\,\Psi_L^{\pm}(g(\lambda)-\varphi) + r_T^T(\lambda)\,\Psi_T^{\pm}(\lambda-\varphi)\right]. \tag{4.43}$$

Let $\eta_T = \lambda+\varphi$, thus $\lambda = \eta_T - \varphi$ and (4.43) becomes

$$\Psi_T^{\pm}(\eta_T) = \pm\left[r_T^L(\eta_T-\varphi)\,\Psi_L^{\pm}(g(\eta_T-\varphi)-\varphi) + r_T^T(\eta_T-\varphi)\,\Psi_T^{\pm}(\eta_T-2\varphi)\right]. \tag{4.44}$$

Substituting (4.32) in (4.44), we got

$$\Psi_T^{\pm}(\eta_T) = \pm\left[\mathrm{res}_L^{\pm}\frac{r_T^L(\eta_T-\varphi)}{g(\eta_T-\varphi)-(\varphi+\lambda_L)} + \mathrm{res}_T^{\pm}\frac{r_T^T(\eta_T-\varphi)}{\eta_T-(2\varphi+\lambda_T)}\right]. \tag{4.45}$$

The generated transversal poles are then

$$\eta_T = \lambda_{LT} = g^{-1}(\varphi+\lambda_L)+\varphi, \tag{4.46a}$$

$$\eta_T = \lambda_{TT} = 2\varphi+\lambda_T \tag{4.46b}$$

with their respective residues

$$\mathrm{res}_{LT}^{\pm} = \pm\,\mathrm{res}_L^{\pm}\frac{r_T^L(g^{-1}(\varphi+\lambda_L))}{g'(g^{-1}(\varphi+\lambda_L))} \tag{4.47a}$$

$$\mathrm{res}_{TT}^{\pm} = \pm\,\mathrm{res}_T^{\pm}\,r_T^T(\varphi+\lambda_T) = \mp\,\mathrm{res}_T^{\pm}\,R_{TV}^{TV}(\varphi+\lambda_T). \tag{4.47b}$$

Using the relation between r_T^L and r_L^T in (4.40) and (4.15c), (4.47a) simplifies to

$$\mathrm{res}_{LT}^{\pm} = \pm\,\mathrm{res}_L^{\pm}\,r_L^T(g^{-1}(\varphi+\lambda_L)) = \pm\frac{1}{\kappa}\mathrm{res}_L^{\pm}\,R_{TV}^{L}(\varphi+\lambda_L). \tag{4.48}$$

As for the generation of longitudinal poles, having a longitudinal or transversal wave of incidence angle λ_α, $\alpha = L$ or T, on the bottom face of the wedge with a given residue, this incident wave is reflected by the wedge faces and gives rise to transversal reflected waves of angle λ_{TT} if $\alpha = T$ [see Eq. (4.36a)] and λ_{LT} if $\alpha = L$ [see Eq. (4.36b)] with the bottom face of the wedge respectively. The residue of these reflected waves are respectively found using Eqs. (4.47b) and (4.48). These generated transversal poles can also be propagated. They are then considered as initial transversal poles in the form of (4.32) for the pole propagation algorithm. Thus, for the propagation of these generated poles $\lambda_{\beta T}$, initial poles on the form (4.32) are:

$$\lambda_\beta = \lambda_{\beta T} \quad \text{and} \quad \mathrm{res}_\beta^{\pm} = \mathrm{res}_{\beta T}^{\pm}. \tag{4.49}$$

We then observe that the generated poles without mode conversion correspond to a 2φ rotation angle around the origin O [see (4.36a) and (4.46b)]. Note that the residues of the generated poles

in sections 4.2.1.1.b and 4.2.1.1.c can be sum up by the following equations

$$\mathrm{res}^{\pm}_{LL} = \pm R^{L}_{L}(\lambda_L + \varphi)\,\mathrm{res}^{\pm}_{L}, \tag{4.50a}$$
$$\mathrm{res}^{\pm}_{TT} = \mp R^{TV}_{TV}(\lambda_T + \varphi)\,\mathrm{res}^{\pm}_{T}, \tag{4.50b}$$
$$\mathrm{res}^{\pm}_{TL} = \mp \kappa R^{L}_{TV}(\lambda_T + \varphi)\,\mathrm{res}^{\pm}_{T}, \tag{4.50c}$$
$$\mathrm{res}^{\pm}_{LT} = \pm \frac{1}{\kappa} R^{TV}_{L}(\lambda_L + \varphi)\,\mathrm{res}^{\pm}_{L}. \tag{4.50d}$$

The arguments $\varphi \pm \lambda_\alpha$, $\alpha = L$ or T, of the displacement reflection amplitude in (4.50) represent the incident angle on each face of the wedge: see for example Fig. 4.4 for the initial poles $\pm\theta'_{\mathrm{inc}}$. The angle of incidence on the bottom face of the wedge is $\varphi + \theta'_{\mathrm{inc}}$ and the angle of incidence on its upper face is $\varphi - \theta'_{\mathrm{inc}}$. The reflected wave on the upper face of the wedge in red on Fig. 4.4 is incident on the bottom face of the wedge and its incidence angle on this face is $\varphi + (2\varphi - \theta'_{\mathrm{inc}})$. The succession of reflections on each wedge face is well taken into account with this pole propagation.

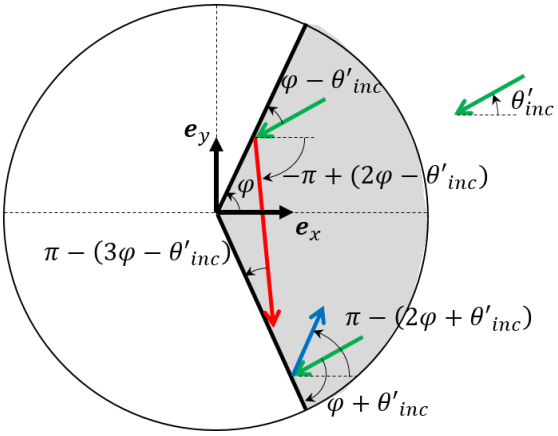

Figure 4.4: Generated reflected waves on the two wedge faces without wave conversion.

For the sake of simplicity, let us denote the j_{th} generated pole of type β by λ^{j}_{β}, $j \in \mathbb{N}^*$. For the incident type $\beta = \alpha$, $\lambda^{1}_{\alpha} = \theta'_{\mathrm{inc}}$ and $\lambda^{2}_{\alpha} = -\theta'_{\mathrm{inc}}$ if $\theta'_{\mathrm{inc}} \neq 0$. Using (4.28) and (4.26), the residue of these initial poles are:

- for $\alpha = L$

$$\mathrm{res}^{+}(\Psi_L, \lambda^{1}_{L}) = \frac{1}{4\pi i}, \tag{4.51a}$$
$$\mathrm{res}^{-}(\Psi_L, \lambda^{1}_{L}) = \frac{1}{4\pi i}, \tag{4.51b}$$

$$\mathrm{res}^{+}(\Psi_L, \lambda_L^2) = \frac{1}{4\pi i}, \tag{4.52a}$$
$$\mathrm{res}^{-}(\Psi_L, \lambda_L^2) = -\frac{1}{4\pi i}, \tag{4.52b}$$

- for $\alpha = T$

$$\mathrm{res}^{+}(\Psi_T, \lambda_T^1) = \frac{1}{4\pi i}, \tag{4.53a}$$
$$\mathrm{res}^{-}(\Psi_T, \lambda_T^1) = \frac{1}{4\pi i}, \tag{4.53b}$$

$$\mathrm{res}^{+}(\Psi_T, \lambda_T^2) = -\frac{1}{4\pi i}, \tag{4.54a}$$
$$\mathrm{res}^{-}(\Psi_T, \lambda_T^2) = \frac{1}{4\pi i}. \tag{4.54b}$$

If $\theta'_{\mathrm{inc}} = 0$, $\lambda_\alpha^1 = \theta'_{\mathrm{inc}} = -\theta'_{\mathrm{inc}} = 0$ and its residue using (4.28) and (4.26) is:

- for $\alpha = L$

$$\mathrm{res}^{+}(\Psi_L, \lambda_L^1) = \frac{1}{2\pi i}, \tag{4.55a}$$
$$\mathrm{res}^{-}(\Psi_L, \lambda_L^1) = 0, \tag{4.55b}$$

- for $\alpha = T$

$$\mathrm{res}^{+}(\Psi_T, \lambda_T^1) = 0, \tag{4.56a}$$
$$\mathrm{res}^{-}(\Psi_T, \lambda_T^1) = \frac{1}{2\pi i}. \tag{4.56b}$$

Due to (4.10), for each j_{th} generated pole of type β, λ_β^j, its opposite $-\lambda_\beta^j$ is also a pole. Each pole $\pm\lambda_\beta^j$ has a symmetric $\mathrm{res}^{+}(\Psi_\beta, \pm\lambda_\beta^j)$ and an antisymmetric $\mathrm{res}^{-}(\Psi_\beta, \pm\lambda_\beta^j)$ residues. The final problem being the sum of the symmetric and antisymmetric problems, the residue of these poles to the Sommerfeld amplitude $\mathrm{res}(\Psi_\beta, \pm\lambda_\beta^j)$ is therefore the sum of their antisymmetric and symmetric residues. Thus, using (4.10), we have

$$\mathrm{res}(\Psi_L, \lambda_L^j) = \mathrm{res}^{+}(\Psi_L, \lambda_L^j) + \mathrm{res}^{-}(\Psi_L, \lambda_L^j), \tag{4.57a}$$
$$\mathrm{res}(\Psi_L, -\lambda_L^j) = \mathrm{res}^{+}(\Psi_L, -\lambda_L^j) - \mathrm{res}^{-}(\Psi_L, -\lambda_L^j), \tag{4.57b}$$
$$\mathrm{res}(\Psi_T, \lambda_T^j) = \mathrm{res}^{+}(\Psi_T, \lambda_T^j) + \mathrm{res}^{-}(\Psi_T, \lambda_T^j), \tag{4.57c}$$
$$\mathrm{res}(\Psi_T, -\lambda_T^j) = -\mathrm{res}^{+}(\Psi_T, -\lambda_T^j) + \mathrm{res}^{-}(\Psi_T, -\lambda_T^j). \tag{4.57d}$$

For this pole propagation algorithm, we need starting points which correspond to initial poles which are $\lambda = \theta'_{\text{inc}}$ and $\lambda = -\theta'_{\text{inc}}$ (see section 4.2.1.1.a). Knowing these initial poles and their corresponding residue given in (4.51) and (4.52) for a longitudinal incident wave and in (4.53) and (4.54) for a transversal incident wave, the reflected longitudinal and transversal poles with their respective residue generated by initial poles can be found using (4.36) and (4.37) in section 4.2.1.1.b and (4.46) and (4.47) in section 4.2.1.1.c. For each generated poles, process defined in sections 4.2.1.1.b and 4.2.1.1.c can be applied. It is then an iterative scheme which has for starting point the initial poles.

An example of application of this SI pole propagation algorithm is provided in section 4.2.1.1.d.

4.2.1.1.d Example of application of the SI pole propagation algorithm

An example of the construction of the reflected poles is shown in Fig. 4.5 in terms of displacement. The proportionality factor (4.23) is taken into account in the residue of the transversal reflected waves with mode conversion and the factor (4.24) is taken into account in the residue of the longitudinal reflected waves with mode conversion.

This example is given only for the symmetric problem with a longitudinal initial pole [see Eq. (4.28)]. The initial starting point in this example is $\lambda_L^1 = \theta'_{\text{inc}} \neq 0$ which is the incidence plane wave on the wedge. Its residue is given by (4.51a).

This incident pole gives rise to a longitudinal reflected pole λ_L^3 defined in (4.36a) and its symmetric residue is calculated with (4.37). Pole $\lambda_L^1 = \theta'_{\text{inc}}$ also gives rise to a reflected transversal pole λ_T^1 defined in (4.46a) and its symmetric residue is calculated with (4.48). This residue is multiplied by κ because it is in term of displacement [see Eq. (4.23)].

This reflected transversal wave also gives rise to reflected transversal and longitudinal waves using (4.46b) and (4.36b) with $\lambda_T = \lambda_T^1$. Their symmetric residue is calculated with (4.47b) and (4.41) respectively with $\text{res}_T^+ = \text{res}_T^+(\lambda_T^1)$. The residue of the pole λ_L^5 is multiplied by the factor $1/\kappa$ because it is in term of displacement [see Eq. (4.24)].

This pole propagation algorithm then allows to find all the poles in the complex λ plane. This procedure could be applied indefinitely. We thus need a condition to stop the iterative scheme.

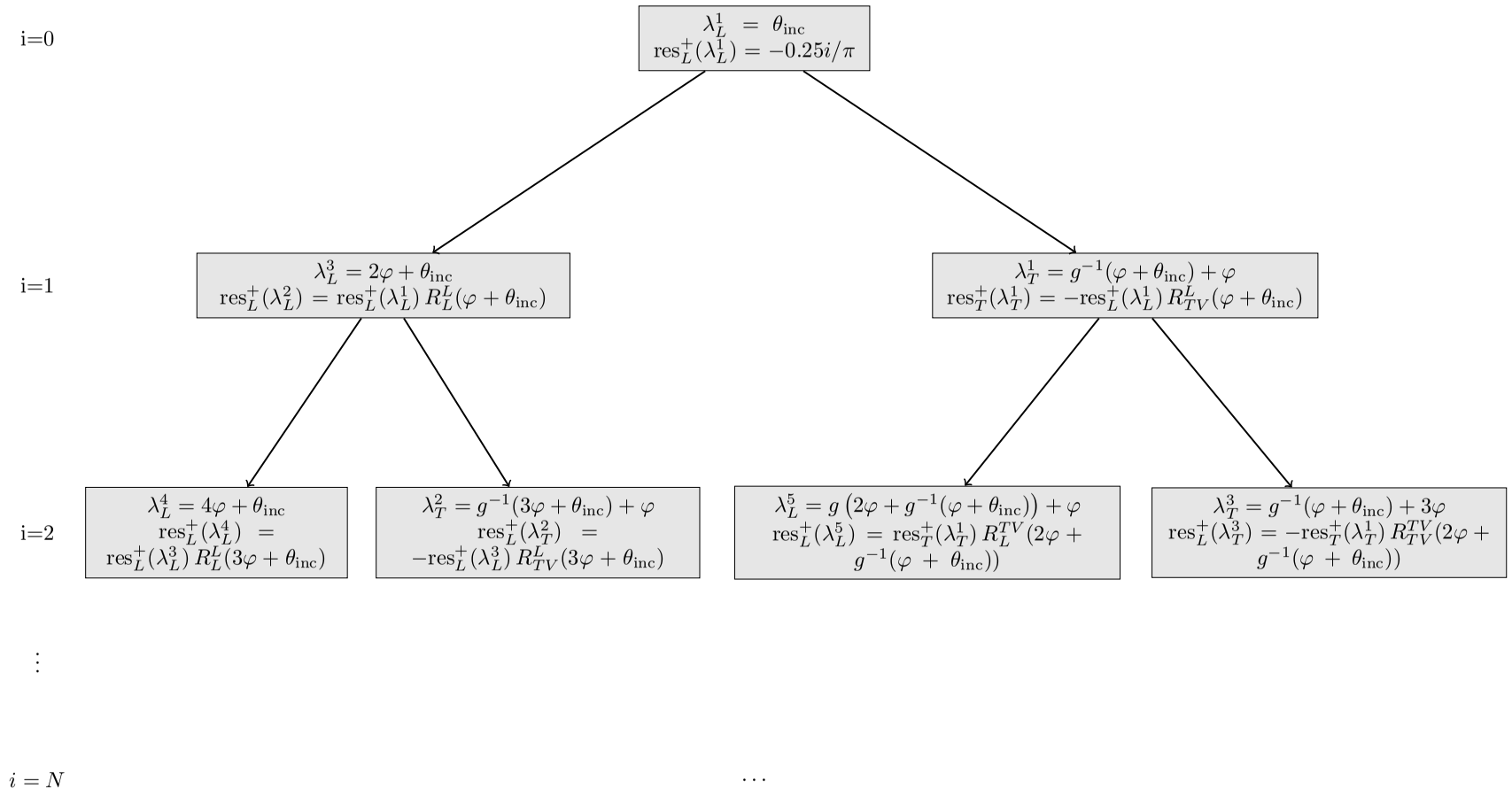

Figure 4.5: Example of application of the pole propagation algorithm in term of displacement.

4.2.1.1.e Stop condition for the iterative scheme

Let us first begin by determining the contribution of these poles for a better comprehension of their physical meaning.

As for the half-plane case (see chapter 2), the Sommerfeld integral (4.9) is approximated using the steepest descent method. To use the steepest descent method, the original contours γ_+ and γ_- of (4.9) are deformed to the steepest descent contours $\mathrm{SDC}_{-\pi}$, SDC_0 and SDC_π (see Fig. 4.3). Indeed, stationary phase points of (4.9) are $\lambda = 0 \pm m\pi, m \in \mathbb{N}$. Babich et al. [17] show that the contour deformations

$$\gamma_+ \rightsquigarrow \mathrm{SDC}_{-\pi} + \mathrm{SDC}_0, \quad \gamma_- \rightsquigarrow \mathrm{SDC}_\pi - \mathrm{SDC}_0 \quad \Rightarrow \quad \gamma_+ + \gamma_- \rightsquigarrow \mathrm{SDC}_{-\pi} + \mathrm{SDC}_\pi \tag{4.58}$$

are possible. The steepest descent contour SDC_0 is thus cancelled during the contour deformation. Poles of the integrand of (4.9)

$$\lambda = \pm\lambda_\beta - \theta', \tag{4.59}$$

λ_β being found using the iterative scheme described in section 4.2.1.1, whose real parts are contained in the strip $\mathrm{Re}(\lambda) \in]-\pi, \pi]$ are crossed during the contour deformation. Their contribution must then be taken into account. Therefore, applying the residue theorem to (4.9), the contributions of poles $\lambda = \pm\lambda_\beta - \theta'$ to the integral (4.9) are

$$\psi_\beta^{\mathrm{GE}}(k_\beta r, \theta') = 2\pi i \,\mathrm{res}(\Psi_\beta, \pm\lambda_\beta)\, e^{-ik_\beta r \cos(\pm\lambda_\beta - \theta')} \quad \text{if} \quad -\pi < \mathrm{Re}(\pm\lambda_\beta - \theta') \leqslant \pi. \tag{4.60}$$

With the pole propagation algorithm in section 4.2.1.1, $\mathrm{Re}(\lambda_\beta) > 0$ since the initial poles $\pm\theta_{\mathrm{inc}}$ are contained in the strip $[-2\varphi, 2\varphi]$. Furthermore, observation points $\theta' \in]0, \pi[$ since this approach is limited to wedge angle less than π (see section 4.2.1.2). These two notes allow to have

$$-\pi < \mathrm{Re}(\lambda_\beta - \theta') \leqslant \pi \quad \Rightarrow \quad \theta' \geqslant \mathrm{Re}(\lambda_\beta) - \pi. \tag{4.61}$$

For the poles $\lambda = \lambda_\beta - \theta'$, Eqs. (4.60) and (4.61) then lead to

$$\psi_\beta^{\mathrm{GE}}(k_\beta r, \theta') = 2\pi i \,\mathrm{res}(\Psi_\beta, \lambda_\beta)\, e^{ik_\beta r \cos((\lambda_\beta - \pi) - \theta')} H(\theta' - (\mathrm{Re}(\lambda_\beta) - \pi)). \tag{4.62}$$

Similarly, the contributions of poles $\lambda = -\lambda_\beta - \theta'$ to (4.9) are

$$\psi_\beta^{\mathrm{GE}}(k_\beta r, \theta') = 2\pi i \,\mathrm{res}(\Psi_\beta, -\lambda_\beta)\, e^{ik_\beta r \cos((\pi - \lambda_{p\beta}) - \theta')} H((\pi - \mathrm{Re}(\lambda_{\mathrm{p}\beta})) - \theta'). \tag{4.63}$$

H(.) is the Heaviside step function and $\mathrm{res}(\Psi_\beta, \lambda_\beta)$ and $\mathrm{res}(\Psi_\beta, -\lambda_\beta)$ are the residues found in (4.57). These contributions correspond to the reflected waves of type β associated to the unit reflected wave vectors $\mathbf{p}_\beta = (-\cos\lambda_\beta, \mp\sin\lambda_\beta)_{(\mathbf{e}_x, \mathbf{e}_y)}$ and making an angle of $\theta'_\beta = \mp(\pi - \lambda_\beta)$ with the wedge bisector. For example, on Fig. 4.4, the reflected wave in red on the upper face of the wedge makes an angle of $-\pi + \lambda_\beta$, $\lambda_\beta = 2\varphi - \theta'_{\mathrm{inc}}$, with the wedge bisector and the reflected

wave in blue on the bottom wedge face makes an angle of $\pi - \lambda_\beta$, $\lambda_\beta = 2\varphi + \theta'_{\text{inc}}$, with the wedge bisector.

In terms of displacement, using (4.19), the longitudinal reflected waves are polarized in the direction

$$\mathbf{d}_L(\theta'_L) = (\cos\theta'_L, \sin\theta'_L)_{(\mathbf{e}_x,\mathbf{e}_y)} \tag{4.64}$$

and according to (4.20), transversal reflected waves are polarized in the direction

$$\mathbf{d}_T(\theta'_T) = (-\sin\theta'_T, \cos\theta'_T)_{(\mathbf{e}_x,\mathbf{e}_y)}. \tag{4.65}$$

Still using (4.19) and (4.20), for the poles $\lambda_\beta - \theta'$ of the integrand in (4.9), the displacement reflected field is then

$$\mathbf{u}_\beta^{\text{GE}}(k_\beta r, \theta') = -2\pi k_\beta \,\text{res}(\Psi_\beta, \lambda_\beta)\, e^{ik_\beta r\cos((\lambda_\beta-\pi)-\theta')} H(\theta' - (\text{Re}(\lambda_\beta) - \pi))\, \mathbf{d}_\beta(\lambda_\beta - \pi) \tag{4.66}$$

and for the poles $-\lambda_\beta - \theta'$, it is

$$\mathbf{u}_\beta^{\text{GE}}(k_\beta r, \theta') = -2\pi k_\beta \,\text{res}(\Psi_\beta, -\lambda_\beta)\, e^{ik_\beta r\cos((\pi-\lambda_\beta)-\theta')} H((\pi - \text{Re}(\lambda_\beta)) - \theta')\, \mathbf{d}_\beta(\pi - \lambda_\beta). \tag{4.67}$$

The multiple reflections of the incident wave are stopped when the generated poles λ_β give rise to outgoing waves of angle $\pm(\pi - \lambda_\beta)$ with the wedge bisector (see Fig. 4.6). These outgoing waves could no longer reach a face of the wedge and therefore they could not be reflected anymore. They correspond thus to shadow boundaries of reflected waves. Indeed, the reflected waves of angle $\pi - \lambda_\beta$ with the wedge bisector are reflected from the bottom face of the wedge and observation points over this shadow boundary, $\theta' > \pi - \lambda_\beta$ are in the shadow region of these reflected waves (see Fig. 4.6). Reflected waves of angle $\lambda_\beta - \pi$ with the wedge bisector are reflected from the upper face of the wedge and observation points below this shadow boundary, $\theta' < \lambda_\beta - \pi$ are in the shadow region of these reflected waves. From Fig. 4.6, Heaviside step functions in the Geometrico-Elastodynamic field [see Eq. (4.66) and Eq. (4.67)] are then found back.

The condition to have an outgoing wave is then

$$|\text{Re}(\lambda_\beta) - \pi| < \varphi. \tag{4.68}$$

It then allows us to find all the poles which lead to multiplied reflected waves in the wedge. This condition of outgoing wave ends the pole propagation algorithm of the Sommerfeld integral. This pole propagation is used in the section 4.3.2 to obtain the UTD diffraction coefficient.

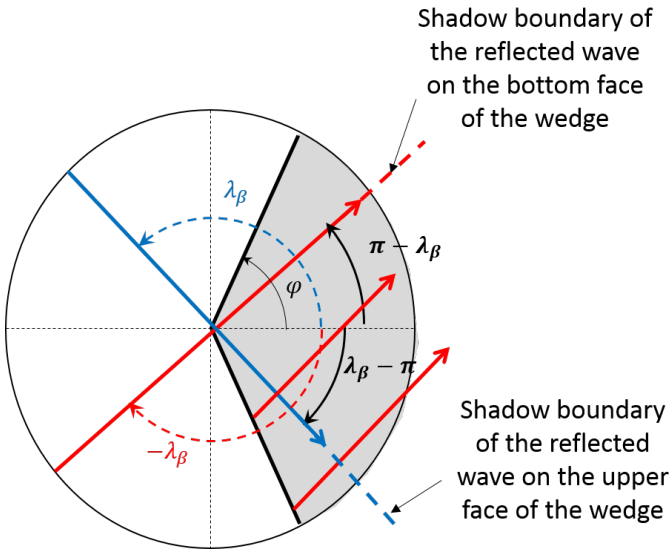

Figure 4.6: Outgoing reflected waves in the solid wedge.

Let us now summarize the different steps stated in [37] for the determination of the GTD diffraction coefficient using the Sommerfeld integral approach.

4.2.1.2 SI GTD diffraction coefficient

To find the Sommerfeld Integral (SI) GTD diffraction coefficients, authors in [37] used the Sommerfeld algorithm of pole propagation in the strip

$$\{\lambda \,/\, |\mathrm{Re}\,\lambda - \pi/2| < \varphi\}. \tag{4.69}$$

They chose this strip because in this strip they could resolved the new system of functional equations that will be introduced in the sequel. After having determined poles in this strip, they separated the unknown Sommerfeld amplitudes into singular $\Psi_\beta^{\pm(\mathrm{sing})}$ and unknown regular terms $\Psi_\beta^{\pm(\mathrm{reg})}$ in the strip (4.69) as

$$\Psi_\beta^{\pm}(\lambda) = \Psi_\beta^{\pm(\mathrm{sing})}(\lambda) + \Psi_\beta^{\pm(\mathrm{reg})}(\lambda) \tag{4.70}$$

where

$$\Psi_\beta^{\pm(\mathrm{sing})}(\lambda) = \sum_j \frac{\mathrm{res}^{\pm}(\pm\lambda_\beta^j)}{2} \cot\left(\frac{\lambda \mp \lambda_\beta^j}{2}\right) \tag{4.71}$$

with λ_β^j being the j_{th} generated pole of type β found using the pole propagation algorithm of the Sommerfeld approach (see section 4.2.1.1), $j \in \{1, 2, \ldots, N_\beta\}$. N_β is the number of poles of

type β contained in the strip (4.69). $\Psi_\beta^{\pm(\mathrm{reg})}$ is an holomorphic function in this strip. Expressions (4.70) are substituted in the systems of functional equations (4.11). In the new systems of two equations, the four unknown parameters are $\Psi_\beta^{\pm(\mathrm{reg})}$ and $c_1^\pm$ which are unknown constants. In the strip (4.69), Kamotski et al. [37] are able to resolve this new system of functional equations. The different steps of resolution of these new systems of functional equations in the strip (4.69) are given in [25, 37]. This system is resolved numerically and then allows to find the Sommerfeld amplitude $\Psi_\beta^{\pm(\mathrm{reg})}(\lambda)$ in the strip (4.69) only for wedge angle less than π ($\varphi < \pi/2$) [37]. To find the Sommerfeld amplitude in all the complex plane, the analytic continuation of systems (4.11) is used [37]. They then have to successfully manage the branch cuts of the g function (4.12) when doing this analytic continuation in the complex plane.

The Sommerfeld amplitudes are then completely determined. The Sommerfeld integrals (4.9) have two saddle points at $\lambda = \pi$ and $\lambda = -\pi$ which give a contribution to the integral as said in section 4.2.1.1.e. An asymptotic evaluation of these Sommerfeld integrals by the steepest descent method (see appendix A.2) leads to the following diffracted elastodynamic potentials

$$\psi_\beta^{(\mathrm{GTD})}(k_\beta r, \theta') = i\sqrt{2i\pi}\left[\Psi_\beta(\theta' - \pi) - \Psi_\beta(\pi + \theta')\right] \frac{e^{ik_\beta r}}{\sqrt{k_\beta r}}, \tag{4.72}$$

where the Sommerfeld amplitude Ψ_β is calculated using its singular and regular parts. In the far-field approximation, the diffracted field in term of displacement is

$$\mathbf{u}^{(\mathrm{GTD})}(r, \theta') = D_L^{\mathrm{SI}}(\theta') \frac{e^{ik_L r}}{\sqrt{k_L r}} \mathbf{e}_{r'} + D_T^{\mathrm{SI}}(\theta') \frac{e^{ik_T r}}{\sqrt{k_T r}} \mathbf{e}_{\theta'} \tag{4.73}$$

where

$$D_\beta^{\mathrm{SI}}(\theta') = -k_\beta\sqrt{2i\pi}\left[\Psi_\beta(\theta' - \pi) - \Psi_\beta(\pi + \theta')\right], \tag{4.74}$$

are the so-called GTD diffraction coefficients and

$$\mathbf{e}_{r'} = (\cos\theta', \sin\theta')_{(\mathbf{e}_x, \mathbf{e}_y)}, \tag{4.75a}$$

$$\mathbf{e}_{\theta'} = (-\sin\theta', \cos\theta')_{(\mathbf{e}_x, \mathbf{e}_y)}. \tag{4.75b}$$

Because of the singular part of the Sommerfeld amplitude [see Eq. (4.71)], these diffraction coefficients diverge at observation directions $\theta' = \pi - \lambda_\beta^j$ and $\theta' = \lambda_\beta^j - \pi$ which are shadow boundaries of reflected waves of type $\beta = L$ or T (see section 4.2.1.1.e). Limits of the GTD diffraction coefficients at these directions are

$$D_\beta^{\mathrm{SI}}(\theta') \approx -k_\beta\sqrt{2i\pi}\,\frac{\mathrm{res}(\Psi_\beta, -\lambda_\beta^j)}{\epsilon}, \quad \text{when } \theta' = \pi - \lambda_\beta^j + \epsilon \tag{4.76a}$$

$$D_\beta^{\mathrm{SI}}(\theta') \approx k_\beta\sqrt{2i\pi}\,\frac{\mathrm{res}(\Psi_\beta, \lambda_\beta^j)}{\epsilon}, \quad \text{when } \theta' = \lambda_\beta^j - \pi + \epsilon \tag{4.76b}$$

where $\epsilon \in \mathbb{R}$ and $|\epsilon| \ll 1$.

In the literature, there exist another method for the scattering of a plane wave from a traction-free wedge, the Laplace transform method [38] also valid for wedge angles less than π, which is described in section 4.2.2.

4.2.2 Laplace transform (LT)

For simplicity in notations in this section, we introduce basis $(\mathbf{e}_1, \mathbf{e}_2)$ with

$$\mathbf{e}_1 = \mathbf{e}_{x_1} \quad \text{and} \quad \mathbf{e}_2 = \mathbf{e}_{y_1} \tag{4.77}$$

and $(\mathbf{e}^{(1)}, \mathbf{e}^{(2)})$ with

$$\mathbf{e}^{(1)} = \mathbf{e}_{x_2} = \cos 2\varphi\, \mathbf{e}_{x_1} + \sin 2\varphi\, \mathbf{e}_{y_1} \quad \text{and} \quad \mathbf{e}^{(2)} = \mathbf{e}_{y_2} = \sin 2\varphi\, \mathbf{e}_{x_1} - \cos 2\varphi\, \mathbf{e}_{y_1}. \tag{4.78}$$

These basis are presented on Fig. 4.7. Cartesian components of any position vector $\mathbf{x}$ in the basis $(\mathbf{e}_1, \mathbf{e}_2)$ is (x_1, x_2). In this section, the basis $(\mathbf{e}_1, \mathbf{e}_2)$ is used. It is then different from the basis $(\mathbf{e}_x, \mathbf{e}_y)$ used in the Sommerfeld approach described in section 4.2.1.

Let us introduced the Fourier transform of an integrable function $f(x_1)$

$$\hat{f}(\xi) = \int_{\mathbb{R}} f(x_1)\, e^{ix_1\xi}\, \mathrm{d}x_1. \tag{4.79}$$

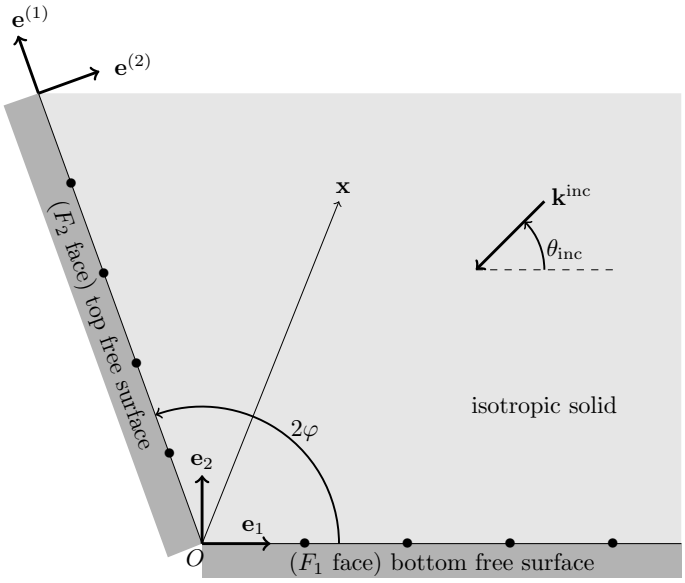

Figure 4.7: The wedge of angle 2φ whose faces are stress-free is illuminated by a plane wave of propagation vector $\mathbf{p}_{\text{inc}}$. Bullets are fictitious points on the wedge faces.

In this approach, the searched quantity is the elastodynamic displacement field of the wave. Gautesen and Fradkin [38] expressed the total displacement field $\mathbf{u}(\mathbf{x}) = (u_1(\mathbf{x}), u_2(\mathbf{x}))_{(\mathbf{e}_1,\mathbf{e}_2)}$ in function of displacement field on the wedge faces (also called trace of the displacement) as

$$H(2\varphi-\theta)u_p(\mathbf{x}) = u_p^{\text{inc}}(\mathbf{x}) - \sum_{i=1}^{2}\int_0^\infty \Big[\sigma_{i2}^{(p)}(x_1-l,x_2)\,u_i(l,0) + \sum_{j=1}^{2}\sum_{m=1}^{2}\sigma_{jm}^{(p)}(x_1-l\cos 2\varphi, x_2-l\sin 2\varphi)\,e_j^{(i)}e_m^{(2)}u^{(i)}(l)\Big]dl, \quad p=1,2. \tag{4.80}$$

Let us detail the different quantities involved in (4.80).

- $H(.)$ is the Heaviside step function.
- $\mathbf{u}(l,0)$ is the displacement field at points $\mathbf{x}_0 = (l,0)_{(\mathbf{e}_1,\mathbf{e}_2)}$ on the bottom face of the wedge.
- $u^{(2)}(l)$ and $u^{(2)}(l)$ are respectively the tangential and normal displacements at points $\mathbf{x}_0 = (l\cos 2\varphi, l\sin 2\varphi)_{(\mathbf{e}_1,\mathbf{e}_2)}$ on the upper face of the wedge, given by

$$u^{(i)}(l) = \mathbf{u}(l\cos 2\varphi, l\sin 2\varphi)\cdot\mathbf{e}^{(i)}, \quad i=1,2. \tag{4.81}$$

- $\sigma_{jm}^{(p)}(\mathbf{x}-\mathbf{x_0})$ are the components of the two-dimensional (2D) free space Green's tress tensor $\sigma^{(p)}(\mathbf{x}-\mathbf{x_0})$ - the stress field produced at $\mathbf{x}$ due to a unit oscillating point force, situated at $\mathbf{x}_0$ and acting along the p-th direction. The expression of the 2D free space Green's tress tensor $\sigma^{(p)}(\mathbf{x}-\mathbf{x_0})$ given in [38] is

$$-4i\sigma_{ij}^{(p)}(\mathbf{x}) = -\frac{2}{\kappa^2}\frac{\partial^3}{\partial x_i\,\partial x_j\,\partial x_p}U_L^{2D} + \left(1-\frac{2}{\kappa^2}\right)\delta_{ij}\frac{\partial}{\partial x_p}U_L^{2D} - \frac{(-1)^p}{\kappa^2}\frac{\partial}{\partial x_{3-p}}\left[(-1)^i\frac{\partial^2}{\partial x_{3-i}\,\partial x_j} + (-1)^j\frac{\partial^2}{\partial x_i\,\partial x_{3-j}}\right]U_T^{2D}, \tag{4.82}$$

where

$$U_L^{2D} = H_0^{(1)}(k_L r) \quad \text{and} \quad U_T^{2D} = H_0^{(1)}(k_T r) \tag{4.83}$$

are the outgoing Hankel functions of order zero which have the divergence of cylindrical waves at infinity:

$$\frac{i}{4}H_0^{(1)}(k_\beta r) \approx \sqrt{\frac{i}{8\pi}}\frac{e^{ik_\beta r}}{\sqrt{k_\beta r}} \quad \text{when} \quad |k_\beta r| \gg 1, \quad \beta = L \text{ or } T. \tag{4.84}$$

The Green function $\sigma^{(p)}$ in (4.80) then propagates a field produced by fictitious points along each face of the wedge into the whole space as in the Kirchhoff Approximation (see section 1.3). Indeed, fictitious points on the bottom face of the wedge are parametrized by

$\mathbf{x}_0 = (l,0)_{(\mathbf{e}_1,\mathbf{e}_2)}$ and by $\mathbf{x}_0 = (l\cos 2\varphi, l\sin 2\varphi)_{(\mathbf{e}_1,\mathbf{e}_2)}$ on the upper face of the wedge (see Fig. 4.7).

To find the total displacement $\mathbf{u}(\mathbf{x})$ whose coordinates are given in (4.80), the displacement field on the upper face $\mathbf{u}(l\cos 2\varphi, l\sin 2\varphi) = (u^{(1)}(l), u^{(2)}(l))_{(\mathbf{e}^{(1)},\mathbf{e}^{(2)})}$ and on the bottom face of the wedge $\mathbf{u}(l,0) = (u_1(l,0), u_2(l,0))_{(\mathbf{e}_1,\mathbf{e}_2)}$ need to be found.

To simplify Eq. (4.80), the problem is also split into symmetric and antisymmetric problems (see the begin of section 4.2) as in the Sommerfeld approach described in section 4.2.1.

In the symmetric problem (see Fig. 4.2), the upper face of the wedge acts like the bottom face of the wedge because the two wedge faces are impacted by two plane waves which have the same incidence angle on each face of the wedge. By example, for a longitudinal incident wave (its propagation vector is the same than its polarization vector) on the wedge faces, the blue polarization vector on the bottom face of the wedge is equivalent to the red polarization vector on its upper face and the red polarization vector on the upper face of the wedge is equivalent to the blue polarization vector on its upper face (see Fig. 4.2a). For the symmetric problem, the displacement field on the upper face of the wedge is thus the same than the one of the bottom face of the wedge.

For the antisymmetric problem, the polarization vectors of the incident waves on the bottom face of the wedge is opposite to the one of the incident waves on the upper face of the wedge (see Fig. 4.2b for a longitudinal incident wave). For the antisymmetric problem, the displacement field on the upper face of the wedge is thus opposite the one of the bottom face of the wedge. Let us use the superscripts " $+$ " for the symmetric problem and " $-$ " for the antisymmetric problem as in the Sommerfeld approach. The symmetric and antisymmetric problems then relate displacement fields on the top (F_2 face) and bottom (F_1 face) free surfaces of the wedge by:

$$u^{(i)\pm}(l) = \pm u_i(l,0), \quad i = 1,2,\ l > 0. \tag{4.85}$$

This procedure then reduces the number of unknown parameters in (4.80) from four to two which are the tangential $u_1(l,0)$ and normal $u_2(l,0)$ displacements on the bottom face of the wedge.

The resolution of the problem by this approach is done only for wedge angle less than π [38]. That restriction leads to simplification in Eq. (4.80) by working only in the region $x_2 < 0$ where the total displacement field [left-hand side of (4.80)] is null. Eq. (4.80) then reduces to

$$\begin{aligned} u_p^{\text{inc}}(\mathbf{x}) = \sum_{i=1}^{2} \int_0^{\infty} \Big[& \sigma_{i2}^{(p)}(x_1 - l, x_2)\, u_i^{\pm}(l,0) \\ & + \sum_{j=1}^{2}\sum_{m=1}^{2} \sigma_{jm}^{(p)}(x_1 - l\cos 2\varphi, x_2 - l\sin 2\varphi)\, e_j^{(i)} e_m^{(2)} u^{(i)}(l) \Big] \mathrm{d}l, \quad p = 1,2 \quad \text{for } x_2 < 0. \end{aligned} \tag{4.86}$$

Knowing that the displacement field can be decomposed into longitudinal displacement $\mathbf{u}_L$ and

transverse displacement $\mathbf{u}_T$,

$$\mathbf{u} = \mathbf{u}_L + \mathbf{u}_T \quad \text{with} \quad \nabla \times \mathbf{u}_L = 0 \quad \text{and} \quad \nabla \cdot \mathbf{u}_T = 0, \tag{4.87}$$

contributions of longitudinal and transversal waves are treated separately by applying a divergence and a curl operators to (4.86). By applying the Fourier transform (4.79) in x_1 to the resulting two equations and limiting observation points further to $x_2 = 0^-$, Gautesen and Fradkin [38] then showed that the unknown parameters $u_i(l,0)$, $i = 1,2$ respect the following system of functional equations:

$$A(\xi) \begin{pmatrix} \hat{u}_1(\xi) \\ \hat{u}_2(\xi) \end{pmatrix} = \begin{pmatrix} f_T(\xi) - \hat{U}_T(\xi) \\ f_L(\xi) - \hat{U}_L(\xi) \end{pmatrix} \tag{4.88}$$

which links the Laplace transform of displacements on the bottom face of the wedge (face 1) $u_i(l,0)$ expressed as

$$\hat{u}_i(\xi) = k_T \int_0^\infty u_i(l,0) e^{ik_T\, l\, \xi}\, dl \tag{4.89}$$

with the rotation $U_T = \nabla \times \mathbf{u}$ and the dilatation $U_L = \nabla \cdot \mathbf{u}$ on the top face being expressed as

$$\hat{U}_T(\xi) = \pm[-a(T_T)\hat{u}_1(T_T) + \bar{b}_T(\xi)\hat{u}_2(T_T)], \tag{4.90a}$$
$$\hat{U}_L(\xi) = \pm[\bar{b}_L(\xi)\hat{u}_1(T_L) + a(T_L)\hat{u}_2(T_L)]. \tag{4.90b}$$

Parameters in (4.90) are defined as

$$a(\xi) = \kappa^2 - 2\xi^2, \tag{4.91}$$
$$b_\beta(\xi) = 2\xi\gamma_\beta(\xi), \tag{4.92}$$
$$T_\beta(\xi) = \xi \cos 2\varphi + \gamma_\beta(\xi) \sin 2\varphi, \tag{4.93}$$
$$\bar{b}_\beta(\xi) = 2\, T_\beta\, \eta_\beta. \tag{4.94}$$

with $\beta = L$ or T, κ being defined in (4.13) and

$$\gamma_\beta(\xi) = \sqrt{\kappa_\beta^2 - \xi^2} \quad \text{with} \quad \kappa_L = 1 \quad \text{and} \quad \kappa_T = \kappa, \tag{4.95a}$$
$$\eta_\beta(\xi) = \xi \sin 2\varphi - \gamma_\beta(\xi) \cos 2\varphi. \tag{4.95b}$$

In (4.88),

$$A(\xi) = \begin{pmatrix} a(\xi) & -b_T(\xi) \\ b_L(\xi) & a(\xi) \end{pmatrix}. \tag{4.96}$$

We also have in (4.88)

$$f_\beta(\xi) = \tag{4.97}$$
$$\begin{cases} \mp 2\pi\kappa^2[\sin\theta_{\text{inc}}\,\delta(\xi-\kappa_\beta\cos\theta_{\text{inc}})\sin(2\varphi-\theta_{\text{inc}})\,\delta(\xi-\kappa_\beta\cos(2\varphi-\theta_{\text{inc}}))] \text{ if } \beta=\alpha \\ 0 \quad \text{else} \end{cases}$$

where α is the type of the incident wave. These functions then present information about incident wave and its symmetric with respect to the wedge bisector. These information are contained in the Dirac delta function of (4.97). These two waves are the poles of the f_β functions because the Dirac delta function can be represented as the sum of two distributions [38]

$$2\pi\delta(\xi-\xi_0) = i\left[\frac{1}{\xi-\xi_0+i0} - \frac{1}{\xi-\xi_0-i0}\right]. \tag{4.98}$$

These initial poles of the symmetric and the antisymmetric problems, incident pole $\xi_\alpha = \kappa_\alpha\cos\theta_{\text{inc}}$ and its symmetric $\xi_\alpha = \kappa_\alpha\cos(2\varphi-\theta_{\text{inc}})$, can therefore be propagated using an iterative scheme as in the Sommerfeld approach obtained from the system of functional equations (4.88).

4.2.2.1 Laplace transform pole propagation

Knowing that the dilatation U_L is related to longitudinal waves and the rotation U_T to transversal waves, for a given initial pole ξ_α with the corresponding symmetric and antisymmetric vector residues $(\text{res}_1^{\alpha(\pm)}, \text{res}_2^{\alpha(\pm)})_{(\mathbf{e}_1,\mathbf{e}_2)}$, the longitudinal $\xi_{\alpha L} = \cos\theta_{\alpha L}$ and transversal $\xi_{\alpha T} = \kappa\cos\theta_{\alpha T}$ generated poles using (4.88) and (4.90) are obtained by the relationship

$$\xi_\alpha = T_L(\xi_{\alpha L}), \tag{4.99a}$$
$$\xi_\alpha = T_T(\xi_{\alpha T}). \tag{4.99b}$$

Equations (4.99) have two solutions given by

$$\xi_{\alpha L,\alpha T} = T_{L,T}(\xi_\alpha) \quad \text{or} \quad \xi_{\alpha L,\alpha T} = T_{L,T}^{-1}(\xi_\alpha) \tag{4.100}$$

where

$$T_\beta^{-1}(\xi) = \xi\cos 2\varphi - \gamma_\beta(\xi)\sin 2\varphi. \tag{4.101}$$

For $\xi = \kappa_\beta\cos\theta$, $\theta\in[0,2\varphi]$, functions $T_\beta(\xi)$ and $T_\beta^{-1}(\xi)$ correspond to a -2φ and 2φ rotation angle around the origin O respectively. It has been shown in the Sommerfeld pole propagation that the generated poles without mode conversion were obtained by a rotation of angle 2φ of the initial pole around the origin O. Consequently, $T_\beta(\xi)$ are extraneous poles. Poles $T_{\alpha L,\alpha T}(\xi_\alpha)$ are then extraneous poles. They are thus removed from the solution [38]. The generated poles

which lead to physical reflected waves are then

$$\xi_{\alpha L,\alpha T} = T_{L,T}^{-1}(\xi_\alpha). \tag{4.102}$$

Let us denote initial longitudinal pole by $\xi_L = \cos\theta_L, \alpha = L$. Using (4.99) and (4.102), the generated longitudinal and transversal poles are then:

$$\xi = T_L^{-1}(\xi_L) = \cos(\theta_L + 2\varphi), \tag{4.103a}$$

$$\xi = T_T^{-1}(\xi_L) = \kappa \cos\left(\arccos\left(\frac{1}{\kappa}\cos\theta_L\right) + 2\varphi\right). \tag{4.103b}$$

Using the notation $\xi = \kappa_\beta \cos\theta$, the reflected angles θ of these generated poles are then

$$\theta_{LL} = \pm(\theta_L + 2\varphi), \tag{4.104a}$$

$$\theta_{LT} = \pm\left(\arccos\left(\frac{1}{\kappa}\cos\theta_L\right) + 2\varphi\right). \tag{4.104b}$$

Using the relation (4.2), these reflected angles correspond to the same than the ones found by the Sommerfeld integral algorithm in the polar frame (r, θ') [see Eq. (4.36a) and (4.46a)]:

$$\theta'_{LL} = \theta'_L + 2\varphi, \tag{4.105a}$$

$$\theta'_{LT} = g^{-1}(\theta'_L + \varphi) + \varphi. \tag{4.105b}$$

The same process is applied for an initial transversal pole and is not reported here. Residues of these generated poles lead to displacement vector amplitudes of the reflected field on a planar surface in the Laplace domain. They are given in appendix A of [38]. In this appendix, the complete iterative scheme of the Laplace transform approach is described.

For simplicity, we use the pole propagation algorithm of SI method described in section 4.2.1.1 for uniform solutions in section 4.3 as it naturally leverages the work already developed in Chapter 2 for the treatment of the half-pane.

The knowledge of all the generated poles allow to decompose the Laplace transform $\hat{\mathbf{u}}$ of the total field as

$$\hat{\mathbf{u}}(\xi) = \hat{\mathbf{u}}^{\text{sing}}(\xi) + \hat{\mathbf{u}}^{\text{reg}}(\xi) \tag{4.106}$$

where the singular part $\hat{\mathbf{u}}^{\text{sing}}$ possess the poles found using the Laplace transform pole propagation algorithm [38] and the regular term $\hat{\mathbf{u}}^{\text{reg}}$ is unknown.

Let us now summarize the different steps stated in [38] for the determination of the GTD diffraction coefficient using the Laplace transform approach.

4.2.2.2 LT GTD diffraction coefficient

To find the LT GTD diffraction coefficient, the regular term $\hat{\mathbf{u}}^{\text{reg}}$ has to be calculated. For that, the Laplace transform of the total field in the functional system of equations (4.88) is substituted by 4.106. The resulting system of functional equations with unknown function $\hat{\mathbf{u}}^{\text{reg}}$ is also resolved numerically [38] as the regular part in the Sommerfeld approach. At the end of the numerical resolution of the regular part, the Laplace transform of the displacement on the bottom wedge face is then known. With the Laplace transform of the displacement on the bottom wedge face being known, it is possible to find the diffracted field in the far-field approximation $k_\beta r \gg 1$. This approximation leads to a simplification in the Hankel function (4.84)

$$\frac{i}{4}H_0^{(1)}\left(k_\beta\sqrt{(x_1-l)^2+x_2^2}\right) \approx \sqrt{\frac{i}{8\pi}}\frac{e^{ik_\beta r}}{\sqrt{k_\beta r}}\,e^{-ik_\beta l\cos\theta}. \tag{4.107}$$

The far-field approximation leads to great simplifications for the calculation of the right term of (4.80) so that the remaining terms in the integrand over the bottom face of the wedge in (4.80) corresponds to the Laplace transform of the displacement on the bottom wedge face.

Additionally, the incident field can be expressed in function of the Dirac delta function. We have

$$e^{-ik_\alpha r\cos(\theta-\theta_{\text{inc}})} = \int_{-\infty}^{+\infty}\delta(\lambda-\theta)\,e^{-ik_\alpha r\cos(\lambda-\theta_{\text{inc}})}\mathrm{d}\lambda. \tag{4.108}$$

The phase stationary point of the left hand side of (4.108) is $\lambda = \theta_{\text{inc}} + \pi$. Approximating this integral with the phase stationary method (explained in appendix A.1) leads to

$$\int_{-\infty}^{+\infty}\delta(\theta-\lambda)\,e^{-ik_\alpha r\cos(\lambda-\theta_{\text{inc}})}\mathrm{d}\lambda \approx \sqrt{\frac{2\pi}{i}}\delta(\theta-\pi-\theta_{\text{inc}})\frac{e^{ik_\alpha r}}{\sqrt{k_\alpha r}}. \tag{4.109}$$

Finally, using (4.107) and (4.109), [38] showed that the GTD diffracted field in the high frequency approximation can be expressed as

$$H(2\varphi-\theta)\mathbf{u}^{(\text{GTD})}(\mathbf{x}) \approx D_L^{\text{LT}}(\theta,\theta_{\text{inc}})\frac{e^{ik_L r}}{\sqrt{k_L r}}\mathbf{e}_r + D_T^{\text{LT}}(\theta,\theta_{\text{inc}})\frac{e^{ik_T r}}{\sqrt{k_T r}}\mathbf{e}_\theta \tag{4.110}$$

where

$$\mathbf{e}_r = (\cos\theta,\sin\theta)_{(\mathbf{e}_1,\mathbf{e}_2)}, \tag{4.111a}$$

$$\mathbf{e}_\theta = (-\sin\theta,\cos\theta)_{(\mathbf{e}_1,\mathbf{e}_2)}, \tag{4.111b}$$

with the LT (Laplace transform) diffraction coefficients for the symmetric and antisymmetric

problem $D_\beta^{\mathrm{LT}(\pm)}$ are:

$$\begin{aligned}\sqrt{8\pi i}D_L^{\mathrm{LT}(\pm)}(\theta,\theta_{\mathrm{inc}}) &= 2\pi\kappa^2 D_L^{\mathrm{LT\,(inc)}} \\ &+ \sin 2\theta\,\hat{u}_1(-\cos\theta) + (\kappa^2 - 2\cos^2\theta)\,\hat{u}_2(-\cos\theta) \\ &\mp [\sin 2(2\varphi-\theta)\,\hat{u}_1(-\cos(2\varphi-\theta)) + (\kappa^2 - 2\cos^2(2\varphi-\theta))\,\hat{u}_2(-\cos(2\varphi-\theta))],\end{aligned} \tag{4.112a}$$

$$\begin{aligned}\sqrt{8\pi i}D_T^{\mathrm{LT}(\pm)}(\theta,\theta_{\mathrm{inc}}) &= 2\pi D_T^{\mathrm{LT\,(inc)}} \\ &+ \kappa\,[\cos 2\theta\,\hat{u}_1(-\kappa\cos\theta) + \sin 2\theta\,\hat{u}_2(-\kappa\cos\theta)] \\ &\pm \kappa[\cos 2(2\varphi-\theta)\,\hat{u}_1(-\kappa\cos(2\varphi-\theta)) + \sin 2(2\varphi-\theta)\,\hat{u}_2(-\kappa\cos(2\varphi-\theta))]\end{aligned} \tag{4.112b}$$

where

$$D_\beta^{\mathrm{LT\,(inc)}} = \begin{cases}\delta(\theta-\pi-\theta_{\mathrm{inc}}) \pm \delta(\theta-\pi-2\varphi+\theta_{\mathrm{inc}}) & \text{if} \quad \alpha=\beta \\ 0 \quad \text{else.}\end{cases} \tag{4.113}$$

The Laplace transform displacement having singular terms, these diffraction coefficient diverge at some observation directions. These directions are shadow boundaries of the geometrical field as in the Sommerfeld approach.

In the LT approach, the total displacement is not expressed in function of a Sommerfeld integral which is classically met for diffraction problems encountered in electromagnetism, acoustics and elastodynamics. The far-field asymptotic approximation is found thanks to the asymptotic of the Hankel function. However, comparisons with published Sommerfeld and experimental results [80] show good agreements for two wedge angles, $80°$ and $100°$. These comparisons are shown in appendix D. These two approaches of resolution lead to GTD solution at high frequency which diverges at reflected shadow boundaries.

4.3 Scattering of a plane wave by an elastic wedge : uniform asymptotics

At high frequency approximation, the scattering of a plane wave by an elastic wedge leads to the GTD solution for the diffracted field and to geometrico-elastodynamic field. The GTD solution diverges near and at specular directions because the approximation method used, the steepest descent method (for the Sommerfeld approach), does not handle the interference of incident/reflected and diffracted waves. It is therefore important to use a uniform approximation method such as the Van Der Waerden or the Pauli-Clemmow methods to manage such a phenomenon. These methods have already been applied in the half-plane case for which the scattered solution is expressed in the form of a Sommerfeld integral (see chapter 2). For an elastic wedge, the GTD diffraction can be derived using two different methods: the Sommerfeld integral

(SI) [described in section 4.2.1] and the Laplace transform (LT) [described in section 4.2.2]. The Laplace transform (LT) method, code belonging to CEA, does not involve a Sommerfeld integral but according to some numerical experiments (see appendix D) it gives results close to the ones of the Sommerfeld integral (SI) method. Furthermore, the LT GTD diffraction coefficients diverge at the shadow boundaries of the incident or reflected field as the SI GTD diffraction coefficients. Therefore, uniformisation process applied to the SI solution can also been applied to the LT solution. Indeed, UAT (Uniform Asymptotic Theory of Diffraction) principles, obtained with the Van Der Waerden approximation method of the Sommerfeld integral, were applied to the LT results by Fradkin et al. [81] and lead to uniform results of the total field. In this section, the UAT [81] for the scattering of a plane wave from a wedge is recalled in section 4.3.1. It is follow by the development of the UTD solution using the Pauli-Clemmow procedure in section 4.3.2.

4.3.1 Uniform Asymptotic Theory of Diffraction (UAT)

As seen previously in section 1.4.2, UAT consists in modifying the geometrico-elastocynamics field without modifying the diffracted field. The Heaviside functions in the GE field [see Eq. (4.62)] are then replaced by a sum of Fresnel function $\overline{F}$ (1.15) and an $\widehat{\overline{F}}$ function defined in (1.16) in chapter 1. Displacement UAT total field for the wedge is then expressed as [81] (see appendix A.4.2):

$$\mathbf{u}^{\mathrm{tot(UAT)}}(\mathbf{x}) = \sum_{\beta}\left(\sum_{j}\left[\overline{F}(\xi_\beta^j) - \widehat{\overline{F}}(\xi_\beta^j)\right]\,\mathbf{u}_\beta^{\mathrm{geo}(j)} + \sum_{j}\left[\overline{F}(\xi_\beta^{-j}) - \widehat{\overline{F}}(\xi_\beta^{-j})\right]\,\mathbf{u}_\beta^{\mathrm{geo}(-j)}\right) + \mathbf{u}^{(\mathrm{GTD})}(\mathbf{x}). \tag{4.114}$$

In this expression of the total UAT field, $\beta = L$ or T is the type of the scattered wave, j is the index of the generated pole λ_β^j associated to corresponding pole $-\lambda_\beta^j$ using the Sommerfeld algorithm of pole propagation. $\mathbf{u}_\beta^{\mathrm{geo}(j)}$ and $\mathbf{u}_\beta^{\mathrm{geo}(-j)}$ are the incident/reflected field defined as using (4.66) and (4.67):

$$\mathbf{u}_\beta^{\mathrm{geo}(j)} = -2\pi k_\beta \,\mathrm{res}(\Psi_\beta, \lambda_\beta^j)\, e^{ik_\beta r\cos((\lambda_\beta^j-\pi)-\theta')}\,\mathbf{d}_\beta(\lambda_\beta^j-\pi), \tag{4.115a}$$

$$\mathbf{u}_\beta^{\mathrm{geo}(-j)} = -2\pi k_\beta \,\mathrm{res}(\Psi_\beta, -\lambda_\beta^j)\, e^{ik_\beta r\cos((\pi-\lambda_\beta^j)-\theta')}\,\mathbf{d}_\beta(\pi-\lambda_L^j). \tag{4.115b}$$

The detour parameters ξ_β^j and ξ_β^{-j} are defined as

$$\xi_\beta^j = -\mathrm{sgn}(\theta' - (\lambda_\beta^j - \pi))\sqrt{2k_\beta r\cos^2\left(\frac{\lambda_\beta^j-\theta'}{2}\right)} \tag{4.116a}$$

$$\xi_\beta^{-j} = -\mathrm{sgn}((\pi - \lambda_\beta^j) - \theta')\sqrt{2k_\beta r\cos^2\left(\frac{\lambda_\beta^j-\theta'}{2}\right)}. \tag{4.116b}$$

As seen in section 1.4.2, the Fresnel function smooths the GE field whereas the $\widehat{\widehat{F}}$ function introduces a divergence at shadow boundaries. Indeed, near the shadow boundaries $\lambda_\beta^j - \pi$, $\theta' = \lambda_\beta^j - \pi + \epsilon$ ($\epsilon \in \mathbb{R}$ and $|\epsilon| \ll 1$) and the term $\widehat{\widehat{F}}(\xi_\beta^j)\, \mathbf{u}_\beta^{\mathrm{geo}(j)}$ of (4.114) at the leading order $(k_\beta r)^{-1/2}$ is

$$-\widehat{\widehat{F}}(\xi_\beta^j)\, \mathbf{u}_\beta^{\mathrm{geo}(j)} \approx -k_\beta \sqrt{2i\pi}\, \frac{\mathrm{res}(\Psi_\beta, \lambda_\beta^j)}{\epsilon}\, \frac{e^{ik_\beta r}}{\sqrt{k_\beta r}}\, \mathbf{d}_\beta(\lambda_\beta^j - \pi) \tag{4.117}$$

and near the shadow boundaries $\pi - \lambda_\beta^j$, $\theta' = \pi - \lambda_\beta^j + \epsilon$,

$$-\widehat{\widehat{F}}(\xi_\beta^{-j})\, \mathbf{u}_\beta^{\mathrm{geo}(-j)} \approx k_\beta \sqrt{2i\pi}\, \frac{\mathrm{res}(\Psi_\beta, -\lambda_\beta^j)}{\epsilon}\, \frac{e^{ik_\beta r}}{\sqrt{k_\beta r}}\, \mathbf{d}_\beta(\pi - \lambda_\beta^j). \tag{4.118}$$

The divergence introduces by the function $\widehat{\widehat{F}}$ is thus opposite to the GTD divergence [compare (4.117) to (4.76a) and (4.118) to (4.76b)]. GTD divergence at shadow boundaries is then suppressed and the remaining field is therefore continuous.

UAT then permits to have a uniform field but as said in section 1.4.2, in NDT configurations, it requires to build fictitious reflected rays coming from pencils radiated by points on the emitter transducer. Its implementation is then complicated. There exists another uniform theory of diffraction, the Uniform Theory of Diffraction, UTD which is amenable to simple implementation. In chapter 1, UTD has been developed for a simple canonical geometry, a half-plane, to show its feasibility. In the following, it is derived for a more complex canonical geometry, a 2D wedge whose faces are stress-free.

4.3.2 Uniform Theory of Diffraction (UTD)

UTD is generally preferred to UAT in numerical physical fields because it does not alter the geometrical field to render the total field uniform. In our case, that means that the specular model of CIVA (see section 1.2), based on ray pencils and modelling the geometrical field, is kept untouched. UTD only modifies the amplitude of diffracted rays using a transition function as in the half-plane case. UTD formulation then needs to be established in the wedge case for elastodynamics.In that purpose, the Sommerfeld formulation (4.9) is used as a start point since the Pauli-Clemmow approximation can be applied to this kind of integrals (see section A.3).

During the deformation of the Sommerfeld contours γ_+ and γ_- into the steepest descent contours $SDC_{-\pi}$ and SDC_π (see Fig. 4.3), many integrand poles $\pm(\lambda_\beta^j - \theta')$ of the integral (4.8) may be crossed as explained in section 4.2.1.1.e. It then differs of the half-plane case for which there was only one pole crossed during the contour deformation. Here, the Pauli-Clemmow approximation which deals with many coalescing simple poles and a stationary phase point is used (see appendix

A.3.2). Applying this Pauli-Clemmow procedure then leads to the following expression

$$\mathbf{u}^{\mathrm{tot(UTD)}}(\mathbf{x}) = \mathbf{u}^{\mathrm{GE}}(\mathbf{x}) + \sum_{\beta} \mathbf{u}_{\beta}^{(\mathrm{UTD})}(\mathbf{x}) \tag{4.119}$$

where the geometrico-elastodynamic field is defined as

$$\mathbf{u}^{(\mathrm{GE})}(\mathbf{x}) = \mathbf{u}^{\mathrm{inc}}(\mathbf{x}) + \sum_{\beta} \left(\mathbf{u}_{\beta}^{\mathrm{GE}(j)}(\mathbf{x}) + \mathbf{u}_{\beta}^{\mathrm{GE}(-j)}(\mathbf{x}) \right), \tag{4.120}$$

$\mathbf{u}_{\beta}^{\mathrm{GE}(j)}$ and $\mathbf{u}_{\beta}^{\mathrm{GE}(-j)}$ being defined in (4.115). Using Eq. (4.73), the GTD diffracted field can be split into two contributions, one for the longitudinal diffracted waves and a second for the transversal diffracted waves. The UTD diffracted field is then also constituted of two contributions expressed as [see Eq. A.50]

$$\mathbf{u}_{\beta}^{(\mathrm{UTD})}(\mathbf{x}) = (-1)^{M_\beta+1}\, \mathbf{u}_{\beta}^{(\mathrm{GTD})}(\mathbf{x}) \left(\sum_{j=1}^{M_\beta} F(\zeta\, a_{\beta}^{j}) \prod_{\substack{k=1 \\ k\neq j}}^{M_\beta} \frac{s_{\beta}^{k}}{(s_{\beta}^{j} - s_{\beta}^{k})} \right) \tag{4.121}$$

where

$$a_{\beta}^{j} = -i(s_{\beta}^{j})^2 = 2\cos^2\left(\frac{\lambda_{\beta}^{j} - \theta'}{2} \right) \tag{4.122}$$

allows to determine the proximity of a pole $\pm(\lambda_{\beta}^{j} - \theta')$ of the Sommerfeld integral (4.8) to the stationary phase point of the integral (4.9), $\pm\pi$. This proximity means that the observation point is near of a incident/reflected shadow boundary, $\theta' = \pm(\pi - \lambda_{\beta}^{j})$. $F()$ in (4.121) is the transition function defined in (2.44) in chapter 2. $\zeta = k_\beta r$ is the far-field parameter. M_β is the total number of the integrand poles $\pm(\lambda_{\beta}^{j} - \theta')$ of the Sommerfeld integral (4.8) which give rise to outgoing waves. The poles crossed during the contour deformation are the ones which contribute to the geometrical field. The real part of these poles are contained in the strip $]-\pi, \pi]$ as ssaid just before in section 4.2.1.1.e.

As for the half-plane, far away from all the shadow boundaries, $\pm(\lambda_{\beta}^{j} - \theta') \neq \pm\pi$, the argument of the transition function is large and therefore $F \to 1$ as seen on figure (2.8) in chapter 2. In that case, it can be seen that the remaining term

$$(-1)^{M_\beta+1} \left(\sum_{j=1}^{M_\beta} \prod_{\substack{k=1 \\ k\neq j}}^{M_\beta} \frac{s_{\beta}^{k}}{(s_{\beta}^{j} - s_{\beta}^{k})} \right) = 1. \tag{4.123}$$

Far away from all shadow boundaries, UTD solution then gives back GTD solution. Near a

shadow boundary,

$$\pm(\lambda_\beta^j - \theta') \to \pm\pi \quad \Longleftrightarrow \quad s_\beta^j \to 0 \quad \text{and therefore} \quad \mathbf{u}_\beta^{(\mathrm{UTD})} \to \mathbf{u}_\beta^{(\mathrm{GTD})} F(\zeta\, a_\beta^j). \tag{4.124}$$

Near the shadow boundaries, using (4.124), (4.73), (4.76) and (2.51),

$$\mathbf{u}_\beta^{(\mathrm{UTD})} \approx \begin{cases} \pi k_\beta \operatorname{sgn}\epsilon \operatorname{res}(\Psi_\beta, \lambda_\beta^j)\, e^{ik_\beta r}\, \mathbf{d}_\beta(\lambda_\beta^j - \pi) & \text{for} \quad \theta' = \lambda_\beta^j - \pi + \epsilon \\ -\pi k_\beta \operatorname{sgn}\epsilon \operatorname{res}(\Psi_\beta, -\lambda_\beta^j)\, e^{ik_\beta r}\, \mathbf{d}_\beta(\pi - \lambda_\beta^j) & \text{for} \quad \theta' = \pi - \lambda_\beta^j + \epsilon \end{cases}. \tag{4.125}$$

The UTD diffracted field is then discontinuous when crossing shadow boundaries. Expressing the Heaviside step function in the geometrico-elastodynamic fields (4.66) and (4.67) as (2.58), these reflected fields can be written as

$$\mathbf{u}_\beta^{\mathrm{ref}} \approx \begin{cases} -\pi k_\beta \operatorname{res}(\Psi_\beta, \lambda_\beta^j)\, e^{ik_\beta r}\, (1 + \operatorname{sgn}\epsilon)\, \mathbf{d}_\beta(\lambda_\beta^j - \pi) & \text{for } \theta' = \lambda_\beta^j - \pi + \epsilon \\ -\pi k_\beta \operatorname{res}(\Psi_\beta, -\lambda_\beta^j)\, e^{ik_\beta r}\, (1 - \operatorname{sgn}\epsilon)\, \mathbf{d}_\beta(\pi - \lambda_\beta^j) & \text{for } \theta' = \pi - \lambda_\beta^j + \epsilon \end{cases}. \tag{4.126}$$

The discontinuities of the reflected field is thus opposite to the ones of the UTD diffracted field. As a consequence of this, UTD total field (4.119) is then continuous.

UTD and UAT (see section 4.3.1) giving continuous results, numerical comparisons are done in section 4.4 between these two uniform corrections for a plane wave scattering by a solid wedge. This comparison is done because as shown in appendix A, sections A.3 and A.4, UAT is more precise than UTD since it includes all terms of order $\zeta^{-1/2}$, $\zeta = k_\beta r$ being the far-field parameter.

4.4 Numerical Results

4.4.1 Comparison between UAT and UTD

To compare UAT and UTD, observation points are chosen to be equidistant to the wedge edge. They are thus along the arc of angle 2φ and at a distance $r = n\lambda_{0(\alpha)}$, $n \in \mathbb{N}$ (see the dashed arc on Fig. 4.8). 2φ is the wedge angle and $\lambda_{0(\alpha)}$ is the wavelength of the incident wave in the medium. The orthonormal frame $(O; \mathbf{e}_{x_1}, \mathbf{e}_{y_1})$ is used in this section. The polar coordinates of observation points are then (r, θ), with θ being the angle between the bottom face of the wedge and the observation direction (see Fig. 4.8). The wedge is constituted of isotropic ferritic steel with Poisson's ratio $\nu = 0.29$, longitudinal velocity $c_L = 5900$ m.s^{-1} and transversal velocity $c_T = 3230$ m.s^{-1}. Below, the subscript r is used for "reflected", the term res refers to the displacement amplitude of a studied plane wave, the subscript of res indicates the different

modes which allow the generation of this plane wave for instance res_{LL} is the amplitude of the L wave reflected by one wedge face after that this face was impacted by a L wave. θ_{inc_1} refers to the angle between the incident plane wave and the bottom face F_1 of the wedge and θ_{inc_2} the angle between the incident plane wave and the upper face F_2 of the wedge (see Fig. 4.8).

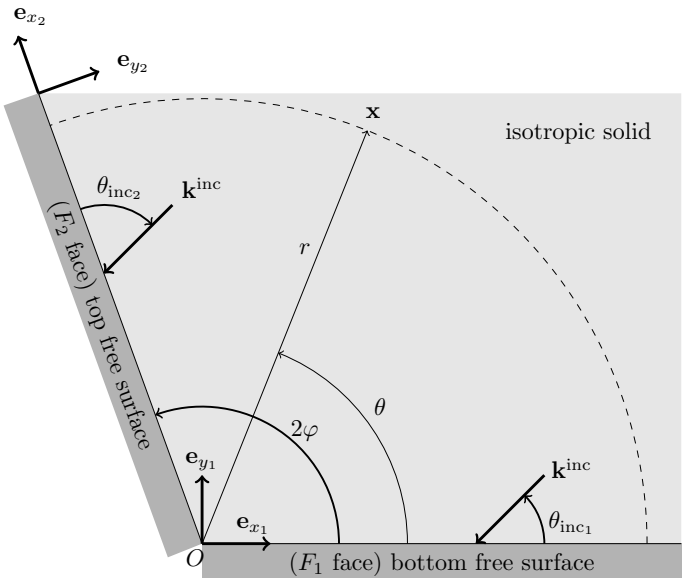

Figure 4.8: The wedge of angle 2φ whose faces are stress-free is illuminated by a plane wave of propagation vector $\mathbf{k}^{\mathrm{inc}}$. Observation points are along the dashed arc of angle 2φ.

The first case under consideration is a solid wedge of angle $110°$ irradiated by a longitudinal plane wave making an angle of $90°$ with the bottom face F_1 of the wedge. The incident is thus characterized by $\theta_{\mathrm{inc}_1} = 90°$ and $\theta_{\mathrm{inc}_2} = 20°$. This case is represented on Fig. 4.9. The different reflections on the wedge faces are presented on Fig. 4.9a. The incident longitudinal plane wave and its reflections without mode conversion are represented in red and when mode conversion occurs, the reflected transversal plane waves on the bottom face of the wedge are in green and those reflected on the upper wedge face are in blue. In general, when no mode conversion occurs, the same color is used for the incident and the reflected waves. Fig. 4.9a also specifies the displacement amplitude of the reflected planes waves for a unit incident displacement amplitude. This case then presents 4 shadow boundaries :

1. shadow boundary of the LTT transversal reflected waves at $\theta \approx 11°$. For $\theta > 11°$, these reflected waves do no more exist. We then have a Heaviside step function across $\theta \approx 11°$,
2. shadow boundary of the LLL longitudinal reflected waves at $\theta \approx 50°$,
3. shadow boundary of the LLT transversal reflected waves at $\theta \approx 69°$,
4. shadow boundary of the LL longitudinal reflected waves at $\theta \approx 90°$.

The shadow boundaries are well discernible on Fig. 4.9b which represents the wave fronts of the scattered waves simulated using the finite differences software Simsonic [82] in 2D. This software was used because the user has a large control on the simulation parameters (mesh of the geometry, boundary conditions, input signal, outputs). The plotted quantity is the displacement velocity of the waves in the solid. This snapshot has been chosen at a propagation time where all the scattered waves can be distinguished. The direction of the outgoing reflected waves respects the same code color as the one used on Fig. 4.9a. The four outgoing reflected waves then interfere with the diffracted waves in regions delineate by yellow ellipses on Fig. 4.9b. As the configuration is 2D, the diffracted waves are cylindrical and their wave front is therefore an arc in the plane of observation. Longitudinal diffracted cylindrical wave interferes with the reflected longitudinal waves $rL\,90^\circ$ and $rL\,50^\circ$. The second cylindrical wave front corresponds to the transversal diffracted wave which interferes locally with $rT\,69^\circ$ and $rT\,11^\circ$. The diffracted L wave front is in phase advance with respect to the T one since longitudinal waves are faster than transversal ones. Before the interference with these reflected and diffracted waves, these reflected waves do not exist. That's why the half-lines starting from the wedge edge and along directions $\theta = 11^\circ, 50^\circ, 69^\circ$ and 90° are shadow boundaries of reflected rays. The displacement total fields for different observation points at $r = 8\lambda_{0(L)}$ are represented on Fig. D.1a using GTD, UAT [see Eq. (4.114)] and UTD [see Eqs. (4.119) and (4.121)] formulations. GTD total field diverges at shadow boundaries whereas UAT and UTD are continuous at these shadow boundaries. The absolute error between UAT and UTD displacement total fields presented in Fig. D.1b shows that the error between UAT and UTD is decreasing in far-field and is more important near shadow boundaries where some pics are observed. Far away from shadow boundaries, UAT and UTD tend towards GTD solution and the error between these two uniform GTD approximations is therefore very low.

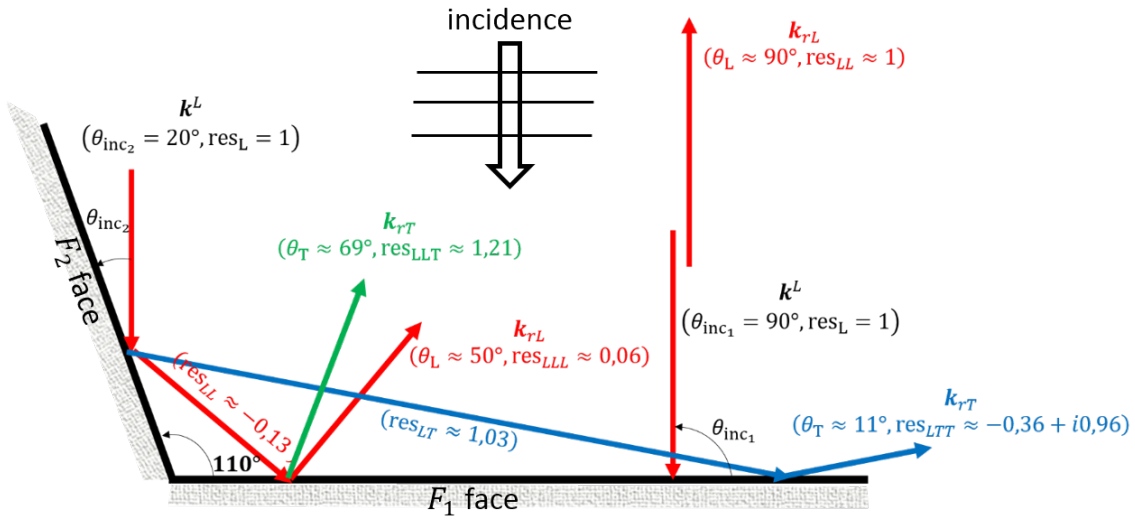

(a) Different reflections on the wedge faces

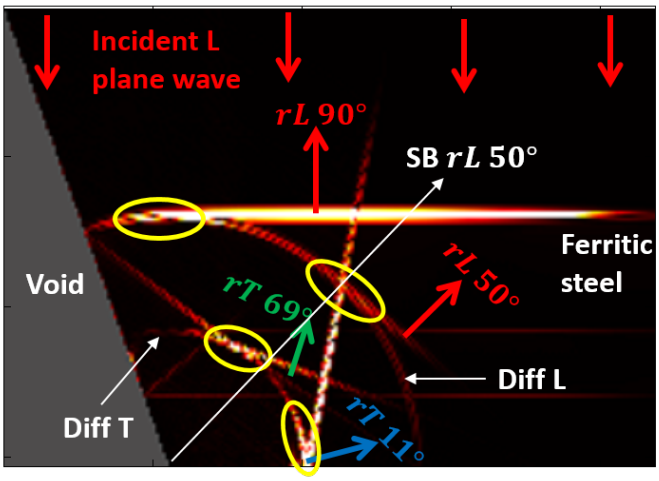

(b) Snapshot of the scattered wave fronts obtained with the software Simsonic [82]. "SB" = Shadow boundary and "Diff β" is the diffracted wave of type β

Figure 4.9: Scattering of a longitudinal plane wave by a wedge of angle 110° at interfaces solid/void.

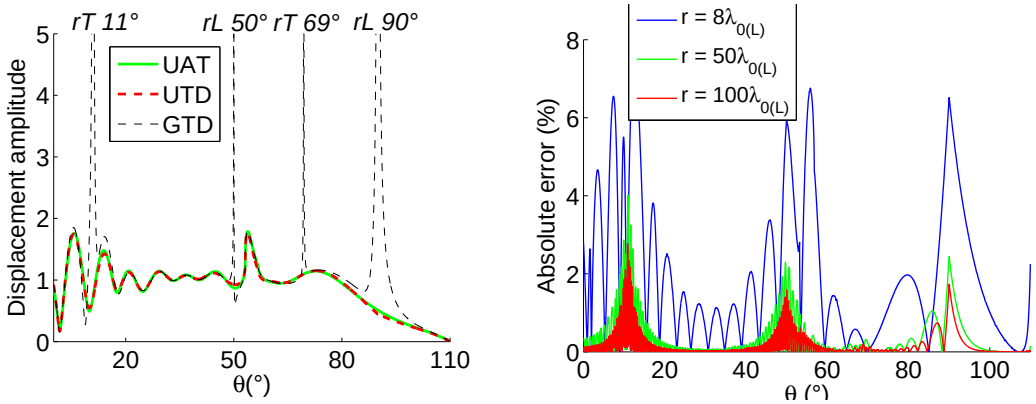

(a) Displacement total field amplitude at $r = 8\lambda_{0(L)}$ predicted by different models: GTD, UAT and UTD

(b) Absolute error between UAT and UTD displacement total fields in percent of the incident amplitude at different observation distances

Figure 4.10: Scattering of a longitudinal plane wave of incidence angle $\theta_{\text{inc}_1} = 90°$ by a free-stress wedge of angle 110°. Displacement total fields are normalized by the incident amplitude.

Other configurations have been tested to compare UAT and UTD.

- A wedge of angle 80° irradiated by a transversal plane wave with an incidence angle $\theta_{\text{inc}_1} = 50°$ on the bottom face of the wedge. The different reflections that occur in the wedge are represented on Fig. 4.11a. This case leads to three reflected shadow boundaries: the transversal reflected shadow boundary (TTT) at $\theta_T = 30°$, the longitudinal reflected shadow boundary (TTL) at $\theta_L \approx 51°$ and the transversal reflected shadow boundary (TTT) at $\theta_T = 70°$. The displacement total fields for different observation points at $r = 8\lambda_{(0)T}$ are represented on Fig. 4.11b using GTD, UAT and UTD formulations. GTD total field diverges at shadow boundaries whereas UAT and UTD are continuous at these shadow boundaries and lead to close results as in the previous case.

- A wedge of angle 110° irradiated by a transversal plane wave with an incidence angle $\theta_{\text{inc}_1} = 55°$ on the bottom face of the wedge. This problem is symmetric because the incidence angle (half of the wedge angle) on the bottom face of the wedge is the same than the incidence angle on its upper face. Fig. 4.12a then show the different reflections that occur in the wedge only for an incident plane wave on the bottom face of the wedge. On this figure we have three reflected shadow boundaries: one longitudinal at $\theta \approx 95°$ and two transversal at $\theta \approx 52°$ and 108°. With the symmetry of the problem, an incidence longitudinal plane wave on the upper face of the wedge also induces three shadow boundaries. That's why the GTD total field presented on Fig. 4.12b diverges at six directions of observation. Near and at these the six reflected shadow boundaries, UAT and UTD total fields are continuous as expected. Near the shadow boundaries $\theta_T = 108°$ and $\theta_T = 2°$

close to the wedge faces ($\theta = 110°$ on F_2 face and $\theta = 0°$ on F_1 face) the discrepancies between UAT and UTD increase.

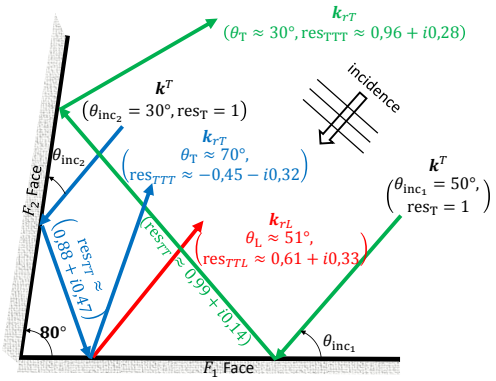

(a) Different reflections on the wedge faces

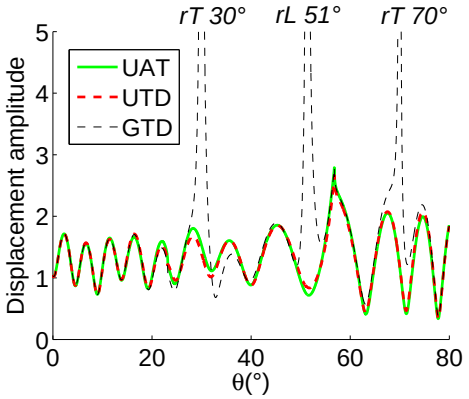

(b) Displacement total field amplitude at $r = 8\lambda_0$ predicted by different models: GTD, UAT and UTD

Figure 4.11: Scattering of a transversal plane wave of incidence angle $\theta_{\text{inc}_1} = 50°$ by a free-stress wedge of angle $80°$. Displacement total fields are normalized by the incident amplitude.

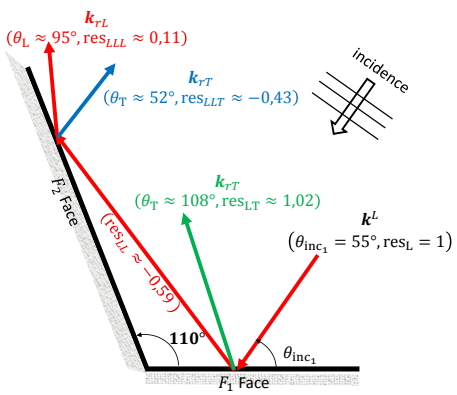

(a) Different reflections on the wedge faces

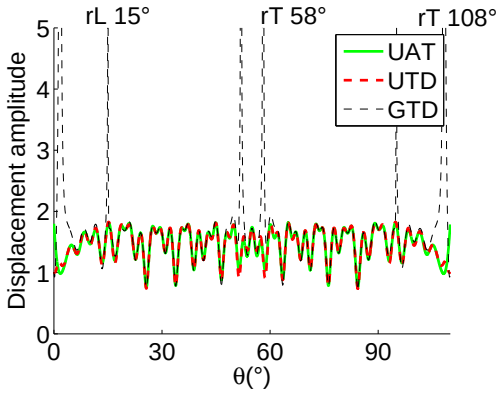

(b) Displacement total field amplitude at $r = 8\lambda_{0(L)}$ predicted by different models: GTD, UAT and UTD

Figure 4.12: Scattering of a longitudinal plane wave of incidence angle $\theta_{\text{inc}_1} = 55°$ by a free-stress wedge of angle $110°$. Displacement total fields are normalized by the incident amplitude.

During these numerical tests, the case of a solid free-stress wedge of angle $90°$ irradiated by a longitudinal plane wave making an angle of $45°$ with the wedge faces has also been studied. It is a particular case where two reflected waves have the same shadow boundary. The different

reflected waves are pictured on Fig. 4.13. On this figure, the transversal reflected wave on the upper face of the wedge in blue (see Fig. 4.13a) is at the same angle $\theta_T \approx 23°$ than the transversal reflected wave always in blue on the bottom face of the wedge (see Fig. 4.13b). These reflected transversal waves have different residues and consequently displacement amplitudes since they correspond to different modes (LLT on Fig. 4.13a and LTT on Fig. 4.13b). It is also the case for the shadow boundary of the transversal reflected waves in green (modes LLT on Fig. 4.13a and LTT on Fig. 4.13b) on each face of the wedge. These waves have different residues and share the same shadow boundary. In this configuration, $\theta = 23°$ and $\theta = 67°$ are not simple poles and the developed UTD based on Pauli-Clemmow formulation for different simple poles (see appendix A.3.2 and [83]) could not be applied because in the product in his expression (4.121), for a given index j, there exist some indexes k for which $s_\beta^j = s_\beta^k$. However, UAT expression (4.114) always provides a uniform total field solution even in the presence of poles of order 2 (see Fig. 4.14).

Note that in this case at $\theta = 45°$, there are two modes of "corner echo" LLL which correspond to the same path but in different directions. These two modes sum up and give rise to only one mode for which the reflected field is continued and does not admit shadow boundaries. Thus, the GTD diffraction coefficient does not diverge at $\theta = 45°$ (see Fig. 4.14).

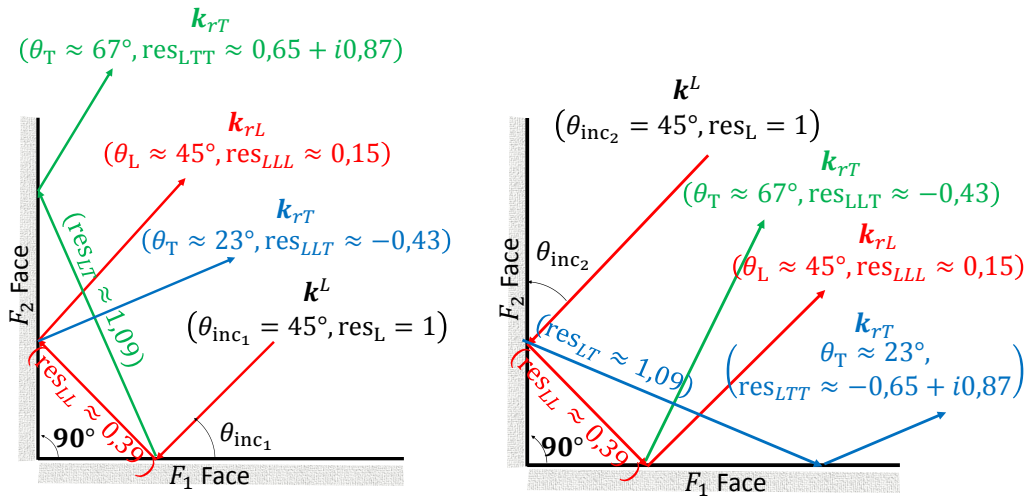

(a) Different reflections on the wedge faces for an incident plane wave on the bottom face of the wedge

(b) Different reflections on the wedge faces for an incident plane wave on the upper face of the wedge

Figure 4.13: Scattering of a longitudinal plane wave of incidence angle $\theta_{\text{inc}_1} = 45°$ by a stress-free wedge of angle 90°.

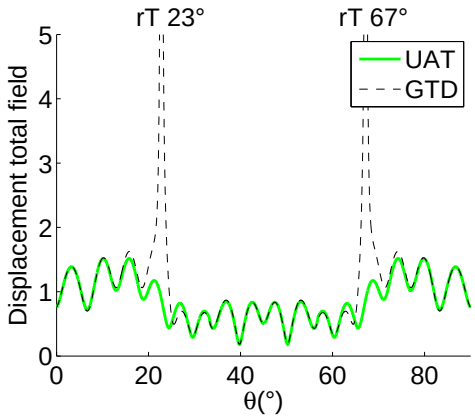

Figure 4.14: Displacement total field amplitude normalized by the incident amplitude at $r = 8\lambda_{0(L)}$ and predicted by different models: GTD and UAT.

To conclude these comparisons between UTD and UAT, there are some slight discrepancies between UAT and UTD total fields which are observed on Figs. D.1a, 4.11b and 4.12b near shadow boundaries. The developed UTD wedge just handle the coalescence of several different simple poles with the phase stationary point contrary to UAT which always treats the interference of reflected and diffracted waves. After some numerical tests, we notice that the error between UAT and UTD are less than the error incertitude encountered in NDT applications.

To better quantify the developed UTD model for Non-Destructive Testing (NDT) applications, as described in section 4.4.2, the diffracted UTD field has been implemented in the software platform CIVA and mixed to the CIVA "specular model" (see section 1.2 in chapter 1) in order to compare this mixed model to other CIVA models for specimen echoes simulation.

4.4.2 The mixed model "specular model + UTD"

As said in section 1.2 in chapter 1, the specimen echoes (entry or backwall surfaces, ...) or echoes produced by specimen interfaces have so far been modeled in CIVA using a “ray” model, the "specular model". This model is based on geometrical elastodynamics and therefore is mainly useful to simulate specular reflections on scatterers. The developed "UTD wedge" model simulates rays diffracted by structure edges and allows to have a uniform total field in the structure, this total field being constituted of the reflected field on the structures faces and of the field diffracted by structure edges. The "UTD wedge" model has been developed in 2D configurations in this chapter meaning that incidence and observation directions are in the plane perpendicular to the wedge edge.

In the CIVA specular model, each discretization point on the radiating transducer crystal emits a pencil which propagates through the structure to the receiver transducer crystal (see Fig. 1.2 in chapter 1). There are thus more than one pencil emitted from the radiating transducer. Each

of them respect the Snell-Descartes law of reflection on the specimen faces. The UTD wedge developed in this chapter has been implemented in CIVA in the same manner as the Geometrical Theory of Diffraction (GTD) for the flaw response (see section 1.4 in chapter 1) and is consequently based on the plane wave approximation and on the field reciprocity principle explained in section 1.3 also in chapter 1. These notions, the plane wave approximation and the field reciprocity principle, mean that only one direction of incidence on the diffracting edge emitted from the radiating transducer and one direction of diffracted wave emitted from the diffracting edge to the receiver transducer are considered. CIVA UTD model has therefore one diffracted ray which is opposite to the local direction of incidence of the receiver transducer. It thus do not consider all the diffracted rays from the diffracting edge to the receiver transducer and, moreover, it just considers one incidence direction on the wedge edges. This CIVA UTD model is then not implemented as a complete ray model like the CIVA specular model. The both models have then different inputs.

In the sequel, very small emitter transducers are used so that the local incidence direction on the wedge edges is close to the rays emitted from the surface crystal of the emitter transducer to the wedge edges. very small receiver transducers are also used for the same reason: the direction opposite to the local incidence direction from the receiver transducer to the wedge edges is close to the diffracted rays emitted from the wedge edges to the surface crystal of the receiver transducer. Emitted waves by a small transducer are shown in Fig. 4.15. On this figure, the emitter transducer being very small, it could be assimilated to a point, the blue point on the specimen entry surface of the specimen which owns three wedges whose edges are E_1, E_2 and E_3 and its backwall has two faces denoted by F_1 and F_2. The wave fronts on Fig. 4.15 are simulated using the pencil method (see section 1.2). The pencils emitted by points on the transducer crystal are reflected in red arrows on Fig. 4.15a by the backwall faces and give rise to diffracted rays in yellow arrows at the wedge edges in a complete ray mode (see Fig. 4.15a). In the UTD model, only the diffraction direction opposite to the local incidence direction at the wedge edges emitted by the receiver transducer is considered. In Fig. 4.15b where the emitted transducer also corresponds to the receiver transducer, this unique direction in yellow for the edge E_1 is close to the yellow arrows on Fig. 4.15a. With the use of a small transducer, "UTD model" and CIVA specular model have approximately the same inputs.

Furthermore, "UTD model" has been theoretically "adjusted" in 2D configurations (see appendix E for more details) to the other CIVA models for specimen echoes simulation as the specular model and the Kirchhoff model introduced in section 1.3. This "adjustment" of models allows the CIVA "UTD model" to model the same physical quantity as the other CIVA models for the specimen echoes. Consequently the echoes simulated with the CIVA "UTD model" can be compared quantitatively with those obtained with other CIVA models.

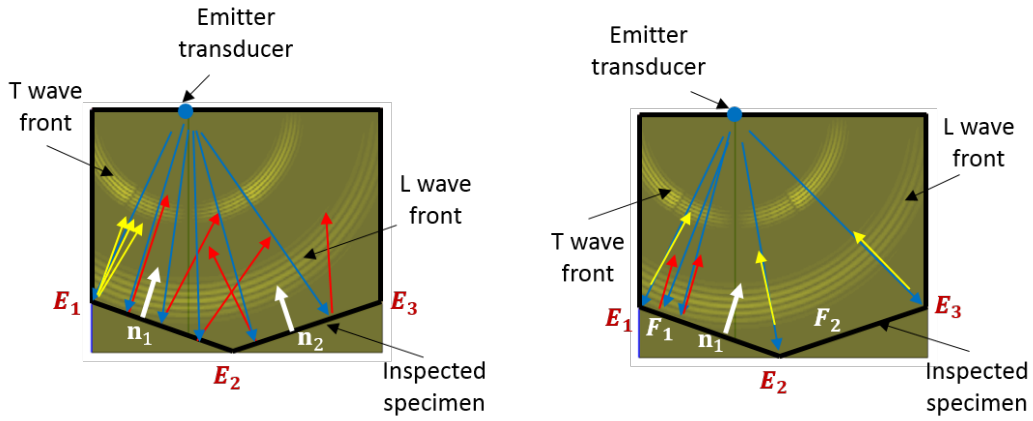

(a) A complete ray model

(b) UTD model : diffracted rays is opposite to the local incidence direction on the wedge edges

Figure 4.15: Rays model with a small emitter/receiver transducer. Blue arrows - rays emitted by the emitter transducer crystal, red arrows - reflected rays on the wedge faces, yellow arrows - rays diffracted by the wedge edges. $\mathbf{n}_1$ and $\mathbf{n}_2$ are inner normals to the backwall surface.

The mixed model "specular + UTD" model is compared to the Kirchhoff model (see section 1.3) or to CIVA-Athena 2D which uses finite elements in a numerical box and the pencil method outside this finite elements box. For these comparisons, as said in the previous paragraph, very small transducers are used. Comparisons of the mixed "specular + UTD" model with the Kirchhoff and CIVA-Athena 2D models are done in pulse/echo configuration, meaning that the emitter transducer is also the receiver transducer. The used transducers are circular and are in direct contact with the entry surface of the specimen. The inspected specimens have the same geometry as the one of Fig. 4.15. They then always own three wedges of edges E_1, E_2 and E_3 and the backwall wedge has two faces denoted F_1 and F_2. The wedge angles are denoted by $\widehat{E}_j, j = 1, 2$ or 3. In all the validation configurations, $\widehat{E}_1 = \widehat{E}_3 \approx 108°$ and $\widehat{E}_2 \approx 142°$.

4.4.2.1 First validation of the mixed "specular + UTD" model

The first validation of the mixed model consists in inspecting a specimen illustrated on Fig. 4.16 with a small circular transducer of diameter 0.5 mm in direct contact with the entry surface of the specimen. This transducer radiates longitudinal waves and at a central frequency of 2 MHz.

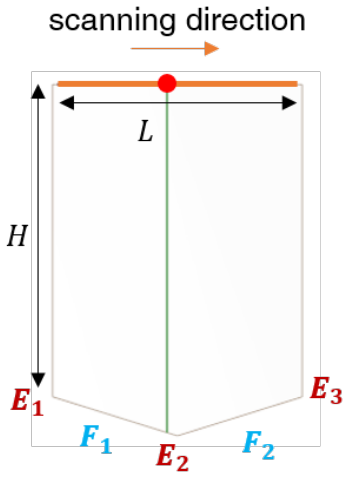

Figure 4.16: First validation configuration: steel specimen ($H = 80$ mm, $L = 60$ mm) inspected with a small transducer of diameter 0.5 mm in direct contact with the entry surface of the specimen at a central frequency of 2 MHz.

A scan of the transducer along the direction represented in orange on Fig. 4.16 allows to image the specimen using the so-called B-scan representation. At each position of the tranduscer, the B-scan gives information about the amplitude and time of flight of echoes due to scatterers. The B-scan is a representation of echoes waveform using a color code versus time (in ordinate) and the scanning position (in abscissa). The different B-scans simulated with the specular model, mixed "specular + UTD" model, CIVA-Athena 2D and Kirchhoff models are presented for the backwall specimen echoes simulation of the configuration of Fig. 4.16 on Fig. 4.17.

The B-scan obtained using the specular model (see Fig. 4.17a) shows only reflection echoes from the faces F_1 and F_2 of the backwall wedge. There is no more reflected echo on the face F_2 of the wedge when the transducer position is after 32 mm and there is no more reflected echo on the face F_1 of the backwall specimen when the transducer position is before 25 mm. On Fig. 4.18, using ray tracing, reflection on face F_1 starts when the probe is at 25 mm (see Fig. 4.18a), it means that before this probe position, the probe is in the shadow region of the reflected rays on face F_1. Reflection on face F_2 ends when the probe is at 32 mm (see Fig. 4.18b), meaning that after this probe position, the probe is in the shadow region of the reflected rays on face F_2. The specular model is then discontinuous at these positions, 25 mm and 32 mm contrary to CIVA-Athena 2D and Kirchhoff models which lead to a continuous solution. That is because they model diffraction by the structure irregularities in addition to the reflection by its surface.

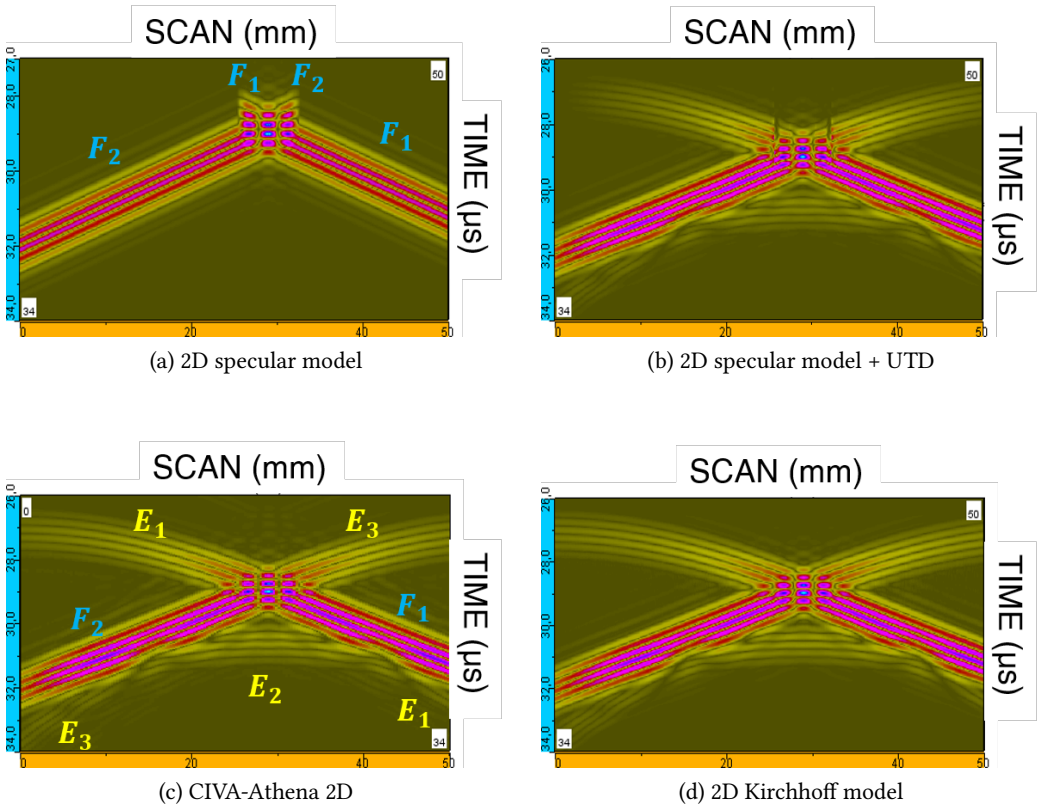

(a) 2D specular model

(b) 2D specular model + UTD

(c) CIVA-Athena 2D

(d) 2D Kirchhoff model

Figure 4.17: B-scans obtained with different models for the specimen echoes for the configuration shown in Fig. 4.16

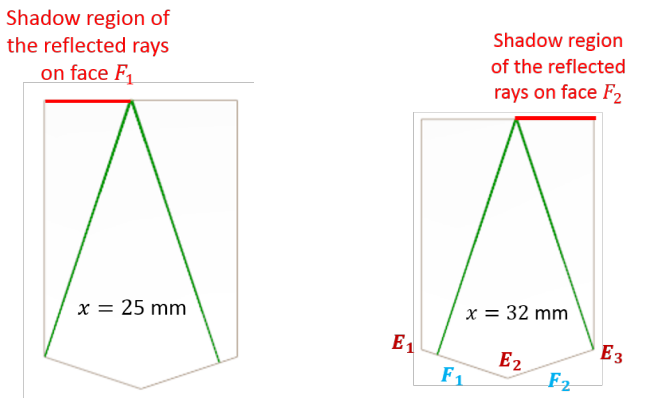

(a) Shadow boundary of the echoes reflection from face F_1 at $x = 25$ mm

(b) Shadow boundary of the echoes reflection from face F_2 at $x = 32$ mm

Figure 4.18: Shadow boundaries of the longitudinal echoes reflection from face F_1 and F_2 using ray tracing.

Echoes reflected by faces F_1 and F_2 and echoes diffracted by edges E_1, E_2 and E_3 appear on the Athena B-scan (see Fig. 4.17c). There is a similarity between the Athena B-scan, the Kirchhoff (see Fig. 4.17d) and "specular + UTD" model (see Fig. 4.17b) B-scans. Some artefacts are observable on the mixed model near shadow boundaries. As explained hereafter, that artefacts are due to the fact that contrary to the specular model only one incident and one diffraction directions are considered in the UTD model. In configuration on Fig. 4.16, with the UTD model, there exists one position $d = 25.6$ mm of the transducer where the local incident direction on the edge E_1 is perpendicular to the backwall face F_1 as shown on Fig. 4.19b. When the transducer is before this distance $x < d = 25.6$ mm, the diffracted ray which is opposite to the local incident direction is always in the shadow region of the reflected rays on the face F_1 of the wedge (see Fig. 4.19a) and when the transducer is after this distance $x > d = 25.6$ mm, the diffracted ray is in the illuminated region of the reflected rays on the face F_1 (see Fig. 4.19c). It is the same process for the face F_2 of the wedge. For a small transducer, "UTD model" has then only one shadow boundary at $x = d = 25.6$ mm on each face of the wedge contrary to the specular model which has many shadow boundaries.

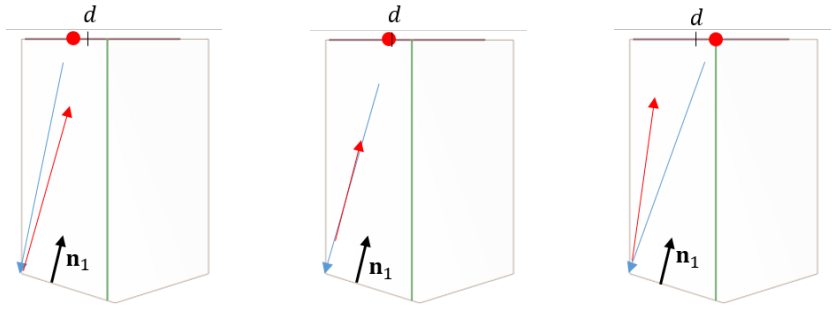

(a) Tranduscer before the distance $d = 25.6$ mm

(b) Tranduscer at the distance $d = 25.6$ mm

(c) Tranduscer after the distance $d = 25.6$ mm

Figure 4.19: Reflection of the local incident ray on the face F_1 at different positions (red points) of the transducer, $\mathbf{n}_1$ is the inner normal to the face F_1. Blue arrow - incident local direction, red arrow - reflected ray on face F_1.

To better visualize the different shadow boundaries of the specular model, a ray tracing is used for the configuration shown in Fig. 4.16 at a position of the transducer near one of the shadow boundaries of the specular model on Figs. 4.20 and 4.21. On Fig. 4.20, when the transducer is at $x = 25.7$ mm, there are only two incident rays which are reflected in the direction of the transducer (see green and blue arrows on Fig. 4.20b and Fig. 4.20c). At another position of the transducer, $x = 26.1$ mm, there are four incident rays whose reflection on the backwall specimen come back on the transducer including the two reflected rays on Fig. 4.20 (see Fig. 4.21b and Fig. 4.21c). That means that at $x = 25.7$ mm on Fig. 4.20, the transducer is in the shadow region

of the red and black reflected rays on Fig. 4.21. Each of the four reflected rays on Fig. 4.21c has its shadow boundary. The specular model then has many shadow boundaries contrary to the "UTD model".

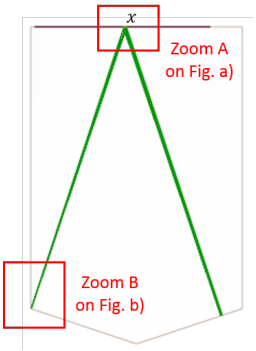

(a) Emitted and reflected rays coming back on the transducer

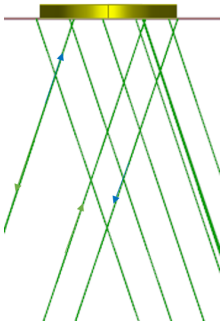

(b) Zoom A of Fig. 4.20a

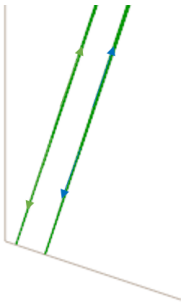

(c) Zoom B of Fig. 4.20a

Figure 4.20: Rays emitted by the transducer at $x = 25.7$ mm which returned back to the transducer for the configuration shown in Fig. 4.16.

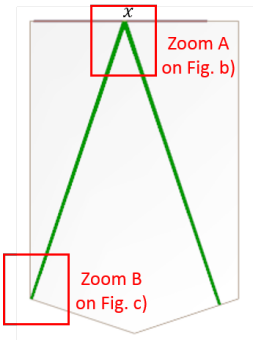

(a) Emitted and reflected rays coming back on the transducer

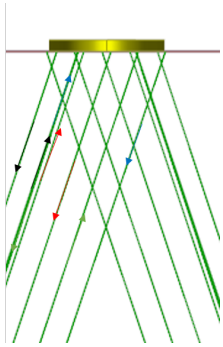

(b) Zoom A of Fig. 4.21a

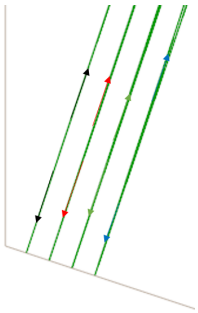

(c) Zoom B of Fig. 4.21a

Figure 4.21: Rays emitted by the transducer at $x = 26.1$ mm which returned back to the transducer for the configuration shown in Fig. 4.16.

The combination of these two models (specular and UTD for edge diffraction) employing different inputs, one incidence and one observation directions for the "UTD model" against many incidence and observation directions in the CIVA specular model, creates therefore artefacts. All the discontinuities of the specular model at shadow boundaries are therefore not compensated by the CIVA "UTD model". Avoiding these artefacts requires modifying the UTD implementa-

tion so that all incident rays emitted by the emitter and the receiver transducers using the pencil method are taken into account. That requires to not use the plane wave approximation in the UTD implementation and thus allows to take into account the other shadow boundaries of the specular model. These requirements imply a growth in the number of calls of the LT (Laplace transform) GTD code since the GTD diffraction coefficient is calculated at each couple of incidence and observation directions. That is not conceivable with the current LT GTD code because time computation with 1500 calls of the LT GTD code (500 positions of the transducer) is around ~ 10 min against a few seconds for the specular and Kirchhoff models for 500 positions of the transducer. An optimisation of the LT GTD code needs to be done in that purpose.

Despite these artefacts, a comparison of the echoes obtained with the specular, "UTD + specular", Kirchhoff and CIVA-Athena 2D models is shown on Figs. 4.22 and 4.23 at different positions of the transducer always for the configuration on Fig. 4.16. The CIVA-Athena model can be considered as reference model since it is based on finite elements and Kirchhoff is considered to be less accurate in modelling edge diffraction compare to GTD according to validations for half-cracks especially for T waves (see for example the Fig. 1.7 in section 1.3). As far as we know, the validity of the Kirchhoff model for modelling diffraction by a wedge edge has never been studied.

On these figures, transducer positions are represented in vertical black line on the Specular and CIVA-Athena B-scans. The echo received by the transducer, called the A-scan, is represented at each position of the transducer. On Fig. 4.22, far away from the shadow boundaries of the specular model which are localized between 25.4 mm and 26.3 mm, at $x = 14.7$ mm, CIVA-Athena in blue and Kirchhoff in green lead to approximately the same amplitude for the echo diffracted by the edge E_1 (first echo in the left top A-scan of Fig. 4.22). There is a difference of 3 dB between "UTD + specular" model in red dashed line and the other models (Kirchhoff and CIVA-Athena models). The second echo in this A-scan is the one obtained by the interference of the echo reflected by the face F_2 and the echo diffracted by the edge E_3. In this second echo, "UTD+specular" is close to the CIVA-Athena and to the Kirchhoff models. There is a difference of 0.8 dB between "UTD+specular" and CIVA-Athena models and a difference of 0.4 dB between "UTD+specular" and Kirchhoff models. Such errors are acceptable since the order of measurements incertitude in NDT is around 2 dB in pulse-echo. For observation points close to the shadow boundaries, at $x = 23.4$ mm and $x = 24.9$ mm, the mixed model is always close to the CIVA-Athena and to the Kirchhoff models. The interference between the echo diffracted by the wedge edge E_1 and the echo reflected by the face F_1 is simulated in the same manner in all models since the top right A-scans on Fig. 4.22 have the same waveform and the bottom left A-scans also have the same waveform. However at $x = 25.5$ mm, the amplitude of the interference of the echo diffracted by the edge E_1 and the one reflected on the face F_1 obtained with the "UTD+specular" differs from the amplitude obtained with the other models. This position of the transducer corresponds to a shadow boundary of the specular model on the F_1 wedge face. Indeed, at this probe position, the A-scan of the specular model in black line has an echo which corresponds to the reflected echo on the face F_1. The fact that the "UTD+specular" does not model this shadow boundary alters

(as seen on Fig. 4.19, the only shadow boundary detected by the "UTD model" is at $x = 25.6$ mm) its result.

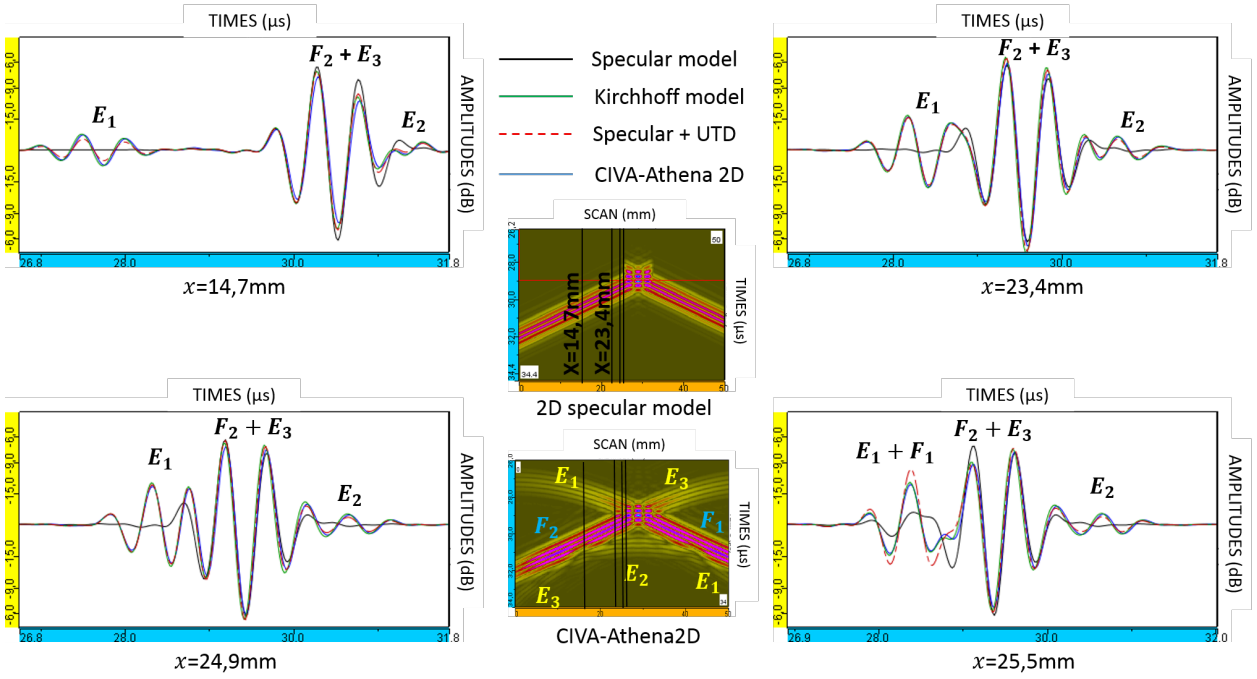

Figure 4.22: A-scans at different positions of the transducer, $x \leqslant 25.5$ mm, using different simulation models. The different positions are indicated by vertical black lines on the CIVA-Athena B-scan.

On Fig. 4.23 where the observation directions are after the shadow boundaries of the specular model (localized between 25.4 mm and 26.3 mm), the same observation is done. Waveform and amplitude of the echoes obtained with "UTD+specular", Kirchhoff and CIVA-Athena models are close except at $x = 27.9$ mm where there is a difference between the three models. At the end of this comparison, we can conclude that the developed UTD model in elastodynamics renders the geometrico-elastodynamic field (modelled here with the specular model) continuous. The waveform of the echoes obtained with the mixed model "UTD + specular" is similar to the one obtained with the CIVA-Athena and Kirchhoff models. In the configuration of Fig. 4.16, the amplitude of the mixed model echoes is very close to the one of the Kirchhoff and CIVA-Athena models except at positions of the transducer where the specular model has a shadow boundary not determined in the UTD model due to the plane wave approximation employed in the CIVA UTD model.

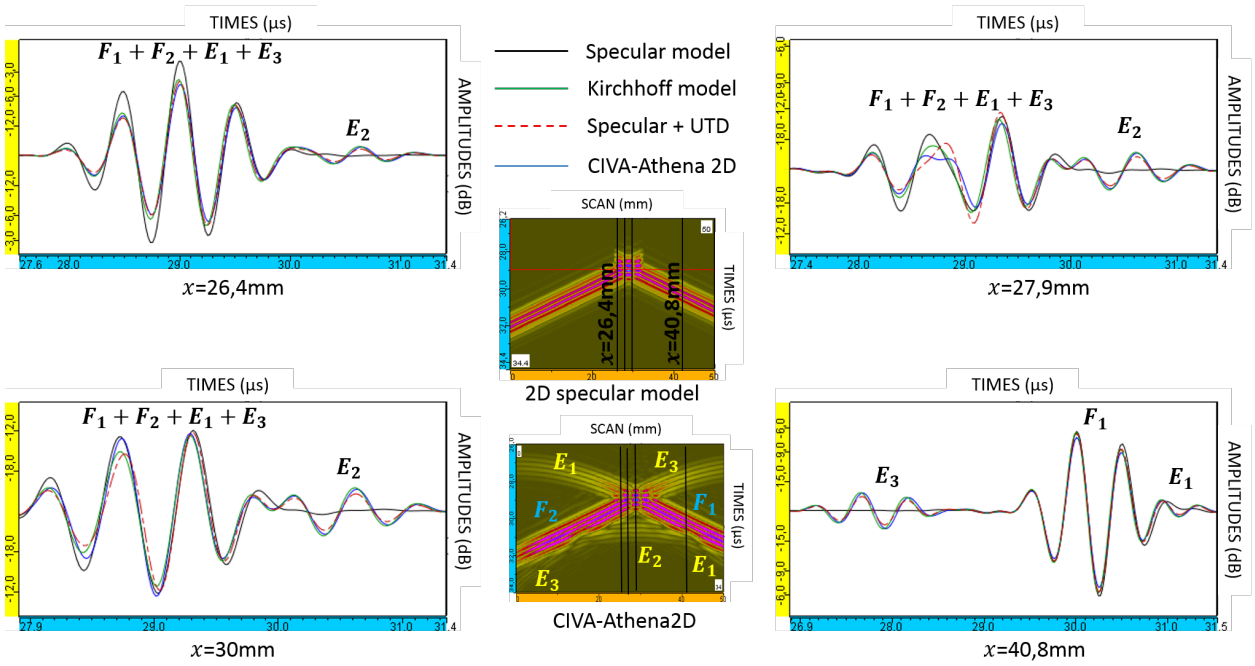

Figure 4.23: A-scans at different positions of the transducer, $x \geqslant 26.4$ mm, using different simulation models. The different positions are indicated by vertical black lines on the CIVA-Athena B-scan.

A comparison of these three models is performed in another configuration hereafter.

4.4.2.2 Second validation of the mixed "specular + UTD" model

The second validation of the mixed model consists in inspecting the specimen illustrated on Fig. 4.24 with a small circular transducer of diameter 1 mm in direct contact with the entry surface of the specimen. This transducer radiates longitudinal waves at a central frequency of 2 MHz. The main changes compared to the configuration in Fig. 4.16 is the specimen height (smaller than the one of Fig. 4.24) and the diameter of the transducer (bigger than the one of Fig. 4.24) .

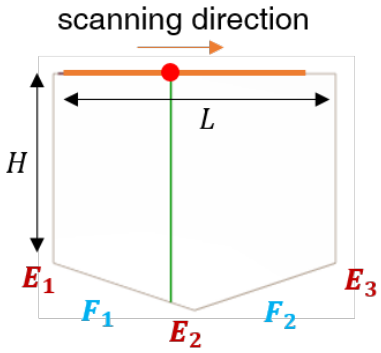

Figure 4.24: Second validation configuration: steel specimen ($H = 40$ mm, $L = 60$ mm) inspected with a small transducer of diameter 1 mm in direct contact with the entry surface of the specimen at a central frequency of 2 MHz.

A scan of the transducer along the direction represented by the orange arrow on Fig. 4.24 allows to obtain a B-scan representation. The different B-scans simulated with the specular model, mixed "specular model + UTD", CIVA-Athena 2D and Kirchhoff model are presented on Fig. 4.25 for the backwall specimen echoes simulation of the configuration of Fig. 4.24.

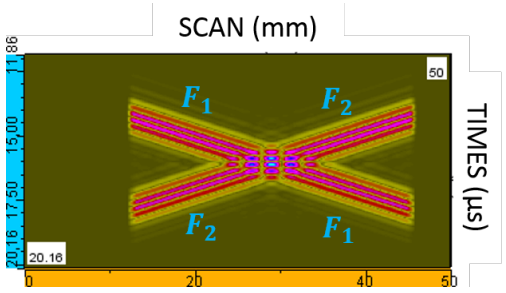

(a) 2D specular model

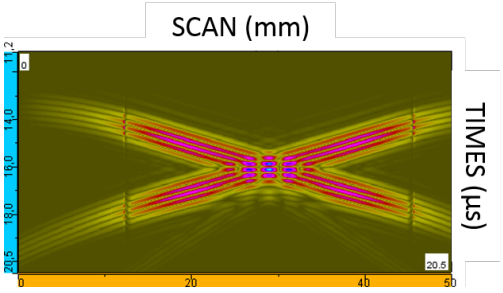

(b) 2D specular model + UTD

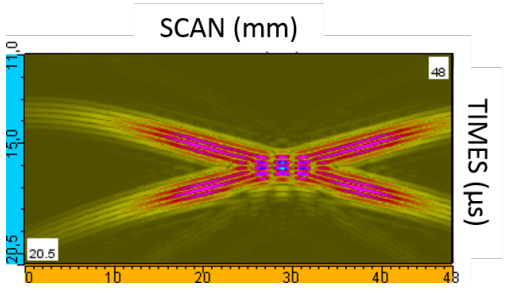

(c) CIVA-Athena 2D

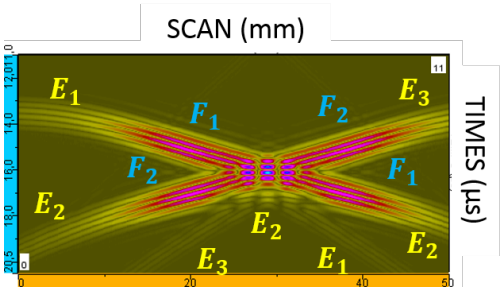

(d) 2D Kirchhoff model

Figure 4.25: B-scans obtained with different models for the specimen echoes for the configuration shown in Fig. 4.24

The B-scan obtained using the specular model (see Fig. 4.25a) shows only reflection echoes from the faces F_1 and F_2 of the backwall wedge. There is no more reflected echo on the face F_2 of the wedge when the transducer position is after 46 mm and when it is also before 12 mm. The specular model is then discontinuous at these positions, 12 mm and 46 mm. Echoes reflected by faces F_1 and F_2 and echoes diffracted by edges E_1, E_2 and E_3 appear notably on the Kirchhoff B-scan (see Fig. 4.25d). There is a similarity between the Kirchhoff B-scan and the CIVA-Athena (see Fig. 4.25c) and "specular model + UTD" (see Fig. 4.25b) B-scans. Some artefacts are observable on the mixed model near shadow boundaries. As explained in the previous case, these artefacts are due to the fact that for one transducer position, the UTD model considers only one incidence direction and also one direction of diffracted rays from the wedge edge to the transducer.

A comparison of the maximum amplitude at each position of the transducer is carried out using the echodynamic curves (maximal amplitude of each A-scan versus the scanning position) on Fig. 4.26. The obtained echodynamic scanning using the "specular + UTD", CIVA-Athena and Kirchhoff models have approximately the same form. Around $x = 12$ mm and $x = 46$ mm, there are discontinuities in the echodynamic curves using the mixed model. These discontinuities are linked to the artefacts in its B-scan on Fig. 4.25b. The mixed model is close to the CIVA-Athena model and to the Kirchhoff model except near of $x = 0$ mm. The maximal error between the mixed model and the CIVA-Athena model is of 4.5 dB near the specimen boundary at $x = 0$ mm. In this second configuration, the mixed model gives close results to CIVA-Athena and differs from the Kirchhoff model near the specimen boundary at $x = 0$ mm. This position of the transducer, $x = 0$ mm, corresponds to a grazing incidence on the specimen boundary.

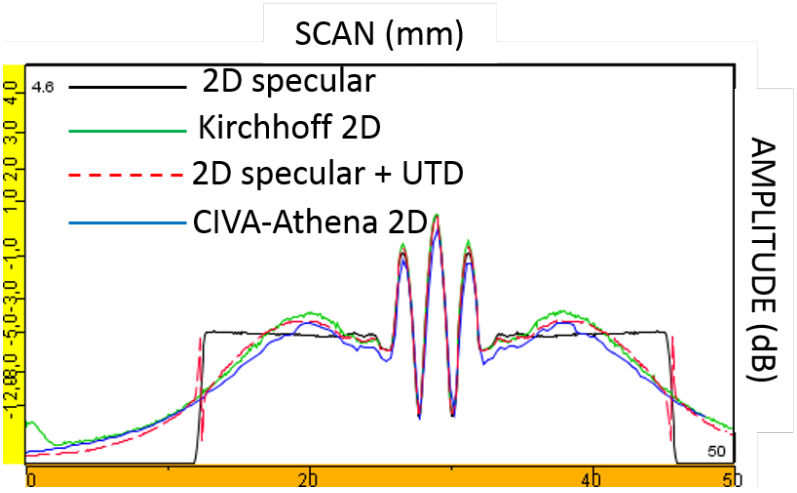

Figure 4.26: Echodynamic curve using different simulation models.

These two validations have been done with longitudinal waves.

4.4.2.3 Third validation of the mixed "specular + UTD" model

The third validation configuration is similar to the second validation configuration (see Fig. 4.24) at the only difference that the emitter transducer radiates transversal waves.

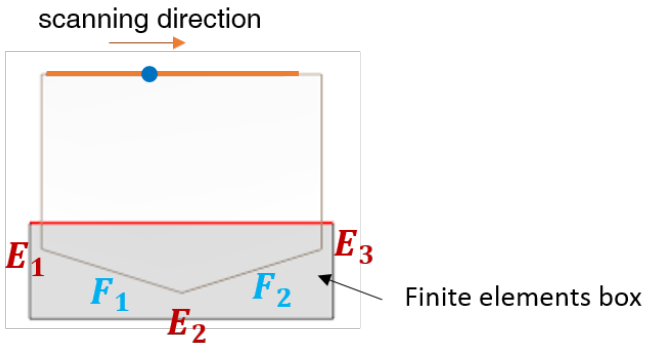

Figure 4.27: Third validation configuration: almost the same configuration as the second validation in Fig. 4.24. The emitter transducer in blue point radiates transversal waves.

In this third configuration, the different B-scans simulated with the specular model, mixed "specular model + UTD", CIVA-Athena 2D and Kirchhoff model are presented on Fig. 4.28 for the backwall specimen echoes simulation of the configuration of Fig. 4.27 with the emitter transducer that radiates transversal waves.

As for the second validation configuration at section 4.4.2.2, the B-scan obtained using the specular model (see Fig. 4.28a) the specular model is discontinuous at 12 mm and 46 mm since they correspond to shadow boundaries of the reflected rays on the backwall faces F_1 and F_2 (see Fig. 4.29). It has other discontinuities points as explained in the first validation configuration with the help of Figs. 4.20 and 4.21.

Echoes reflected by faces F_1 and F_2 and echoes diffracted by edges E_1, E_2 and E_3 appear on the "specular + UTD" B-scan (see Fig. 4.28b). In the CIVA-Athena model, the finite elements are applied in the box depicted on Fig. 4.27 which contains the three backwall wedges. Amplitude of the diffracted echoes predicted by the CIVA-Athena model is higher than the one obtained with the Kirchhoff and the "UTD + specular" models (see B-scans on Fig. 4.28). They are some unexplained echoes in CIVA-AThena and Kirchhoff B-scans which are between the reflected echo on face F_1 (F_2 respectively) and the diffracted echo by the wedge edge E_1 (E_2 respectively).

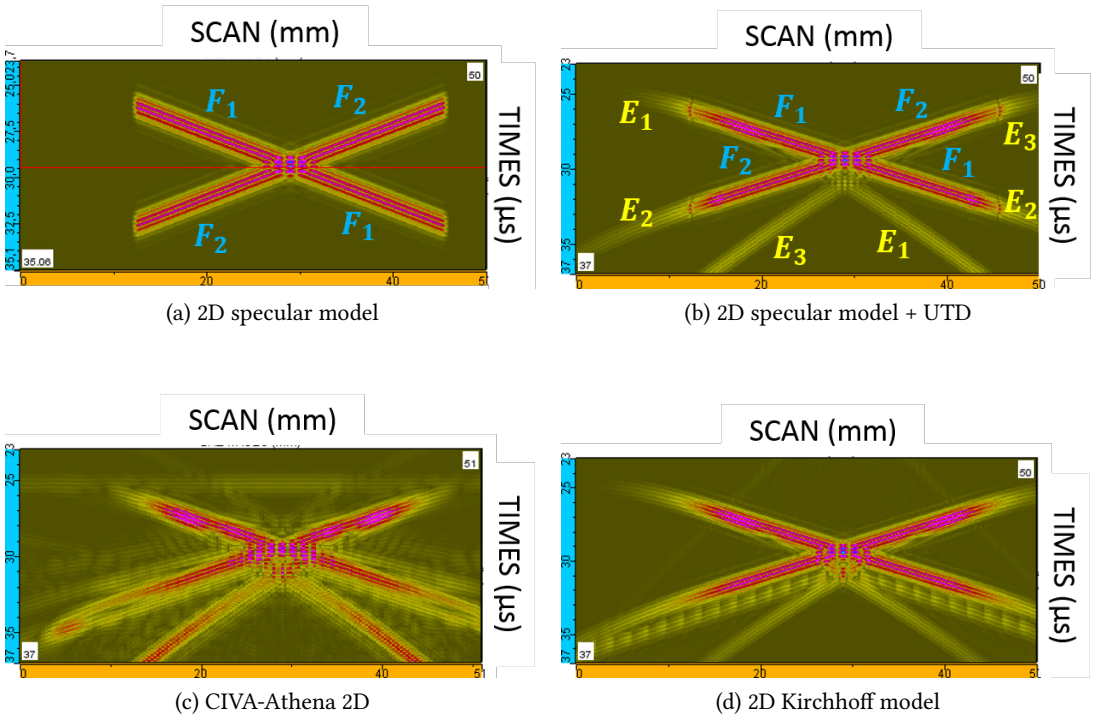

(a) 2D specular model

(b) 2D specular model + UTD

(c) CIVA-Athena 2D

(d) 2D Kirchhoff model

Figure 4.28: B-scans obtained with different models for the specimen echoes for the configuration shown in Fig. 4.27

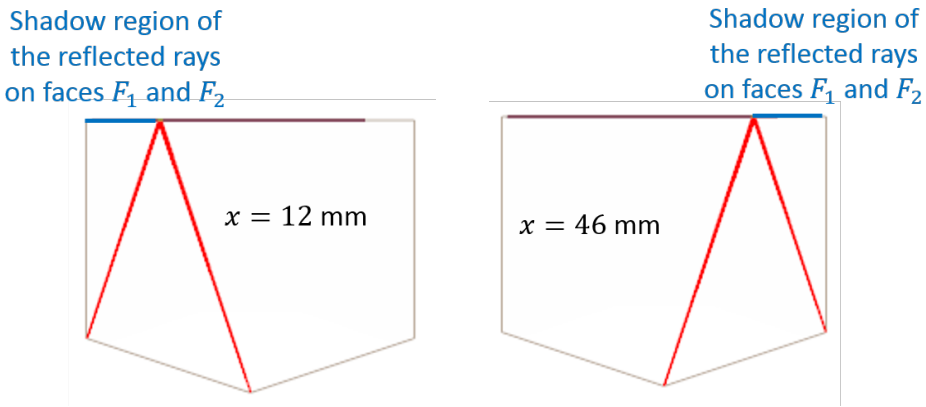

(a) Shadow boundary of the echoes reflection from face F_1 at $x = 12$ mm

(b) Shadow boundary of the echoes reflection from face F_2 at $x = 46$ mm

Figure 4.29: Shadow boundaries of the transversal echoes reflection from face F_1 and F_2 using ray tracing.

As for the second validation, a comparison of the maximal amplitudes of echoes contained in the time domain above the red line on the specular B-scan (see Fig. 4.28a) at each position of the

transducer (echodynamic curve) using different models ("UTD + specular", Kirchhoff and CIVA-Athena) is carried out on Fig. 4.30. The obtained echodynamic curves using the "specular + UTD" and Kirchhoff models have approximately the same form. Around $x = 12$ mm and $x = 46$ mm, discontinuities in the echodynamic curveof the mixed model are observed. These discontinuities are linked to the artefacts in its B-scan on Fig. 4.28b. The "specular + UTD" and Kirchhoff models differ from the CIVA-Athena model in amplitude. The maximum error between the mixed model and the CIVA-Athena model is around the artefacts of the mixed model. This error is estimated at around 6 dB. Near $x = 30$ mm, there is an error of around 2 dB between the mixed model and the CIVA-Athena model. With transversal waves, error between these two models are more important than in previous cases where longitudinal waves were considered.

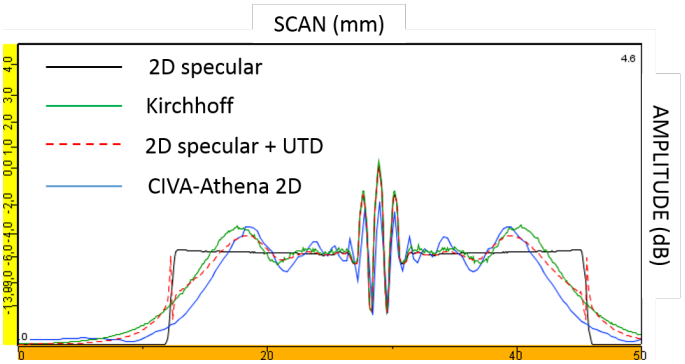

Figure 4.30: Echodynamic scanning using different simulation models.

4.4.2.4 conclusions of the "specular + UTD" model

To conclude the section 4.4.2, a UTD model has been implemented in the platform software CIVA to compute echoes from wedges in 2D configurations using the plane wave approximation and the field reciprocity principle. CIVA "UTD model" has been combined with the specular model in order to add diffraction effects to reflection accounted by the specular model. It has been compared to the existing CIVA models for specimen echoes simulation such as the specular model, the Kirchhoff model and the CIVA-Athena 2D model. Small transducers have been used to minimize the inconvenients due to the plane wave approximation (the model considers only as inputs a single incidence and observation directions). The wave approximation introduces artefacts which are localized with a small transducer. In the studied configurations, for longitudinal incident waves, the mixed model "specular + UTD" model gives results close to CIVA-Athena (considered as the reference model) and to Kirchhoff models except near artefacts of the mixed model. For transverse incident waves, the difference of amplitude between the mixed "specular + UTD" and the CIVA-Athena models is more important than for incident longitudinal waves.

The first obtained results of this mixed model are positive. All the studied configurations in order to validate the mixed model have been done for the same wedge angles, 108° and 142°. Further

work needs to be done in order to validate the CIVA mixed model by testing it with different wedge angles and also testing mode conversion. A supplementary work must be done in order to have a completely UTD ray model in order to have more accurate results and no more artefacts. In order to reduce its computation time which is in the order of 10 min in all these configurations, an optimisation of the Laplace transform (LT) GTD code needs to be done.

4.5 Conclusion

There exist in the littetrature two methods of resolution of a plane wave scattering by a 2D elastic wedge used for computing GTD diffraction coefficient, the Sommerfeld integral (SI) and the Laplace transform (LT). These two methods are limited to wedge angles less than π. As in the case of half-plane, such coefficients diverge near shadow boundaries of the geometrico-elastodynamic field composed of incident waves and reflected waves coming from multiple reflections in the wedge. Each resolution method, SI or LT, proposes an algorithm of pole propagation knowing the initial poles which are linked to the incident wave on the wedge faces and to its symmetric which respect to the wedge bisector. The poles found by this propagation algorithm lead to the incident and multiplied reflected waves in the wedge.

To remove the GTD divergence near shadow boundaries, the Uniform Theory of Diffraction (UTD) has been proposed for the case of the wedge applying the Pauli-Clemmow process to the Sommerfeld integral as in the case of the half-plane. In the Pauli-Clemmow process, the coalescence of many simple poles with a stationary phase point has been considered. The UTD diffracted field which is finite but discontinuous at shadow boundaries so that the total UTD field is spatially continuous.

This UTD solution has then been applied using the GTD diffraction coefficient provided by the LT method. It has been first compared to the existing UAT solution [81]. Some slight differences between UTD and UAT solutions are observed specifically near shadow boundaries. The error between the two models remains less than the incertitude error encountered in NDT applications.

A UTD wedge model has been implemented in the software platform CIVA and coupled to the CIVA specular model which just models reflection on the backwall faces. UTD then completes this model by adding to it diffraction and compensating its discontinuity near shadow boundaries. This mixed model "specular + UTD" has been compared to other models of CIVA for the specimen echos such as Kirchhoff and CIVA-Athena 2D (based on finite elements method and considered as the reference model) models in 2D configurations. These comparisons have been done with small transducers due to the plane wave approximation employed for the UTD implementation. This strategy of implementation leads to artefacts in the mixed model near shadow boundaries of the specular model. However, UTD implementation can be improved in the futur. The mixed model gives results close to those of CIVA-Athena 2D and Kirchhoff for longitudinal and transverse incident waves except near artefacts for transverse incident waves.

Further tests (varying wedge angles and taking mode conversion in account) need to be done in order to validate the UTD. A supplementary work has to be done in order to implement a completely UTD ray model in order to improve the simulation validity and remove the observed artefacts.

Chapter 5

Computation of diffraction coefficient for all wedge angles in the "acoustic" case

Dans le chapitre 4, les solutions de diffraction par un dièdre à interface solide/vide sont toutes limitées à des angles de dièdre inférieurs à π. Cette limitation est problématique pour des applications au Contrôle Non-Destructif (CND).

La méthode des "fonctions spectrales" proposée par Croisille et Lebeau [11] peut permettre de résoudre la diffraction par des dièdres de tout angle. Cette méthode est donc employée et détaillée dans ce chapitre dans le cas de la diffraction d'une onde plane "acoustique" par un dièdre à interface fluide/vide. Cette étude nous permet ainsi d'évaluer la précision de calcul de cette méthode par comparaison avec la solution analytique de la GTD classique de la littérature (cas "acoustique" ou électromagnétique). Pour un bon choix de paramètres de la base d'approximation utilisée dans la méthode des "fonctions spectrales", cette méthode donne des résultats proches de ceux de la solution analytique GTD.

5.1 Introduction

In the previous chapter, chapter 4, two existing methods in the literature for the scattering of an elastic plane wave by wedges less than π have been studied. These two methods, the Sommerfeld integral and the Laplace transform require a numerical resolution of this scattering problem in elastodynamics. The existence and the uniqueness of the solution of this scattering problem for wedges of all angles has been proved by Katmoski and Lebeau [79]. They used the so-called "spectral functions method" developed in [11] where the diffraction of an acoustic wedge by an immersed solid wedge in a fluid was studied. In [11], the study was limited to the angles less than π. Katmoski and Lebeau [79] then showed that the spectral functions method could model diffraction by wedge whose angle is less than π as well as diffraction by wedge whose angle is greater than π. With the spectral functions method, the diffraction is modeled thanks to spectral functions. As these functions could not have an analytic formulation, they need to be calculated numerically such as the fonctions in the Sommerfeld or Laplace method for the elastodynamics case (see chapter 4). Croisille and Lebeau [11] proposed a numerical algorithm to calculate these spectral functions for the diffraction of an acoustic wedge by a immerge solid wedge.

In this chapter, the spectral functions method is used to resolve the diffraction of an acoustic wave by a free-stress wedge of all angles. The numerical resolution employed in [11] is used to find the diffraction coefficients in high frequency regime and is more detailed than in [11]. The aim of this chapter is to reproduce and to detail the methodology used in [11] in a simple case of diffraction problem so that the proposed methodology could be used in more complex diffraction problems as the diffraction of an elastic plane wave by a free-stress wedge.

Section 5.2 presents the problem and the diffraction coefficients are derived thanks to the spectral functions. The resolution of the problem is discussed in section 5.3. Results of the method are given in section 5.4. They are compared to the GTD solution deduced from the Sommerfeld exact formulation in acoustics, which is an analytical solution.

5.2 Problem statement

Let us consider a stress-free fluid wedge Ω_f of angle 2φ constituted of the junction of two faces F_1 and F_2 (see Fig. 5.1). For this study, we use the Cartesian coordinate systems $(O;\mathbf{e}_{x_1},\mathbf{e}_{y_1})$ linked to the face F_1 of the wedge and $(O;\mathbf{e}_{x_2},\mathbf{e}_{y_2})$ linked to the face F_2. These Cartesian coordinate systems have the same origin located on the wedge edge which coincides with the z-axis. Let $\mathbf{x}=(x_1,y_1)_{(\mathbf{e}_{x_1},\mathbf{e}_{y_1})}=(x_2,y_2)_{(\mathbf{e}_{x_2},\mathbf{e}_{y_2})}$ be a position vector. $\mathbf{x}=(r,0)$ in a local basis of polar coordinates associated to the Cartesian coordinates (x_1,y_1). The time convention used in this chapter is $\exp(i\omega t)$. It is opposite to the time convention used in the previous chapters. In order to have the same time convention than the one of previous chapter, the opposite of the phase of the incident and scattered plane waves has to be considered. The wedge is thus irradiated by a

velocity potential plane wave in the form

$$g^{\text{inc}}(\mathbf{x},t) = A\, e^{i(\omega t - \mathbf{k}^{\text{inc}}\cdot\mathbf{x})} \tag{5.1}$$

where A is the amplitude of the incident velocity potential, ω is the circular frequency, t is time and

$$\mathbf{k}^{\text{inc}} = k_0(-\cos\theta_{\text{inc}}, -\sin\theta_{\text{inc}})_{(\mathbf{e}_{x_1},\mathbf{e}_{y_1})} \tag{5.2}$$

is the wave vector of the incident wave with $k_0 = \omega/c_0$ being the wave number - c_0 is the sound velocity in the fluid. The velocity potential in the fluid g satisfies the motion equation in the fluid wedge Ω_f

$$\partial_t^2 g - c_0^2 \triangle g = 0 \tag{5.3}$$

and the Dirichlet boundary conditions on the wedges faces

$$g\mid_{F_j} = 0, \quad j = 1,2. \tag{5.4}$$

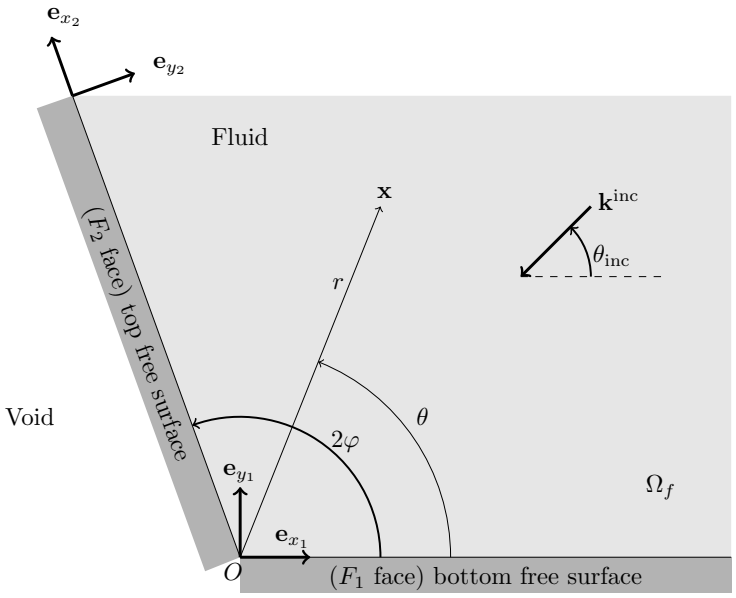

Figure 5.1: The wedge of angle 2φ whose faces are stress-free is illuminated by a plane wave of wave vector $\mathbf{k}^{\text{inc}}$.

The dimensionless form of the problem is obtained by defining the function h by

$$g(\mathbf{x},t) = 2A\, e^{i\omega t}\, h(k_0\mathbf{x}). \tag{5.5}$$

The dimensionless function h is the sum of the incident dimensionless wave h_{inc} and of the scattered dimensionless wave h_{scat}

$$h = h_{\text{inc}} + h_{\text{scat}}. \tag{5.6}$$

Let us denote the scattered dimensionless wave h_{scat} by v,

$$v = h_{\text{scat}}. \tag{5.7}$$

Using (5.5) and (5.1), the expression of the incident dimensionless plane wave is

$$h_{\text{inc}} = \frac{1}{2}\, e^{-i(\mathbf{k}_{\text{inc}}\cdot\mathbf{x})/k_0}. \tag{5.8}$$

The system (5.3)-(5.4) is equivalent to the following system of equations for the dimensionless problem

$$\begin{cases} (\triangle + 1)v = 0 & \text{in } \Omega_f, \\ v = -h_{\text{inc}} & \text{on } F_j, \quad j = 1, 2 \end{cases}. \tag{5.9}$$

In order to satisfy radiation condition at infinity that allows only for the outgoing waves at infinity (the energy of outgoing waves attenuates with distance), the limiting absorption principle is used. This principle means that absorption in the medium occurs and thus the scattered waves attenuate with the distance. It then consists in substituting the wave number k_0 by a complex one $k_0 e^{-i\epsilon} = \omega e^{-i\epsilon}/c_0$ with $\epsilon > 0$. This replacement then induces a complex circular frequency. With this principle, the velocity potential is defined as

$$g^\epsilon(\mathbf{x}, t) = 2A\, e^{i\omega t}\, h^\epsilon(|k_0|\mathbf{x}) \tag{5.10}$$

with

$$h^\epsilon = h^\epsilon_{\text{inc}} + v^\epsilon \tag{5.11}$$

and

$$h^\epsilon_{\text{inc}}(x_1, y_1) = \frac{1}{2}\, e^{i\, e^{-i\epsilon}(x_1 \cos\theta_{\text{inc}} + y_1 \sin\theta_{\text{inc}})}. \tag{5.12}$$

This velocity potential g^ϵ also satisfies the wave motion (5.3) and leads to the following system of equations for the dimensionless problem

$$(S^*_\epsilon) \quad \begin{cases} (\triangle + e^{-2i\epsilon})v^\epsilon = 0 & \text{in } \Omega_f, \\ v^\epsilon = -h^\epsilon_{\text{inc}} & \text{on } F_j. \end{cases} \tag{5.13}$$

This solution v^ϵ allows us to work in the space of distributions in which it is possible to differentiate functions whose derivatives do not exist in the classical sense. Besides, Fourier transform

do exist for all tempered distributions. Let us introduced the Fourier transform of a tempered distribution $f(x)$

$$\hat{f}(\xi) = \mathcal{F}(x \mapsto f(x)) = \int_{\mathbb{R}} f(x)\, e^{-ix\xi}\, \mathrm{d}x \tag{5.14}$$

and the double Fourier transform of a tempered distribution $f(x, y)$

$$\hat{f}(\xi, \eta) = \iint_{\mathbb{R}^2} f(x, y)\, e^{-i(x\xi + y\eta)}\, \mathrm{d}x\, \mathrm{d}y \tag{5.15}$$

with its inverse given by

$$f(x, y) = \frac{1}{4\pi^2} \iint_{\mathbb{R}^2} \hat{f}(\xi, \eta) e^{i(x\xi + y\eta)}\, \mathrm{d}\xi\, \mathrm{d}\eta. \tag{5.16}$$

Let Ω being an $\mathbb{R}^n$ open set, $n \in \mathbb{N}^*$. A measure function is said to be in the space $L^2(\Omega)$ if it is square-integrable, i.e.

$$\int_{\Omega} |f|^2\, \mathrm{d}\mu < +\infty, \tag{5.17}$$

μ being the measure on the space Ω.

The solution to our initial problem (5.9) using (5.13) is then

$$v = \lim_{\epsilon \to 0} v^\epsilon. \tag{5.18}$$

Let us note v^0 this limit. Its integral representation is found in section 5.2.1.

5.2.1 Outgoing solution: integral representation

Let v^ϵ be a solution of $(\triangle + e^{-2i\epsilon})(v^\epsilon) = 0$ in Ω_f. Let us introduce the function w^ϵ, a solution of

$$(\triangle + e^{-2i\epsilon})(w^\epsilon) = 0 \text{ in } \mathbb{R}^2 \setminus \Omega_f \tag{5.19}$$

with boundary conditions

$$w^\epsilon|_\Gamma = v^\epsilon|_\Gamma \quad \text{where} \quad \Gamma = \partial\Omega_f = F_1 \cup F_2. \tag{5.20}$$

We thus have introduced a function w^ϵ which satisfies the motion equation outside the fluid wedge, in the void on Fig. 5.1 and has the same trace than the scattered dimensionless wave v^ϵ on the boundaries of the wedge. We also introduce the function f^ϵ defined in $\mathbb{R}^2$ which is equal to v^ϵ in Ω_f and to w^ϵ in $\mathbb{R}^2 \setminus \Omega_f$:

$$f^\epsilon = \begin{cases} v^\epsilon & \text{in} \quad \Omega_f \\ w^\epsilon & \text{in} \quad \mathbb{R}^2 \setminus \Omega_f. \end{cases} \tag{5.21}$$

With this trick, the new function f^ϵ satisfies the following property (according to the jump formula and to theorems proved in [11] for the regularity in L^2): there exists a function $\alpha \in L^2(\Gamma)$ so that in the distributional sense in $\mathbb{R}^2$ we have

$$(\triangle + e^{-2i\epsilon})(f^\epsilon) = -\alpha\, \delta_\Gamma. \tag{5.22}$$

δ_Γ is the Dirac delta operator on the wedge boundary $\Gamma = F_1 \cup F_2$. Then, the unique and possible decomposition of $\alpha \in L^2(\Gamma)$, allows us to write

$$\alpha\, \delta_\Gamma = \alpha_1(x_1, 0)\, \delta_{F_1} + \alpha_2(x_2, 0)\, \delta_{F_2} \tag{5.23}$$

where δ_{F_1} and δ_{F_2} are Dirac delta operators (also called integration measures) on the faces F_1 and F_2 of the wedge respectively defined for any test function ϕ as

$$\delta_{F_1}(\phi) = \int_0^{+\infty} \phi(r, 0)\, \mathrm{d}r \quad \text{and} \quad \delta_{F_2}(\phi) = \int_0^{+\infty} \phi(r\cos 2\varphi, r\sin 2\varphi)\, \mathrm{d}r \tag{5.24}$$

where r is the distance from the wedge edge to the observation point which is on one face of the wedge. $\delta_{F_1}(\phi)$ is thus the integral of ϕ on the face F_1 and $\delta_{F_2}(\phi)$ is the integral of ϕ on the face F_2. Thus, according to (5.22),

$$f^\epsilon = -\left[\triangle + e^{-2i\epsilon}\right]^{-1} (\alpha_1\, \delta_{F_1} + \alpha_2\, \delta_{F_2})\,. \tag{5.25}$$

Using (5.21), we finally have

$$v^\epsilon(\mathbf{x}) = v_1^\epsilon(x_1, y_1) + v_2^\epsilon(x_2, y_2) \quad \text{in} \quad \Omega_f \tag{5.26}$$

with

$$v_j^\epsilon(x_j, y_j) = -\left[\triangle + e^{-2i\epsilon}\right]^{-1} \left[\alpha_j(x_j, 0)\, \delta_{F_j}\right]. \tag{5.27}$$

The double Fourier transform of (5.27) calculated using (5.15), gives the following relation

$$\hat{v_j^\epsilon} = \left[\xi^2 + \eta^2 - e^{-2i\epsilon}\right]^{-1} \hat{\alpha_j}. \tag{5.28}$$

The dimensionless velocity potential v_j^ϵ is then found by applying the inverse Fourier transform in ξ and η to (5.28):

$$v_j^\epsilon = \frac{1}{4\pi^2} \iint_{\mathbb{R}^2} \hat{v_j^\epsilon}\, e^{i(x_j\xi + y_j\eta)}\, \mathrm{d}\xi\, \mathrm{d}\eta. \tag{5.29}$$

Let us defined

$$L^\epsilon(\xi, y_j) = \int_{-\infty}^{+\infty} \frac{e^{iy_j\eta}}{\xi^2 + \eta^2 - e^{-2i\epsilon}} \mathrm{d}\eta. \tag{5.30}$$

Using (5.28), the dimensionless velocity potential v_j^ϵ in (5.29) therefore depends on L^ϵ as

$$v_j^\epsilon = \frac{1}{4\pi}\int_{-\infty}^{+\infty} L^\epsilon(\xi, y_j)\,\hat{\alpha_j}(\xi)\,e^{ix_j\xi}\mathrm{d}\xi. \tag{5.31}$$

For $\epsilon \neq 0$, integral (5.30) converges because its numerator $\xi^2 + \eta^2 - e^{-2i\epsilon}$ is not defined for

$$\eta = \pm\sqrt{e^{-2i\epsilon} - \xi^2} = \pm\zeta_0^\epsilon \tag{5.32}$$

which is a complex number. Integration in (5.30) is along the real axis, thus this pole ζ_0^ϵ will never be crossed by the integration contour of (5.30) (the real axis) for $\epsilon \neq 0$. In that case, integral (5.30) could then be calculated using the residue theorem which leads to the following result

$$L^\epsilon(\xi, y_j) = (\pi i)\frac{e^{i|y_j|\zeta_0^\epsilon}}{\zeta_0^\epsilon}. \tag{5.33}$$

Using (5.33) in (5.31), for $\epsilon \neq 0$, the dimensionless velocity potential v_j^ϵ simplifies to

$$v_j^\epsilon(x_j, y_j) = \frac{i}{4\pi}\int_{-\infty}^{+\infty} \frac{e^{i|y_j|\zeta_0^\epsilon(\xi)}e^{ix_j\xi}}{\zeta_0^\epsilon(\xi)}\hat{\alpha_j}(\xi)\,\mathrm{d}\xi. \tag{5.34}$$

This velocity potential repects the absorption principle at infinity if the real part of $i|y_j|\zeta_0^\epsilon$ is negative so that the exponential in the integral decreases with the distance y_j. That relation means that $\mathrm{Im}(\zeta_0^\epsilon) > 0$. Function $\zeta_0^\epsilon(\xi)$ then satisfies for ξ real

$$\zeta_0^\epsilon(\xi) = i\sqrt{\xi^2 - e^{-i\epsilon}} \text{ si } |\xi| \geq 1, \tag{5.35a}$$

$$\zeta_0^\epsilon(\xi) = -\sqrt{e^{-i\epsilon} - \xi^2} \text{ si } |\xi| \leq 1. \tag{5.35b}$$

The branch points of the function $\zeta_0^\epsilon(\xi)$ are $\pm\,e^{-i\epsilon} = \pm\cos(\epsilon) \mp i\sin(\epsilon)$. For $\epsilon > 0$, integral (5.34) is well defined because the singular points of the integrand of (5.34), the branch points of ζ_0^ϵ which are also the integrand poles, are complex and are therefore never crossed by the integration contour which is the real axis. The integration contour of (5.34), the real axis, is deformed into the contour Γ_0 illustrated on Fig. 5.2 so that these singular points $\pm\,e^{-i\epsilon}$ are still not crossed by the new contour Γ_0 when $\epsilon \to 0$. Arrows $\mathcal{F}_1$ and $\mathcal{F}_2$ on Fig. 5.2 are described later in section 5.3.2.2.

Thus, even for $\epsilon = 0$, integral

$$v_j^0(x_j, y_j) = \frac{i}{4\pi}\int_{\Gamma_0} \frac{e^{i|y_j|\zeta_0^0(\xi)}e^{ix_j\xi}}{\zeta_0^0(\xi)}\hat{\alpha_j}(\xi)\,\mathrm{d}\xi \tag{5.36}$$

is a convergent integral. Using (5.18) and (5.26), our initial solution is then

$$v(\mathbf{x}) = v_1^0(x_1, y_1) + v_2^0(x_2, y_2) \tag{5.37}$$

with $v_j^0(x_j, y_j)$ being expressed in (5.36). Let us now find the far-field approximation of the solution (5.37).

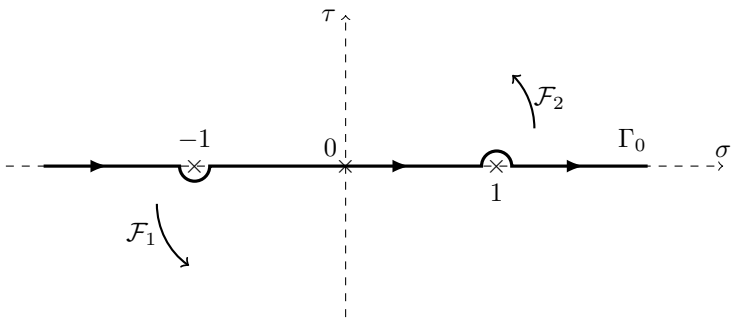

Figure 5.2: Integration contour Γ_0 in the complex plane $\xi = \sigma + i\tau$. Arrows $\mathcal{F}_1$ and $\mathcal{F}_2$ show the deformation of Γ_0 into the imaginary axis.

5.2.2 High frequency approximation of the scattered field

Variable change $\xi = \cos\beta$, $\mathrm{d}\xi = -\sin\beta\,\mathrm{d}\beta$ allows us to transform (5.36) for $j = 1$ in

$$v_1^0(r\cos\theta, r\sin\theta) = \frac{i}{4\pi}\int_{C_0} e^{ir(\cos\beta\cos\theta - |\sin\theta|\sin\beta)}\hat{\alpha}_1(\cos\beta)\,\mathrm{d}\beta, \tag{5.38}$$

where C_0 is depicted on Fig. 5.3.

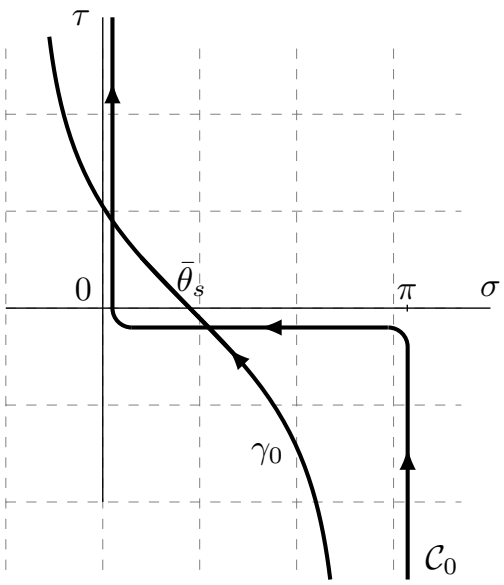

Figure 5.3: Integration path $\mathcal{C}_0$ and the steepest descent path γ_0 in the complex plane $\lambda = \sigma + i\tau$. $\bar{\theta}_s$ is the phase stationary point.

Let us introduce the variable $\bar{\theta}$ defined as

$$\begin{cases} \bar{\theta} = \theta & \text{if } \theta < \pi \\ \bar{\theta} = 2\pi - \theta & \text{if } \theta \geq \pi \end{cases}. \tag{5.39}$$

Finally, using (5.39) in (5.38), we have

$$v_1^0(r\cos\theta, r\sin\theta) = \frac{i}{4\pi}\int_{C_0} e^{ir\cos(\beta+\bar{\theta})}\hat{\alpha}_1(\cos\beta)\,\mathrm{d}\beta. \tag{5.40}$$

The same process is applied to (5.36) for $j = 2$ and leads to

$$v_2^0(r\cos(\varphi-\theta), r\sin(\varphi-\theta)) = \frac{i}{4\pi}\int_{C_0} e^{ir\cos(\beta+\overline{2\varphi-\theta})}\hat{\alpha}_2(\cos\beta)\,\mathrm{d}\beta \tag{5.41}$$

with $\overline{2\varphi-\theta}$ defined in the same way as (5.39). The saddle point of this two last equations, is respectively $\beta = \bar{\theta}_s = \pi - \bar{\theta}$ and $\beta = \bar{\theta}_s = \pi - \overline{2\varphi-\theta}$. These saddle points are always in the interval $[0, \pi]$. Poles of the integrand functions $\hat{\alpha}_1$ and $\hat{\alpha}_2$ can be crossed during the deformation contour of C_0 into the steepest descent path γ_0 (see Fig. 5.3). Since the imaginary part of the poles of $\hat{\alpha}_1$ and $\hat{\alpha}_2$ is always positive (see section 5.3.2.1), poles of $\hat{\alpha}_1$ which are crossed are

$$\{\theta_1^k \mid \mathrm{Re}(\theta_1^k) \leq \pi - \bar{\theta})\}, \quad k \in \mathbb{N} \tag{5.42}$$

and those of $\hat{\alpha}_2$ are

$$\{\theta_2^k \mid \mathrm{Re}(\theta_2^k) \leq \pi - \overline{2\varphi-\theta})\}, \quad k \in \mathbb{N}. \tag{5.43}$$

Being crossed, these poles contribute to the integrals (5.36) and lead to the geometrical field. Their contribution is calculated using the residue theorem and is respectively:

$$v_1^{0(\mathrm{poles})}(x_1, y_1) = \frac{1}{2}\frac{V_1^k}{\sin\theta_1^k}\, e^{ir\cos\left(\theta_1^k+\bar{\theta}\right)}, \quad k \in \mathbb{N} \tag{5.44}$$

and

$$v_2^{0(\mathrm{poles})}(x_2, y_2) = \frac{1}{2}\frac{V_2^k}{\sin\theta_2^k}\, e^{ir\cos\left(\theta_2^k+\overline{2\varphi-\theta}\right)}, \quad k \in \mathbb{N} \tag{5.45}$$

with V_1^k and V_2^k being the residues of the poles θ_1^k and θ_2^k to the spectral functions $\hat{\alpha}_1$ and $\hat{\alpha}_2$ respectively. These poles and their corresponding residues are determined in section 5.3.2.1. The contribution of the poles θ_1^k in (5.44) [θ_2^k in (5.45) respectively] corresponds to the incident (for the first pole, $k = 1$) and reflected waves ($k > 1$) on the F_1 (F_2 respectively) face of the wedge.

The contribution of the integrand crossed poles during the contour deformation having been calculated, the resulting integral after the contour deformation is approximated using the steepest

descent method (see appendix A.2). The contribution of the saddle points $\bar{\theta}_s$ is respectively:

$$v_1^{0(\text{diff})}(x_1, y_1) = \frac{e^{-i\frac{\pi}{4}}}{2\sqrt{2\pi}} \frac{e^{-ir}}{\sqrt{r}} \hat{\alpha}_1(-\cos\theta) \tag{5.46}$$

and

$$v_2^{0(\text{diff})}(x_2, y_2) = \frac{e^{-i\frac{\pi}{4}}}{2\sqrt{2\pi}} \frac{e^{-ir}}{\sqrt{r}} \hat{\alpha}_2(-\cos(2\varphi - \theta)). \tag{5.47}$$

Finally at far-field, $r \gg 1$, using (5.37), (5.44) - (5.47), the GTD total field is

$$v^{\text{tot(GTD)}} = v^{(\text{GE})} + v^{\text{diff(GTD)}} \tag{5.48}$$

where

$$v^{(\text{GE})} = \sum_k \frac{V_1^k}{2\sin\theta_1^k} e^{ir\cos\left(\theta_1^k + \bar{\theta}\right)} H(\pi - \bar{\theta} - \text{Re}(\theta_1^k)) + \frac{V_2^k}{2\sin\theta_2^k} e^{ir\cos\left(\theta_2^k + \bar{\theta}\right)} H(\pi - \overline{2\varphi - \theta} - \text{Re}(\theta_2^k)) \tag{5.49}$$

and

$$v^{\text{diff(GTD)}} = \frac{e^{-i\frac{\pi}{4}}}{2\sqrt{2\pi}} \frac{e^{-ir}}{\sqrt{r}} [\hat{\alpha}_1(-\cos\theta) + \hat{\alpha}_2(-\cos(2\varphi - \theta))]. \tag{5.50}$$

Using (5.5) and (5.50), the GTD diffraction coefficient is defined as

$$D^{\text{GTD}} = \frac{e^{-i\frac{\pi}{4}}}{\sqrt{2\pi}} [\hat{\alpha}_1(-\cos\theta) + \hat{\alpha}_2(-\cos(2\varphi - \theta))] \tag{5.51}$$

where $\hat{\alpha}_1$ and $\hat{\alpha}_2$ are unknown spectral functions.

An analytic expression of the diffraction coefficient of the scattering of a plane wave with a wedge at interfaces fluid/void is known. This analytic expression is obtained using the Sommerfeld integral method. Bo [84] gives its expression in his thesis for a wedge at interfaces fluid/solid (Neumann boundary conditions). For the Dirichlet boundary conditions, there is a change of sign to consider [12, 17]:

$$\begin{aligned} D^{\text{GTD(Som)}} = \frac{e^{i\frac{\pi}{4}}}{2n\sqrt{2\pi}} \Bigg[& \cot\left(\frac{\pi + (\theta + \theta_{\text{inc}})}{2n}\right) + \cot\left(\frac{\pi - (\theta + \theta_{\text{inc}})}{2n}\right) \\ & - \cot\left(\frac{\pi + (\theta - \theta_{\text{inc}})}{2n}\right) - \cot\left(\frac{\pi - (\theta + \theta_{\text{inc}})}{2n}\right) \Bigg] \end{aligned} \tag{5.52}$$

with $n = 2\varphi/\pi$.

One of the aims of this chapter is to compute the spectral functions $\hat{\alpha}_1(\xi)$ and $\hat{\alpha}_2(\xi)$ in order to find the GTD diffraction coefficient (5.51). The accuracy of the spectral functions method could therefore be evaluated by comparing results of (5.51) with (5.52). The section 5.3 is then devoted to the computation of the spectral functions $\hat{\alpha}_1$ and $\hat{\alpha}_2$.

5.3 Spectral functions computation

To compute the spectral functions, many steps are necessary. Let us begin by determining the functional equations satisfied by spectral functions $\hat{\alpha}_1$ and $\hat{\alpha}_2$.

5.3.1 Functional equations of spectral functions

The velocity potential in the boundary conditions of the system (5.13) is substituted by its expression (5.37). It then leads to the following system of equations for the boundary conditions on each wedge face:

$$\begin{cases} v_1^0(x_1,0) + v_2^0(x_2\cos 2\varphi, x_2 \sin 2\varphi) = -v_{\text{inc}}^0 \mid_{F_1} \\ v_1^0(x_1\cos 2\varphi, x_1 \sin 2\varphi) + v_2^0(x_2,0) = -v_{\text{inc}}^0 \mid_{F_2} \end{cases}. \tag{5.53}$$

Using the potential velocity expression on each face of the wedge given in Eq. (5.36), we have

$$v_j^0(x_j,0) = \frac{i}{4\pi}\int_{\Gamma_0} \frac{e^{ix_j\xi}}{\zeta_0^0(\xi)}\,\hat{\alpha}_j(\xi)\,\mathrm{d}\xi \tag{5.54a}$$

$$\text{and} \quad v_j^0(x_j\cos 2\varphi, x_j\sin 2\varphi) = \frac{i}{4\pi}\int_{\Gamma_0} \frac{e^{ix_j(\xi\,\cos 2\varphi + |\sin 2\varphi|\,\zeta_0^0(\xi))}}{\zeta_0^0(\xi)}\,\hat{\alpha}_j(\xi)\,\mathrm{d}\xi. \tag{5.54b}$$

Applying the Fourier transform [see Eq. (5.14)] to (5.54a), we have

$$\mathcal{F}(x_j \mapsto v_j^0(x_j,0))(\xi) = \frac{i}{4\pi}\int_{\Gamma_0} \frac{\hat{\alpha}_j(\lambda)}{\zeta_0^0(\lambda)}\left(\int_0^\infty e^{-ix_j(\xi-\lambda)}dx_j\right)\mathrm{d}\lambda, \tag{5.55}$$

$$= \frac{1}{4\pi}\int_{\Gamma_0} \frac{\hat{\alpha}_j(\lambda)}{\zeta_0^0(\lambda)(\xi-\lambda)}\mathrm{d}\lambda$$

and

$$\mathcal{F}\left(x_j \mapsto v_j^0\left(x_j\cos 2\varphi, x_j\sin 2\varphi\right)\right)(\xi) = \frac{i}{4\pi}\int_{\Gamma_0} \frac{\hat{\alpha}_j(\lambda)}{\zeta_0^0(\lambda)}\left(\int_0^\infty e^{-ix_j\left(\xi-\lambda\,\cos 2\varphi - |\sin 2\varphi|\,\zeta_0^0(\lambda)\right)}dx_j\right)\mathrm{d}\lambda, \tag{5.56}$$

$$= \frac{1}{4\pi}\int_{\Gamma_0} \frac{\hat{\alpha}_j(\lambda)}{\zeta_0^0(\lambda)\left[\xi-\lambda\,\cos 2\varphi - |\sin 2\varphi|\,\zeta_0^0(\lambda)\right]}\mathrm{d}\lambda.$$

At the right side of (5.53), we have the incident field on each face of the wedge. According to

Eq. (5.12), the dimensionless incident wave on the faces F_1 and F_2 of the wedge is respectively:

$$v^0_{\text{inc}}(x_1,0) = \frac{1}{2}\, e^{i\, x_1 \cos\theta_{\text{inc}}}, \tag{5.57a}$$

$$v^0_{\text{inc}}(x_2,0) = \frac{1}{2}\, e^{i\, x_2 \cos(2\varphi-\theta_{\text{inc}})}. \tag{5.57b}$$

The Fourier transform [see Eq. (5.14)] is also applied to (5.57) and gives us the following expressions

$$\begin{aligned}\mathcal{F}(x_1 \mapsto v^0_{\text{inc}}(x_1,0))(\xi) &= \frac{1}{2}\int_0^\infty e^{-ix_1(\xi-\cos\theta_{\text{inc}})}dx_1, \\ &= \frac{1}{2i(\xi-\cos\theta_{\text{inc}})},\end{aligned} \tag{5.58}$$

and

$$\begin{aligned}\mathcal{F}(x_2 \mapsto v^0_{\text{inc}}(x_2,0))(\xi) &= \frac{1}{2}\int_0^\infty e^{-ix_2(\xi-\cos(2\varphi-\theta_{\text{inc}}))}dx_2, \\ &= \frac{1}{2i(\xi-\cos(2\varphi-\theta_{\text{inc}}))}.\end{aligned} \tag{5.59}$$

Therefore, applying the Fourier transform to (5.53) leads to the following functional system of equations:

$$\begin{cases} DM(\Sigma_1)(\xi) + TM(\Sigma_2)(\xi) = \dfrac{1}{\xi - Z_1} \\ TM(\Sigma_1)(\xi) + DM(\Sigma_2)(\xi) = \dfrac{1}{\xi - Z_2} \end{cases} \tag{5.60}$$

where $Z_1 = \cos\theta_{\text{inc}}$, $Z_2 = \cos(2\varphi - \theta_{\text{inc}})$, $\Sigma_1 = \hat{\alpha}_1$, $\Sigma_2 = \hat{\alpha}_2$, DM is an integral operator defined as

$$DM(\Sigma_1)(\xi) = \int_{\Gamma_0} DM(\xi,\lambda)\,\Sigma_1(\lambda)\,\mathrm{d}\lambda \tag{5.61}$$

with

$$DM(\xi,\lambda) = \frac{1}{2i\pi}\frac{m(\lambda)}{\xi-\lambda} \tag{5.62}$$

where

$$m(\lambda) = \frac{1}{\zeta^0_0(\lambda)}, \tag{5.63}$$

and TM is also an integral operator defined as

$$TM(\Sigma_1)(\xi) = \int_{\Gamma_0} TM(\xi,\lambda)\,\Sigma_1(\lambda)\,\mathrm{d}\lambda \tag{5.64}$$

with

$$TM(\xi,\lambda) = \frac{1}{2i\pi}\frac{m(\lambda)}{\xi - \lambda\cos 2\varphi - |\sin 2\varphi|\zeta^0_0(\lambda)}. \tag{5.65}$$

Note that the function TM can be expressed as

$$TM(\xi,\lambda) = \frac{1}{2i\pi}\frac{m(\lambda)}{\xi - T_0(\lambda)}, \tag{5.66}$$

where

$$T_0(\lambda) = \lambda\cos\widetilde{2\varphi} - \sin\widetilde{2\varphi}\,\zeta_0^0(\lambda) = \cos(\theta + \widetilde{2\varphi}) \quad \text{if} \quad z = \cos\theta \tag{5.67}$$

with

$$\widetilde{2\varphi} = 2\varphi \quad \text{if} \quad 0 < 2\varphi < \pi \qquad \text{and} \qquad \widetilde{2\varphi} = 2\pi - 2\varphi \quad \text{if} \quad \pi < 2\varphi < 2\pi. \tag{5.68}$$

In all cases, $\widetilde{2\varphi} \in]0,\pi[$. T_0 function is similar to the translation operator of the Laplace transform method defined in (4.101) in section 4.2.2 of the chapter 4.

This function T_0 in (5.67) operates in the domain

$$T_0 : \Omega_0 \longrightarrow \mathbb{C} \tag{5.69}$$

where the domain Ω_0 is defined as

$$\Omega_0 = \{\xi \in \mathbb{C},\ \xi = \cos\theta,\ 0 < \mathrm{Re}\,\theta < \pi - \widetilde{2\varphi}\}. \tag{5.70}$$

Knowing that in the complex plane $\theta = \sigma + i\tau$,

$$\cos\theta = \cos\sigma\ \cosh\tau + i\sin\sigma\ \sinh\tau, \tag{5.71}$$

the upper boundary of Ω_0 which is for $\mathrm{Re}\,\theta = \sigma = \pi - \widetilde{2\varphi}$ is parametrized by

$$\xi = \cos\theta = -\cos\widetilde{2\varphi}\ (\cosh\tau - i\sinh\tau), \quad \tau \in \mathbb{R}. \tag{5.72}$$

This last equation is the parametric equation of an hyperbola in the complex plane. Domain Ω_0 is therefore delineated by the hyperbola

$$\partial\Omega_0^+ = \{\xi \in \mathbb{C}, \xi = \cos\theta, \mathrm{Re}\,\theta = \pi - \widetilde{2\varphi}\}. \tag{5.73}$$

Domain Ω_0 and its upper boundary $\partial\Omega_0^+$ are illustrated on Fig. 5.4. Domain Ω_0 is the dotted area in Fig. 5.4. Its lower boundary is the semi-axis $[-\cos\widetilde{2\varphi}, +\infty[$. Arrows $\mathcal{F}_1$ and $\mathcal{F}_2$ on Fig. 5.4 are described later in section 5.3.2.

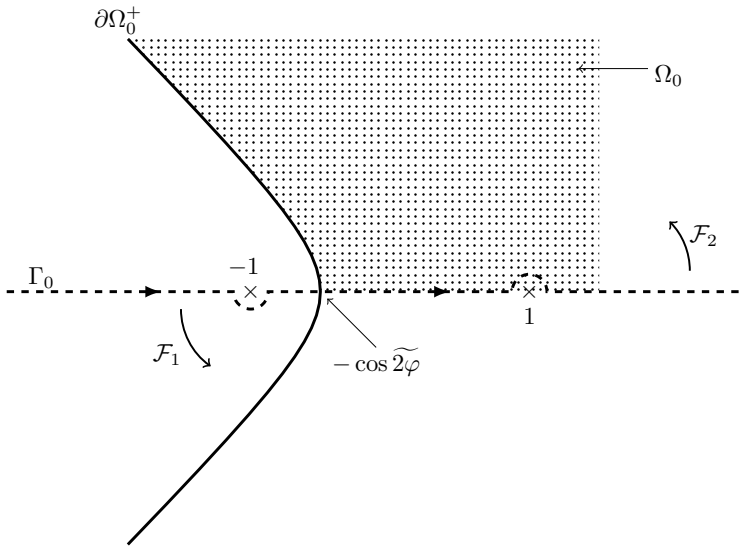

Figure 5.4: Domain Ω_0 (the dotted area) and its upper boundary $\partial\Omega_0^+$. The lower boundary of Ω_0 is the semi-axis $[-\cos\widetilde{2\varphi}, +\infty[$. Arrows $\mathcal{F}_1$ and $\mathcal{F}_2$ show the deformation of Γ_0 (in thick dashed line) into $\partial\Omega_0^+$.

Having found our system of functional equations, let us now resolve it following the methodology of [11].

5.3.2 System resolution

The resolution of the system of functional equations (5.60) will allows us to find the value of the spectral function $\Sigma_1 = \hat{\alpha}_1$ and $\Sigma_2 = \hat{\alpha}_2$. With these values, the diffraction coefficients could be computed [see Eq. (5.51)].

According to [11], DM and TM integral operators are constituted of a "singular term" and of a "regular term". They show that for a singular function

$$\phi(\xi) = \frac{V}{\xi - z}, \quad V \in \mathbb{C} \quad \text{and} \quad z \in \mathbb{C}\backslash]-\infty, -1] \text{ with } \operatorname{Im} z \geqslant 0, \tag{5.74}$$

DM and TM integral operators defined respectively in (5.61) and (5.64) could be decomposed using the residue theorem (explained in the sequel) as

$$DM(\phi)(\xi) = \int_{\Gamma_0} DM(\xi, \lambda) \cdot \frac{V}{\lambda - z}\, \mathrm{d}\lambda = \frac{m(z) \cdot V}{\xi - z} + D_p(V, z)(\xi), \tag{5.75a}$$

$$TM(\phi)(\xi) = \int_{\Gamma_0} TM(\xi, \lambda) \cdot \frac{V}{\lambda - z}\, \mathrm{d}\lambda = \frac{m(z) \cdot V}{\xi - T_0(z)} \mathbb{1}(z \in \Omega_0) + T_p(V, z)(\xi), \tag{5.75b}$$

where the function T_0 is defined in (5.67) and where

$$\mathbb{1}(z \in \Omega_0) = \begin{cases} 1 & \text{if } z \in \Omega_0, \\ 0 & \text{else} \end{cases} \tag{5.76}$$

and integrals D_p and T_p are holomorphic on $\mathbb{C}\backslash]-\infty, -1]$. Such integrals are expressed as

$$D_p(h,z)(\xi) = \int_{\Gamma_1} DM(\xi,\lambda) \cdot \frac{V}{\lambda - z} \mathrm{d}\lambda, \tag{5.77a}$$

$$T_p(h,z)(\xi) = \frac{1}{2\pi i} \int_{\partial\Omega_0^+} \frac{m(\lambda)}{\xi - T_0(\lambda)} \cdot \frac{V}{\lambda - z} \mathrm{d}\lambda. \tag{5.77b}$$

Contours Γ_1 and $\partial\Omega_0^+$ are illustrated on Figs. 5.5 and 5.4 respectively.

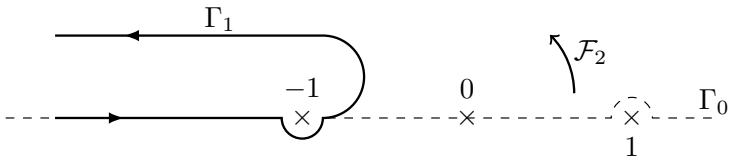

Figure 5.5: Contour Γ_1. Arrow $\mathcal{F}_2$ shows the deformation of Γ_0 (in dashed line) into Γ_1.

Decomposition (5.75) is obtained by applying the residue theorem when deforming contour Γ_0 into Γ_1 for DM and into $\partial\Omega_0^+$ for TM. The contribution of the integrand poles crossed during this contour deformation must be taken into account. The function ϕ in (5.74) has a pole at $\xi = z$, $z \in \mathbb{C}\backslash]-\infty, -1]$ with $\operatorname{Im} z \geqslant 0$. The imaginary part of this pole is therefore positive. Thus, in (5.75a), the integrand pole $\lambda = z$ is always crossed when deforming Γ_0 into Γ_1 since the $\mathcal{F}_2$ arrow in Fig. 5.5 shows that to obtain Γ_1, the right part of the contour Γ_0, $]-1, +\infty[$, crosses the upper half-plane $\{\lambda \in \mathbb{C}, \operatorname{Im}(\lambda) > 0\}$ during the deformation contour. On the same way, in (5.75b), the integrand pole $\lambda = z$ is crossed when deforming Γ_0 into $\partial\Omega_0^+$ if it is in Ω_0 since the $\mathcal{F}_2$ arrow in Fig. 5.4 shows that to obtain $\partial\Omega_0^+$, the right part of the contour Γ_0, $]-\cos\widetilde{2\varphi}, +\infty[$, crosses the domain Ω_0 during the deformation contour. That is why in (5.75b), the pole contribution exists only for $z \in \Omega_0$.

The contribution of the integrand poles in (5.75) constitutes the "singular term" of the DM and TM integral operators. D_p and T_p are called "regular terms" because they are holomorphic on $\mathbb{C}\backslash]-\infty, -1]$. This decomposition (5.75) of the DM and TM operators has been established for an arbitrary singular function ϕ in (5.74). In the sequel, using the decomposition of the DM and TM operator for a function of the form of (5.74), it will be showed that the unknown spectral functions Σ_1 and Σ_2 in the system (5.60) have a singular part. In another words, it will allow us to find the poles of the spectral functions with their respective residue. This singular part leads

to the geometrical field when doing the far-field approximation of the exact solution as seen in section 5.2.2.

The first step for the resolution of the system (5.60) is then to determine the singular part of these spectral functions.

5.3.2.1 Singular part

It is well known that poles of the spectral functions lead to incident and reflected field on the wedge faces (see section 5.2.2). As said previously, the singular part of the spectral functions contains poles. In order to determine these poles, we need a start point. As for the Sommerfeld algorithm of pole propagation detailed in section 4.2.1, the initial poles correspond to those which lead to the incident field on the face wedges. Here, the symmetry of the problem is not used meaning that we do not introduce the symmetry of the incident wave with respect to the wedge bisector as in the Sommerfeld approach in section 4.2.1.

Knowing the incident field, on the wedge faces, we then define the spectral function Σ_j as

$$\Sigma_j(\xi) = \frac{V_j}{\xi - Z_j} + X_j'(\xi), \quad j = 1, 2 \tag{5.78}$$

where

$$Z_1 = \cos\theta_{\text{inc}} \tag{5.79a}$$

$$Z_2 = \cos(2\varphi - \theta_{\text{inc}}) \tag{5.79b}$$

are the initial poles with unknown residue V_1 and V_2 and the functions X_j' are unknown, $j = 1, 2$. From (5.75a), we know that

$$DM(\Sigma_j)(\xi) = \frac{m(Z_j) \cdot V_j}{\xi - Z_j} + D_p(V_j, Z_j)(\xi) + DM(X_j')(\xi). \tag{5.80}$$

If we choose $V_j = m^{-1}(Z_j)$, the right hand side of the system (5.60) is suppressed by the first term in the right hand side of (5.80). The system (5.60) then becomes

$$\begin{cases} DM(X_1')(\xi) + TM(X_2')(\xi) = -TM\left(\dfrac{V_2}{\xi - Z_2}\right)(\xi) - D_p(V_1, Z_1)(\xi) \\ \\ TM(X_1')(\xi) + DM(X_2')(\xi) = -TM\left(\dfrac{V_1}{\xi - Z_1}\right)(\xi) - D_p(V_2, Z_2)(\xi) \end{cases}. \tag{5.81}$$

Besides, from (5.75b), we know that

$$TM\left(\frac{V_j}{\xi - Z_j}\right)(\xi) = \frac{m(Z_j) \cdot V_j}{\xi - T_0(Z_j)} \mathbb{1}(Z_j \in \Omega_0) + T_p(V_j, Z_j)(\xi). \tag{5.82}$$

Thus, in the first line of the system (5.81), X_1' has a pole at $\xi = Z_1^2 = T_0(Z_2)$ if $Z_2 \in \Omega_0$ and similarly in its second line, X_2' has a pole at $\xi = Z_2^2 = T_0(Z_1)$ if $Z_1 \in \Omega_0$. The superscript "2" used in Z_j^2, $j = 1, 2$ refers to the second pole of the spectral functions Σ_j. T_0 function defined in (5.67) is then called translation operator because it translates a pole of the spectral function Σ_j, $j = 1, 2$, to a pole of the spectral function Σ_k, $k = 1, 2$, $k \neq j$. $Z_j^2 = T_0(Z_k)$, $k \neq j$ is linked to the reflected wave of the incident wave on the face F_k which is incident on the face F_j of the wedge. The unknown function X_j' in (5.78) is then decomposed as

$$X_j'(\xi) = \frac{V_j^2}{\xi - Z_j^2} + X_j''(\xi), \quad j = 1, 2 \tag{5.83}$$

where $Z_j^2 = T_0(Z_k), k = 1, 2$ and $k \neq j$ is the generated pole, V_j^2 is its corresponding residue and the function X_j'' is unknown. At this stage, substituting (5.83) in (5.78), spectral function has then the following decomposition:

$$\Sigma_j(\xi) = \frac{V_j}{\xi - Z_j} + \frac{V_j^2}{\xi - Z_j^2} + X_j''(\xi), \quad j = 1, 2. \tag{5.84}$$

Let us choose the residues of these generated poles Z_j^2, $j = 1, 2$, as

$$V_j^2 = -m^{-1}(Z_j^2)m(Z_k)V_k \mathbb{1}(Z_k \in \Omega_0), \quad j, k \in \{1, 2\}, k \neq j \quad \text{and} \quad Z_j^2 = T_0(Z_k), \tag{5.85}$$

so that the singular term of $DM(X_j')(\xi)$ using the formula (5.75a) suppress the singular term in the TM operator in (5.82). With this process, the poles $\xi = Z_j^2$ in the system of functional equations are eliminated as it has been the case for the initial poles Z_1 and Z_2. The system (5.81) is then one more time modified and yields

$$\begin{cases} DM(X_1'')(\xi) + TM(X_2'')(\xi) = -TM\left(\dfrac{V_2^2}{\xi - T_0(Z_2)}\right)(\xi) - D_p(V_1, Z_1)(\xi) - T_p(V_2, Z_2)(\xi) \\ -D_p(V_2^2, T_0(Z_2))(\xi) \\ \\ TM(X_1'')(\xi) + DM(X_2'')(\xi) = -TM\left(\dfrac{V_1^2}{\xi - T_0(Z_1)}\right)(\xi) - D_p(V_2, Z_2)(\xi) - T_p(V_1, Z_1)(\xi) \\ -D_p(V_1^2, T_0(Z_1))(\xi) \end{cases} . \tag{5.86}$$

This new system has the same structure as the one of (5.81). The pole propagation process is the same used for the determination of poles Z_j^2 with their respective residue. This process stops when the generated poles are no longer in the domain Ω_0 defined in (5.70). All the generated poles then belong to Ω_0. Their imaginary part is then always positive due to the definition of the domain Ω_0 (see Fig. 5.4).

At the end of this process, spectral functions have the decomposition

$$\Sigma_j = Y_j + X_j, \tag{5.87}$$

where Y_j is the singular part (it contains the poles), X_j is the regular part and $j = 1, 2$ is the face index. The singular part is expressed as

$$Y_j(\xi) = \sum_i \frac{V_j^i}{\xi - Z_j^i}, \tag{5.88}$$

where $i \in \mathbb{N}*$, $Z_j^1 = Z_j$ defined in (5.79) is the initial pole on each face of the wedge,

$$Z_j^{i+1} = T_0(Z_k^i), \quad j,k \in \{1,2\}, \quad k \neq j \tag{5.89}$$

are the different generated poles with their respective residue

$$V_j^{i+1} = -m^{-1}(T_0(Z_k^i))\, m(Z_k^i))\, V_k^i\, \mathbb{1}(Z_k^i \in \Omega_0), \quad k \neq j. \tag{5.90}$$

These generated poles can be put in the form

$$Z_j^i = \cos\theta_j^i. \tag{5.91}$$

This form has been used in section 5.2.2 for the determination of the geometrical field.

The singular part of the spectral functions is sufficient to calculate the geometrico-elastodynamic field as seen in section 5.2.2 in Eqs. 5.44 and (5.45). There are completely known with this pole propagation process (5.88). However, to determine the diffracted field, both singular and regular parts of the spectral functions are required since the diffracted field expressed in (5.50) depend on the spectral function $\Sigma_1 = \hat{\alpha}_1$ [see (5.87) for $j = 1$] and $\Sigma_2 = \hat{\alpha}_2$ [see (5.87) for $j = 2$]. Determination of the spectral function regular part is thus essential.

The second step of the system resolution is thus about the determination of the regular part X_j of the spectral function Σ_j [see Eq. (5.87)]. The regular part is determined by using the Galerkin collocation method. Section 5.3.2.2 gives the principal steps of this resolution method.

5.3.2.2 Regular part

After the determination of all the poles which constitute the singular part of the solution using the pole propagation process explained in section 5.3.2.1, the remaining right hand side of (5.60) is composed of D_p and T_p functions. Thus, the system 5.60 becomes by construction

$$\begin{cases} DM(X_1)(\xi) + TM(X_2)(\xi) = -\sum_k \left(D_p(V_1^k, Z_1^k)(\xi) + T_p(V_2^k, Z_2^k)(\xi) \right) \\ TM(X_1)(\xi) + DM(X_2)(\xi) = -\sum_k \left(T_p(V_1^k, Z_1^k)(\xi) + D_p(V_2^k, Z_2^k)(\xi) \right) \end{cases}, \tag{5.92}$$

where X_j, $j = 1, 2$ are the regular part of the spectral function (5.87), D_p and T_p functions are defined in (5.77) and Z_j^k are the poles of the spectral function Σ_j with their respective residue V_j^k. These poles are determined in section 5.3.2.1. D_p and T_p functions being holomorphic functions on $\mathbb{C}\backslash]-\infty, -1]$ according to [11], the right hand side of this new system (5.92) is then also holomorphic on $\mathbb{C}\backslash]-\infty, -1]$ and therefore the functions X_j are also holomorphic on this domain.

All distributions f on $\mathbb{R}^2$ which are holomorphic on $\mathbb{C}\backslash]-\infty, -1]$ could be written on the form

$$f(z) = \frac{1}{2\pi i} \int_{-\infty}^{-1} \frac{[f(\mu)]}{z - \mu} \, \mathrm{d}\mu \tag{5.93}$$

according to the Cauchy's integral formula where $[f(\mu)] = (f(\mu + i0^+) - f(\mu + i0^-)) \, \mathbb{1}(\mu \in]-\infty, -1])$ is the jump function. The measure $[f(\mu)] \, \mathrm{d}\mu$ can be approximated by diracs, $[f(\mu)] \, \mathrm{d}\mu = \sum p_k \delta_{\mu_k}$, $p_k \in \mathbb{C}$. The function f can therefore be approximated as

$$f(z) = \sum_{k=1}^{N} \frac{p_k}{z - \mu_k}, \ \mu_k \in]-\infty, -1], \ p_k \in \mathbb{C}. \tag{5.94}$$

The function $X_j(\xi)$ being holomorphic on $\mathbb{C}\backslash]-\infty, -1]$, it can be approximated as (5.94) in the basis φ_k, $1 \leq k \leq N$ given by

$$\varphi_k(\xi) = \frac{d_k}{\xi + a_k}, \ d_k \in \mathbb{C} \text{ and } a_k \in [1, \infty[. \tag{5.95}$$

The basis $(\varphi_1, \ldots, \varphi_N)$ generates a finite dimensional subspace of $L^2(\mathbb{R})$. The discretization of the solution $X_j(\xi)$ in this finite basis is called a Galerkin approximation.

In the sequel, the integration contour Γ_0 pictured on Fig. 5.2 is deformed into the imaginary axis. If $f(\lambda)$ is an holomorphic function on $\mathbb{C}\backslash]-\infty, -1]$, the function

$$\tilde{f}(y) = f(iy) \tag{5.96}$$

is introduced so that $\tilde{f}$ is holomorphic on $\mathbb{C} \setminus i[1, \infty[$. The variable change $\lambda = iy$ allows us to work with the Galerkin basis

$$e_{a_k}(y) = \frac{d_k}{y - ia_k} = i\tilde{\varphi}(y), \quad \text{with} \quad d_k \in \mathbb{C} \quad \text{and} \quad a_k \in [1, \infty[, \tag{5.97}$$

where $e_{a_k} \in L^2(\mathbb{R})$ and its $L^2(\mathbb{R})$ norm is

$$\begin{aligned} \|e_{a_k}\|^2_{L^2(\mathbb{R})} &= \int_{-\infty}^{\infty} e_{a_k}(y)\overline{e_{a_k}}(y)\mathrm{d}y \\ &= d_k^2 \int_{-\infty}^{\infty} \frac{1}{y^2 + {a_k}^2}\mathrm{d}y \\ &= \frac{\pi}{a_k} d_k^2. \end{aligned}$$

The $\bar{z}$ notation, z being complex, refers to the complex conjugate of z.

In order to have a unit Galerkin basis in $L^2(\mathbb{R})$, we choose

$$d_k = \sqrt{\frac{a_k}{\pi}}. \tag{5.98}$$

Having an approximation basis of the regular part of the spectral functions, $X_j(\xi)$ can therefore be expressed as

$$X_j(\xi) = \sum_{k=1}^{N} \tilde{X}_j^k \, \varphi_k(\xi), \quad \tilde{X}_j^k \in \mathbb{C}. \tag{5.99}$$

The coordinates $\tilde{X}_j^k$ are unknown. The system (5.92) then becomes

$$\begin{cases} \sum_{k=1}^{N} \left[\tilde{X}_1^k \int_{\Gamma_0} DM(\xi,\lambda)\varphi_k(\lambda)\,\mathrm{d}\lambda + \tilde{X}_2^k \int_{\Gamma_0} TM(\xi,\lambda)\varphi_k(\lambda)\,\mathrm{d}\lambda \right] = u_1(\xi), \\ \sum_{k=1}^{N} \left[\tilde{X}_1^k \int_{\Gamma_0} TM(\xi,\lambda)\varphi_k(\lambda)\,\mathrm{d}\lambda + \tilde{X}_2^k \int_{\Gamma_0} DM(\xi,\lambda)\varphi_k(\lambda)\,\mathrm{d}\lambda \right] = u_2(\xi), \end{cases} \tag{5.100}$$

where

$$u_1(\xi) = -\sum_k \Big(D_p(V_1^k, Z_1^k)(\xi) + T_p(V_2^k, Z_2^k)(\xi) \Big) \tag{5.101a}$$

$$\text{and} \quad u_2(\xi) = -\sum_k \Big(T_p(V_1^k, Z_1^k)(\xi) + D_p(V_2^k, Z_2^k)(\xi) \Big). \tag{5.101b}$$

The variable changes $\lambda = iy$ and $\xi = ix$ in (5.100) gives the following system

$$\begin{cases} \sum_{k=1}^{N} \left[\tilde{X}_1^k \int_{-\infty}^{\infty} \widetilde{DM}(x,iy)\, e_{a_k}(y)\mathrm{d}y + \tilde{X}_2^k \int_{-\infty}^{\infty} \widetilde{TM}(x,iy)\, e_{a_k}(y)\mathrm{d}y \right] = \tilde{u}_1(x) \\ \sum_{k=1}^{N} \left[\tilde{X}_1^k \int_{-\infty}^{\infty} \widetilde{TM}(x,iy)\, e_{a_k}(y)\mathrm{d}y + \tilde{X}_2^k \int_{-\infty}^{\infty} \widetilde{DM}(x,iy)\, e_{a_k}(y)\mathrm{d}y \right] = \tilde{u}_2(x) \end{cases}, \tag{5.102}$$

where $\widetilde{DM}(x,iy) = DM(ix,iy)$. Following [11], we introduce another subspace of finite di-

mension in $L^2(\mathbb{R})$ which is generated by vectors e_{b_k} defined as

$$e_{b_k}(y) = \frac{d_k}{y - ib_k}, \quad d_k = \sqrt{\frac{b_k}{\pi}} \tag{5.103}$$

with

$$\mathrm{Re}(b_k) \in [1, \infty[\quad \text{and} \quad \mathrm{Im}(b_k) = 0^-. \tag{5.104}$$

The b_k are called collocation points. The system (5.102) is projected in this subspace generated by vectors e_{b_k} in order to lead to a linear system of equations which could be inversed to find the coordinates $\tilde{X}_j^k$ of the regular part X_j of the spectral function Σ_j. With these collocation points, the integrals in the obtained linear system of equations can be calculated analytically. Using the dot product in $L^2(\mathbb{R})$, for a function $\phi \in L^2(\mathbb{R})$, the projection of $\tilde{\phi}(y) = \phi(iy)$ in the subspace of finite dimension in $L^2(\mathbb{R})$ generated by the vectors e_{b_k} is

$$\begin{aligned}
(\tilde{\phi}|e_{b_k})_{L^2(\mathbb{R})} &= \int_{-\infty}^{\infty} \tilde{\phi}(y)\, \overline{e_{b_k}}(y) \mathrm{d}y \\
&= d_k \int_{-\infty}^{\infty} \tilde{\phi}(y)\, \frac{1}{y + ib_k} \mathrm{d}y \\
&= (-2i\pi)\, d_k\, \tilde{\phi}(-ib_k) \\
&= (-2i\pi)\, d_k\, \phi(b_k).
\end{aligned} \tag{5.105}$$

Using (5.105), the projection of the system (5.102) in the subspace of finite dimension in $L^2(\mathbb{R})$ generated by the vectors e_{b_k} leads to the following new system

$$\begin{cases}
\sum_{k=1}^N \left[\tilde{X}_1^k \int_{-\infty}^{\infty} DM(b_1, iy) e_{a_k}(y)\, \mathrm{d}y + \tilde{X}_2^k \int_{-\infty}^{\infty} TM(b_1, iy) e_{a_k}(y)\, \mathrm{d}y\right] = u_1(b_1) \\
\sum_{k=1}^N \left[\tilde{X}_1^k \int_{-\infty}^{\infty} DM(b_2, iy) e_{a_k}(y)\, \mathrm{d}y + \tilde{X}_2^k \int_{-\infty}^{\infty} TM(b_2, iy) e_{a_k}(y)\, \mathrm{d}y\right] = u_1(b_2) \\
\qquad\qquad \vdots \\
\sum_{k=1}^N \left[\tilde{X}_1^k \int_{-\infty}^{\infty} DM(b_N, iy) e_{a_k}(y)\, \mathrm{d}y + \tilde{X}_2^k \int_{-\infty}^{\infty} TM(b_N, iy) e_{a_k}(y)\, \mathrm{d}y\right] = u_1(b_N) \\
\sum_{i=k}^N \left[\tilde{X}_1^k \int_{-\infty}^{\infty} TM(b_1, iy) e_{a_k}(y)\, \mathrm{d}y + \tilde{X}_2^k \int_{-\infty}^{\infty} DM(b_1, iy) e_{a_k}(y)\, \mathrm{d}y\right] = u_2(b_1) \\
\sum_{i=k}^N \left[\tilde{X}_1^k \int_{-\infty}^{\infty} TM(b_2, iy) e_{a_k}(y)\, \mathrm{d}y + \tilde{X}_2^k \int_{-\infty}^{\infty} DM(b_2, iy) e_{a_k}(y)\, \mathrm{d}y\right] = u_2(b_2) \\
\qquad\qquad \vdots \\
\sum_{i=k}^N \left[\tilde{X}_1^k \int_{-\infty}^{\infty} TM(b_N, iy) e_{a_k}(y)\, \mathrm{d}y + \tilde{X}_2^k \int_{-\infty}^{\infty} DM(b_N, iy) e_{a_k}(y)\, \mathrm{d}y\right] = u_2(b_N).
\end{cases} \tag{5.106}$$

Points $b_1, b_2, \ldots, b_N$ are collocation points. The obtained system (5.106) is a linear system of equations and can be put in a matrix format:

$$\begin{bmatrix} [D] & [T] \\ [T] & [D] \end{bmatrix} \begin{bmatrix} \bar{X}_1 \\ \bar{X}_2 \end{bmatrix} = \begin{bmatrix} U_1 \\ U_2 \end{bmatrix} \tag{5.107}$$

where

$$\bar{X}_j = \begin{bmatrix} \tilde{X}_j^1 \\ \vdots \\ \tilde{X}_j^N \end{bmatrix}, \tilde{X}_j^k \in \mathbb{C}; \quad U_j = \begin{bmatrix} u_j(b_1) \\ \vdots \\ u_j(b_N) \end{bmatrix}, u_j(b_k) \in \mathbb{C} \tag{5.108}$$

and

$$[D]_{lk} = \int_{-\infty}^{\infty} DM(b_l, iy) e_{a_k}(y)\, \mathrm{d}y \tag{5.109}$$

and

$$[T]_{lk} = \int_{-\infty}^{\infty} TM(b_l, iy) e_{a_k}(y)\, \mathrm{d}y \tag{5.110}$$

are the matrix elements of $[D]$ and $[T]$ respectively. System (5.107) can be rewritten as

$$\begin{cases} ([D] + [T])\,(\bar{X}_1 + \bar{X}_2) = U_1 + U_2 \\ ([D] - [T])\,(\bar{X}_1 - \bar{X}_2) = U_1 - U_2 \end{cases}. \tag{5.111}$$

To find the regular part of the spectral functions (5.99), its coordinates in the Galerkin basis φ_k, $1 \leq k \leq N$ defined in (5.95) must be determined. These coordinates are solutions of the linear system of equations (5.107) or (5.111). To resolve such a system, the matrices $[D]$ and $[T]$ and its right hand side $U_{1,2}$ must be calculated. Let us begin by determining $[D]$ and $[T]$ matrices.

Matrices calculation

A particularity of the chosen Galerkin basis φ_k, $1 \leq k \leq N$ in (5.97) is that it allows us to have an analytic expression of $[D]$ and $[T]$ matrices.

Using (5.62), the $[D]_{lk}$ elements defined in (5.109) could be expressed as

$$(-2i\pi)[D]_{lk} = -id_k \mathcal{D}(a_k, b_l) \tag{5.112}$$

with the function $\mathcal{D}(a, b)$ defined for $a > 1$ and $b > 1$ as

$$\mathcal{D}(a,b) = \int_{-\infty}^{+\infty} \frac{m(iy)}{y+ib} \frac{1}{y-ia} \mathrm{d}y = \int_{-\infty}^{+\infty} \frac{1}{y+ib} \frac{1}{y-ia} \frac{1}{\zeta_0^0(iy)} \mathrm{d}y. \tag{5.113}$$

Using (5.65), the $[T]_{lk}$ elements defined in (5.110) could be expressed as

$$(-2i\pi)[T]_{lk} = -d_k \mathcal{T}(a_k, b_l) \tag{5.114}$$

where the function $\mathcal{T}(a, b)$ is defined for $a > 1$ and $b > 1$ as

$$\mathcal{T}(a,b) = \int_{-\infty}^{+\infty} \frac{1}{b - iy\cos 2\varphi + |\sin 2\varphi|\sqrt{1+y^2}} \frac{1}{y-ia} \frac{1}{\zeta_0^0(iy)} \mathrm{d}y. \tag{5.115}$$

According to (5.35), $\mathcal{D}(a,b)$ and $\mathcal{T}(a,b)$ functions can be simplified using the relation

$$\zeta_0^0(iy) = -\sqrt{1+y^2}. \tag{5.116}$$

Let us first calculate the $\mathcal{T}(a,b)$ function. The variable change

$$y = \frac{2x}{1-x^2}, \tag{5.117}$$

which corresponds to

$$\frac{1+x^2}{1-x^2} = \sqrt{1+y^2} \tag{5.118}$$

is applied to (5.115). With this variable change,

$$\mathrm{d}y = 2\frac{x^2+1}{(1-x^2)^2}\,\mathrm{d}x \tag{5.119}$$

and

$$\mathcal{T}(a,b) = 2\int_{-1}^{1} \frac{x^2-1}{b\,(1-x^2) - 2ix\cos 2\varphi + |\sin 2\varphi|(1+x^2)} \frac{1}{2x - ia(1-x^2)}\,\mathrm{d}x \tag{5.120}$$

Let us define the polynomial functions $P(x)$ and $Q(x)$ as

$$P(x) = b(1-x^2) - 2ix\cos 2\varphi + |\sin 2\varphi|(1+x^2), \tag{5.121}$$

$$Q(x) = 2t - ia(1-x^2). \tag{5.122}$$

The integrand of the $\mathcal{T}(a,b)$ function (5.120) is a rational function which can be decomposed in partial fraction. The partial fraction decomposition of a rational function of the form $(c_0+c_1x+c_2x^2)/(PQ)$ is

$$\frac{c_0+c_1x+c_2x^2}{PQ} = \frac{\gamma x+\delta}{P} + \frac{\alpha x+\beta}{Q} \tag{5.123}$$

with

$$\alpha\mathrm{det} = |\sin 2\varphi|\left(\frac{c_1}{2} + \frac{c_0}{ia}\right) + \frac{c_0+c_2}{2}\left(i\cos 2\varphi - \frac{1}{ia}(|\sin 2\varphi| + b)\right), \tag{5.124a}$$

$$\beta\mathrm{det} = \left(i\cos 2\varphi + \frac{1}{ia}(|\sin 2\varphi| - b)\right)\left(\frac{c_1}{2} + \frac{c_0}{ia}\right) + \frac{c_0+c_2}{2}|\sin 2\varphi|, \tag{5.124b}$$

$$\gamma = -\frac{\alpha}{ia}(|\sin 2\varphi| - b), \tag{5.124c}$$

$$\delta = \frac{1}{ia}[\beta(|\sin 2\varphi| + b) - c_0], \tag{5.124d}$$

$$\mathrm{det} = \frac{\triangle}{a^2}, \tag{5.124e}$$

$$\triangle = a^2 + b^2 + 2ab\cos\varphi - (\sin\varphi)^2 \neq 0. \tag{5.124f}$$

The integrand of the $\mathcal{T}(a,b)$ function (5.120) is of the form $(-1+x^2)/(PQ)$. We then have in this case, $c_0 = -1$, $c_1 = 0$ and $c_3 = 1$. Applying these values in (5.124a), the partial fraction decomposition (5.123) of the integrand function in (5.120) then gives the following parameters:

$$\alpha = \frac{ia}{\triangle}\sin\widetilde{2\varphi}, \tag{5.125a}$$

$$\beta = \frac{1}{\triangle}\left[\sin\widetilde{2\varphi} - b - a\cos(\widetilde{2\varphi})\right], \tag{5.125b}$$

$$\gamma = \frac{1}{\triangle}\sin\widetilde{2\varphi}\left[b - \sin\widetilde{2\varphi}\right], \tag{5.125c}$$

$$\delta = \frac{1}{i\triangle}\left[a + (2b-1)\cos\widetilde{2\varphi}\right]. \tag{5.125d}$$

Using this partial fraction decomposition, $\mathcal{T}(a,b)$ function (5.120) can be written as

$$\mathcal{T}(a,b) = 2\int_{-1}^{1}\left(\frac{\gamma x+\delta}{P(x)} + \frac{\alpha x+\beta}{Q(x)}\right)dx, \tag{5.126}$$

with γ, δ, α and β given in (5.125).

Let us introduce $\mathrm{rog}(x)$ and $\mathrm{sog}(x)$ complex functions defined as

$$\mathrm{rog}(x) = \frac{1}{\sqrt{x^2-1}}\ln(x+\sqrt{x^2-1}), \tag{5.127}$$

$$\mathrm{sog}(x) = \frac{1}{x}\left(\frac{\pi}{2} - \mathrm{rog}(x)\right). \tag{5.128}$$

These functions are used in the sequel to calculate $\mathcal{T}(a,b)$ [see Eq. (5.126)] and $\mathcal{D}(a,b)$ [see Eq. (5.113)] functions. It is therefore important to know their analytic properties. These analytic properties are given hereafter.

For $x \in]0,1[$,

$$\mathrm{rog}(-x) = -\mathrm{rog}(x) + \frac{\pi}{\sqrt{1-x^2}}, \tag{5.129}$$

and for $x \in]1,\infty[$,

$$\mathrm{rog}(-x+i0^-) = -\mathrm{rog}(x) + \frac{i\pi}{\sqrt{x^2-1}}. \tag{5.130}$$

Note that we have the following formula for $\mathrm{Re}(\theta) \in]0,\pi[$

$$\mathrm{rog}(x) = \frac{\theta}{\sin\theta}, \quad \text{if} \quad x = \cos(\theta) \tag{5.131}$$

and the lemma

Lemma 5.3.1 *The function* $\mathrm{rog}(a)$ *defined for* $a > 1$ *by*

$$\mathrm{rog}(a) = \int_{-1}^{1}\frac{1}{a(1-x^2)+2ix}\,dx \tag{5.132}$$

is holomorphic on $\mathbb{C}\backslash]-\infty,-1]$ *and extends in holomorphic function on* $\mathbb{C}\setminus\{-1\}$.

Proof The roots of the polynomial $a(1-x^2)+2ix, a\in\mathbb{C}$ are $x_\pm=\frac{1}{a}(i\pm\sqrt{a^2-1})$. When these roots $x_\pm$ are distinct, they are different of ±1. We have $x_+=x_-=i/a$ if and only if $a=\pm1$, and $x_\pm(a=1)=i$, $x_\pm(a=-1)=-i$. Thus, when these roots $x_\pm$ have the same value, they are always different of ±1. The roots $x_\pm$ are then not included in the integral domain $[-1,1]$. Therefore, formula (5.132) is an homolorphic function of $a\in\mathbb{C}\setminus\{-1\}$. □

rog function being holomorphic near of $a=1$, its expression (5.127) could not be used near of 1 since Eq. (5.127) has a singularity at $x=1$. In order to determine rog function in the neighbourhood of $x=1$, let us define

$$z=\left(1-1/x^2\right)^{1/2}. \tag{5.133}$$

rog function (5.127) can therefore be written as

$$\mathrm{rog}(x)=\frac{1}{2xz}\ln\left(\frac{1+z}{1-z}\right). \tag{5.134}$$

The Taylor series expansion at $z=0$ of the logarithm function leads to the expression of rog function in the neighbourhood of $x=1$:

$$\mathrm{rog}(x)=\frac{1}{x}\left(1+\frac{z^2}{3}+\frac{z^4}{5}+\ldots+\frac{z^{n-1}}{n}\right). \tag{5.135}$$

We then have $\mathrm{rog}(1)=1$ using (5.135) and $\mathrm{rog}(0)=\pi/2$ using (5.127).

Lemma 5.3.2 *The function* $\mathrm{sog}(x)$ *defined in* (5.128) *for* $x>1$ *is holomorphic on* $\mathbb{C}\backslash]-\infty,-1]$ *and extends in holomorphic function on* $\mathbb{C}\setminus\{-1\}$.

Proof sog function defined in (5.128) depends on the rog function which is holomorphic on $\mathbb{C}\setminus\{-1\}$. sog function presents a singularity at $x=0$. To remove the indetermination near $x=0$, let us define $y=\left(1-x^2\right)^{1/2}$. We then have $x=-i\left(y^2-1\right)^{1/2}$ using the same definition of the square root as in (5.35b). Thus,

$$\mathrm{rog}(x)=\frac{\pi}{2y}+\frac{i}{y}\ln\left(y+\sqrt{y^2-1}\right)$$

and therefore,

$$\mathrm{sog}(x)=-\frac{\pi}{2}\frac{x}{y(y+1)}+\frac{1}{y}\mathrm{rog}(y)\quad\text{with}\quad y\to1.$$

rog function being well defined at $y=1$ and then at $x=0$, sog function has no more indetermination at $x=0$. □

Knowing the analytic properties of functions rog and sog, we can now calculate the integrals $\mathcal{T}(a,b)$ (5.126) and $\mathcal{D}(a,b)$ (5.113). It is shown in appendix F that

$$\int_{-1}^{1} \frac{\alpha x+\beta}{Q(x)}\,dx = \alpha \operatorname{sog}(a) + i\beta \operatorname{rog}(a) \tag{5.136}$$

and that

$$\int_{-1}^{1} \frac{\gamma x+\delta}{P(x)}\,dx = \frac{i\gamma}{b-\sin\widetilde{2\varphi}}\left[\left(\frac{\pi}{2}-\widetilde{2\varphi}\right)-\cos\widetilde{2\varphi}\operatorname{rog}(b)\right]+\delta\operatorname{rog}(b). \tag{5.137}$$

Finally, using (5.136), (5.137) and (5.126),

$$\mathcal{T}(a,b) = 2\left[T_1(a,b)+T_2(a,b)\right] \tag{5.138}$$

with

$$T_1(a,b) = \alpha\operatorname{sog}(a) + i\beta\operatorname{rog}(a), \tag{5.139a}$$

$$T_2(a,b) = \frac{i\gamma}{b-\sin\widetilde{2\varphi}}\left[\left(\frac{\pi}{2}-\widetilde{2\varphi}\right)-\cos\widetilde{2\varphi}\operatorname{rog}(b)\right]+\delta\operatorname{rog}(b). \tag{5.139b}$$

Lemma 5.3.3 *The function $\mathcal{T}(a,b)$ defined in (5.115) for $a>1$ and $b>1$ extends in holomorphic function on the domain $a\in\mathbb{C}\setminus\{-1\}$ and $b\in\mathbb{C}\setminus\{-1\}$ due to lemmas 5.3.1 and 5.3.2 since Eq. (5.138) depends on* rog *and* sog *functions.*

To calculate integral $\mathcal{D}(a,b)$ given in (5.113), the following partial fraction decomposition is also used:

$$\frac{1}{y+ib}\,\frac{1}{y-ia} = \frac{-i}{b+a}\left(\frac{1}{y-ia}-\frac{1}{y+ib}\right) \quad \text{if } a+b\neq 0. \tag{5.140}$$

Integral $\mathcal{D}(a,b)$ given in (5.113) can then be rewritten as

$$\mathcal{D}(a,b) = \frac{i}{b+a}\int_{-\infty}^{+\infty}\left(\frac{1}{y-ia}\,\frac{1}{\sqrt{1+y^2}}-\frac{1}{y+ib}\,\frac{1}{\sqrt{1+y^2}}\right)\mathrm{d}y, \quad \text{if } a+b\neq 0. \tag{5.141}$$

Using the variable change (5.117), we have for $a\geq 1$,

$$\int_{\mathbb{R}}\frac{1}{y-ia}\,\frac{1}{\sqrt{1+y^2}}\mathrm{d}y = 2i\int_{-1}^{1}\frac{1}{a(1-x^2)+2ix}\,dx = 2i\operatorname{rog}(a) \tag{5.142}$$

and for $b\geq 1$

$$\int_{\mathbb{R}}\frac{1}{y+ib}\,\frac{1}{\sqrt{1+y^2}}\mathrm{d}y = \overline{\int_{\mathbb{R}}\frac{1}{y-ib}\,\frac{1}{\sqrt{1+y^2}}\mathrm{d}y} = \overline{2i\operatorname{rog}(b)} = -2i\operatorname{rog}(b). \tag{5.143}$$

From (5.142) and (5.143), Eq. (5.141) reduces to

$$\mathcal{D}(a,b) = \frac{-2}{a+b}\left[\mathrm{rog}(a) + \mathrm{rog}(b)\right]. \tag{5.144}$$

Lemma 5.3.4 *The function $\mathcal{D}(a,b)$ defined in (5.113) for $a > 1$ and $b > 1$ extends in holomorphic function on the domain $a \in \mathbb{C} \setminus \{-1\}$ and $b \in \mathbb{C} \setminus \{-1\}$ due to lemmas 5.3.1 and 5.3.2 since Eq. (5.144) depends on* rog *and* sog *functions.*

We have

$$\mathcal{D}(a,b) \to 0^-$$

and

$$\mathcal{T}(a,b) \to 0$$

when $b \to +\infty$.

At the end of this section, $[D]$ and $[T]$ matrices are completely determined using (5.112) and (5.114) respectively. Their analytical properties are also known. In order to resolve the linear system of equations (5.107) or (5.111), their right hand side constituted of U_1 and U_2 must also be calculated.

Determination of the right hand side of the system of equations

Using (5.101), the right hand side of the system (5.106) which is calculated at the collocation points b_l defined in (5.104), $l \in \{1, 2, \ldots, N\}$, is

$$u_1(b_l) = -\sum_k \Big(D_p(V_1^k, Z_1^k)(b_l) + T_p(V_2^k, Z_2^k)(b_l) \Big), \tag{5.145a}$$

$$u_2(b_l) = -\sum_k \Big(T_p(V_1^k, Z_1^k)(b_l) + D_p(V_2^k, Z_2^k)(b_l) \Big), \tag{5.145b}$$

where D_p and T_p functions are defined in (5.77) and Z_j^k defined in (5.89), $j = 1, 2$, $k \in \mathbb{N}^*$, is the k-th pole of the spectral function Σ_j with its corresponding residue V_j^k defined in (5.90). This section is devoted to the analytic calculation of the $u_1(b_l)$ and $u_2(b_l)$ defined in (5.145) for $l \in \{1, 2, \ldots, N\}$ in order to compute the right hand side of the system (5.106).

By construction of D_p function in (5.75a), we have

$$D_p(h,z)(b_l) = \frac{1}{2i\pi}\int_{\Gamma_0} \frac{m(\lambda)}{b_l - \lambda}\frac{V}{\lambda - z}\mathrm{d}\lambda \; - \; V\frac{m(z)}{b_l - z}. \tag{5.146}$$

Deforming the contour Γ_0 pictured on Fig. 5.2 into the imaginary axis by applying the variable

change $\lambda = iy$ leads to

$$\begin{cases} D_p(V,z)(b_l) = \frac{1}{2\pi}\int_{-\infty}^{+\infty} \frac{m(iy)}{y+ib_l}\frac{V}{y+iz}\mathrm{d}y \; - \; V\frac{m(z)}{b_l-z} & \text{if } \mathrm{Re}(z) \leq 0 \\ \\ D_p(V,z)(b_l) = \frac{1}{2\pi}\int_{-\infty}^{+\infty} \frac{m(iy)}{y+ib_l}\frac{V}{y+iz}\mathrm{d}y & \text{if } \mathrm{Re}(z) > 0 \end{cases} . \tag{5.147}$$

Indeed, the integrand singularities in (5.146) are points $\lambda = b_l$ and $\lambda = z$. During the deformation of Γ_0 into the imaginary axis, the crossed spaces are $\{\lambda, \mathrm{Re}\lambda > 0 \text{ and } \mathrm{Im}\lambda > 0\}$ and $\{\lambda, \mathrm{Re}\,\lambda < 0 \text{ and } \mathrm{Im}\,\lambda < 0\}$. Collocation points b_l (5.104) are therefore not crossed during this contour deformation since their real part is positive and their imaginary part is negative. However, the pole z defined in (5.74) has a positive imaginary part and is therefore crossed if and only if $\mathrm{Re}(z) > 0$. Their residue is

$$V\frac{m(z)}{b_l - z}.$$

This residue then suppresses the second term in the right hand side of (5.146) when $\mathrm{Re}(z) > 0$. Using the $\mathcal{D}$ function definition in (5.113), in both cases $\mathrm{Re}(z) > 0$ or $\mathrm{Re}(z) < 0$, the following identity is found:

$$D_p(z,V)(b_l) = \frac{V}{2\pi}\mathcal{D}(-z,b_l) - V\frac{m(z)}{b_l-z}. \tag{5.148}$$

Similarly, by construction of the T_p function in (5.75b), we have

$$T_p(z,V)(b_l) = \frac{1}{2i\pi}\int_{\Gamma_0} \frac{m(\lambda)}{b_l - T_0(\lambda)}\frac{V}{\lambda - z}\,\mathrm{d}\lambda - V\frac{m(z)}{b_l - T_0(z)}\mathbb{1}(z \in \Omega_0). \tag{5.149}$$

The integrand contour Γ_0 pictured on Fig. 5.2 is still deformed into the imaginary axis by applying the variable change $\lambda = iy$ to obtain

$$\begin{cases} T_p(V,z)(b_l) = \frac{1}{2\pi i}\int_{-\infty}^{+\infty} \frac{m(iy)}{b_l - T_0(iy)}\frac{V}{y+iz}\,\mathrm{d}y - V\frac{m(z)}{b_l - T_0(z)}\mathbb{1}(z \in \Omega_0) & \text{if } \mathrm{Re}(z) \leq 0 \\ \\ T_p(V,z)(b_l) = \frac{1}{2\pi i}\int_{-\infty}^{+\infty} \frac{m(iy)}{b_l - T_0(iy)}\frac{V}{y+iz}\,\mathrm{d}y & \text{if } \mathrm{Re}(z) > 0. \end{cases} \tag{5.150}$$

Indeed, as for the previous case, only the pole $\lambda = z$ of the integrand function in (5.149) contributes to the integral if and only if $\mathrm{Re}(z) > 0$. Its residu is

$$\begin{cases} 0 & \text{if } z \notin \Omega_0 \\ \\ V\frac{m(z)}{b_l - T_0(z)} & \text{if } z \in \Omega_0 \end{cases},$$

due to the fact that the T_0 function is defined only for $z \in \Omega_0$ (5.69). This residue then suppresses

the second term in the right hand side of (5.149) when $\mathrm{Re}(z) > 0$. We also find using the $\mathcal{T}$ function definition in (5.115), in both cases $\mathrm{Re}(z) > 0$ or $\mathrm{Re}(z) < 0$, the following identity:

$$T_p(V,z)(b_l) = \frac{h}{2i\pi}\mathcal{T}(-z,b_l) - V\,\frac{m(z)}{b_l - T_0(z)}\mathbb{1}(z \in \Omega_0). \tag{5.151}$$

Expressions (5.148) of D_p and (5.151) of T_p functions are incorporated in the right hand side of the system (5.145) with $z = Z_1^k$ and $h = V_1^k$ for $u_1(b_l)$ and $z = Z_2^k$ and $h = V_2^k$ for $u_2(b_l)$. In this new expression, with the pole propagation process explained in section 5.3.2.1, singular terms of D_p and T_p functions cancel each other. The remaining term in the right hand side of the system (5.145) is therefore

$$\begin{cases} +(2\pi i)\,u_1(b_1) = -\sum_k \left(i\mathcal{D}(-Z_1^k,b_1)\left[V_1^k\right] + \mathcal{T}(-Z_2^k,b_1)\left[V_2^k\right]\right) + \dfrac{2\pi i}{b_1 - Z_1} \\ \qquad\qquad\qquad\qquad \vdots \\ +(2\pi i)\,u_1(b_N) = -\sum_k \left(i\mathcal{D}(-Z_1^k,b_N)\left[V_1^k\right] + \mathcal{T}(-Z_2^k,b_N)\left[V_2^k\right]\right) + \dfrac{2\pi i}{b_N - Z_1} \\ +(2\pi i)\,u_2(b_1) = -\sum_k \left(i\mathcal{D}(-Z_2^k,b_1)\left[V_2^k\right] + \mathcal{T}(-Z_1^k,b_1)\left[V_1^k\right]\right) + \dfrac{2\pi i}{b_1 - Z_2} \\ \qquad\qquad\qquad\qquad \vdots \\ +(2\pi i)\,u_2(b_N) = -\sum_k \left(i\mathcal{D}(-Z_2^k,b_N)\left[V_2^k\right] + \mathcal{T}(-Z_1^k,b_N)\left[V_1^k\right]\right) + \dfrac{2\pi i}{b_N - Z_2}. \end{cases} \tag{5.152}$$

The right hand side of the system (5.145) is then determined with the $\mathcal{D}$ (5.144) and $\mathcal{T}$ (5.138) functions which are well known.

At the end of this level, the system (5.107) is well defined. Matrices $[D]$ and $[T]$ as well as vectors U_1 and U_2 have been calculated. System (5.107) is resolved numerically. For that, the NAG numeric subroutine library for Fortran is used. With the resolution of this linear system of equations, the coordinates $\tilde{X}_j^k$ of the regular term X_j of the spectral functions is known and therefore the regular term X_j is known using (5.99). The spectral functions Σ_j are then completely determined using (5.87) which depends on the singular part Y_j calculated using (5.88), and on the regular part X_j. The spectral functions being calculated, the diffraction coefficients are computed using (5.51) with $\hat{\alpha}_1 = \Sigma_1$ and $\hat{\alpha}_2 = \Sigma_2$.

Some numerical solutions of the diffraction coefficient using this methodology are presented in the sequel.

5.4 Numerical results

In this section, diffraction coefficient (5.51) is compared to the one of the Sommerfeld method (5.52). Diffraction coefficients are then computed by spectral functions method using (5.51). In

this expression, spectral functions need to be calculated for

$$\xi = \xi_1 = -\cos\theta \quad \text{and} \quad \xi = \xi_2 = -\cos(2\varphi - \theta), \tag{5.153}$$

where θ is the observation angle in the wedge (see Fig. 5.1).

For the Galerkin basis defined in (5.97), the parameters $a_k \in [1, \infty[$ are chosen as an exponential law [11]:

$$a_k = p_0 + \epsilon \left(10^{\frac{k-1}{h_0}} - 1\right), \quad k \in \mathbb{N}^*. \tag{5.154}$$

After several numerical experiments of our spectral function code, the value of the different parameters in (5.154) have been set as

$$p_0 = 2, \quad \epsilon = 0.05 \quad \text{and} \quad h_0 = 3. \tag{5.155}$$

The collocation points b_k (5.104) are chosen as

$$b_k = a_k - 1 - i10^{-3}. \tag{5.156}$$

We chose $N = 18$ collocation points b_k and elements a_k in the Galerkin basis.

Diffraction coefficients computed using spectral functions and Sommerfeld method for wedge angles less than π are presented on Fig. 5.6. Under this condition, the two faces of the wedge are insonified by the incident plane wave.

On Fig. 5.6, diffraction coefficients obtained with Spectral functions give close results to those of the Sommerfeld method at some observation points. On Fig. 5.6a where a wedge of angle $2\varphi = 80°$ is irradiated by a plane wave of angle $\theta_{\text{inc}} = 55°$, both models give close results for observation points included between $10°$ and $50°$ and for other observation points there are slight differences between the two methods. This analysis also applies to the cases of a wedge of angle $2\varphi = 110°$ irradiated by a plane wave of angle $\theta_{\text{inc}} \approx 90°$ (see Fig. 5.6b) and of a wedge of angle $2\varphi = 140°$ irradiated by a plane wave of angle $\theta_{\text{inc}} = 70°$ (see Fig. 5.6c). The same observation is also done for wedge angle greater than π for the $270°$ wedge (see Figs. 5.7a and 5.7b).

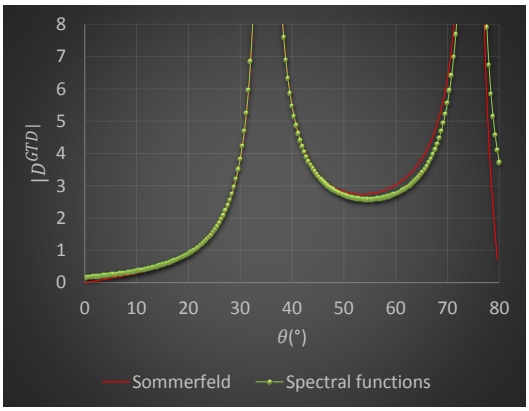

(a) $2\varphi = 80°$, $\theta_{\text{inc}} = 55°$

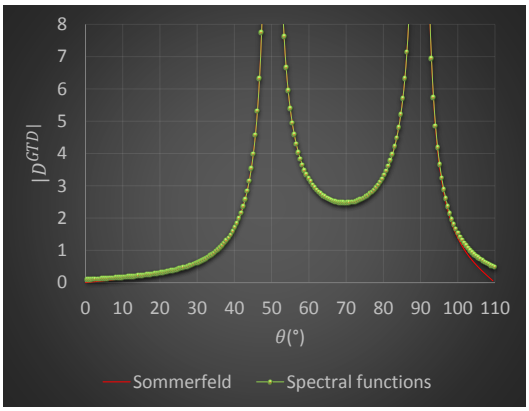

(b) $2\varphi = 110°$, $\theta_{\text{inc}} \approx 90°$

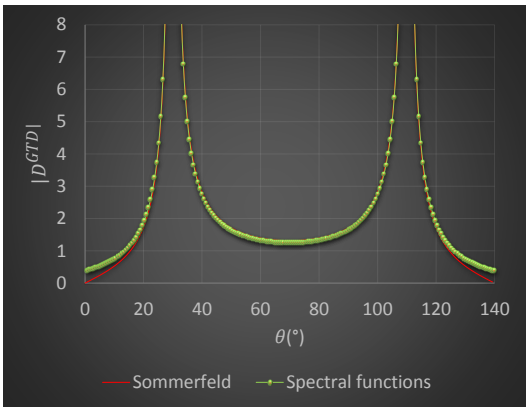

(c) $2\varphi = 140°$, $\theta_{\text{inc}} = 70°$

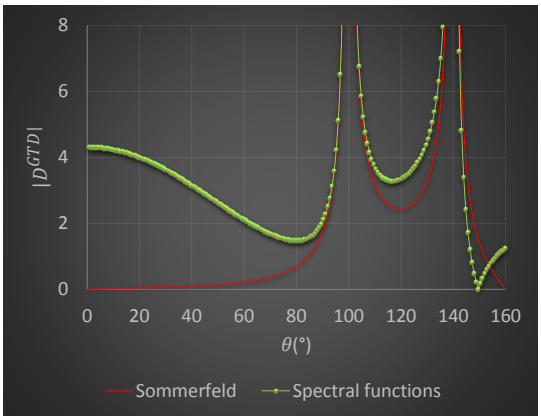

(d) $2\varphi = 160°$, $\theta_{\text{inc}} = 40°$

Figure 5.6: Diffraction coefficient computed with spectral functions and with the Sommerfeld method for wedge angles less than π.

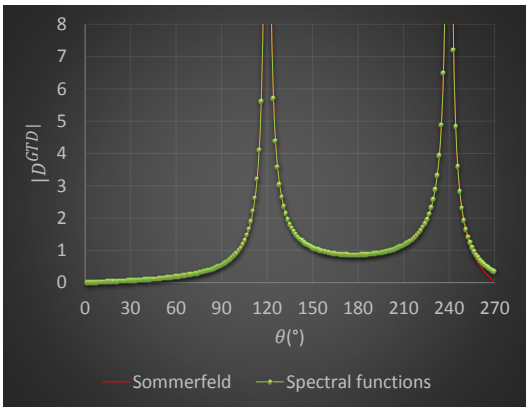

(a) $2\varphi = 270°$, $\theta_{\text{inc}} = 60°$

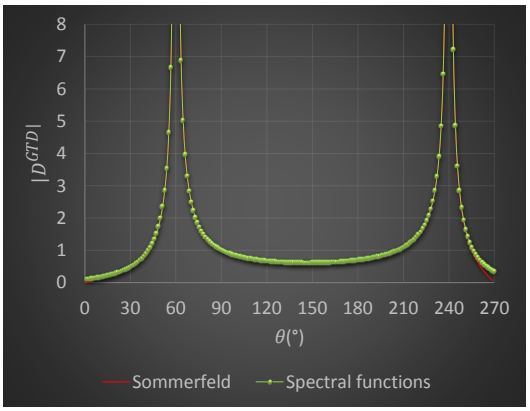

(b) $2\varphi = 270°$, $\theta_{\text{inc}} = 120°$

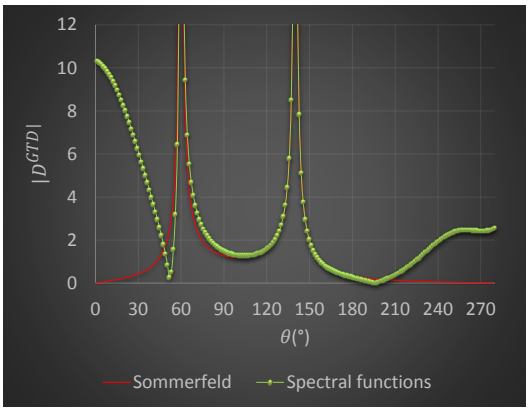

(c) $2\varphi = 280°$, $\theta_{\text{inc}} = 240°$

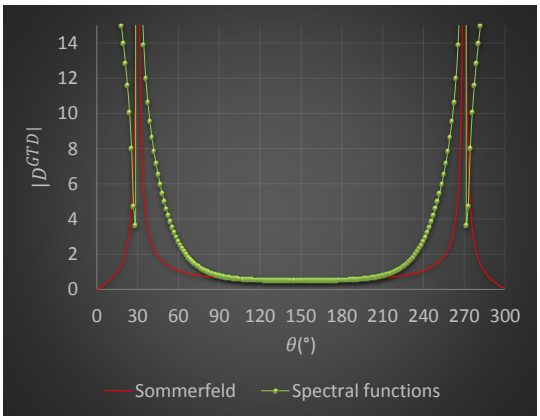

(d) $2\varphi = 300°$, $\theta_{\text{inc}} = 150°$

Figure 5.7: Diffraction coefficient computed with spectral functions and with the Sommerfeld method for wedge angles greater than π.

On Figs. 5.6d, 5.7c and 5.7d, differences between the spectral functions and the Sommerfeld methods are more important. The discrepancies between Sommerfeld and spectral functions methods are explained by the fact that with the chosen Galerkin basis (5.95), the approximated regular term (5.99) is not a good approximation of the regular term near $\xi = -a_k$ because the Galerkin basis φ_k tends to infinity. Our calculation points which are linked to the observation angle in the wedge (5.153) being in the interval $[-1, 1]$, the parameter p_0 in (5.154) is replaced by a big value so that $-a_k$ will always be far away from our calculation points. Another numerical experiment has then been done with p_0 chosen as

$$p_0 = 20 \tag{5.157}$$

and the collocation points b_k as

$$b_k = a_k - 6 - i10^{-3} \tag{5.158}$$

with always $N = 18$ collocation points and elements in the Galerkin basis. With these new input values, the numerical experiments presented in Figs. 5.6 and 5.7 are reproduced in Figs. 5.8 and 5.9 respectively.

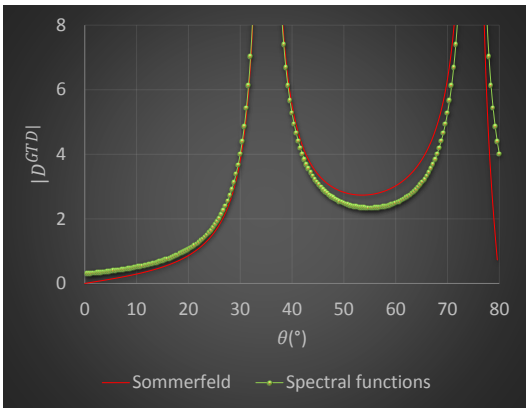

(a) $2\varphi = 80°$, $\theta_{\text{inc}} = 55°$

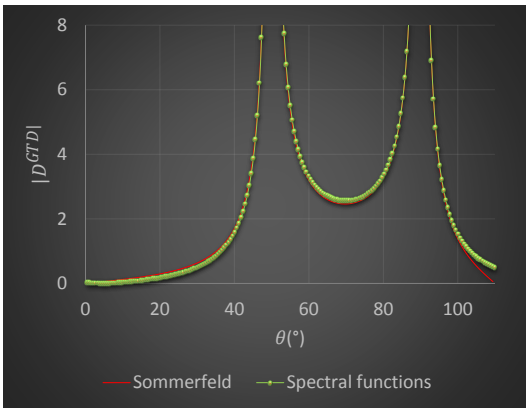

(b) $2\varphi = 110°$, $\theta_{\text{inc}} \approx 90°$

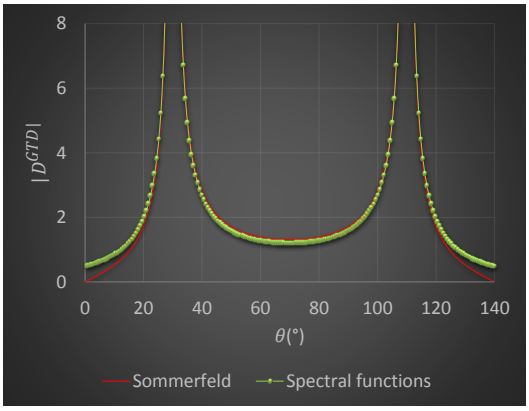

(c) $2\varphi = 140°$, $\theta_{\text{inc}} = 70°$

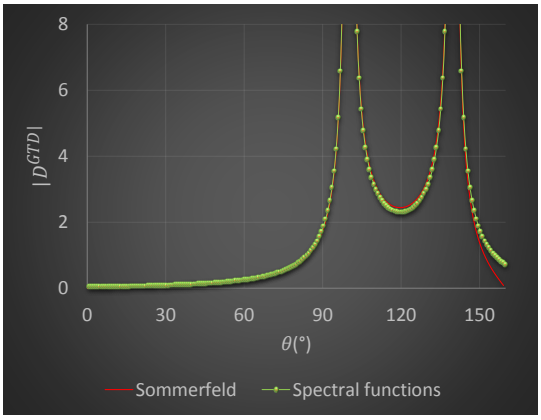

(d) $2\varphi = 160°$, $\theta_{\text{inc}} = 40°$

Figure 5.8: Diffraction coefficient computed with spectral functions and with the Sommerfeld method for wedge angles less than π.

With this modification of the parameters, Sommerfeld and spectral functions solutions are much more closer than before (compare Figs. 5.6d, 5.7c and 5.7d with Figs. 5.8d, 5.9c and 5.9d respectively). Results with the spectral functions can therefore be improved with a judicious choice of the parameters in the Galerkin basis.

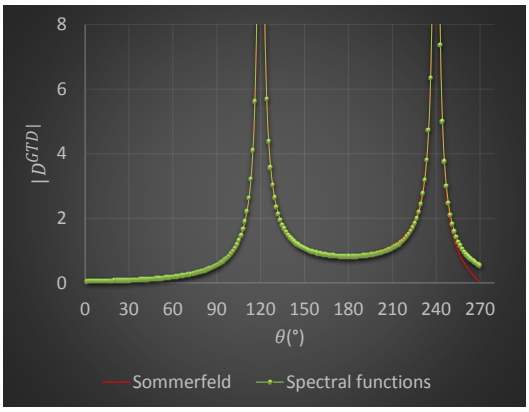

(a) $2\varphi = 270°$, $\theta_{\text{inc}} = 60°$

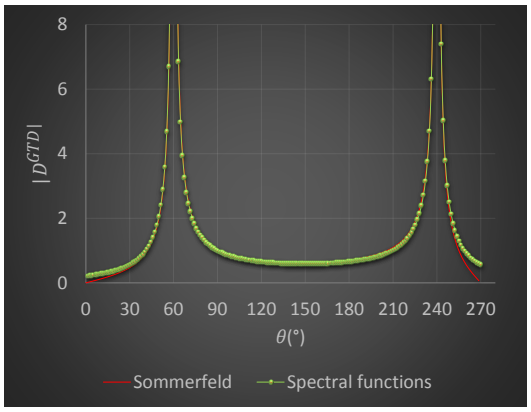

(b) $2\varphi = 270°$, $\theta_{\text{inc}} = 120°$

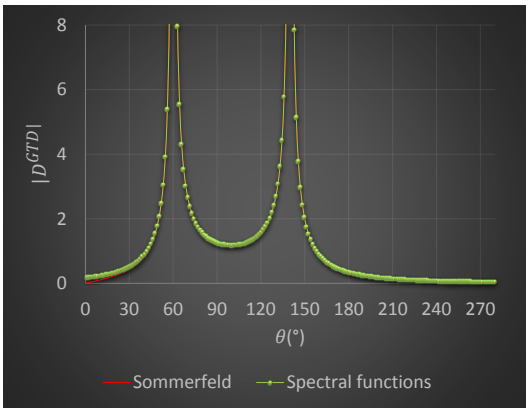

(c) $2\varphi = 280°$, $\theta_{\text{inc}} = 240°$

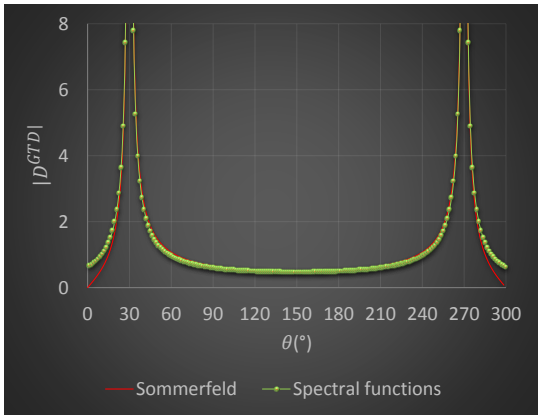

(d) $2\varphi = 300°$, $\theta_{\text{inc}} = 150°$

Figure 5.9: Diffraction coefficient computed with spectral functions and with the Sommerfeld method for wedge angles greater than π.

There exists another solution for improving the spectral functions results. That solution is explained in [11]. It consists on deforming the contour Γ_0 in integrals of (5.60) into a contour Γ_2 pictured on Fig. 5.10. The half-space $\{\lambda, \operatorname{Im} \lambda < 0\}$ is crossed during this contour deformation as shown by the F_1 arrow on Fig. 5.10.

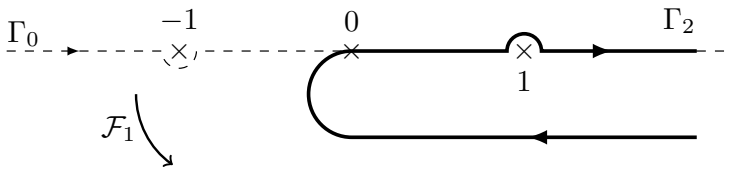

Figure 5.10: Contour Γ_2. Arrow $\mathcal{F}_1$ shows the deformation of Γ_0 into Γ_2.

Therefore, during this contour deformation, the poles

$$\lambda = \xi, \quad \text{with } \mathrm{Im}(\xi) < 0$$

of the DM function (5.62) are crossed and therefore, for $\xi \in \mathbb{C}$, $\mathrm{Im}(\xi) < 0$,

$$DM(\Sigma_j)(\xi) = \int_{\Gamma_0} DM(\xi,\lambda)\Sigma_j(\lambda)\,\mathrm{d}\lambda = \int_{\Gamma_2} DM(\xi,\lambda)\Sigma_j(\lambda)\,\mathrm{d}\lambda + m(\xi)\Sigma_j(\xi). \tag{5.159}$$

The poles

$$\lambda = T_0^{-1}(\xi) = \xi\,\cos\widetilde{2\varphi} - \sin\widetilde{2\varphi}\,\zeta_0(\xi) = \cos(\theta - \widetilde{2\varphi}) \quad \text{if} \quad \xi = \cos\theta$$

of the TM function (5.65) are crossed during this deformation contour only and only if $\xi \in \Omega_0^-$ (see dotted area on Fig. 5.11) defined as

$$\Omega_0^- = \{\xi \in \mathbb{C},\ \mathrm{Im}(\xi) < 0,\ \xi = \cos(\theta),\ \widetilde{2\varphi} < \mathrm{Re}(\theta) < \pi\} \tag{5.160}$$

because T_0^{-1} operates in the domain

$$T_0^{-1} : \Omega_0^- \longrightarrow \mathbb{C}. \tag{5.161}$$

The domain Ω_0^- is delineated by the hyperbola

$$\partial\Omega_0^- = \{\xi \in \mathbb{C},\ \mathrm{Im}(\xi) < 0, \xi = \cos\theta, \mathrm{Re}\,\theta = \widetilde{2\varphi}\}. \tag{5.162}$$

Domain Ω_0^- and contour $\partial\Omega_0^-$ are illustrated on Fig. 5.11. $\partial\Omega_0^-$ is the lower boundary of Ω_0^- and the semi-axis $]-\infty, \cos\widetilde{2\varphi}]$ is its upper boundary.

The TM integral operator then gives for $\xi \in \mathbb{C}$, $\mathrm{Im}(\xi) < 0$,

$$TM(\Sigma_j)(\xi) = \int_{\Gamma_0} TM(\xi,\lambda)\Sigma_j(\lambda)\,\mathrm{d}\lambda = \int_{\Gamma_2} TM(\xi,\lambda)\Sigma_j(\lambda)\,\mathrm{d}\lambda - M(\xi)\,\Sigma_j[T_0^{-1}(\xi)] \tag{5.163}$$

where

$$M(\xi) = m(\xi)\,\mathbb{1}(\xi \in \Omega_0^-). \tag{5.164}$$

Using (5.159) and (5.163) in the system of functional equations (5.60), the system (5.60) is then equivalent to this new system for $\xi \in \mathbb{C}$, $\mathrm{Im}(\xi) < 0$:

$$\begin{cases} \Sigma_1(\xi) = g_1(\xi) + \Sigma_2(T_0^{-1}(\xi))\,\mathbb{1}(\xi \in \Omega_0^-) \\ \\ \Sigma_2(\xi) = g_2(\xi) + \Sigma_1(T_0^{-1}(\xi))\,\mathbb{1}(\xi \in \Omega_0^-) \end{cases} \tag{5.165}$$

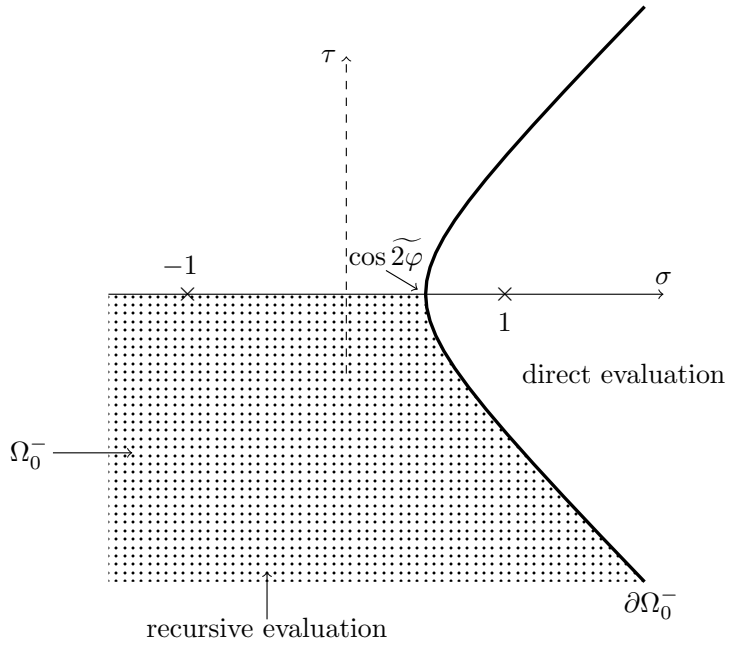

Figure 5.11: Domain Ω_0^- and its lower boundary $\partial\Omega_0^-$ in the complex plane $\xi = \sigma + i\tau$. The upper boundary of Ω_0^- is the semi-axis $]-\infty, \cos\widetilde{2\varphi}]$.

where

$$\begin{cases} g_1(\xi) = m(\xi)^{-1}\left[\dfrac{1}{\xi - Z_1} - \int_{\Gamma_2} DM(\xi,\lambda)\,\Sigma_1(\lambda)\,\mathrm{d}\lambda - \int_{\Gamma_2} TM(\xi,\lambda)\,\Sigma_2(\lambda)\,\mathrm{d}\lambda\right] \\ g_2(\xi) = m(\xi)^{-1}\left[\dfrac{1}{\xi - Z_2} - \int_{\Gamma_2} TM(\xi,\lambda)\,\Sigma_1(\lambda)\,\mathrm{d}\lambda - \int_{\Gamma_2} DM(\xi,\lambda)\,\Sigma_2(\lambda)\,\mathrm{d}\lambda\right] \end{cases}. \tag{5.166}$$

To calculate g_j functions, we need to calculate

$$\begin{aligned} \int_{\Gamma_2} DM(\xi,\lambda)\,\Sigma_j(\lambda)\mathrm{d}\lambda &= \int_{\Gamma_2} DM(\xi,\lambda)\,[X_j(\lambda) + Y_j(\lambda)]\,\mathrm{d}\lambda \\ &= \sum_k \tilde{X}_j^k \int_{\Gamma_2} DM(\xi,\lambda)\,\varphi_k(\lambda)\,\mathrm{d}\lambda + \sum_i \int_{\Gamma_2} DM(\xi,\lambda)\,\frac{V_j^i}{\lambda - Z_j^i}\,\mathrm{d}\lambda \end{aligned}$$

and

$$\int_{\Gamma_2} TM(\xi,\lambda)\,\Sigma_j(\lambda)\mathrm{d}\lambda = \sum_k \tilde{X}_j^k \int_{\Gamma_2} TM(\xi,\lambda)\,\varphi_k(\lambda)\,\mathrm{d}\lambda + \sum_i \int_{\Gamma_2} TM(\xi,\lambda)\,\frac{V_j^i}{\lambda - Z_j^i}\,\mathrm{d}\lambda.$$

Integrals over the contour Γ_2 must then be properly calculated in order to use formula (5.165). This formula is called recursive formula because the direct formula in (5.87) is used to calculate

the spectral functions in the right hand side of system (5.165) if $T_0^{-1}(\xi) \notin \Omega_0^-$ and if $T_0^{-1}(\xi) \in \Omega_0^-$, the formulae for the spectral functions in (5.165) are one more time used. This process is repeated until $T_0^{-1}(\xi) \in \Omega_0^-$. For $\mathrm{Im}(\xi) < 0$, this procedure is summed up on Fig. 5.11. This procedure allows to propagate the accuracy of the spectral functions for $\xi \notin \Omega_0^-$, $\mathrm{Im}(\xi) < 0$ in the domain Ω_0^-. Indeed, with the chosen Galerkin basis, the approximation of the regular term (5.99) is quite accurate in $\xi \notin \Omega_0^-$, $\mathrm{Im}(\xi) < 0$.

The variable change $\lambda = iy$ is one more time applied to evaluate integrals over Γ_2. We found using

$$N\mathcal{D}(a,b) = \frac{1}{2\pi}\,\mathcal{D}(a,b) - \frac{m(b)}{a+b},$$

with $\mathcal{D}$ function being defined in (5.113) that

$$\begin{aligned}\int_{\Gamma_2} DM(\xi,\lambda)\,\varphi_k(\lambda)\,\mathrm{d}\lambda &= i\int_{-\infty}^{\infty} DM(\xi,iy)\,\varphi_k(iy)\,\mathrm{d}y \\ &= d_k\,N\mathcal{D}(a_k,\xi)\end{aligned} \tag{5.167}$$

where φ_k is the Galerkin basis given in Eq. (5.95).

Similarly, knowing that $\mathrm{Im}(Z_j^i) > 0$, Z_j^i being the generated poles (see section 5.3.2.1), for $\pm\mathrm{Re}(Z_j^i) > 0$, we have

$$\int_{\Gamma_2} DM(\xi,\lambda)\,\frac{V_j^i}{\lambda - Z_j^i}\,\mathrm{d}\lambda = \frac{1}{2\pi}\,V_j^i\,\mathcal{D}(-Z_j^i,\xi) - \frac{V_j^i}{\xi - Z_j^i}m(\xi) = V_j^i\,N\mathcal{D}(-Z_j^i,\xi). \tag{5.168}$$

For the TM contributions, the poles $\lambda = T_0^{-1}(\xi)$ are taken into account if and only if $\xi \in \Omega_0^-$. Thus, for $\xi \in \Omega_0^-$,

$$\begin{aligned}\int_{\Gamma_2} TM(\xi,\lambda)\,\frac{V_j^i}{\lambda - Z_j^i}\,\mathrm{d}\lambda &= \int_{-\infty}^{\infty} TM(\xi,iy)\cdot\frac{V_j^i}{y + iZ_j^i}\,\mathrm{d}y - \frac{V_j^i}{T_0^-(\xi) - Z_j^i}m(\xi) \\ &= \frac{1}{2i\pi}\,V_j^i\,\mathcal{T}(-Z_j^i,\xi) - \frac{V_j^i}{T_0^-(\xi) - Z_j^i}m(\xi) \\ &= V_j^i\,N\mathcal{T}(-Z_j^i,\xi),\end{aligned} \tag{5.169}$$

where

$$N\mathcal{T}(a,b) = \frac{1}{2i\pi}\mathcal{T}(a,b) - \frac{m(b)}{T_0^{-1}(b) + a}.$$

We then have for $\xi \in \Omega_0^-$,

$$m(\xi)\,\tilde{g}_1(\xi) - \frac{1}{\xi - Z_1} = \tag{5.170}$$
$$-\Big(\textstyle\sum_i V_1^i\,N\mathcal{D}(-Z_1^i,\xi) + \sum_k \tilde{X}_1^k\,d_k\,N\mathcal{D}(a_k,\xi) + \sum_i V_2^i\,N\mathcal{T}(-Z_2^i,\xi) + \sum_k \tilde{X}_2^k\,d_k\,N\mathcal{T}(a_k,\xi)\Big)$$

and

$$m(\xi)\,\tilde{g}_2(\xi) - \frac{1}{\xi - Z_2} = \tag{5.171}$$
$$-\Big(\sum_i V_2^i\, N\mathcal{D}(-Z_2^i,\xi) + \sum_k \tilde{X}_2^k\, d_k\, N\mathcal{D}(a_k,\xi) + \sum_i V_1^i\, N\mathcal{T}(-Z_1^i,\xi) + \sum_k \tilde{X}_1^k\, d_k\, N\mathcal{T}(a_k,\xi)\Big).$$

To apply this recursive procedure, calculation points ξ must have a negative imaginary part since the system (5.165) is defined for $\xi \in \mathbb{C}$, $\mathrm{Im}(\xi) < 0$. The considered calculation points are then

$$\xi_1 = -\cos\theta - \epsilon_{\mathrm{rec}}\, i \quad \text{and} \quad \xi_2 = -\cos(2\varphi - \theta) - \epsilon_{\mathrm{rec}}\, i \tag{5.172}$$

with $\epsilon_{\mathrm{rec}} = 10^{-3}$.

This recursive solution is now applied to the cases treated on Figs. 5.6a, 5.6b, 5.7c and 5.7d for which there have been important differences between the Sommerfeld diffraction coefficients and the spectral function diffraction coefficient calculated with the direct evaluation. The chosen values of the Galerkin basis are given in (5.155). The results obtained with the recursive solution are drawn on Fig. 5.12. The diffraction coefficients present discontinuities at junctions between direct and recursive evaluations which are caused by the recursive recursive procedure.

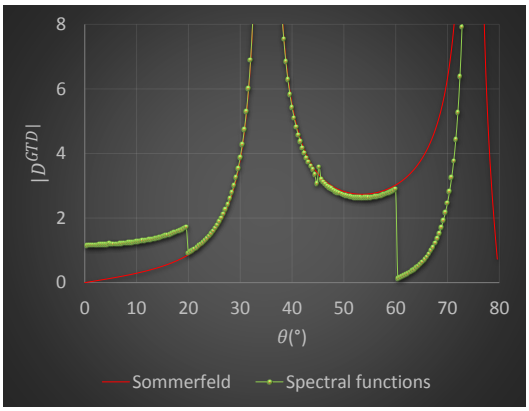

(a) $2\varphi = 80°$, $\theta_{\text{inc}} = 55°$

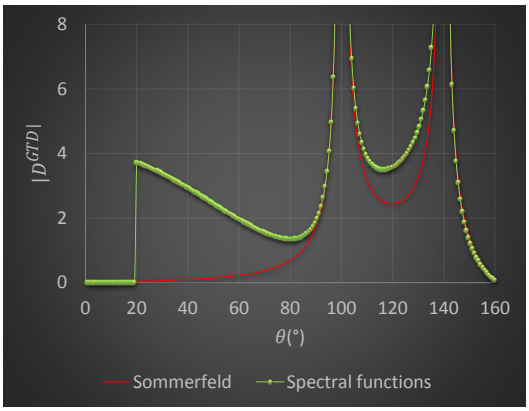

(b) $2\varphi = 160°$, $\theta_{\text{inc}} = 40°$

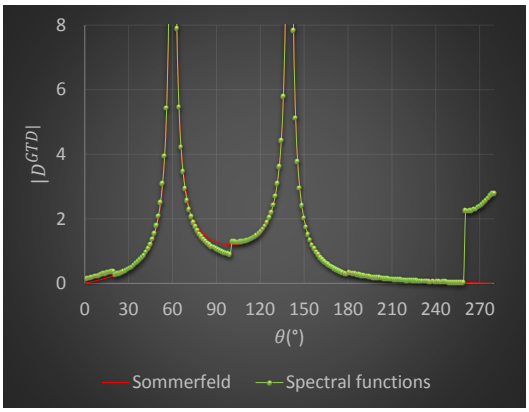

(c) $2\varphi = 300°$, $\theta_{\text{inc}} = 150°$

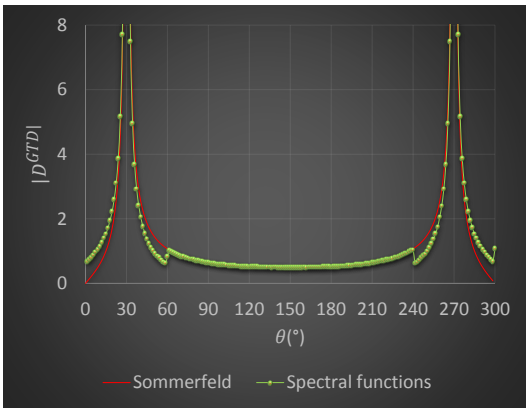

(d) $2\varphi = 280°$, $\theta_{\text{inc}} = 240°$

Figure 5.12: Diffraction coefficient computed with the recursive formula of spectral functions and with the Sommerfeld method.

Except these discontinuities, an improvement of the spectral functions diffraction coefficient is observed for some intervals of the observation points: $\theta \in [20°, 60°]$ for Fig. 5.12a, $\theta \in [0°, 20°]$ and for $\theta \in [140°, 160°]$ for Fig. 5.12b, $\theta \in [0°, 20°]$ and $\theta \in [100°, 260°]$ for Fig. 5.12c and $\theta \in [60°, 240°]$ for Fig. 5.12d. In these intervals, spectral functions diffraction coefficient well fit the Sommerfeld diffraction coefficient. Obviously, further investigations need to be carried out to find out the origin of these discontinuities.

Finally, the adopted solution using the spectral functions method is to choose judicious parameters of the Galerkin basis in order to model diffraction by wedges of all angles.

5.5 Conclusion

This chapter shows the feasibility of the spectral functions method to model diffraction from wedges at interfaces fluid/void. The diffraction coefficient obtained using the spectral functions has been compared to the one obtained with the Sommerfeld integral method which gives rise to an analytic solution. For a judicious choice of the approximation basis in the spectral functions method, the computed diffraction coefficients are close to those of the analytic solutions. In order to have a more accurate solution with the spectral functions method, a recursive procedure is employed. The obtained results with this procedure present discontinuities. Further investigations need to be carried out to find out the origin of these discontinuities and try to improve the validity of the recursive solution.

The spectral functions method could therefore be used in complex diffraction cases. It models diffraction by wedges of any angle as shown in this chapter.

Conclusions and future work

The aim of the works carried out during this thesis is to implement in the software platform CIVA a generic ray model for the specimen echoes simulation which is able to account for both reflection and diffraction. The CIVA "specular model" existing at the beginning of the thesis is a ray method which models only specular reflection at the specimen boundaries. This model has been extended during this thesis by adding diffraction by surface irregularities. The main outcomes of this thesis are given hereafter.

Concluding remarks

In order to find how to extend this CIVA "specular model", a short review of the high frequency scattering models in elastodynamics is done in chapter 1. Indeed, there exists a ray model for diffraction called the Geometrical Theory of Diffraction (GTD) which models diffraction by edges but diverges at observation directions close to incident and specular reflection directions. This divergence makes "*a priori*" the combination of GTD with the CIVA "specular model" impossible: the existing GTD uniform corrections in elastodynamics presented in this chapter, the Physical Theory of Diffraction (PTD) and the Uniform Asymptotic Theory of Diffraction (UAT) cannot be easily used to extend the CIVA "specular model". Indeed, PTD does not depend on the geometrical elastodynamics and UAT requires to compute fictitious reflected rays to remove the GTD divergence which can be quite complex to do.

In this thesis, the Uniform Theory of Diffraction (UTD), another uniform correction of the GTD already developed in electromagnetism, has been developed within the context of elastodynamics. This uniform correction is simple to implement since it just multiplies the GTD diffraction coefficient by a smoothing function. This uniform correction removes the GTD divergence near and at shadow boundaries and leads to a discontinuity of the diffracted field. This discontinuity compensates the one of the geometrical elastodynamics field, leading to a continuous total field. This uniform model is a ray model and does not involve fictitious reflected rays as the UAT. This model can therefore be easily combined with the CIVA "specular model".

As a first step, in chapter 2, UTD is developed in elastodynamics for a simple canonical geometry, a half-plane, to show its feasibility. UTD solution in elastodynamics is obtained in the same

manner as in electromagnetism but the theoretical formalism is much more intricate: the Pauli-Clemmow approximation is applied to the exact solution of the scattering of a plane wave from a half-plane which is expressed in terms of a Sommerfeld integral. GTD and the developed UTD model being ray models, they then depend only on the geometry of the scatterer at the incident point.

To apply GTD and UTD, the scatterer at the diffraction point is approximated by an infinite edge. As a consequence, GTD and UTD are not able to deal with the finite length of the edge. Then, at **a second step** of this thesis, two incremental methods are developed in chapter 3: they allow to simulate diffraction by finite edges that are encountered in NDT applications. They consist in modelling the field diffracted by a finite edge as a sum of spherical waves emitted by discretization points on the diffracting edge. These models can be coupled with the GTD or with one of its uniform corrections, because the spherical waves amplitude modelled by these incremental models includes the diffraction coefficient of the selected model (GTD or one of its uniform correction). These models are established for 3D configurations for which the edge length is influent. The first developed model, called the Incremental Theory of Diffraction (ITD), is extended from electromagnetism, and the second, called “Huygens model”, is based on the Huygens principle. These models are then applied to the GTD solution for a half-plane in CIVA to model 3D defects echoes diffraction and are then successfully validated by a comparison with experimental data in 3D NDT configurations. These incremental models can also be applied to GTD solution for a wedge in 3D configurations but this solution has not been developed yet. It exists only in 2D configurations where the edge wedge is infinite.

The diffraction of an elastic plane wave by a wedge in 2D configuration is addressed in chapter 4, wedges being geometries classically encountered in inspected specimens. A review of two GTD solutions existing for this problem, but both limited to wedge angles less than π - the Sommerfeld integral (SI) and the Laplace transform (LT) -, is first done. Then, the UTD solution for wedge problem is developed, still using the Pauli-Clemmow approximation, as for the half-plane case. This UTD solution is applied to the LT GTD solution and is implemented in the software platform CIVA where it is coupled to the "specular model": this integration builds a generic model of specimen echoes accounting for both reflection and diffraction. Numerical validations show that this mixed model gives results close to the ones obtained using the Finite Elements Method (FEM) for longitudinal waves with a lower computation time ($\sim$ 10 min for 500 positions of the transducer) than FEM ($\sim$ 8 hours for 150 positions of the transducer). The discrepancies between these two models are much important for transversal waves. These results also furnish the validity of the UTD concept i.e. its capacity to easily model reflection by surfaces and diffraction by edges in the case of a wedge. However, this mixed "UTD + specular" model leads to few artefacts, because in the "UTD model", the incident field at a diffraction point on the edge is approximated by one plane wave, whereas the "specular model" takes into account all the incident rays at this diffraction point. These artefacts should be eliminated by considering in the "UTD model" all the incident rays rather than a mean plane wave.

However, the UTD solution for a wedge developed in chapter 4 is established using a GTD solution limited to wedge angles less than π (LT method). Therefore, this UTD approach does not cover all ultrasonic NDT configurations. As **a last step** of this thesis, in chapter 5, a preliminary study is then carried out for a wedge at fluid/void interfaces in order to model diffraction for a wider range of wedge angles. In this study, diffraction is modelled using to the so-called "spectral functions method". With this method, the diffraction coefficient depends on spectral functions which have to be determined. These spectral functions are constituted of a singular term and a regular term. The regular part of the spectral functions is determined using a Galerkin collocation method. For a judicious choice of the Galerkin approximation basis, results obtained with this method are close to those obtained by the well-known GTD analytic (Sommerfeld) solution for wedge angles less than π, and also for wedge angle greater than π. Spectral functions method then shows its ability to model diffraction by wedge of any angle for the diffraction of a plane wave by a wedge at fluid/void interfaces. They could be used in the future in elastodynamics to treat diffraction problems with all wedge angles.

The works realised during this thesis led to two publications in peer-reviewed journals [36, 57], to one submitted publication in a peer-reviewed journal [69], to two communications in international conferences with conference proceedings (ICU 2015 [40] and AFPAC 2015 [85]) and to communications without conference proceedings (GDRE 2014, Doctoriales COFREND 2015, AFPAC 2016) .

Different perspectives could be outlined at the end of this thesis.

Perspectives

The different perspectives at the end of this thesis are listed below.

- The divergence factor of the diffracted wave found by Achenbach and Gautesen [23] for a spherical incident wave has to be checked in case of mode conversion.
- We saw that the diffraction coefficients have a discontinuity near and at critical angles due to head waves. Further investigations need to be done to well model the interference of head waves and diffracted waves. These works will be the continuity of the work of Fradkin et al. [56] and of the internship of Yu-Lin Huang.
- Concerning the chapter 3 of this dissertation, the experimental validation of the incremental models has to be done in more other 3D inspection configurations (also with transversal waves, defects of different length) to study the limits of these incremental models.
- Another perspective is to apply the developed incremental models to a 3D wedge. The first step for reaching that objective will be to find the GTD solution for a 3D wedge.

- Laplace transform (LT) GTD code needs to be optimized in order to have a lower computation time for the "UTD model". Nevertheless, the long-term objective is to give up the LT GTD code for the "spectral functions" code in elastodynamics.
- With a lower computation time for the chosen GTD code, the "UTD model" could be computed using a complete ray model as the CIVA "specular model" so that both of them use the same approximation for the fields on the edge point. With the same inputs, the mixed "UTD + specular" model is expected not to have artefacts any more.
- For diffraction by half-plane, Kirchhoff approximation is known to be less accurate than GTD. To see if the same is true for the wedge case, many other experiments for the validation of the mixed model have to be carried out, especially with transversal waves.
- Further investigations need to be carried out to find out the origin of the discontinuities of the recursive solution using the spectral functions method.
- The methodology of the spectral functions method is under study in elastodynamics by a master intern, Samar Chehade. The aim of this internship is to model diffraction by a wedge of any angle in elastodynamics. This work is a preparation to the thesis that will follow mine. The diffraction by a 3D wedge in elastodynamics will be addressed during this thesis.

Appendix A

Approximation methods

A.1 Stationary phase method

Considering an oscillatory integral of the following form

$$I(\zeta) = \int_a^b h(\lambda)\, e^{i\zeta\, q(\lambda)} \mathrm{d}\lambda \tag{A.1}$$

where a and $b \in \mathbb{R}$, $\zeta \gg 1$, h and q are real-valued smooth functions on $[a, b]$. Let us assume that g has a stationary point $\lambda_s \in [a, b]$ defined as

$$\left.\frac{\mathrm{d}q}{\mathrm{d}\lambda}\right|_{\lambda=\lambda_s} = 0. \tag{A.2}$$

Let us assume moreover that the second derivative of fonction q at the stationary point is nonzero

$$q_{\lambda\lambda} = \left.\frac{\mathrm{d}^2 q}{\mathrm{d}\lambda^2}\right|_{\lambda=\lambda_s} \neq 0. \tag{A.3}$$

The Taylor expansion of $q(\lambda)$ at the second order has the form

$$q(\lambda) = q(\lambda_s) + \frac{q_{\lambda\lambda}}{2}\left(\lambda - \lambda_s\right)^2. \tag{A.4}$$

The integral I (A.1) can then be written as

$$I(\zeta) = e^{i\zeta\, q(\lambda_s)} \int_a^b h(\lambda)\, e^{i\zeta\, \frac{q_{\lambda\lambda}}{2}(\lambda-\lambda_s)^2}\, \mathrm{d}\lambda. \tag{A.5}$$

For $\zeta \gg 1$, the exponential $\exp(i\zeta\ (\lambda - \lambda_s)^2\ q_{\lambda\lambda}/2)$ is highly oscillatory for $\lambda \neq \lambda_s$. The oscillations give rise to cancellation except in a neighbourhood of the stationary point λ_s. Thus,

using

$$\int_{-\infty}^{+\infty} e^{-\zeta\lambda^2}\mathrm{d}\lambda = \sqrt{\frac{\pi}{\zeta}}, \tag{A.6}$$

we have at the leading order $\zeta^{-1/2}$

$$I(\zeta) \approx \sqrt{\frac{2i\pi}{\zeta q_{\lambda\lambda}}}\, h(\lambda_s)\, e^{i\zeta\, q(\lambda_s)}. \tag{A.7}$$

Stationary phase method then allows to approximate integrals (A.1) defined on real intervals. But diffraction problem often deals with integrals in the complex plane. Such integrals are approximated using the steepest descent method.

A.2 Steepest descent method

Considering an integral of the following form

$$I(\zeta) = \int_{\gamma} h(\lambda)\, e^{-\zeta\, q(\lambda)} d\lambda \tag{A.8}$$

where ζ is real positive and γ is the contour integration in the complex λ plane. Functions $h(.)$ and $q(.)$ are analytical functions of the complex variable λ except at some singular points. The exponential term has at least one saddle point defined as

$$\frac{\mathrm{d}q}{\mathrm{d}\lambda} = 0, \quad \lambda = \lambda_s. \tag{A.9}$$

Furthermore, the second derivative of the function q at the saddle point is assumed to be nonzero

$$q_{\lambda\lambda} = \left.\frac{d^2q}{d\lambda^2}\right|_{\lambda=\lambda_s} \neq 0. \tag{A.10}$$

The Taylor expansion of $q(\lambda)$ near the saddle point λ_s at the second order has the form

$$q(\lambda) = q(\lambda_s) + \frac{q_{\lambda\lambda}}{2}\left(\lambda - \lambda_s\right)^2. \tag{A.11}$$

Let

$$q(\lambda) - q(\lambda_s) = u(\lambda) + iv(\lambda) \tag{A.12}$$

with

$$u(\lambda) = \frac{|q_{\lambda\lambda}(\lambda-\lambda_s)^2|}{2}\cos\left(\arg q_{\lambda\lambda} + 2\arg(\lambda-\lambda_s)\right) \tag{A.13a}$$

$$v(\lambda) = \frac{|q_{\lambda\lambda}(\lambda-\lambda_s)^2|}{2}\sin\left(\arg q_{\lambda\lambda} + 2\arg(\lambda-\lambda_s)\right). \tag{A.13b}$$

v is zero in the neighbourhood of λ_s for

$$\arg(\lambda-\lambda_s) = -\frac{1}{2}\arg q_{\lambda\lambda} \mod (\pi). \tag{A.14}$$

Below, we choose for $\arg(\lambda-\lambda_s)$ in (A.14) the acute angle $-\arg q_{\lambda\lambda}/2$. Applying (A.14) in (A.13a) gives

$$u(\lambda) = \frac{|q_{\lambda\lambda}(\lambda-\lambda_s)^2|}{2}. \tag{A.15}$$

In the neighbourhood of λ_s, the term $q(\lambda) - q(\lambda_s)$ is then real and positive on the steepest descent direction i.e. the straight line standing at the angle $-(1/2)\arg q_{\lambda\lambda}$ to the horizontal line. It provides the direction of maximal exponential decay of the integrand. Indeed, the deformation of the integration path γ into this steepest descent path SDP characterized by

$$v = 0 \quad \Leftrightarrow \quad \mathrm{Im}\, q(\lambda) = \mathrm{Im}\, q(\lambda_s) \tag{A.16}$$

in the λ complex-plane [see Eq. A.12], gives the following integral

$$I(\zeta) = e^{-\zeta q(\lambda_s)}\int_{SDP} h(\lambda)\, e^{-\zeta\, u(\lambda)}\mathrm{d}\lambda \tag{A.17}$$

which is no more an oscillating integral. The steepest descent path SDP is characterized by

$$v = 0 \quad \Leftrightarrow \quad \mathrm{Im}\, q(\lambda) = \mathrm{Im}\, q(\lambda_s). \tag{A.18}$$

The integral (A.17) can therefore be approximated using Laplace method which stipulates the dominant contribution to the integral is from points of the neighbourhood of the saddle point λ_s since elsewhere on the steepest decent contour, the integrand falls off extremely rapidly. Applying Laplace method to (A.17) for sufficiently large ζ [86] then gives

$$I(\zeta) \sim h(\lambda_s)\, e^{-\zeta q(\lambda_s)}\sqrt{\frac{2\pi}{\zeta\, q_{\lambda\lambda}}}. \tag{A.19}$$

The advantage of considering a minus sign in the exponent factor of (A.8) is that with the choice of the acute angle (A.14), the principal value of the square root in (A.19) is considered [86]. Note that during the deformation of γ to the steepest descent path, if any singularities of the integrand

are crossed, their contribution must be properly accounted for the integral evaluation.

This steepest descent method has been extended to n-fold integral by Bleistein [86].

n-fold integral

n-fold integral is integral of the following form:

$$I_n(\zeta) = \int_\gamma h(\boldsymbol{\lambda})\, e^{-\zeta\, q(\boldsymbol{\lambda})} \mathrm{d}\lambda_1\, \mathrm{d}\lambda_2\, \mathrm{d}\lambda_3\, \ldots\, \mathrm{d}\lambda_n, \qquad \boldsymbol{\lambda} = (\lambda_1, \lambda_2, \cdots, \lambda_n) \tag{A.20}$$

where n is the number of dimensions and $\boldsymbol{\lambda}$ is a vector in the space $\mathbb{C}^n$. According to [86],

$$I_n(\zeta) \sim h(\lambda_s)\, e^{-\zeta q(\lambda_s)} \left[\frac{2\pi}{\zeta}\right]^{\frac{n}{2}} \frac{1}{\sqrt{\det Q_n(\lambda_s)}} \tag{A.21}$$

where Q_n is the Hessian matrix of the function q.

The steepest descent method deforms the complex integration path onto a path where the integral does not oscillate any more. It gives the contribution of the saddle point to the integral. It is then convenient to use it when the saddle point is far away from other singular points as the integrand poles. When the saddle point is near a pole, the steepest descent is no more accurate. There exist other methods to approximate the oscillating integral in this condition.

A.3 Pauli-Clemmow approximation

This method of approximation allows to deal with the coalescence of a saddle point with a simple pole. The function

$$f(\lambda) = \frac{g(\lambda)}{(\lambda - \lambda_p)^k} \tag{A.22}$$

with g being an holomorphic function in the λ complex plane, is singular at $\lambda = \lambda_p$. If the index $k = 1$, λ_p is said to be a simple pole of the function f.

Here the considered integral is

$$I(\zeta) = \int_\gamma h(\lambda)\, e^{\zeta\, q(\lambda)} \mathrm{d}\lambda \tag{A.23}$$

where ζ is always a real positive. Note that the considered integral $I(\zeta)$ in this section differs from the integral (A.8) by the minus sign in the exponential term.

A.3.1 A simple pole singularity near the saddle point

Let $h(\zeta)$ in (A.8) possess a simple pole at $\lambda = \lambda_p$. It has been shown in A.19 that the steepest descent path in the complex λ plane is characterised by

$$\operatorname{Im} q(\lambda) = \operatorname{Im} q(\lambda_s). \tag{A.24}$$

Applying to (A.8) the transformation

$$q(\lambda) = q(\lambda_s) - s^2 \tag{A.25}$$

mapped the initial γ contour and also the steepest descent contour into a straight line along real axis in the complex s plane. The saddle point is now at $s = 0$ in this plane and the pole is at $s = s_p = q(\lambda_p) - q(\lambda_s)$. Equation (A.8) then becomes

$$I(\zeta) = \int_{-\infty}^{+\infty} G(s)\, e^{-\zeta s^2} \mathrm{d}s \tag{A.26}$$

with

$$G(s) = h(\lambda)\, e^{-\zeta q(\lambda_s)} \frac{\mathrm{d}\lambda}{\mathrm{d}s}. \tag{A.27}$$

The Pauli-Clemmow procedure consists in writting G in the following form

$$G(s) = \frac{T(s)}{s - s_p} \tag{A.28}$$

with the function $T(\cdot)$ being analytic on $\mathbb{R}$. Thus, its Taylor expansion whose coefficients are C_n at $s = 0$ is

$$T(s) = G(s)\,(s - s_p) = \sum_{n=0}^{\infty} C_n s^n. \tag{A.29}$$

Including (A.29) in (A.27), the following equation is obtained

$$G(s) = \sum_{n=0}^{\infty} \frac{C_n s^n}{s - s_p} = \sum_{n=0}^{\infty} \frac{C_n s^n (s + s_p)}{s^2 - s_p^2}. \tag{A.30}$$

Equation (A.30) in (A.26) leads to

$$I(\zeta) = \sum_{n=0}^{\infty} C_n \int_{-\infty}^{+\infty} \frac{e^{-\zeta s^2}}{s^2 - s_p^2} s^n (s + s_p)\, \mathrm{d}s. \tag{A.31}$$

Integrals in (A.31) are in the following form

$$\int_{-\infty}^{+\infty} \frac{e^{-\zeta s^2}}{s^2 - s_p^2} s^m \, \mathrm{d}s \tag{A.32}$$

with $m \in \mathbb{N}$. For odd $m = 2i + 1$, $i \in \mathbb{N}$, the integrand of this integral is also odd and thus

$$\int_{-\infty}^{+\infty} \frac{e^{-\zeta s^2}}{s^2 - s_p^2} s^{2i+1} \, \mathrm{d}s = 0. \tag{A.33}$$

For even $m = 2i$, $i \in \mathbb{N}$, the integrand is also even and leads to

$$\int_{-\infty}^{+\infty} \frac{e^{-\zeta s^2}}{s^2 - s_p^2} s^{2i} \, \mathrm{d}s = 2 \int_{0}^{+\infty} \frac{e^{\zeta s^2}}{s^2 - s_p^2} s^{2i} \, \mathrm{d}s. \tag{A.34}$$

The first order ($i = 0$) integral is

$$J = \int_{-\infty}^{+\infty} \frac{e^{-\zeta s^2}}{s^2 - s_p^2} \, \mathrm{d}s. \tag{A.35}$$

According to [15],

$$J = -\frac{1}{s_p^2} \sqrt{\frac{\pi}{\zeta}} F(-i\zeta s_p^2) \tag{A.36}$$

where F is the transition function defined in (2.44). Substituting (A.36) in (A.31), we have then at the first order $n = 0$ [corresponding to $i = 0$ in (A.36)],

$$I(\zeta) \approx -\frac{C_0}{s_p} \sqrt{\frac{\pi}{\zeta}} F(-i\zeta s_p^2). \tag{A.37}$$

Using Eq. (A.29),

$$C_0 = T(0) = -s_p \, G(0). \tag{A.38}$$

The approximation of the integral (A.26) at the first order $n = 0$ is then reduced to

$$I(\zeta) \approx G(0) \sqrt{\frac{\pi}{\zeta}} F(-i\zeta s_p^2). \tag{A.39}$$

Applying the phase stationary method explained on appendix A.1 to the exact integral (A.26), the phase stationary point contribution is obtained. This contribution corresponds to the GTD

diffracted field and is therefore called $I^{\text{diff(GTD)}}$:

$$I^{\text{diff(GTD)}}(\zeta) = G(0)\sqrt{\frac{\pi}{\zeta}}. \tag{A.40}$$

The approximated field in (A.39) is the UTD diffracted field:

$$I^{\text{diff(UTD)}}(\zeta) = I^{\text{diff(GTD)}}(\zeta)\, F(-i\zeta s_p^2). \tag{A.41}$$

Then, UTD diffracted field is a first-order apsymptotic expansion of the exact solution expressed in form of a Sommerfeld integral. It modifies the classical contribution of the stationary phase point by multiplying it with a transition function. An extensive study of the UTD solution is done in [15, 16].

The integrand $h(\lambda)$ in (A.8) could have M simple poles at $\lambda = \lambda_{p_1}, \ldots, \lambda_{p_M}$. Pauli-Clemmow procedure can still be applied to deal with the coalescence of the saddle point with several simple poles [83].

A.3.2 Several simple poles singularities near the saddle point

In this case, the function $G(.)$ defined in (A.27) is considered as

$$G(s) = \frac{T(s)}{\prod_{k=1}^{M}(s - s_{p_k})} \tag{A.42}$$

with $s_{p_k} = q(\lambda_{p_k}) - q(\lambda_s)$ being the simple pole singularities of G. Using, the equality

$$\frac{1}{\prod_{k=1}^{M}(s - s_{p_k})} = \sum_{k=1}^{M} \frac{A_k}{s - s_{p_k}} \tag{A.43}$$

with

$$A_k = \frac{1}{\prod_{\substack{j=1 \\ j\neq k}}^{M}(s_{p_k} - s_{p_j})}, \tag{A.44}$$

the function $G(s)$ can be written as

$$G(s) = \sum_{n=0}^{\infty} C_n s^n \sum_{k=1}^{M} \frac{A_k}{s - s_{p_k}} = \sum_{n=0}^{\infty} C_n s^n \sum_{k=1}^{M} \frac{A_k(s + s_{p_k})}{s^2 - s_{p_k}^2}. \tag{A.45}$$

Then,

$$I(\zeta) = \sum_{n=0}^{\infty} \sum_{k=1}^{M} C_n A_k \int_{-\infty}^{+\infty} \frac{s^n (s + s_{p_k})}{s^2 - s_{p_k}^2} e^{-\zeta s^2} ds \tag{A.46}$$

At the first order $n = 0$, using (A.33), (A.34) and (A.36), we get

$$I(\zeta) \approx C_0 \sum_{k=1}^{M} A_k s_{p_k} \left(-\frac{1}{s_{p_k}^2} \sqrt{\frac{\pi}{\zeta}} F(-i\zeta s_{p_k}^2) \right) \tag{A.47}$$

Using (A.45),

$$C_0 = T(0) = (-1)^M G(0) \left(\prod_{k=1}^{M} s_{p_k} \right) \tag{A.48}$$

Therefore, substituting C_0 in (A.47) by its value defined in (A.48) and using (A.44),

$$I(\zeta) \approx (-1)^{M+1} \sqrt{\frac{\pi}{\zeta}} G(0) \sum_{k=1}^{M} F(-i\zeta s_{p_k}^2) \prod_{\substack{j=1 \\ j \neq k}}^{M} \frac{s_{p_j}}{(s_{p_k} - s_{p_j})}. \tag{A.49}$$

Finally, using the phase stationary point approximation of the integral (A.26) showed in (A.40),

$$I^{\text{diff(UTD)}}(\zeta) = (-1)^{M+1} I^{\text{diff(GTD)}} \left(\sum_{k=1}^{M} F(-i\zeta s_{p_k}^2) \prod_{\substack{j=1 \\ j \neq k}}^{M} \frac{s_{p_j}}{(s_{p_k} - s_{p_j})} \right). \tag{A.50}$$

This UTD solution then deals with the coalescence of the poles λ_{p_k} with the phase stationary point λ_s. As seen in chapter 4, UTD leads to a discontinuous diffracted field which compensates the geometrical field. The UTD proposed here is an approximation of the first order since it is obtained at $n = 0$. There exists another uniform asymptotic expansion of the integral (A.26) obtained with the Van-Der-Waerden method.

A.4 Van-Der-Waerden approximation

This method is described in [15, 16].

A.4.1 A simple pole singularity near the saddle point

In the Van-Der-Waerden approximation, the function $G(.)$ defined in (A.26) is expressed as

$$G(s) = \frac{T(s_p)}{s - s_p} + H(s) \tag{A.51}$$

where $H(.)$ is an holomorphic function and $T(.)$ is the function defined in the Pauli-Clemmow procedure in (A.28). $T(s_p)$ is related to the residue R_p of the pole s_p to the integral (A.26) by the relation

$$R_p = T(s_p)\, e^{-\zeta s_p^2}. \tag{A.52}$$

Including this new expression of $G(.)$ in (A.26) and using Eq. (A.36), the integral I becomes

$$I(\zeta) = -\frac{T(s_p)}{s_p}\sqrt{\frac{\pi}{\zeta}}\, F(-i\zeta s_p^2) + \int_{-\infty}^{+\infty} H(s) e^{-\zeta s^2}\, \mathrm{d}s. \tag{A.53}$$

The approximation of the second term in (A.53) by the stationary phase method explained in section A.1 substituting G by its expression in (A.51) leads to

$$\int_{-\infty}^{+\infty} H(s) e^{-\zeta s^2}\, ds = \sqrt{\frac{\pi}{\zeta}} H(0) = \sqrt{\frac{\pi}{\zeta}} \left[G(0) + \frac{T(s_p)}{s_p} \right]. \tag{A.54}$$

The integral I in (A.53) at the order $\zeta^{-1/2}$ is therefore

$$I(\zeta) \approx \sqrt{\frac{\pi}{\zeta}} \frac{T(s_p)}{s_p} \left[1 - F(-i\zeta s_p^2) \right] + \sqrt{\frac{\pi}{\zeta}} G(0). \tag{A.55}$$

The transition function F in (2.44) depends on the Fresnel function $\overline{F}(.)$ defined in (1.15). According to [53],

$$\overline{F}(X) + \overline{F}(-X) = 1. \tag{A.56}$$

As said in section 2.3.1, the transition function F is multivalued due to the presence of the square root $X^{1/2}$ in its expression. The branch cut along the negative imaginary axis $\{\mathrm{Im}\, X < 0, \mathrm{Re}\, X = 0\}$ (see Fig. A.1) allows to work with the square root principal value (the positive square root). With this branch cut, $\arg X \in]-\pi/2, 3\pi/2[$.

In [15], they showed that $\mathrm{Im}(-i\zeta s_p^2) < 0$ and that the pole s_p does not cross the branch cut of the square root $\{\mathrm{Im}\, X < 0, \mathrm{Re}\, X = 0\}$ when $\mathrm{Re}(-i\zeta s_p^2) > 0$ (see Fig. A.1). In this case, the transition function (2.44) is related to the Fresnel function by the relation

$$F(-i\zeta s_p^2) = -2is_p \sqrt{\pi\zeta} e^{-\zeta s_p^2}\, \overline{F}\left(s_p \sqrt{-i\zeta} \right) \tag{A.57}$$

where the positive square root has been used. When $\mathrm{Re}(-\mathrm{i}\zeta \mathrm{s}_\mathrm{p}^2) < 0$, the pole s_p crosses the branch cut $\{\mathrm{Im}\, X < 0, \mathrm{Re}\, X = 0\}$ and therefore, there is a change of the square root determination. The negative square root is known considered. Using the negative square root in (2.44),

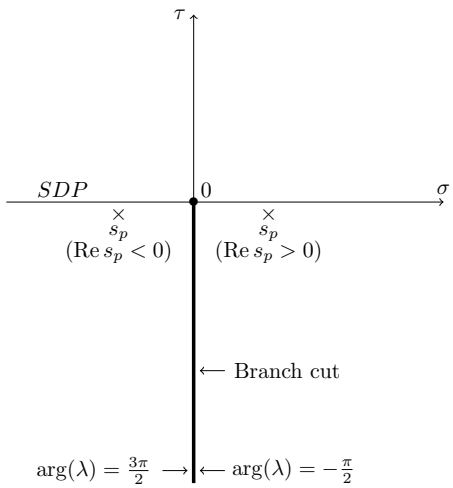

Figure A.1: Branch cut of the square root in the $\lambda = \sigma + i\tau$ complex plane.

(1.15) and (A.56),

$$F(-i\zeta s_p^2) = 2is_p\sqrt{\pi\zeta}e^{-\zeta s_p^2}\left[1 - \overline{F}\left(s_p\sqrt{-i\zeta}\right)\right]. \tag{A.58}$$

Therefore, the two above equations (A.57) and (A.58) can be expressed in terms of one expression which is the following one

$$F(-i\zeta s_p^2) = -2is_p\sqrt{\pi\zeta}e^{-\zeta s_p^2}\left[\overline{F}\left(s_p\sqrt{-i\zeta}\right) - H\left[-\mathrm{Re}(-i\zeta s_p^2)\right]\right]. \tag{A.59}$$

Finally, substituting the transition function in (A.55) by its expression (A.59) and using (A.52),

$$I(\zeta) \approx 2i\pi\, R_p\left[\overline{F}\left(s_p\sqrt{-i\zeta}\right) - \widehat{\overline{F}}\left(s_p\sqrt{-i\zeta}\right) - H\left[-\mathrm{Re}(-i\zeta s_p^2)\right]\right] + \sqrt{\frac{\pi}{\zeta}}G(0) \tag{A.60}$$

where $\widehat{\overline{F}}$ is defined in (1.16). Thus,

$$I^{\mathrm{diff(UAT)}}(\zeta) = 2i\pi\, R_p\left[\overline{F}\left(s_p\sqrt{-i\zeta}\right) - \widehat{\overline{F}}\left(s_p\sqrt{-i\zeta}\right) - H\left[-\mathrm{Re}(-i\zeta s_p^2)\right]\right] + I^{\mathrm{diff(GTD)}}. \tag{A.61}$$

This UAT diffracted field depends on the Heaviside step function which is introduced when the pole s_p crosses the branch cut $\{\mathrm{Im}\, X < 0, \mathrm{Re}\, X = 0\}$. To obtain the total field, the pole contribution have to be add. Its contribution is then taken into account by applying the residue theorem to the integral (A.26). The pole contribution expressed as

$$I^{(\mathrm{GE})}(\zeta) = 2i\pi R_p\, H\left[-\mathrm{Re}(-i\zeta s_p^2)\right] \tag{A.62}$$

leads to the Geometrico-Elastodynamics (GE) field. The GE field is then compensated by the UAT

diffracted field and gives a uniform UAT total field [sum of A.62 and (A.61)] expressed as

$$I^{\text{tot(UAT)}}(\zeta) = 2i\pi\, R_p \left[\overline{F}\left(s_p\sqrt{-i\zeta}\right) - \widehat{\overline{F}}\left(s_p\sqrt{-i\zeta}\right)\right] + I^{\text{diff(GTD)}}. \tag{A.63}$$

The first term in bracket in this equation models a smooth GE field represented by the term $2i\pi\, R_p\, \overline{F}$ (see Fig. 1.12) and diverges near shadow boundaries as the GTD diffracted field due to the term $2i\pi\, R_p\, \widehat{\overline{F}}$ (see chapter 1). Its divergence compensates the one of the GTD diffracted field leading to a uniform solution. In UAT, the approximation of the terms of order $\zeta^{-1/2}$ is complete contrary to UTD where the development is done only at the first Taylor order $n = 0$. [54] showed that UTD ans UAT give exactly the same result when all terms of order $\zeta^{-1/2}$ are considered in UTD solution. UAT solution is therefore more accurate than the UTD solution presented in section A.3.1 at order $\zeta^{-1/2}$.

A.4.2 Several simple poles singularities near the saddle point

It is also possible to use the Van-Der-Waerden procedure to deal with the coalescence of the phase stationary point with M simple poles s_{p_k}. With the form of the $G(.)$ function, it is the same treatment as the one of a single simple pole for each pole s_{p_k}. Indeed, in this case, the $G(.)$ function is expressed as

$$G(s) = \sum_{k=1}^{M} \frac{T(s_{p_k})}{s - s_{p_k}} + H(s). \tag{A.64}$$

The UAT total field is therefore

$$I^{\text{tot(UAT)}}(\zeta) = \sum_{k=1}^{M} 2i\pi\, R_{p_k} \left[\overline{F}\left(s_{p_k}\sqrt{-i\zeta}\right) - \widehat{\overline{F}}\left(s_{p_k}\sqrt{-i\zeta}\right)\right] + I^{\text{diff(GTD)}} \tag{A.65}$$

with R_{p_k} being the residue of the pole s_{p_k} to the integral (A.26). Each pole s_{p_k} is treated separately with this UAT expression.

Appendix B

Expressions of the integrand numerator in the Sommerfeld integral solution of a plane wave scattering by a half-plane

Integrands expressions f_β of the Sommerfeld integral (2.3) in chapter 2 for the scattering of an elastic plane wave from a semi-infinite crack are given in [23]. These expressions have been obtained by using the Wiener-Hopf technique. Numerators g_β of f_β [see Eq. (2.4)] are recalled hereafter to avoid cross-references using expressions of f_β given in Eqs. (5.59) of [23].

In all the described equations, the subscript R referred to the Rayleigh wave. $\kappa_R = c_L/c_R$ is a zero of the Rayleigh function (B.9), c_R being the velocity of the Rayleigh wave.

The integrand numerators g_β are:

$$i\kappa^2 g_L(\xi, \mathrm{sgn}(x_2)) = -2V_1 + \frac{\kappa^2 - 2(\xi^2 + \cos^2\Omega_L)}{\sqrt{q_L^2 - \xi^2}}\, U_2 \tag{B.1a}$$

$$i\kappa^2 \,\mathrm{sgn}(x_2)\, g_{TV}(\xi, \mathrm{sgn}(x_2)) = \frac{\kappa^2 - 2(\xi^2 + \cos^2\Omega_L)}{\sqrt{\left(q_T^2 - \xi^2\right)\left(\xi^2 + \cos^2\Omega_L\right)}}\, V_1 + 2\sqrt{\xi^2 + \cos^2\Omega_L}\, U_2 \tag{B.1b}$$

$$i\kappa\, g_{TH}(\xi, \mathrm{sgn}(x_2)) = \frac{1}{\sqrt{\xi^2 + \cos^2\Omega_L}}\, V_2 \tag{B.1c}$$

with

$$U_2 = \frac{-i\,A\,\kappa_\alpha E_2^\alpha \kappa^2 \sqrt{q_\alpha \cos\theta_\alpha + q_L}\sqrt{\xi + q_L}}{2(\kappa^2-1)\,(q_R+\xi)\,(q_R + q_\alpha\cos\theta_\alpha)\,K^+(\xi)K^-(q_\alpha\cos\theta_\alpha)} \tag{B.2a}$$

$$\mathrm{sgn}(x_2)\,V_1 = \frac{(\xi + i\cos\Omega_L)T^{TV} - (\xi + q_\alpha\cos\theta_\alpha)\,B}{i(q_\alpha\cos\theta_\alpha - i\cos\Omega_L)\,d^+(\xi)} \tag{B.2b}$$

$$\mathrm{sgn}(x_2)\,V_2 = \frac{(\xi + i\cos\Omega_L)T^{TH} - (\xi + q_\alpha\cos\theta_\alpha)\,B\,h}{i(q_\alpha\cos\theta_\alpha - i\cos\Omega_L)\,\gamma_T^+(\xi)}. \tag{B.2c}$$

Parameters T^{TV}, T^{TH} and B in (B.2) are defined as

$$T^{TV} = A\kappa_\alpha^2 \frac{\cos\theta_\alpha \sin\Omega_\alpha E_1^\alpha + \cos\Omega_\alpha E_3^\alpha}{d^+(q_\alpha\cos\theta_\alpha)} \tag{B.3a}$$

$$T^{TH} = A\kappa_\alpha^2 \frac{\cos\Omega_\alpha E_1^\alpha - \cos\theta_\alpha \sin\Omega_\alpha E_3^\alpha}{\gamma_T^+(q_\alpha\cos\theta_\alpha)} \tag{B.3b}$$

$$(1-h^2)B = 2i\cos\Omega_L\,\frac{T^{TV} - h\,T^{TH}}{q_\alpha\cos\theta_\alpha + i\cos\Omega_L} \tag{B.3c}$$

with

$$\gamma_T^+(\xi) = \sqrt{q_T + \xi} \tag{B.4a}$$

$$d^+(\xi) = \frac{q_R + \xi}{\kappa\gamma_T^+(\xi)} K^+(\xi)\sqrt{2(\kappa^2-1)} \tag{B.4b}$$

$$h = -i\frac{d^+(i\cos\Omega_L)}{\gamma_T^+(i\cos\Omega_L)}. \tag{B.4c}$$

Parameters E_j^α are expressed as

$$E_j^\alpha = (\kappa^2-2)\delta_{2j}(d_k^\alpha\,p_k^\alpha) + d_2^\alpha p_j^\alpha + d_j^\alpha p_2^\alpha \tag{B.5}$$

where d_k^α are the incident polarization components and p_k^α the incident wave vector components ($k = 1, 2, 3$). The incident unitary wave vector is

$$\mathbf{p}^\alpha = (\sin\Omega_\alpha\cos\theta_\alpha, \sin\Omega_\alpha\sin\theta_\alpha, \cos\Omega_\alpha)_{(\mathbf{e}_1,\mathbf{e}_2,\mathbf{e}_3)} \tag{B.6}$$

and the incident unitary polarization vectors are:

$$\mathbf{d}^L = \mathbf{p}^L, \tag{B.7a}$$

$$\mathbf{d}^{TV} = \frac{1}{\sqrt{1-\left(p_2^{TV}\right)^2}}\left(p_2^{TV}\,\mathbf{d}^L - \mathbf{e}_2\right), \tag{B.7b}$$

$$\mathbf{d}^{TH} = \frac{1}{\sqrt{1-\left(p_2^{TH}\right)^2}}\left(p_3^{TH}\,\mathbf{x_1} - p_1^{TH}\,\mathbf{e}_3\right). \tag{B.7c}$$

K^+ and K^- functions come from the factorization of the function

$$K(\xi) = K^+(\xi)\,K^-(\xi) = \frac{\mathcal{R}_a\left(\sqrt{\xi^2+\cos^2\Omega_L}\right)}{2(\kappa^2-1)\left(\kappa_R^2-\xi^2-\cos^2\Omega_L\right)} \tag{B.8}$$

where $\mathcal{R}_a$ is the Rayleigh function defined as

$$\mathcal{R}_a(\zeta) = (\kappa^2-2\zeta^2)^2 + 4\zeta^2\sqrt{1-\zeta^2}\sqrt{\kappa^2-\zeta^2}. \tag{B.9}$$

K^+ and K^- functions are linked by

$$K^-(\xi) = K^+(-\xi). \tag{B.10}$$

The function K^+ is given by

$$\ln K^+(\xi) = -\frac{1}{\pi}\int_{q_L}^{q_T}\tan^{-1}\left(\frac{4(t^2+\kappa_\alpha^2\cos^2\Omega_\alpha)(t^2-q_L^2)^{1/2}(q_T^2-t^2)^{1/2}}{(\kappa^2\cos^2 2\Omega_T - 2t^2)^2}\right)\frac{1}{t+\xi}\mathrm{d}t. \tag{B.11}$$

Appendix C

Calculation details for the ITD incremental field

Let us show how to evaluate the double integral (3.6). Denoting it by I, it can be written as

$$I = \int_{\mathcal{C}_\varsigma} \int_{\gamma} h(\lambda, \varsigma)\, e^{-s'\, q(\lambda,\varsigma)}\, d\lambda\, d\varsigma \tag{C.1}$$

with

$$q(\lambda, \varsigma) = -i \left[\sin\phi\, \cos\left(\lambda - \overline{\theta}\right)\, \sqrt{k_\beta^2 - k_\alpha^2 \cos^2\varsigma} + k_\alpha \cos\phi \cos\varsigma \right] \tag{C.2}$$

and

$$h(\lambda, \varsigma) = \frac{k_\alpha}{2\pi} f_\beta(-q_\beta(\varsigma)\cos\lambda, \mathrm{sgn}(\sin\theta))\, \sin\varsigma\, \mathbf{t}_\beta(-q_\beta \cos\lambda, \mathrm{sgn}(\sin\theta)) \tag{C.3}$$

with $q_\beta(\varsigma) = \kappa_\beta \sin\varsigma$. Integral I can be approximated using the steepest descent method for n-fold integral (A.21) with $n = 2$:

$$I \sim h(\lambda_s, \varsigma_s)\, \frac{2\pi}{s'}\, \frac{e^{-s' q(\lambda_s, \varsigma_s)}}{\sqrt{\det[Q_2(\lambda_s, \varsigma_s)]}} \tag{C.4}$$

where Q_2 is the Hessian matrix and (λ_s, ς_s) is the phase stationary point determined by

$$\partial_\lambda q = 0, \qquad \text{and} \qquad \partial_\varsigma q = 0. \tag{C.5}$$

Expressions of these partial derivatives are:

$$\partial_\lambda q = i\left[\sin\phi\,\sin(\lambda-\bar{\theta})\,\left(k_\beta^2-k_\alpha^2\cos^2\varsigma\right)^{\frac{1}{2}}\right] \tag{C.6a}$$

$$\partial_\varsigma q = -i\left[k_\alpha^2\sin\phi\,\cos(\lambda-\bar{\theta})\,\sin\varsigma\,\cos\varsigma\,\left(k_\beta^2-k_\alpha^2\cos^2\varsigma\right)^{-\frac{1}{2}}-k_\alpha\cos\phi\,\sin\varsigma\right] \tag{C.6b}$$

The stationary phase point is therefore

$$\lambda_s=\bar{\theta},\quad \varsigma_s=0 \text{ or } \varsigma_s=\frac{k_\beta}{k_\alpha}\cos\phi \tag{C.7}$$

and according to Snell's law of diffraction (3.12), $\varsigma_s=\arccos(\cos\phi\,k_\beta/k_\alpha)=\Omega_\alpha(\phi)$. The case $\varsigma=0$ corresponds to a grazing incidence and it is not considered here. Taking into account that we have the following expressions for the second derivatives

$$\partial^2_{\lambda\lambda} q = i\left[\sin\phi\,\cos(\lambda-\bar{\theta})\,\left(k_\beta^2-k_\alpha^2\cos^2\varsigma\right)^{\frac{1}{2}}\right], \tag{C.8a}$$

$$i\partial^2_{\varsigma\varsigma} q = \frac{k_\alpha^2\sin\phi\cos(\lambda-\bar{\theta})}{\sqrt{k_\beta^2-k_\alpha^2\cos^2\varsigma}}\left[\cos^2\varsigma-\sin^2\varsigma-\frac{k_\alpha^2\sin^2\varsigma\cos^2\varsigma}{k_\beta^2-k_\alpha^2\cos^2\varsigma}\right]-k_\alpha\cos\phi\cos\varsigma, \tag{C.8b}$$

$$\partial^2_{\lambda\varsigma} q=\partial^2_{\varsigma\lambda} q = i\left[k_\alpha^2\sin\phi\sin(\lambda-\bar{\theta})\sin\varsigma\cos\varsigma\left(k_\beta^2-k_\alpha^2\cos^2\varsigma\right)^{-\frac{1}{2}}\right], \tag{C.8c}$$

at the diffraction point $(\lambda_s,\varsigma_s)=(\bar{\theta},\Omega_\alpha(\phi))$,

$$\partial^2_{\lambda\lambda} q\big|_{(\lambda_s,\varsigma_s)} = ik_\beta\sin^2\phi, \tag{C.9a}$$

$$\partial^2_{\varsigma\varsigma} q\big|_{(\lambda_s,\varsigma_s)} = i\frac{k_\alpha^2-k_\beta^2\cos^2\phi}{k_\beta\sin^2\phi}, \tag{C.9b}$$

$$\partial^2_{\lambda\varsigma} q\big|_{(\lambda_s,\varsigma_s)} = 0. \tag{C.9c}$$

Using (C.9), the Hessian matrix at the stationary phase point (λ_s,ς_s) is

$$Q_2(\lambda_s,\varsigma_s)=\begin{bmatrix}\partial^2_{\lambda\lambda} q\big|_{(\lambda_s,\varsigma_s)} & \partial^2_{\lambda\varsigma} q\big|_{(\lambda_s,\varsigma_s)}\\ \partial^2_{\varsigma\lambda} q\big|_{(\lambda_s,\varsigma_s)} & \partial^2_{\varsigma\varsigma} q\big|_{(\lambda_s,\varsigma_s)}\end{bmatrix}=\begin{bmatrix}ik_\beta\sin^2\phi & 0\\ 0 & i\dfrac{k_\alpha^2-k_\beta^2\cos^2\phi}{k_\beta\sin^2\phi}\end{bmatrix}. \tag{C.10}$$

Using (3.12) in (C.10), the Hessian determinant is

$$\det[Q_2(\lambda_s,\varsigma_s)]=-k_\alpha^2\sin^2\Omega_\alpha(\phi). \tag{C.11}$$

We also have at (λ_s, ς_s):

$$q(\lambda_s, \varsigma_s) = -ik_\beta \tag{C.12}$$

and knowing that $q_\beta(\phi) = \kappa_\beta \sin\phi$,

$$h(\lambda_s, \varsigma_s) = \frac{k_\alpha}{2\pi} f_\beta(-\kappa_\beta \sin\phi\cos\theta, \mathrm{sgn}(\sin\theta))\ \sin\Omega_\alpha(\phi)\ \mathbf{e}_\beta(\phi) \tag{C.13}$$

where

$$\mathbf{e}_\beta(\phi) = \mathbf{t}_\beta(-\kappa_\beta \sin\phi\cos\theta, \mathrm{sgn}(\sin\theta)). \tag{C.14}$$

Substituting expressions (C.11), (C.12) and (C.13) in (C.4), we get

$$I \sim -i\,\frac{e^{ik_\beta s'}}{s'} f_\beta(-\kappa_\beta \sin\phi\cos\theta, \mathrm{sgn}(\sin\theta))\ \mathbf{e}_\beta(\phi). \tag{C.15}$$

Finally, substituting f_β by its expression (2.4) in (C.15) with always $q_\beta(\varsigma_s) = \kappa_\beta \sin\phi$ and using the expression of the diffraction coefficient (2.31), the approximated incremental field is

$$I \sim \frac{1}{\sqrt{2i\pi}}\, D_\beta^{\alpha(\mathrm{GTD})}(\Omega_\alpha(\phi), \theta_\alpha, \theta)\, \frac{e^{ik_\beta s'}}{s'}\ \mathbf{e}_\beta(\phi). \tag{C.16}$$

Appendix D

Experimental validation of the Laplace transform GTD diffraction coefficient

Chapman and Fradkin [80] validated the Sommerfeld approach by comparing its results with experimental ones. To realize that, they used two isotropic ferritic steel (longitudinal velocity $c_L = 5800$ m.s^{-1} and transversal velocity $c_T = 3230$ m.s^{-1}) wedges of angle $2\varphi = 80°$ and $100°$ in the forms of cylindrical sectors of radius 150 mm and thickness 100 mm (see Fig. D.1). The wedges were inspected in pulse-echo, meaning that the emitter transducer is also the receiver transducer. Thus, the observation angle θ' with respect to the wedge bisector corresponds to the incidence angle. Transducers of 12 mm diameter crystal are used.

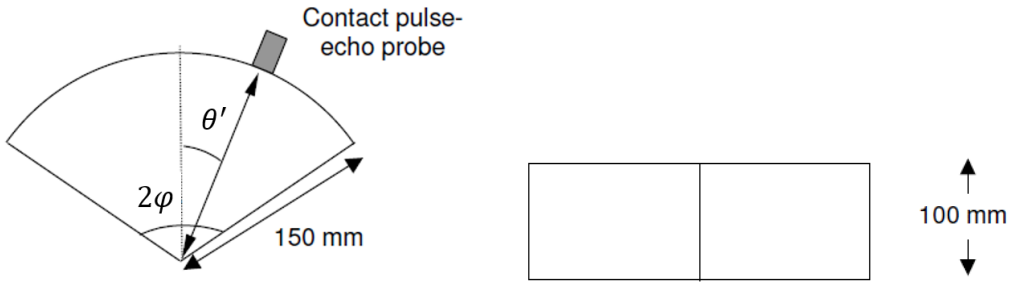

(a) Inspection of the wedge specimen (top view) (b) Thickness of the cylindrical sector (front view)

Figure D.1: (Reproduced from [80]) Inspection of a wedge of angle 2φ in pulse/echo.

In [80], the wedge of angle $100°$ has been inspected at many frequencies (2 and 5 MHz) with longitudinal waves to check that the diffraction coefficient does not depend on the frequency. Experimental results at 2 MHz are represented in circles and those at 5 MHz are represented by

triangles (see Fig. D.2). Due to the symmetry of the problem, in [80] measurements were taken on both side of the wedge transducer to check the symmetry of the results. Dark circles and gray triangles on Figs. D.2 and D.4 represent results when the probe is after the wedge bisector and white circles on Figs. D.2, D.3 and D.4 represent results when the probe is before the wedge bisector.

Results obtained with the Laplace transform (LT) approach are superimposed to numerical [Sommerfeld integral (SI) code] and experimental results on Figs. D.2-D.4. In these configurations, Laplace transform method behaves like the Sommerfeld integral method and gives close results to the experimental ones. Laplace transform and Sommerfeld integral approaches give close results far away from shadow boundaries and both of them diverge as expected at shadow boundaries. For the T waves in Fig. D.4, SI and LT have additional spikes near $\theta' \approx 7°$ which corresponds to an incidence angle of $57°$ on the wedge faces. $57°$ is the critical angle for which head waves are generated (see Fig. 2.10). The GTD theory also breaks down near critical angles leading to a discontinuity of the GTD coefficient. That can explain the difference between simulated diffraction coefficient and the experimental one at $\theta' = 5°$.

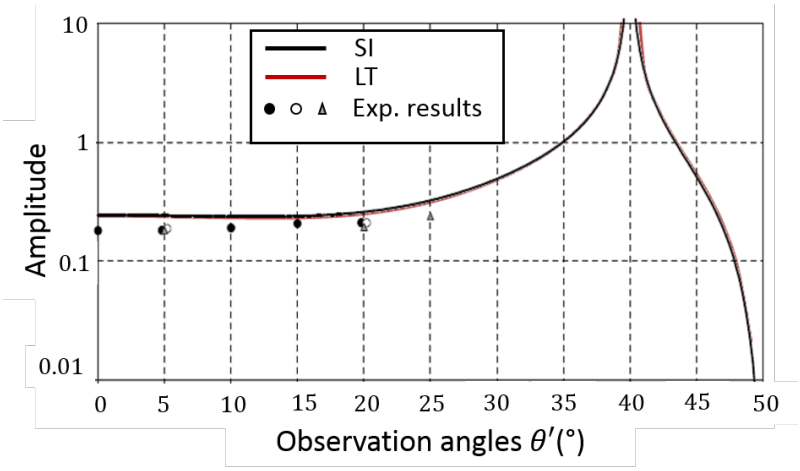

Figure D.2: Amplitude of the backscattering diffraction coefficient D_L^L for a wedge of $100°$. Comparison of the LT results with the Sommerfeld integral (SI) and experimental results. Dark circles (white circles respectively) represent diffraction coefficient when the probe is after (before) the wedge bisector at a frequency of 2 MHz. Gray triangles are diffraction coefficients measured at a frequency of 5 MHz when the probe is after the wedge bisector.

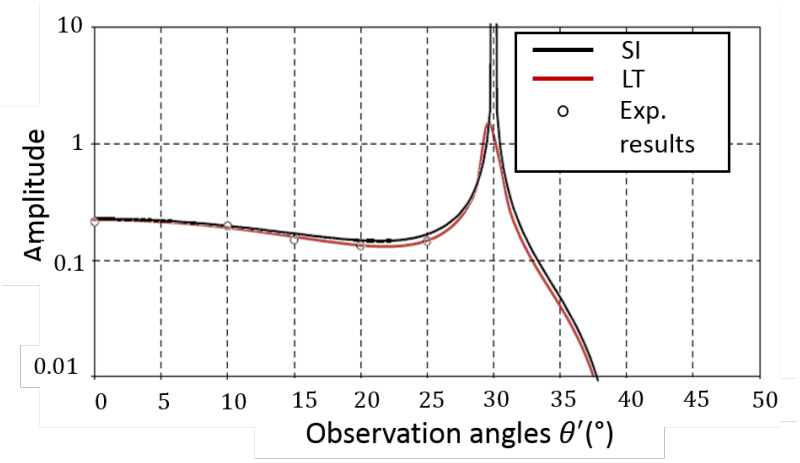

Figure D.3: Amplitude of the backscattering diffraction coefficient D_L^L for a wedge of $80°$. Comparison of the LT results with the Sommerfeld integral (SI) and experimental results. White circles represent diffraction coefficient when the probe is before the wedge bisector at a frequency of 2 MHz.

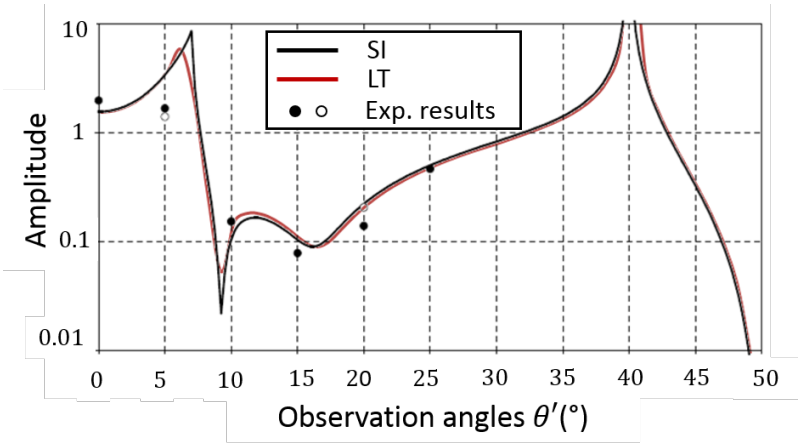

Figure D.4: Amplitude of the backscattering diffraction coefficient D_T^T for a wedge of $100°$. Comparison of the LT results with the Sommerfeld integral (SI) and experimental results. Dark circles (white circles respectively) represent diffraction coefficient when the probe is after (before) the wedge bisector at a frequency of 2 MHz.

Appendix E

UTD implementation in CIVA

The physical parameter modeled in CIVA in an inspection simulation is the voltage $V_R(t)$ measured on the receiving transducer crystal. Darmon and Chatillon [26] have shown that this output voltage can be modeled thanks to the echographic impulse response $f_{\text{echo}}(\mathcal{S},t)$ from a scatterer point (called $\mathcal{S}$, point on the scatterer surface or on the diffracting edge) as

$$V_R(t) = f_{\text{echo}}(\mathcal{S},t) * \text{Sigref}(t) \tag{E.1}$$

with $\text{Sigref}(t)$ being called the reference signal. $\text{Sigref}(t)$ corresponds to the input signal of the inspection simulation and is chosen as the experimental specular echo from a reference block or a calibration flaw. The echographic impulse response from a scatterer point depends on a directivity coefficient $A(\mathcal{S},t)$ of the wave emitted by this scatterer point which has been supposed to be spherical [26]. $f_{\text{echo}}(\mathcal{S},t)$ also depends on the emitted fields by both the emitter and the receiver acting as an emitter towards the scatterer. The echo contribution of a scatterer point is expressed as [26]

$$f_{\text{echo}}(\mathcal{S},t) = 2\pi\rho\, q_\alpha(\mathcal{S})\, q_\beta(\mathcal{S}) \int A(\mathcal{S}, t - T_\alpha(\mathcal{S}) - T_\beta(\mathcal{S}))\, \mathrm{d}t, \tag{E.2}$$

where ρ is the density of the inspected specimen, $T_{\alpha,\beta}(\mathcal{S})$ is the time of flight between the emitter/receiver transducer and the scatterer. The terms q_α and q_β are the amplitude module distribution of the beam of type $\alpha = L, TV$ emitted from the emitter and the beam of type $\beta = L, TV$ emitted from the receiver transducer to the scatterer respectively. The expression (E.2) has been established to deal with 3D configuration for which the scattering of an incident wave from a point on a scatterer surface or on a diffracting edge can be modelled using spherical scattered waves. It is therefore well convenient to implement the Kirchhoff approximation (1.4) and the GTD for a half-plane coupled with Huygens or ITD (Incremental Theory of Diffraction) [see Eqs. (3.2) and (3.21)] in CIVA by the use of (E.2) and (E.1).

For the UTD implementation in CIVA, we are interested in 2D configuartion since the study case

in this thesis is a 2D wedge scattering. For 2D configuration, expression (E.2) is still valid up to a constant multiplier and $A(\mathcal{S}, t)$ is the directivity coefficient of the cylindrical waves emitted by the scatterer point.

The pencil method explained in chapter 1 is used to model the beam propagation. The divergence factor of a pencil is the same as the one of a spherical wave for a 3D configuration and it is also the same as the one of a cylindrical wave for a 2D configuration. For example, on Fig. E.1, the divergence factor of the emitted L wave from the emitter transducer, the red point on the front surface of the specimen, to the scatterers $\mathcal{S}_1$, $\mathcal{S}_2$ and $\mathcal{S}_3$ is respectively $(s_e^1)^{-1}$, $(s_e^2)^{-1}$ and $(s_e^3)^{-1}$ in a 3D configuration and $(s_e^1)^{-1/2}$, $(s_e^2)^{-1/2}$ and $(s_e^3)^{-1/2}$ in a 2D configuration. s_e^1, s_e^2 and s_e^3 are the distance between the emitter transducer and the scatterers $\mathcal{S}_1$, $\mathcal{S}_2$ and $\mathcal{S}_3$ respectively. In this example, the scatterers are wedge edges.

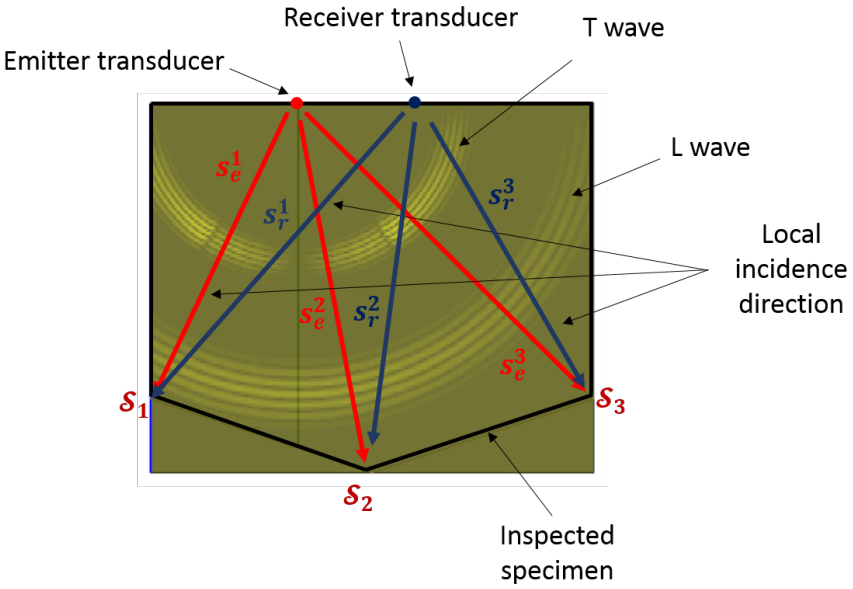

Figure E.1: Distance between the emitter/receiver transducer to the scatterer points.

For an integrable function $f(t)$, t being the time, we define the Fourier transform as

$$\hat{f}(\omega) = \int_{-\infty}^{+\infty} f(t)\, e^{i\omega t}\, \mathrm{d}t, \tag{E.3}$$

where ω is the circular frequency. Then, applying the Fourier transform in time to Eq. (E.2) leads to the echographic impulse response of a scatterer point in the frequency domain

$$f_{\text{echo}}(\mathcal{S}, \omega) = (2\pi)\,(i\omega)\,\rho\, q_\alpha(\mathcal{S})\, q_\beta(\mathcal{S})\, A(\mathcal{S}, \omega)\, e^{i\omega(T_\alpha(\mathcal{S}) + T_\beta(\mathcal{S}))}. \tag{E.4}$$

This echographic impulse response of a scatterer point in the frequency domain can be reduced

to

$$f_{\text{echo}}(\mathcal{S},\omega) = (2\pi)\,(i\omega)\,\rho\,u_\alpha(\mathcal{S})\,u_\beta(\mathcal{S})\,A(\mathcal{S},\omega) \tag{E.5}$$

where $u_\alpha = q_\alpha(\mathcal{S})\,\exp[i\omega T_\alpha(\mathcal{S})]$ and $u_\beta = q_\beta(\mathcal{S})\,\exp[i\omega T_\beta(\mathcal{S})]$ are the incident local plane wave on the scatterer point emitted from the emitter transducer and from the receiver transducer respectively. This formulation just considers one unique incidence direction on the scatterer point obtained thanks to the pencil method. Expression (E.5) is then based on the plane wave approximation and on the field reciprocity.

Let us now determine the directivity coefficient $A(\mathcal{S},t)$ of the cylindrical waves emitted by the scatterer point on the diffracting edge using the UTD model.

The UTD model developed in chapter 4 has been established for 2D configurations to provide a good description of the diffracted field by a wedge near and at shadow boundaries of the geometrical field. To be able to model this UTD diffracted field [see Eq. (4.121)] in CIVA with Eq. (E.2), we need to know the directivity coefficient $A(\mathcal{S},t)$ of the cylindrical wave emitted by the edge wedge. In frequency domain, using (4.121) and (4.110) and expressing the wavenumber as $k_\beta = \omega/c_\beta$ where c_β is the velocity of the wave of type β, the directivity coefficient of cylindrical waves of type $\beta = L$ or T emitted by an edge wedge is

$$A^{\text{UTD}}(\mathcal{S},\omega) = (-1)^{M_\beta+1}\,D_\beta^{\text{LT}}(\theta,\theta_{\text{inc}})\,\sqrt{\frac{c_\beta}{\omega}}\left(\sum_{j=1}^{M_\beta} F(\zeta\,a_\beta^j)\prod_{\substack{k=1\\k\neq j}}^{M_\beta}\frac{s_\beta^k}{(s_\beta^j - s_\beta^k)}\right) \tag{E.6}$$

where θ (θ_{inc} respectively) is the angle of the incident local plane wave emitted by the receiver (emitter respectively) transducer on a face of the wedge.

Let us introduce the UTD diffraction coefficient

$$D_\beta^{\text{LT (UTD)}}(\zeta,\theta,\theta_{\text{inc}}) = (-1)^{M_\beta+1}\,D_\beta^{\text{LT}}(\theta,\theta_{\text{inc}})\left(\sum_{j=1}^{M_\beta} F(\zeta\,a_\beta^j)\prod_{\substack{k=1\\k\neq j}}^{M_\beta}\frac{s_\beta^k}{(s_\beta^j - s_\beta^k)}\right), \tag{E.7}$$

the directivity coefficient of the cylindrical waves of type β in the frequency domain (E.6) can be rewritten as

$$A^{\text{UTD}}(\mathcal{S},\omega) = D_\beta^{\text{LT (UTD)}}(\zeta,\theta,\theta_{\text{inc}})\,\sqrt{\frac{c_\beta}{\omega}}. \tag{E.8}$$

Here, being in a 2D configuration, the radiated wave by source points on the emitter transducer crystal is a cylindrical wave. The far-field parameter ζ in the diffracted UTD field (E.7) must then take into account the nature of the emitted wave, a cylindrical incident wave in this case, as specified in chapter 2 in order to have the divergence factor of a cylindrical wave in reflection

when applying UTD and then to have a compensation of the geometrical field near shadow boundaries. The far-field parameter ζ of a cylindrical incident wave defined in (2.45) recalled hereafter

$$\zeta = k_\beta L_\beta = k_\beta \frac{s_r\, s_e}{s_r + s_e \dfrac{\sin^2\theta_\alpha}{\sin^2\theta_\beta}\dfrac{c_\beta}{c_\alpha}} \tag{E.9}$$

is then considered. $\theta_\alpha = \theta_{\text{inc}}$, θ_β is the angle of the reflected wave of type β (θ_α and θ_β respect Snell-Descartes law of reflection), $1/c_\alpha$ is slowness of the incident wave and $1/c_\beta$ is the the one of the scattered wave of type β. The parameter s_r in (E.9) is the distance from the receiver transducer to the scatterer wedge and s_e the distance from the emitter transducer to the scatterer wedge. Note that the far-field parameter considered here is for a wave propagating in one medium. With this far-field parameter, only the case where probes are in contact with the specimen can be treated.

Let us define the parameter E^{UTD}

$$E^{\text{UTD}} = \sqrt{\frac{c_\beta}{\omega}} \tag{E.10}$$

which depends on the frequency. Applying the Fourier transform in time to (E.1),

$$V_R(\omega) = f_{\text{echo}}(\mathcal{S}, \omega)\, \text{Sigref}(\omega) \tag{E.11}$$

and using (E.11), (E.5) and (E.8), the output voltage modeled with "UTD model" is

$$V_R^{\text{UTD}}(\omega) = f_{\text{echo}}^{\text{UTD}}(\mathcal{S})\, \text{UTDSigref}(\omega) \tag{E.12}$$

with

$$f_{\text{echo}}^{\text{UTD}}(\mathcal{S}) = (2\pi)\rho\, u_\alpha(\mathcal{S})\, u_\beta(\mathcal{S})\, D_\beta^{\text{LT (UTD)}}(\zeta, \theta, \theta_{\text{inc}}). \tag{E.13}$$

and UTDSigref is the UTD reference signal that contains all the terms which depend on the frequency:

$$\text{UTDSigref}(\omega) = (i\omega)\, E^{\text{UTD}}\, \text{Sigref}(\omega). \tag{E.14}$$

To adjust this "UTD model" with specular model and Kirchhoff model so that the echo amplitudes simulated with the "UTD model" could be compared to the ones obtained with specular and Kirchhoff models, the UTD reference signal (E.14) obtained theoretically has been linked to the theoretical Kirchhoff reference signal determined in the sequel since Kirchhoff model is already well adjusted to the specular model.

In order to find the theoretical expression of the KA reference signal and to compare it to the

theoretical UTD reference signal (E.14), the Kirchhoff integral (1.1) is used in a simple case, the scattering of a cylindrical "acoustic" wave by a rigid half-plane. That simple case is chosen because the Green function is quite simple for acoustic waves contrary to the one of the elastic waves 4.82.

In the Kirchhoff approximation (KA) introduced in section 1.3 in chapter 1, for 2D configurations, the scatterers points are on the diffracting contour in the perpendicular plane to the extension direction. Therefore, for a rigid half-plane impacted by a cylindrical wave as illustrated in Fig. E.2, the KA integral is [84]

$$g^{\mathrm{KA}}(\mathbf{x}) = \int_{\mathcal{C}^+} 2g_{\mathrm{inc}}(\mathbf{x}') \frac{\partial}{\partial \mathbf{n}} \left(\frac{1}{\sqrt{8i\pi}} \frac{e^{-ikd}}{\sqrt{kd}} \right) \mathrm{d}h \tag{E.15}$$

where u^{KA} is the potential velocity diffracted field found using the Kirchhoff approximation, u_α is the incident field, k is the wavenumber of the acoustic wave, $d = ((x-h)^2 + y^2)^{1/2}$ is the distance between a point on the diffracting contour $\mathcal{C}^+$ of position vector $\mathbf{x}'$ and the observation point of position vector $\mathbf{x}$ (see Fig. E.2) and $\mathbf{n}$ is the half-plane inner normal.

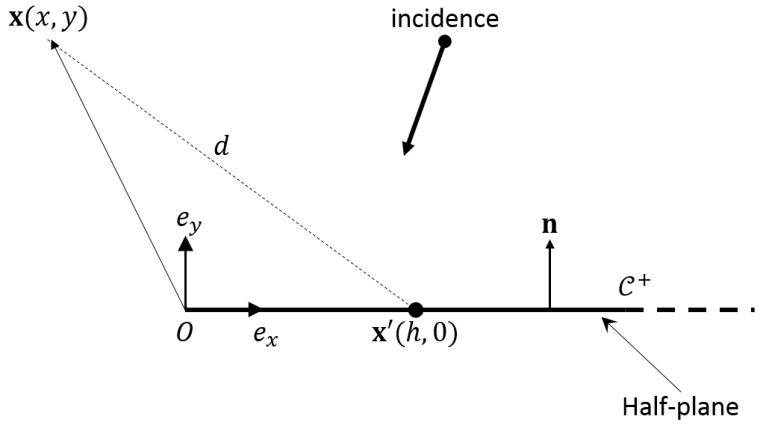

Figure E.2: Scatterer of contour $\mathcal{C}^+$ with an infinite extension in the perpendicular direction to the plane $(\mathbf{e}_x, \mathbf{e}_y)$ impacted by a cylindrical wave.

This integral is reduced to

$$g^{\mathrm{KA}}(\mathbf{x}) = -\frac{i\sqrt{k}}{\sqrt{2i\pi}} \int_{\mathcal{C}^+} g_{\mathrm{inc}}(\mathbf{x}') \frac{e^{-ikd}}{\sqrt{d}} \frac{y}{d} \mathrm{d}h. \tag{E.16}$$

The reflection coefficient for a normal incidence is equal to -1. Therefore, knowing that $k = \omega/c$, c being the velocity of the acoustic wave,

$$g^{\mathrm{KA}}(\mathbf{x}) = -\frac{\sqrt{\omega c}}{\sqrt{-2i\pi}} \int_{\mathcal{C}^+} g_{\mathrm{inc}}(\mathbf{x}') \frac{e^{-ikd}}{\sqrt{d}} \left(-\frac{y}{d} \frac{1}{c} \right) \mathrm{d}h. \tag{E.17}$$

Let us define the parameter E^{KA} as

$$E^{\mathrm{KA}}(\omega) = -\frac{\sqrt{\omega c}}{\sqrt{-2i\pi}} \tag{E.18}$$

which depends on the frequency. According to (E.17), and the theoretical KA diffraction coefficient which is also the directivity coefficient of cylindrical waves emitted by a point on the scatterer is

$$A^{\mathrm{KA}}(\mathcal{S},\omega) = E^{\mathrm{KA}}(\omega)\left(-\frac{y}{d}\frac{1}{c}\right). \tag{E.19}$$

For elastic waves, $A^{\mathrm{KA}}(\mathcal{S},\omega)$ is a more complicated expression. In elastodynamics, $A^{\mathrm{KA}}(\mathcal{S},\omega)$ also depends on the term E^{KA} which comes from the constant coefficient of the Green function (see Eq. 4.82). Using (1.4), the theoretical KA diffraction coefficient which is also the directivity coefficient of cylindrical waves emitted by a point on a scatterer is

$$D^{\alpha}_{\beta}(\omega) = A^{\mathrm{KA}}(\mathcal{S},\omega) = E^{\mathrm{KA}}(\omega)\, D^{\mathrm{KA}}, \tag{E.20}$$

where D^{KA} does not depend on the frequency. Using (E.11), (E.5) and (E.20), the output voltage modeled with "KA model" in 2D configuration is

$$V_R^{\mathrm{KA}}(\omega) = \rho\,(2\pi)\left[\sum_{M\in\mathcal{C}^+} u_\alpha(M)\, u_\beta(M)\, D^{\alpha}_{\beta}(\omega)\, dx\right](i\omega)\mathrm{Sigref}(\omega) \tag{E.21}$$

where $\mathcal{C}^+$ is the lit contour of the diffracting obstacle, M is a point on this contour and dx is an elementary element on the contour $\mathcal{C}^+$. That output voltage could also be put into a form similar to (E.12) :

$$V_R^{\mathrm{KA}}(\omega) = f^{\mathrm{KA}}_{\mathrm{echo}}(\mathcal{S})\,\mathrm{KASigref}(\omega) \tag{E.22}$$

with

$$\mathrm{KASigref}(\omega) = E^{\mathrm{KA}}\,(i\omega)\,\mathrm{Sigref}(\omega), \tag{E.23}$$

and

$$f^{\mathrm{KA}}_{\mathrm{echo}}(\mathcal{S}) = \rho\,(2\pi)\left[\sum_{M\in\mathcal{C}^+} u_\alpha(M)\, u_\beta(M)\, D^{\mathrm{KA}}\, dx\right]. \tag{E.24}$$

The theoretical KA reference signal, KASigref, is linked to the theoretical UTD reference signal, UTDSigref, by

$$\mathrm{UTDSigref}(\omega) = -\frac{\sqrt{-2i\pi}}{\omega}\,\mathrm{KASigref}(\omega). \tag{E.25}$$

This proportionality (E.25) between the two models, "UTD model" and Kirchhoff model, found

theoretically, must always exist. The echo amplitudes simulated with the KA model in CIVA are comparable to the ones of other models in CIVA such as the specular and CIVA-Athena 2D models. The proportionality factor between the theoretical expression of the UTD and KA reference signals must be the same between the CIVA UTD and KA reference signals in CIVA. Therefore, in CIVA, for 2D configurations, UTD is implemented with

$$\mathrm{UTDSigref}_{CIVA}(\omega) = -\frac{\sqrt{-2i\pi}}{\omega}\,\mathrm{KASigref}_{CIVA}(\omega). \tag{E.26}$$

Appendix F

Calculation details of integrals in chapter 5

Integrals to calculate in the subsection "matrice calculation" of section 5.3.2.2 in chapter 5 are in the following form:

$$I_1 = \int_{-1}^{1} \frac{\alpha x + \beta}{Q(x)} \mathrm{d}x \quad \text{and} \quad I_2 = \int_{-1}^{1} \frac{\gamma x + \delta}{P(x)} \mathrm{d}x \tag{F.1}$$

with polynomial functions $P(x)$ and $Q(x)$ defined in (5.121) and (5.122) respectively.

Let us first calculate integral I_1.

$$\begin{aligned}
I_1 &= \int_{-1}^{1} \frac{\alpha x + \beta}{iax^2 + 2x - ia} \mathrm{d}x \\
&= \frac{\alpha}{2ia} \int_{-1}^{1} \frac{2(iax+1)}{iax^2 + 2x - ia} \mathrm{d}x + \int_{-1}^{1} \frac{\beta - \frac{\alpha}{ia}}{iax^2 + 2x - ia} \mathrm{d}x \\
&= \frac{\pi\alpha}{2a} + \left(\frac{\beta}{ia} + \frac{\alpha}{a^2}\right) \int_{-1}^{1} \frac{1}{x^2 + \frac{2}{ia}x - 1} \mathrm{d}x \\
&= \frac{\pi\alpha}{2a} + \left(i\beta - \frac{\alpha}{a}\right) \mathrm{rog}(a) \\
I_1 &= \alpha\, \mathrm{sog}(a) + i\beta\, \mathrm{rog}(a)
\end{aligned} \tag{F.2}$$

with rog and sog functions being defined in (5.132) and (5.128) respectively.

Let us calculate the rog function.

$$\begin{aligned}
\mathrm{rog}(a) &= \int_{-1}^{1} \frac{1}{a(1-x^2)+2ix}\mathrm{d}x \\
&= -\frac{1}{a}\int_{-1}^{1} \frac{1}{\left(x+\frac{1}{ia}\right)^2+\frac{1}{a^2}-1}\mathrm{d}x \\
&= -\frac{1}{a}\int_{-1}^{1} \frac{1}{\left(x+\frac{1}{ia}-\sqrt{1-\frac{1}{a^2}}\right)\left(x+\frac{1}{ia}+\sqrt{1-\frac{1}{a^2}}\right)}\mathrm{d}x \\
&= \frac{1}{2a\sqrt{1-\frac{1}{a^2}}}\int_{-1}^{1} \frac{-1}{\left(x+\frac{1}{ia}-\sqrt{1-\frac{1}{a^2}}\right)}+\frac{1}{\left(x+\frac{1}{ia}+\sqrt{1-\frac{1}{a^2}}\right)}\mathrm{d}x \quad \text{if} \quad a\neq\pm 1 \\
&= -\frac{1}{2a\sqrt{1-\frac{1}{a^2}}}\ln\left(\frac{1-\sqrt{1-\frac{1}{a^2}}}{1+\sqrt{1-\frac{1}{a^2}}}\right) \\
&= \frac{1}{\sqrt{a^2-1}}\ln\left(a+\sqrt{a^2-1}\right). \qquad \text{(F.3)}
\end{aligned}$$

We then found the expression of rog function in (5.127). The chosen branch cut of the square root function is along the negative real axis. The argument of any complex z is included in the domain $]-\pi,\pi]$.

Now let us calculate the integral I_2.

$$\begin{aligned}
I_2 &= \int_{-1}^{1} \frac{\gamma x+\delta}{b(1-x^2)-2ix\cos 2\varphi+|\sin 2\varphi|(1+x^2)}\mathrm{d}x \\
&= \int_{-1}^{1} \frac{\gamma x+\delta}{x^2(|\sin 2\varphi|-b)-2ix\cos 2\varphi+(b+|\sin 2\varphi|)}\mathrm{d}x \\
&= \frac{1}{2(|\sin 2\varphi|-b)}\int_{-1}^{1} \frac{2\gamma\Big[\Big(|\sin 2\varphi|-b\Big)x-i\cos 2\varphi\Big]+2\Big[i\gamma\cos 2\varphi+\delta\Big(|\sin 2\varphi|-b\Big)\Big]}{x^2(|\sin 2\varphi|-b)-2ix\cos 2\varphi+(b+|\sin 2\varphi|)}\,\mathrm{d}x \quad \text{if} \quad b\neq|\sin 2\varphi| \\
&= \frac{i\gamma}{|\sin 2\varphi|-b}\left(\widetilde{2\varphi}-\frac{\pi}{2}\right)+\frac{1}{(|\sin 2\varphi|-b)^2}\int_{-1}^{1} \frac{i\gamma\cos 2\varphi+\delta\Big(|\sin 2\varphi|-b\Big)}{\left(x-\frac{i\cos\varphi}{|\sin 2\varphi|-b}\right)^2-\frac{b^2-1}{(|\sin 2\varphi|-b)^2}}\mathrm{d}x \\
&= \frac{i\gamma}{|\sin 2\varphi|-b}\left(\widetilde{2\varphi}-\frac{\pi}{2}\right)+\frac{1}{|\sin 2\varphi|-b}\left(\delta+\gamma\frac{i\cos 2\varphi}{|\sin 2\varphi|-b}\right)I_3 \qquad \text{(F.4)}
\end{aligned}$$

where

$$I_3=\int_{-1}^{1} \frac{1}{\left(x-\frac{i\cos\varphi}{|\sin 2\varphi|-b}\right)^2-\frac{b^2-1}{(|\sin 2\varphi|-b)^2}}\mathrm{d}t. \qquad \text{(F.5)}$$

We need to determine I_3 to access the value of I_2.

$$
\begin{aligned}
I_3 &= \int_{-1}^{1} \frac{1}{\left(x - \dfrac{i\cos\varphi}{|\sin 2\varphi| - b} - \dfrac{\sqrt{b^2-1}}{|\sin 2\varphi| - b}\right)\left(x - \dfrac{i\cos\varphi}{|\sin 2\varphi| - b} + \dfrac{\sqrt{b^2-1}}{|\sin 2\varphi| - b}\right)} \mathrm{d}x \\
&= \frac{|\sin 2\varphi| - b}{2\sqrt{b^2-1}} \int_{-1}^{1} \frac{1}{\left(x - \dfrac{i\cos\varphi}{|\sin 2\varphi| - b} - \dfrac{\sqrt{b^2-1}}{|\sin 2\varphi| - b}\right)} - \frac{1}{\left(x - \dfrac{i\cos\varphi}{|\sin 2\varphi| - b} + \dfrac{\sqrt{b^2-1}}{|\sin 2\varphi| - b}\right)} \mathrm{d}x \\
&= \frac{|\sin 2\varphi| - b}{\sqrt{b^2-1}} \ln\left(b + \sqrt{b^2-1}\right) \\
&= (|\sin 2\varphi| - b)\,\mathrm{rog}(b). \qquad \text{(F.6)}
\end{aligned}
$$

Finally, using (F.6) in (F.4),

$$
I_2 = \frac{i\gamma}{|\sin 2\varphi| - b}\left(\widetilde{2\varphi} - \frac{\pi}{2} + i\gamma\cos 2\varphi\,\mathrm{rog}(b)\right) + \delta\,\mathrm{rog}(b). \qquad \text{(F.7)}
$$

Bibliography

[1] T. Łodygowski and W. Sumelka. Limitations in application of finite element method in acoustic numerical simulation. *Journal of theoretical and applied mechanics*, 44(4):849–865, 2006.

[2] J. M. Melenk and I. Babuška. The partition of unity finite element method: basic theory and applications. *Computer methods in applied mechanics and engineering*, 139(1):289–314, 1996.

[3] M. Darmon, N. Leymarie, S. Chatillon, and S. Mahaut. Modelling of scattering of ultrasounds by flaws for NDT. In *Ultrasonic wave propagation in non homogeneous media*, pages 61–71. Springer, 2009.

[4] A. Sommerfeld and E.-G. Straus. *Partial differential equations in physics.*, volume 1. Academic Press, 1949.

[5] S. H. Schot. Eighty years of Sommerfeld's radiation condition. *Historia mathematica*, 19(4):385–401, 1992.

[6] Y. Rahmat-Samii and R. Mittra. A Spectral Domain Analysis of High Frequency Diffraction Problems. Technical report, DTIC Document, 1977.

[7] M. Kline. Electromagnetic theory and geometrical optics. Technical report, DTIC Document, 1962.

[8] J. B. Keller. Geometrical theory of diffraction. *J. Opt. Soc. Am.*, 52(2):116–130, 1962.

[9] M. Motamed and O. Runborg. Approximation of high frequency wave propagation problems. In *Highly oscillatory problems*, pages 72–96. Cambridge University Press, 2009.

[10] B. Lu, M. Darmon, C. Potel, L. Ju. Fradkin, and S. Chatillon. Modeling of the interaction of an acoustic wave with immersed targets for telemetry of complex structures. *Procedings of the AFPAC*, 2012.

[11] J.-P. Croisille and G. Lebeau. *Diffraction by an immersed elastic wedge.* Number 1723. Springer Science & Business Media, 1999.

[12] R. G. Kouyoumjian and P. H. Pathak. A uniform geometrical theory of diffraction for an edge in a perfectly conducting surface. In *Proc. of the IEEE*, volume 62. IEEE, 1974.

[13] W. C. Meecham. On the use of the Kirchhoff approximation for the solution of reflection problems. *Eng. Res. Institute, Dep. Phys., Michigan Univ.*, 1955.

[14] P. H. Pathak and R. G. Kouyoumjian. The dyadic diffraction coefficient for a perfectly-conducting wedge. Technical report, DTIC Document, 1970.

[15] D. Bouche and F. Molinet. *Méthodes asymptotiques en électromagnétisme*. Springer-Verlag, 1994.

[16] F. Molinet. *Acoustic High-Frequency Diffraction Theory*. Momentum Press, 2011.

[17] V. M. Babich, M. A. Lyalinov, and V. E. Grikurov. Diffraction theory: The Sommerfeld-Malyuzhinets technique, 2007.

[18] J-D. Benamou, O. Lafitte, I. Solliec, and R. Sentis. A geometric optics method for high-frequency electromagnetic fields computations near fold caustics - Part II. The energy. *Journal of computational and applied mathematics*, 167(1):91–134, 2004.

[19] P. Ya Ufimtsev. *Fundamentals of the physical theory of diffraction*. John Wiley & Sons, 2007.

[20] J. Gutiérrez Meana, J. Á. Martínez Lorenzo, and F. L. Las Heras Andrés. *High frequency techniques: The physical optics approximation and the modified equivalent current approximation (MECA)*. InTech, 2011.

[21] R. K. Chapman. Ultrasonic scattering from smooth flat cracks : An elastodynamic kirchhoff diffraction theory. Technical report, North Western Region NDT Applications Centre, 1982.

[22] A. K. Gautesen J. D. Achenbach and H. McMaken. *Rays methods for waves in elastic solids*. Pitman, 1982.

[23] J. D. Achenbach and A. K. Gautesen. Geometrical theory of diffraction for three-D elastodynamics. *The Journal of the Acoustical Society of America*, 61(2):413–421, 1977.

[24] L. Ju Fradkin and R. Stacey. The high-frequency description of scatter of a plane compressional wave by an elliptic crack. *Ultrasonics*, 50(4):529–538, 2010.

[25] B. V. Budaev and D. B. Bogy. Rayleigh wave scattering by a wedge. *Wave Motion*, 22(3):239–257, 1995.

[26] M. Darmon and S. Chatillon. Main Features of a Complete Ultrasonic Measurement Model: Formal Aspects of Modeling of Both Transducers Radiation and Ultrasonic Flaws Responses. *Open Journal of Acoustics*, 2013.

[27] N. Gengembre. *Modélisation du champ ultrasonore rayonné dans un solide anisotrope et hétérogène par un traducteur immergé*. PhD thesis, Université Paris 7, 1999.

[28] C. Poidevin, L. Roumilly, G. Cattiaux, and T. Sollier. Simulation de la réponse ultrasonore de défauts réalistes dans CIVA. *COFREND-Proceeding*, 2008.

[29] Jason Lambert, Gilles Rougeron, and Lionel Lacassagne. Modèle et méthodes de simulation de contrôle non-destructif par ultrasons massivement parallèles. *COFREND-Proceeding*, 2014.

[30] A. Dross. *http://accromath.uqam.ca/2011/06/mathematiques-de-la-tasse-de-the/*.

[31] B. B. Baker and E. T. Copson. *The mathematical theory of Huygens' principle*. Oxford university press, 1950.

[32] J. J. Bowman, T. B. Senior, and P. L. Uslenghi. Electromagnetic and acoustic scattering by simple shapes. Technical report, DTIC Document, 1970.

[33] R. M. Lewis. Physical optics inverse diffraction. *Antennas and Propagation, IEEE Transactions on Antennas and Propagation*, 17(3):308–314, 1969.

[34] L. Schmerr and S.-J. Song. *Ultrasonic nondestructive evaluation systems*. Springer, 2007.

[35] V. Dorval, S. Chatillon, B. Lu, M. Darmon, and S. Mahaut. A general Kirchhoff approximation for echo simulation in ultrasonic NDT. In *AIP Conference Proceedings-American Institute of Physics*, volume 1430, page 193, 2012.

[36] M. Darmon, V. Dorval, A. Kamta Djakou, L. Ju. Fradkin, and S. Chatillon. A system model for ultrasonic NDT based on the physical theory of diffraction (PTD). *Ultrasonics*, 64:115–127, 2016.

[37] V. V. Kamotski, L. Ju. Fradkin, B. A. Samokish, V. A. Borovikov, and V. M. Babich. On Budaev and Bogy's approach to diffraction by the 2D traction-free elastic wedge. *SIAM Journal on Applied Mathematics*, 67(1):235–259, 2006.

[38] A. K. Gautesen and L. Ju. Fradkin. Diffraction by a Two-Dimensional Traction-Free Elastic Wedge. *SIAM Journal on Applied Mathematics*, 70(8):3065–3085, 2010.

[39] Y. Rahmat-Samii. GTD, UTD, UAT, and STD: a historical revisit and personal observations. *Antennas and Propagation Magazine, IEEE*, 55(3):29–40, 2013.

[40] A. Kamta Djakou, M. Darmon, and C. Potel. Elastodynamic models for extending GTD to penumbra and finite size scatterers. *Physics Procedia*, 70:545–549, 2015.

[41] R. M. Lewis and J. Boersma. Uniform asymptotic theory of edge diffraction. *Journal of Mathematical physics*, 10(12):2291–2305, 1969.

[42] S. W. Lee and G. A. Deschamps. A uniform asymptotic theory of electromagnetic diffraction by a curved wedge. *IEEE Trans. Ant. Prop.*, 24(1):25–34, 1976.

[43] D. S. Ahluwalia. Uniform asymptotic theory of diffraction by the edge of a three-dimensional body. *SIAM J. Appl. Math.*, 10(2):287–301, 1970.

[44] V. A. Borovikov and B. Y. Kinber. *Geometrical theory of diffraction.* Number 37. IET, 1994.

[45] M. Darmon V. Zernov, L. Ju. Fradkin. A refinement of the Kirchhoff approximation to the scattered elastic fields. *Ultrasonics*, 52:830–835, 2012.

[46] B. L. Van Der Waerden. On the method of saddle points. *Appl. Sci. Res., section B*, (1), 1951.

[47] P. C. Clemmow. Some extension to the method of integration by steepest descent. *Quart. Journ. Mech. and Applied Math.*, III:241–256, 1950.

[48] H. McMaken. *Three dimensional diffraction by cracks in elastic solids.* PhD thesis, Northwestern Univsersity, 1980.

[49] N. Tsingos, T. Funkhouser, A. Ngan, and I. Carlbom. Modeling acoustics in virtual environments using the uniform theory of diffraction. In *Proceedings of the 28th annual conference on Computer graphics and interactive techniques*, pages 545–552. ACM, 2001.

[50] M. F. Catedra, J. Perez, F. Saez de Adana, and O. Gutierrez. Efficient ray-tracing techniques for three-dimensional analyses of propagation in mobile communications: application to picocell and microcell scenarios. *Antennas and Propagation Magazine, IEEE*, 40(2):15–28, 1998.

[51] W. D. Burnside. UTD antenna codes through the years. In *Antennas and Propagation Society International Symposium, 1992. AP-S. 1992 Digest. Held in Conjuction with: URSI Radio Science Meeting and Nuclear EMP Meeting., IEEE*, pages 1460–1461. IEEE, 1992.

[52] D. B. Davidson, I. P. Theron, U. Jakobus, F. M. Landstorfer, F. J-C. Meyer, J. Mostert, and J. J. Van Tonder. Recent progress on the antenna simulation program FEKO. In *Communications and Signal Processing, 1998. COMSIG'98. Proceedings of the 1998 South African Symposium on*, pages 427–430. IEEE, 1998.

[53] V. A. Borovikov. *Uniform stationary phase method.* The institution of Electrical Engineers, 1994.

[54] R. G. Rojas. Comparison between two asymptotic methods. *IEEE Trans. Ant. Prop.*, 35(12):1448–1492, 1987.

[55] D. Gridin. High-frequency asymptotic description of head waves and boundary layers surrounding the critical rays in an elastic half-space. *The Journal of the Acoustical Society of America*, 104(3):1188–1197, 1998.

[56] L. Ju. Fradkin, M. Darmon, S. Chatillon, and P. Calmon. A semi-numerical model for near-critical angle scattering. *The Journal of the Acoustical Society of America*, 139(1):141–150, 2016.

[57] A. Kamta Djakou, M. Darmon, L. Ju. Fradkin, and C. Potel. The Uniform geometrical Theory of Diffraction for elastodynamics: Plane wave scattering from a half-plane. *The Journal of the Acoustical Society of America*, 138(5):3272–3281, 2015.

[58] R. Tiberio and S. Maci. An incremental theory of diffraction: scalar formulation. *Antennas and Propagation, IEEE Transactions on*, 42(5):600–612, 1994.

[59] R. Tiberio, S. Maci, and A. Toccafondi. An incremental theory of diffraction: electromagnetic formulation. *Antennas and Propagation, IEEE Transactions on Antennas and Propagation*, 43(1):87–96, 1995.

[60] R. Tiberio, A. Toccafondi, A. Polemi, and S. Maci. Incremental theory of diffraction: A new-improved formulation. *Antennas and Propagation, IEEE Transactions on*, 52(9):2234–2243, 2004.

[61] A. D. Yaghjian. Incremental length diffraction coefficients for arbitrary cylindrical scatterers. *Antennas and Propagation, IEEE Transactions on Antennas and Propagation*, 49(7):1025–1032, 2001.

[62] Y. Z. Umul. Rigorous expressions for the equivalent edge currents. *Progress In Electromagnetics Research B*, 15:77–94, 2009.

[63] U. P. Svensson, R. I. Fred, and J. Vanderkooy. An analytic secondary source model of edge diffraction impulse responses. *The Journal of the Acoustical Society of America*, 106(5):2331–2344, 1999.

[64] U. P. Svensson, P. T. Calamia, and S. Nakanishi. Frequency-domain edge diffraction for finite and infinite edges. *Acta acustica united with acustica*, 95(3):568–572, 2009.

[65] T. K. Stanton and D. Chu. Acoustic diffraction by deformed edges of finite length: Theory and experiment. *The Journal of the Acoustical Society of America*, 116(4):2566–2566, 2004.

[66] M. Darmon, N. Leymarie, S. Chatillon, and S. Mahaut. Modelling of scattering of ultrasounds by flaws for NDT. In *Ultrasonic wave propagation in non homogeneous media*, pages 61–71. Springer, 2009.

[67] M. Darmon, A. Ferrand, V. Dorval, S. Chatillon, and S. Lonné. Recent modelling advances for ultrasonic TOFD inspections. In *41st annuam review of progress in quantitative Non-Destructive Evaluation: Volume 34*, volume 1650, pages 1757–1765. AIP Publishing, 2015.

[68] G. Toullelan, R. Raillon, S. Chatillon, V. Dorval, M. Darmon, and S. Lonné. Results of the 2015 UT modeling benchmark obtained with models implemented in CIVA. In *42nd annual review of progress in quantitative Non-Destructive Evaluation: Incorporating the 6th European-American Workshop on Reliability of NDE*, volume 1706, page 190001. AIP Publishing, 2016.

[69] A. Kamta Djakou, M. Darmon, L. Ju. Fradkin, and C. Potel. Two elastodynamic incremental models: the incremental theory of diffraction (ITD) and a Huygens method. submitted, 2016.

[70] *www.feko.info*.

[71] *http://www.remcom.com/xgtd*.

[72] *www.awe-communications.com/Products/ProMan*.

[73] A. K. Gautesen. Scattering of a Rayleigh wave by an elastic quarter space. *Journal of Applied Mechanics*, 52(3):664–668, 1985.

[74] K. Fujii, S. Takeuchi, Y. Okano, and M. Nakano. Rayleigh wave scattering at various wedge corners. *Bulletin of the Seismological Society of America*, 74(1):41–60, 1984.

[75] A. K. Gautesen. Scattering of a Rayleigh wave by an elastic wedge whose angle is greater than 180 degrees. *Journal of Applied Mechanics*, 68(3):476–479, 2001.

[76] A. K. Gautesen. Scattering of a Rayleigh wave by an elastic wedge whose angle is less than 180. *Wave Motion*, 36(4):417–424, 2002.

[77] A. K. Gautesen. Scattering of a Rayleigh wave by an elastic quarter space-revisited. *Wave Motion*, 35(1):91–98, 2002.

[78] B. V. Budaev and D. B. Bogy. Errata to the paper 'Rayleigh wave scattering by a wedge. II'[Wave motion 24 (1996) 307–317]. *Wave Motion*, 35(3):275, 2002.

[79] V. V. Kamotski and G. Lebeau. Diffraction by an elastic wedge with stress-free boundary: existence and uniqueness. In *Proceedings of the Royal Society of London A: Mathematical, Physical and Engineering Sciences*, volume 462, pages 289–317. The Royal Society, 2006.

[80] R. K. Chapman, S. F. Burch, N. J. Collett, and L. Ju. Fradkin. Ultrasonic inspection of tilted defects using the corner effect modelling and experimental validation. *Insight-Non-Destructive Testing and Condition Monitoring*, 50(2):66–69, 2008.

[81] L. Ju. Fradkin, A. Gautesen, V. Zernov, and M. Darmon. Elastic wave diffraction by infinite wedges. In *Journal of Physics: Conference Series*, volume 269, page 012021. IOP Publishing, 2011.

[82] E. Bossy. *www.simsonic.fr*.

[83] C. Gennarelli and L. Palumbo. A uniform asymptotic expansion of a typical diffraction integral with many coalescing simple pole singularities and a first-order saddle point. *Antennas and Propagation, IEEE Transactions on Antennas and Propagation*, 32(10):1122–1124, 1984.

[84] L. Bo. *Modélisation de la propagation et de l'interaction d'une onde acoustique pour la télémétrie de structures complexes*. PhD thesis, Université du Maine, 2011.

[85] A. Kamta Djakou, M. Darmon, and C. Potel. Elastodynamic models for extending GTD to penumbra and finite size flaws. In *Journal of Physics: Conference Series*, volume 684. IOP Publishing, 2016.

[86] N. Bleistein. Saddle Point Contribution for an n-fod Complex-Valued Integral. *http://www.cwp.mines.edu/ norm/Papers/steepdesc.pdf*, 2012.